

Classification and Petrogenesis

of New Martian Meteorite,

NWA 14904

By

EMILY JANE GACKSTATTER

Bachelor of Science, 2018

Baylor University

Waco, TX

Submitted to the Graduate Faculty

of the College of Science and Engineering

Texas Christian University

In partial fulfillment of the requirements

For the degree of

MASTER OF SCIENCE

DECEMBER 2022

CLASSIFICATION AND PRETROGENESIS
OF NEW MARTIAN METEORITE,
NWA 14904

By

Emily Jane Gackstatter

Thesis Approved:

R Mayne

Dr. Richard Hanson

Major Professor

Steve Singletary

Dr. Justin Filiberto

T. Ba

ACKNOWLEDGMENTS

To my advisor: Dr. Mayne, thank you not only for this opportunity, but for your support, endless patience, and wisdom (both in science and in life). For pushing me to be my best while reminding me that I am still a human that requires sleep. I will be forever grateful for my past two years here at TCU, and truly could not have done it without you.

To my committee: Dr. Hanson, thank you for every class you taught, the abundant questions you answered, and pushing me to be the student I am today. Dr. Singletary, thank you for imparting your knowledge of the probe, and hospitality while I traveled to North Carolina. Dr. Filiberto, thank you for your time, Martian expertise, and understanding throughout this process.

To friends and fellow graduate students: Thank you for keeping me sane, helping me learn, making me laugh, and building memories together these past two years. I truly cherish our camaraderie.

My dog, Miley: for her companionship, and reminding me to go outside.

To my parents: Thank you for always believing in me and providing me with the foundation for success. Your words of encouragement and advice helped tremendously, especially these past few years. This is my canoe:

TABLE OF CONTENTS

ACKNOWLEDGMENTS	ii
TABLE OF CONTENTS.....	iii
LIST OF FIGURES	viii
LIST OF TABLES	xiv
1. INTRODUCTION.....	1
1.1. Sample Background-NWA 14904	1
1.2. Objectives.....	1
2. BACKGROUND.....	3
2.1. Meteorite Classification	3
2.2. Importance and Implication of Martian Meteorites	5
2.3. Martian Meteorites	6
2.3.1. Constraining the Martian Origin of Meteorites	6
2.3.2. Shergottites	8
2.3.3. Nakhrites and Chassignites	11
2.3.4. Ungrouped Martian Meteorites.....	14
2.4. Shock Metamorphism	16
2.4.1. Shock Mechanisms	16
2.4.2. Shock minerals and features	18

3. METHODS.....	19
3.1. Preservation.....	19
3.1.1. 3D Scanner.....	19
3.1.2. Photogrammetry.....	20
3.1.3. Computed Tomography (CT)	20
3.2. Analysis.....	22
3.2.1. Classification.....	22
3.2.2. Thin Sections	24
3.2.3. Petrographic Analysis	24
3.2.4. Scanning Electron Microprobe (SEM)	25
3.2.5. Electron Microprobe (EMP)	27
3.2.6. Modal Abundance Calculation	28
3.2.7. Modal Mineralogy	32
3.2.8. Bulk Composition	34
4. RESULTS.....	36
4.1. Whole-rock description.....	36
4.2. CT Results.....	37
4.3. Modal Mineralogy.....	41
4.4. Bulk Composition	45
4.5. Petrography	46

4.5.1. Textural Descriptions.....	52
4.5.2. Olivine.....	52
4.5.3. Pyroxene	55
4.5.4. Maskelynite.....	58
4.6. Shock Features	60
4.6.1. Introduction.....	60
4.6.2. Shock Melt.....	60
4.6.3. Olivine.....	60
4.6.4. Maskelynite.....	63
4.7. Shock Classification.....	63
4.8. Terrestrial Alteration	63
4.9. Electron Microprobe	68
4.10. Classification.....	72
5. DISCUSSION.....	72
5.1. Confirming Martian Origin	72
5.2. Poikilitic Shergottites	75
5.2.1. Olivine Sampling Bias	78
5.2.2. Bulk Composition	78
5.2.3. Modal Mineralogy	80
5.2.4. Textures and composition	80

5.3. Petrogenesis of NWA 14904.....	89
5.3.1. Two-Stage Crystallization	90
5.3.2. Crystallization Sequence.....	90
5.3.3. Crystallization Depth	91
5.3.4. Shock History.....	92
5.4. Future work	95
5.4.1. Age Dating.....	95
5.4.2. Bulk Composition	95
5.4.3. Oxygen fugacity.....	96
5.4.4. Crystal Size Distribution.....	97
5.4.5. Sm-Nd Crystallization Ages and Cosmic Ray Exposure.....	97
5.4.6. Other thin sections	98
6. CONCLUSION	99
6.1. Classification.....	99
6.2. Formation model for NWA 14904	99
7. APPENDIX	101
7.1. EMP.....	101
7.1.1. Probe Recipes.....	101
7.1.2. Probe Site Locations	105
7.1.3. Probe Data.....	106

7.2. Comparison Data Tables	155
7.3. Elemental Maps.....	168
8. REFERENCES.....	182
9. VITA.....	195
10. ABSTRACT	196

LIST OF FIGURES

Figure 1. Meteorite Classification Scheme (from Weisberg et al., 2006). Meteorites are divided into three main groups based on their formation (chondrites, primitive achondrites, and achondrites) and then into different classes, clans, groups, and subgroups. URE-ureilite, ACA-acapulcoite, LOD-lodranite, ANG- angrite, AUB-aubrite, BRA-brachinitite, WIN-winonaite, HED-howardite-eucrite-diogenite, MES-mesosiderite, MG PAL-main-group pallasite, ES PAL-Eagle Station pallasite, PP PAL- pyroxene pallasite, SHE-shergottite, NAK-nakhlite, CHA-chassignite, OPX-orthopyroxenite	4
Figure 2. The three Geochemical Groupings of Shergottites– enriched, intermediate, and depleted – as defined by their $^{176}\text{Lu}/^{177}\text{Hf}$ vs $^{147}\text{Sm}/^{144}\text{Nd}$ isotopes (from Udry et al., 2020).	10
Figure 3. NSI Scanner at UTCT with the complete 800 g stone of NWA 14904 loaded into the plexiglass cylinder.....	21
Figure 4. Mapping Grid Coordinate system used for both Backscattered Electron Images (BSE) and elemental x-ray maps.	26
Figure 5. Phase Map that shows the extent of the melt (black) within section 01 of NWA 14904.....	31
Figure 6. BSE of Melt showing zoned olivine microlites (light gray getting darker in gray scale value moving from rim to core). Shock melt glass matrix (medium gray) surrounds the zoned olivine microlites. Carbonate alteration of shock melt (dark gray with cracks) is also present and can be seen throughout the melt. White scale bar represents 10 μm	32

Figure 7. NWA 14904 as a whole rock 800g single stone. Sample is ~95mm across in this orientation.....	36
Figure 8. NWA 14904 Whole Rock Features. Sample is ~95mm from front to back in this orientation. Image exposure has been increased to highlight color and textural differences between features. A. fusion crust; B. terrestrial alteration; C. vesicles; D. glass melt.....	37
Figure 9. CT slice of NWA 14904 whole rock. Slice is 60mm across.....	38
Figure 10. CT slices of NWA 14904 174.97 g end cut displaying bimodal texture: poikilitic texture (outlined in red), and non-poikilitic texture. (a) Slice is 64mm across and contains poikilitic areas ~15 mm in length. In comparison (b) Slice is 64 mm across and only contains poikilitic areas ~35mm in length. This demonstrates the different size and shape of the poikilitic and non-poikilitic areas throughout the sample.....	40
Figure 11. CT slice of NWA 14904 174.97 g end cut showing evidence for vesicles in melt glass (outlined in yellow).....	41
Figure 12. Section 01 Phase Map. Different colors represent the presence of different mineral phases in NWA 1409, thin section 01.....	42
Figure 13. Modal Abundance Plot. Displays the modal mineralogy calculated three different ways. 1) with the melt as a separate phase; 2) with the melt removed under the assumption that the melt has the same modal abundances as the whole sample; 3) with the melt included under the assumption that its composition is 100% olivine.....	43
Figure 14. Plane Polarized Light (PPL) Composite Image, showing shock melt pockets (black).....	47
Figure 15. Cross Polarized Light (XPL) Composite Image.....	48

Figure 16. Reflected Light Composite Image.....	49
Figure 17. Backscatter Electron (BSE) Composite Map.	50
Figure 18. BSE Composite Map Showing Poikilitic texture outlined in red, with two different sizes of pyroxene oikocrysts. This highlights the size difference observed between large- and small-scale poikilitic texture.....	51
Figure 19. A variety of olivine textures seen in NWA 14904 a) BSE image of olivine reaction textures next to carbonate veins (A) and pyroxene (dark gray) melt inclusion of with vermicular intergrowth (B); b) BSE image showing melt band inclusion from shock melt in olivine; c) BSE image of shock melted olivine with evidence of olivine dendrites, and leopard olivine; d) PPL image of terrestrial alteration of carbonate veins cross cutting olivine grains.....	54
Figure 20. Pyroxene Textures a) BSE image of small-scale poikilitic texture; b) BSE image of large-scale poikilitic texture; c) BSE image of melt inclusion in olivine showing sieve texture	56
Figure 21. BSE images of two large-scale pyroxene oikocrysts. Cross hairs indicate probe locations from EMP. Cross hairs with circles indicate probe data used for this study, whereas cross hairs without circles indicate a probe analysis where the totals were too low to be used here. In both (a) and (b) the high-Ca analyses lie towards the rim of the pyroxene oikocryst.	57
Figure 22. BSE images of maskelynite a) maskelynite laths; b) angular maskelynite grains; c) carbonate vesicles in maskelynite; d) carbonate vesicles in maskelynite near shock melt pocket; e) carbonate veins cross cutting maskelynite.	59

Figure 23. Shock Effects a) PPL image, shock melt pockets and shock melt veins (black); b) PPL image, shock darkened olivine; c) PPL image, Grain A and Grain B both showing lack of fracture; d) XPL image, Grain A displays an abnormally high birefringence interference color; e) XPL image, olivine grains near shock melt edge show partial destruction or complete vaporization.....	62
Figure 24. Carbonate Veins a-b) Reflected light image of carbonate veins; c-d) BSE images of dendritic textures in carbonate veins	65
Figure 25. BSE image of carbonate filled vesicles in maskelynite.....	66
Figure 26. BSE image showing carbonates altering shock melt. Olivine microlites dominate the melt and are zoned. Their brighter edges suggest that they are more Fe-rich at their rims.	67
Figure 27. Mg# plotted vs. (a) Al ₂ O ₃ (b) Cr ₂ O ₃ (c) CaO (d) TiO ₂ . Low-Ca poikilitic pyroxenes are richer in Mg than their poikilitic counterparts, as reflected by their higher Mg#. High-Ca pyroxenes are higher in Al ₂ O ₃ , Cr ₂ O ₃ , CaO, and TiO ₂ as compared to low-Ca pyroxenes. P=poikilitic, NP=non-poikilitic.....	70
Figure 28. Mn vs Fe plotted for NWA 14904 olivine and compared to reported Mn/Fe trends for Mars, Earth, and the Moon (Papike et al., 2009)	75
Figure 29. Bulk Oxides vs Mg# NWA 14904 (black), intermediate samples (blue), and enriched samples (red). The Mg# for NWA 14904 is anomalously low due to a data collection bias.	79

Figure 30. Comparison of Fo compositional ranges within the non-poikilitic olivine of NWA 14904 and other poikilitic shergottites (both intermediate and enriched). NWA 14904 overlaps the range given for the intermediate shergottites.	81
Figure 31. Pyroxene quadrilateral with NWA 14904 pyroxene compositions compared to other poikilitic shergottites of both the enriched and intermediate geochemical groups. NWA 10169 is not included in this plot as its compositions are not comparable to other specimens due to zonation.	82
Figure 32. Comparison of the range of Mg# in non-poikilitic high-Ca pyroxene within NWA 14904 and the comparative suite of poikilitic shergottites.	83
Figure 33. Comparison of the range of Mg# in non-poikilitic low-Ca pyroxene within NWA 14904 and the comparative suite of poikilitic shergottites.	83
Figure 34. Comparison of the range of Mg# in poikilitic high-Ca pyroxene within NWA 14904 and the comparative suite of poikilitic shergottites.	84
Figure 35. Comparison of the range of Mg# in poikilitic low-Ca pyroxene within NWA 14904 and the comparative suite of poikilitic shergottites.	85
Figure 36. Ti vs Al of pyroxenes within a) NWA 14904 and ;b) from Rahib et al., (2019) “enriched (circle) and intermediate (triangle) poikilitic pyroxenes, including low-Ca (solid symbols) and high-Ca (open symbols). Isobars are calibrated experimentally from Nekvasil et al. (2004) and Filiberto et al. (2010). Most poikilitic pyroxenes have crystallized at the martian lower crust. Exact pressures were not included here as Nekvasil et al. (2004) barometry was calibrated for terrestrial conditions.”	86

Figure 37. Comparison of An-value in maskelynite within NWA 14904 and the comparative suite of poikilitic shergottites.....	87
Figure 38. NWA 14904 Oxide Compositions: chromite (dark purple) and ilmenite (light purple).	88
Figure 39. EMP Probe Site Locations.....	105
Figure 40. Al elemental map.....	168
Figure 41. C elemental map	169
Figure 42. Ca elemental map	170
Figure 43. Co elemental map	171
Figure 44. Cr elemental map.....	172
Figure 45. Fe elemental map.....	173
Figure 46. Mg elemental map	174
Figure 47. Mn elemental map	175
Figure 48. Na elemental map	176
Figure 49. Ni elemental map.....	177
Figure 50. P elemental map.....	178
Figure 51. Si elemental map	179
Figure 52. Ti elemental map	180
Figure 53. S elemental map.....	181

LIST OF TABLES

Table 1. Image Thresholding for Phase Maps.....	30
Table 2. Mineral Densities used in bulk composition calculation.	35
Table 3. Modal Mineralogy Calculations.....	44
Table 4. Bulk Composition	45
Table 5. Summary of EMP Mineral Compositions for all major phases	68
Table 6. Different Bulk Mg# reported for Martian samples in the literature.....	74
Table 7. Comparative Suite of Poikilitic Shergottites.....	77
Table 8. Fritz et al. (2017) Shock Classification Scheme	93
Table 9. Stöffler et al. (2018) Shock Classification Scheme	94
Table 10. Olivine EMP recipe.....	101
Table 11. Pyroxene EMP recipe.....	102
Table 12. Maskelynite EMP recipe.....	102
Table 13. Carbonates EMP recipe.....	103
Table 14. Phosphates EMP recipe.....	103
Table 15. Oxides EMP recipe	104
Table 16. Sulfides EMP recipe.....	104
Table 17. NWA 14904 Olivine Compositions	106
Table 18. NWA 14904 Low-Ca Pyroxene Compositions.....	114

Table 19. NWA 14904 High-Ca Pyroxene Compositions	119
Table 20. NWA 14904 Maskelynite Compositions	126
Table 21. NWA 14904 Carbonate Vein Compositions.....	129
Table 22. NWA 14904 Carbonate Vesicle Compositions.....	135
Table 23. NWA 149404 Chromite Compositions.....	148
Table 24. NWA 14904 Ilmenite Compositions.....	151
Table 25. NWA 14904 Merrillite Compositions.....	152
Table 26. Modal Mineralogy Comparisons.....	155
Table 27. Bulk Composition Comparisons	156
Table 28. Olivine Comparisons.....	157
Table 29. Pyroxene Comparisons.....	159
Table 30. Maskelynite Comparisons	163
Table 31. Oxide Comparisons	164

1. INTRODUCTION

1.1. Sample Background-NWA 14904

The study of extraterrestrial materials and meteorites provides valuable insight into the Solar System. Meteorites are nature's sample return missions, enabling earthbound studies of many solar system bodies that would be otherwise unobtainable. The aim of this work is to classify and characterize a previously unstudied, and therefore unclassified, meteorite: NWA 14904.

NWA 14904 was acquired as an individual 800g stone by Mr. Philip Mani from Mr. Adam Aronson in 2019. Mr. Mani donated two pieces of the stone weighing 174.97g and 4.67g to the Monnig Meteorite Collection. External visual examination of the sample suggested that NWA 14904 was Martian in origin; however, this can only be confirmed through analysis of textures and mineral chemistry.

1.2. Objectives

This study had two distinct stages, each with its own overall goal and objectives.

Goal 1: Preserve a record of the complete sample

Even the most conservative classification procedures require that a section of meteorite is removed for analysis. Mr. Mani requested that a record of the complete 800g stone of NWA 14904 be produced before any material was removed and donated for analysis.

Objective 1.1: Produce 3D models of the exterior of NWA 14904.

Exterior models of NWA 14904 are crucial in preserving a record of the whole-rock sample. Two different modeling methods were used to ensure thorough preservation, and to determine which method best captured the sample's features. This first method utilized an EinScan XP 3D laser scanner and the software provided to produce 3D reconstructions of NWA 14904. The second method utilized a method known as photogrammetry, which entails the combination of high-definition photographs. Agisoft software was used to process the photogrammetry data.

Objective 1.2: Collect data that allow us to examine the interior of NWA 14904 before it is cut.

A computed tomography (CT) scan allowed for an interior view of NWA 14904 to be preserved. These scans can show mineralogical and textural differences in meteorites as well as a 3D view of the geometries. The complete 800g stone was scanned at the High-Resolution X-ray Computed Tomography Facility at The University of Texas at Austin.

Goal 2: Complete a detailed scientific study of NWA 14904 that allows us to place it in context within the existing dataset for Martian meteorites.

Objective 2.1: Classify NWA 14904.

Classification of meteorites is needed to better understand the link between a sample and its parent body, as is described in more detail below (Section 2.1). Classification and

characterization of NWA 14904 was achieved through petrographic observations of mineralogy and texture, and analysis of the mineral chemistry of all major phases.

Objective 2.2: Develop a model for the petrogenesis of NWA 14904.

The data collected in objective 2.1 allowed NWA 14904 to be compared to meteorites within the same classification group to create a petrogenetic model. The results provide insight into the formation of the meteorite, the processes it experienced on the Martian surface, and ejection from its parent body. These goals and objectives allow me to answer the following questions:

- Is the sample from Mars?
- What classification group does this meteorite best fit under?
- Based on the petrologic data, how was this meteorite formed?

2. BACKGROUND

2.1. Meteorite Classification

Classification is an important method in many scientific disciplines. It not only acts as a powerful tool for discovering the relationships between the objects being classified, it also allows us to more easily organize information about them. Meteorites are classified into three main categories based on how they formed: achondrites, chondrites, and primitive achondrites (**Figure 1**). These are then further subdivided into classes, clans, groups, and subgroups, with an end goal of grouping samples from the same parent body together (Weisberg et al., 2006).

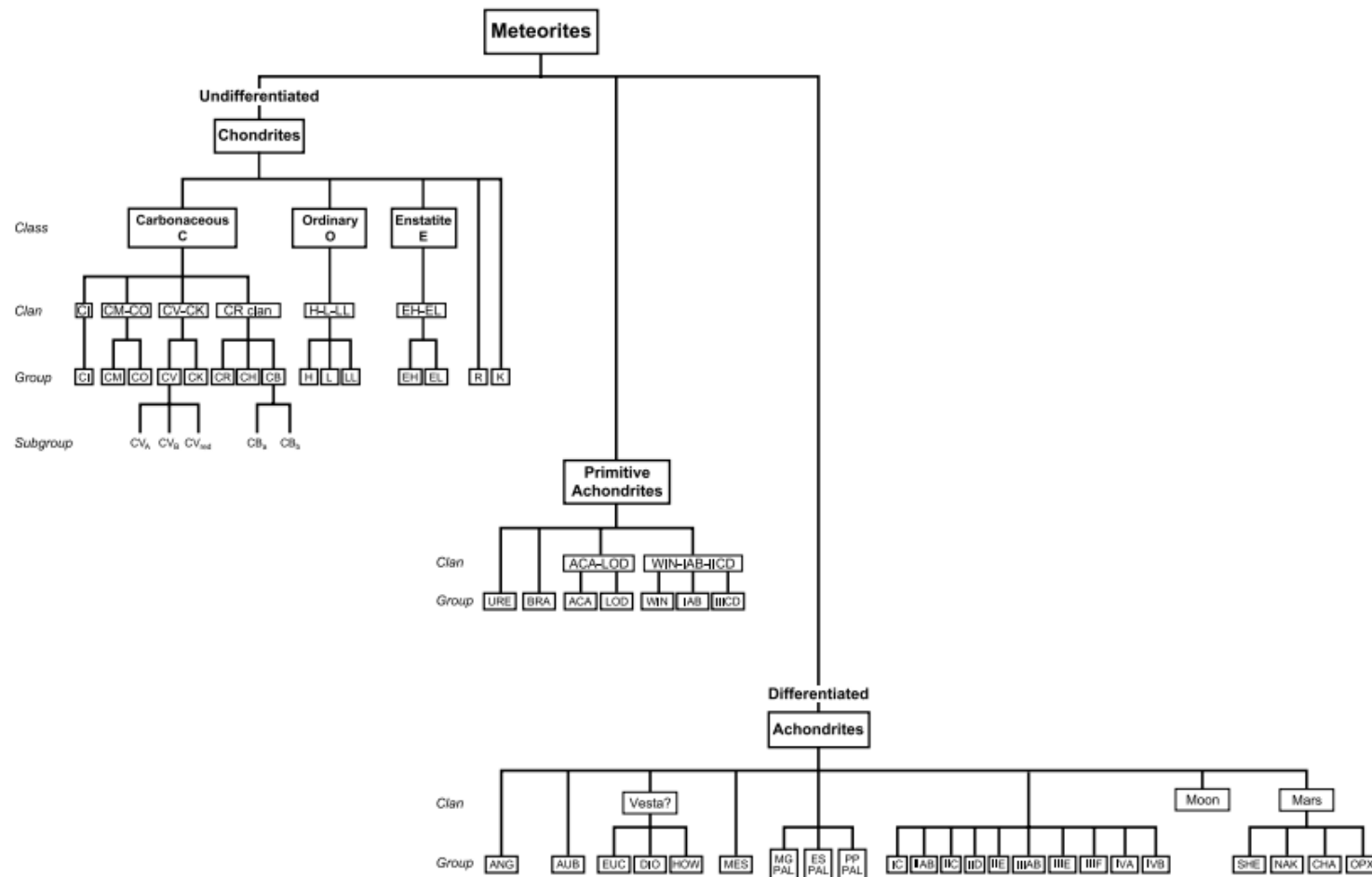


Figure 1. Meteorite Classification Scheme (from Weisberg et al., 2006). Meteorites are divided into three main groups based on their formation (chondrites, primitive achondrites, and achondrites) and then into different classes, clans, groups, and subgroups. URE-ureilite, ACA-acapulcoite, LOD-lodranite, ANG-angrite, AUB-aubrite, BRA-brachinitite, WIN-winonaite, HED-howardite-eucrite-diogenite, MES-mesosiderite, MG PAL-main-group pallasite, ES PAL-Eagle Station pallasite, PP PAL-pyroxene pallasite, SHE-shergottite, NAK-nakhlite, CHA-chassignite, OPX-orthopyroxenite

Chondrites are meteorites that preserve the earliest solids that formed in our solar system. They take their name from chondrules, spherical melt droplets that formed within the proto-planetary disk. They derive from undifferentiated asteroids (or the undifferentiated portion of partially differentiated asteroids) that have not undergone melting, whereas achondrites are igneous meteorites that originate from partially or completely differentiated planetary bodies, such as Mars. As their name suggests, achondrites do not contain chondrules because these meteorites have an igneous origin and formed as a result of chondrite melting. Primitive achondrites lie between the two other groups, having some characteristics from each; many primitive achondrites contain relict chondrules and have trace element compositions similar to chondrites, but they also exhibit igneous textures, suggestive of partial melting in a similar manner to achondrites (Mittlefehldt, 2005). All of these meteorites provide valuable insight into their parent bodies and, in turn, help elucidate the formation and evolution of the Solar System.

2.2. Importance and Implication of Martian Meteorites

Over decades of meteorite collection, observation, and examination, scientists have gained a more in-depth understanding of planetary bodies. Martian meteorites represent the only physical samples available of a planetary surface, excluding Earth, which makes them fundamentally important for furthering scientific knowledge on not only the formation and evolution of Mars, but all of the terrestrial planets (including Earth).

Prior to the identification of meteorites from Mars, the only data available were provided by a few flyby missions, orbiting spacecraft, and most importantly, rovers and landers on its surface (e.g., Viking 1 and 2 in the late 1970s). All of these missions were only

able to gather data from the Martian surface and atmosphere, so the insight they could provide into Martian history was limited (Udry et al., 2020). However, the collection and analysis of Martian meteorites has provided insight into processes fundamental to the formation of Mars, such as magma generation and emplacement, volcanic activity (Elkins-Tanton et al., 2003; Stolper and McSween, 1980), accretion and differentiation (Foley et al. 2005), behavior and content of volatile compounds (Taylor, 2013), and effects of impact events (see recent summary by Udry et al., 2020). Therefore, without the study of meteorites, our understanding of Mars would be far more limited.

2.3. Martian Meteorites

Martian meteorites are currently broadly divided into four separate groups (**Figure 1**): Shergottites, Nakhrites, and Chassignites (known collectively as the SNCs), and those that do not fit into the SNC classification (Weisberg et al., 2006). Before reviewing each of these groups in more detail, the evidence used to first connect these samples to Mars will be discussed.

2.3.1. Constraining the Martian Origin of Meteorites

2.3.1.1. Oxygen isotopes

The SNC meteorites were first grouped together based on their oxygen isotopic compositions (Clayton and Mayeda, 1983; Clayton and Mayeda, 1986; McSween, 1994). The stable isotopes of oxygen (O^{16} , O^{17} , O^{18}) were heterogeneously distributed throughout the early Solar System (Clayton et al., 1973). As a result, objects in our solar system formed from reservoirs with different initial isotopic signatures. This isotopic signature can

subsequently be altered through a process known as fractionation, where chemical and physical processes result in changes to the relative isotopic proportions. A plot of $\delta^{17}\text{O}$ vs. $\delta^{18}\text{O}$, where δ is the enrichment or depletion of these isotopes relative to a standard in parts per mil, gives a linear array of data points which is characteristic of the bulk composition of a particular body and is known as a fractionation line. Oxygen isotopes can, therefore, be used to group meteorites together by their parent body (Clayton, 2006).

Clayton and Mayeda (1983) noted that all SNCs plot on a fractionation line similar to that of the terrestrial fractionation line, but displaced from it (Clayton and Mayeda, 1983; McSween, 1994). This suggests that the SNCs were from a single parent body, but that they could not originate from Earth (Clayton and Mayeda, 1983). However, while oxygen isotopes can be used to group like samples together, these data do not provide any information about which parent body the samples originated from.

2.3.1.2. Age Dating

Shortly after the SNCs were linked together by their oxygen isotopic composition, the first line of evidence linking them to Mars emerged: their age (McSween, 1985; McSween, 1994). The radiometric age dating of shergottite meteorites revealed geologically young crystallization ages of $\sim 1.3\text{ Ga}$ (Shih et al., 1982; Wooden et al., 1982), suggesting that the SNC meteorites, which are igneous in origin, likely originated from a differentiated planetary body. Igneous activity on an asteroidal-sized body late in solar system history is difficult to explain, as asteroids lost their heat very early in solar system history (Wasson and Wetherill, 1979); therefore, young ages indicate a planetary origin. While we now know that the SNCs

come from Mars (Nyquist et al., 1979; Wasson and Wetherill, 1979), age dating alone was not sufficient to make that petrogenic link (McSween, 1994).

2.3.1.3. Trapped Gases

Concrete evidence that some meteorites originated from Mars came later from the isotopic analysis of gas trapped in inclusions of shock-melted glass within Martian meteorites (McSween, 1994; Bogard and Johnson, 1983). These gas bubbles are hypothesized to be implanted through shock metamorphism during impact and ejection of the meteorite and they provide a sample of the atmosphere from the SNC's parent body. The trapped gases were analyzed and compared to measurements of the Martian atmosphere collected by the Viking landers and were found to match (Bogard and Johnson, 1983; Becker and Pepin, 1984; McSween, 1994; Nyquist, 2001). This definitively linked the SNC meteorites to Mars.

2.3.2. *Shergottites*

Shergottites, named after the first sample found, Shergotty, are the most common type of Martian meteorite. Shergottites encompass 89% of all Martian meteorites. They are igneous and mafic to ultramafic in lithology.

2.3.2.1. Petrology and Chemistry

Shergottites are classified in two different ways. The first classification scheme is based on mineralogy and texture, and divides shergottites into four separate groups: basaltic, olivine-phyric, poikilitic, and gabbroic. Augite-rich shergottites, which have older crystallization ages and distinctly different textures than most shergottites, are sometimes

referred to as their own group; however, the traditional classification scheme does not recognize them as such (Herd et al., 2017). Instead, augite-rich shergottites are considered a subgroup as their ejection ages and mineralogy (with the exception of increased abundance of augite) are similar to those of other shergottites (Herd et al., 2017; Udry et al., 2020).

The most abundant shergottites are basaltic shergottites (Udry et al., 2020). They are characterized by the presence of pyroxene (typically pigeonite with lesser augite) and maskelynite (shocked plagioclase) and lack of olivine phenocrysts or megacrysts (e.g., McSween and Treiman 1998). Second in abundance (Udry et al., 2020), olivine-phyric shergottites are porphyritic and contain olivine phenocrysts, and later crystallized finer grained olivine, pyroxene, and maskelynite (e.g., Goodrich, 2002). Poikilitic shergottites contain olivine chadacrysts enclosed by large pyroxene oikocrysts, later crystallized olivine, and maskelynite (Combs et al., 2019; Rahib et al., 2019). Previously, this group was termed lherzolitic shergottites; however, lherzolites by definition contain 40-90% olivine and less than 10% plagioclase and are ultramafic plutonic rocks. The poikilitic shergottites do not meet either of these criteria (Mikouchi, 2009; Walton et al, 2012). Finally, gabbroic shergottites are similar to their basaltic relatives as both form from a relatively evolved parent magma and have undergone previous olivine fractionation and crystallization stages and therefore lack olivine phenocrysts (Udry et al., 2020 and references therein). However, gabbroic shergottites display cumulate textures unlike basaltic shergottites (Udry et al., 2020; Filiberto et al., 2017).

The second classification scheme breaks shergottites down into three geochemical groups based on their incompatible trace elements (ITE), abundance of rare earth elements

(REE), and $^{147}\text{Sm}/^{144}\text{Nd}$ and $^{176}\text{Lu}/^{177}\text{Hf}$ isotopic ratios (Borg and Draper, 2003) (**Figure 2**).

The varying abundances of these trace elements and isotopes are thought to reflect either different magma sources or crustal contamination (Borg and Draper, 2003) and enable shergottites to be separated into enriched, intermediate, or depleted geochemical groups (Bridges and Warren, 2006). REE compositions of enriched shergottites have $(\text{La/Yb})_{\text{CI}}$ ratios >0.8 because they are richer in incompatible lightREEs. Enrichment in ITE is associated with relatively high initial $^{87}\text{Sr}/^{86}\text{Sr}$, $^{207,206,208}\text{Pb}/^{204}\text{Pb}$, and $^{187}\text{Os}/^{188}\text{Os}$ ratios, and relatively low initial $^{142,143}\text{Nd}/^{144}\text{Nd}$ and $^{176}\text{Hf}/^{177}\text{Hf}$ ratios. Depleted shergottites have much lower $(\text{La/Yb})_{\text{CI}}$ ratios of <0.3 with relatively low initial $^{87}\text{Sr}/^{86}\text{Sr}$, $^{207,206,208}\text{Pb}/^{204}\text{Pb}$, and $^{187}\text{Os}/^{188}\text{Os}$ ratios, and relatively high initial $^{142,143}\text{Nd}/^{144}\text{Nd}$ and $^{176}\text{Hf}/^{177}\text{Hf}$ ratios. Intermediate shergottites represent the range between enriched and depleted with $(\text{La/Yb})_{\text{CI}}$ ratios between 0.3-0.8 (Udry et al., 2020 and references therein).

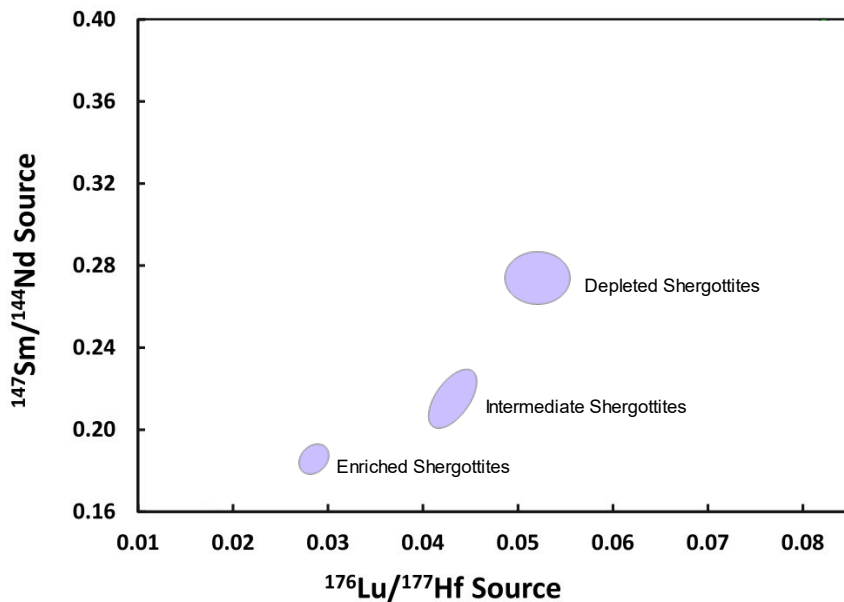


Figure 2. The three Geochemical Groupings of Shergottites – enriched, intermediate, and depleted – as defined by their $^{176}\text{Lu}/^{177}\text{Hf}$ vs $^{147}\text{Sm}/^{144}\text{Nd}$ isotopes (from Udry et al., 2020).

2.3.2.2. Formation Mechanisms

It is theorized that, early in its history, Mars went through a global magma ocean phase (Halliday et al., 2001). As the global magma ocean started to cool, Mars differentiated to produce the shergottite source region. Varying ITE composition ranges resulted from this differentiation as the silicate magmas cooled (Elkins-Tanton et al., 2003). Experimental evidence also suggests that most shergottites are fractionated derivatives of primary melts (Stolper and McSween, 1979); however, some of the olivine-phyric shergottites represent primary melt compositions (e.g., Filiberto and Dasgupta, 2011).

2.3.3. *Nakhrites and Chassignites*

Nakhrites and chassignites are often grouped together because they have marked similarities in crystallization and ejection ages (Nyquist et al., 2001; Udry and Day, 2018), as well as depleted radiogenic isotopic compositions (Carlson and Boyet, 2009; Nyquist et al., 2001). These meteorite groups were named after the first samples found, Nakhla and Chassigny, respectively. Together, nakhrites and chassignites encompass ~ 10% of all Martian meteorites (Udry et al., 2020).

2.3.3.1. Petrology and Chemistry

Nakhrites are augite-rich igneous clinopyroxenites. Their most abundant mineral is augite, while olivine, plagioclase, K-feldspar, Fe-Ti oxides, pyrite, and chalcopyrite are less abundant (Treiman, 2005). Augite and olivine are the most commonly

found coarse-grained minerals, with pyroxenes showing preferential alignment, while olivine is often found between or enclosing augite (Treiman, 2005). Nakhrites show a characteristic fine-grained matrix between larger augite and olivine grains, which contain equant crystals of titanomagnetite and plagioclase laths (Sautter et al., 2002; Treiman, 2005). Various anhydrous minerals lie between the plagioclase laths. The characteristic coarse-grained crystals and fine-grained matrices are seen in nearly all nakhrites (Treiman, 2005). Nakhrites are strongly enriched in REEs, and show LREE enrichment despite being formed from a source mantle strongly depleted in these elements. In the mineral assemblages of concern here, La, U, and Th would typically be expected to show the most incompatible behavior. However, nakhrites show a trend of U and Th abundances being unusually depleted compared to La. While the mechanism of LREE enrichment is unknown, the ratios of U and Th compared to La indicates the source mantle for nakhrites may have undergone an event to strongly deplete the highly incompatible elements (Treiman, 2005). Minerals such as calcium carbonate (most likely calcite), magnesium sulfates, halite, and gypsum are also present, which suggests secondary processes occurred after the initial igneous activity (Gooding et al., 1991).

Chassignites are dunites that contain olivine with minor amounts of chromite inclusions, interstitial plagioclase crystals, orthopyroxene, and various phosphate minerals (Treiman, 2005).

2.3.3.2. Formation Mechanisms

Nakhrites are cumulate rocks, in which pyroxene and olivine are the major cumulus phases (Treiman, 2005; Udry et al., 2020), and therefore their whole-rock compositions do

not reflect the bulk compositions of their parent magmas (Treiman, 2005). Trace element contents in nakhlites, specifically their low levels of U and Th in comparison to La (Jones, 1995; Treiman, 2005) are suggestive of the occurrence of an early partial melting event that depleted the source mantle of incompatible trace elements (Sun and McDonough, 1989).

Nakhlites often show evidence of liquid water infiltration taking place after solidification. This infiltration led to the deposition of salts, the dissolution of olivine, and the precipitation of smectite clays and hydrous iron oxides (Treiman, 2005). These nakhlites were then ejected from Mars due to an impact event, as shown by evidence of shock metamorphism (Bridges and Schwenzer, 2012). The effect of shock metamorphism is not as pronounced in nakhlites as compared to other Martian meteorites (Stöffler, 2000). However, there is still a notable amount of metamorphism present, especially in plagioclase (Treiman, 2005). The pyroxenes and olivine grains show minor shock features as well. The structural shock deformation features include micro-faults and unusual brecciated zones (Gooding et al., 1991).

Chassignites are cumulate igneous rocks formed from a large, differentiated magmatic source. While they were originally thought to have different origins, chassignites and nakhlites are similar in age, geochemistry, and texture (Treiman, 2005; McCubbin et al., 2013; Udry and Day, 2018), and it was, therefore, proposed that they were part of the same magmatic system as a single cumulate pile (Berkley et al., 1980). Then, due to their similarities in $^{87}\text{Sr}/^{86}\text{Sr}$ and $^{143}\text{Nd}/^{144}\text{Nd}$ initial isotopic ratios, it was theorized that both nakhlites and chassignites originated from a single large, lava flow or shallow intrusion (Jones 1989; Jones, 2003) However, the collection and study of more nakhlites and

chassignites revealed a wider range in chemical and mineral composition than was originally observed, suggesting that the two groups come from several igneous intrusions or lava flows (Udry et al., 2020; Corrigan et al., 2015). Sn abundances in chassignites also supports the idea that the two groups must originate from different source melts. Chassignites have a very high Sn/Sm ratio compared to nakhlites, which was likely caused by contamination from Sn in the surrounding country rock, as Sn-bearing minerals are known to be susceptible to leaching by Cl-rich hydrothermal fluids (Humayun and Yang, 2020). These hydrothermal fluids are inferred to have been present at the beginning of magmatism and later dissipated as magmatism continued.

Radiometric age dating provides evidence that, after the magmas cooled, there was a large-scale impact event that caused the spallation of both chassignites and nakhlites at the same time. This explains the similar ages measured for the two groups while allowing for their formation from different source magmas.

2.3.4. Ungrouped Martian Meteorites

2.3.4.1. Allan Hills 84001

Allan Hills 84001 is an igneous cumulate orthopyroxenite. This sample is perhaps the most famous of all Martian meteorites as it was originally suggested it may contain evidence of life on Mars (McKay et al., 1996). However, this hypothesis was later revised (Anders et al., 1996). The main minerals include augite, olivine, and apatite, and minor chromite, maskelynite, and phosphates, and very small amounts of secondary phase minerals (Meyer, 2012; Udry et al., 2020). Carbonates and phyllosilicates are relatively abundant and are the

result of low-temperature aqueous alteration of crustal rocks (Beard et al., 2013). Magnetite was then formed after impact events from shock metamorphism. These impact events produced features such as carbonate pancakes (named for their flattened shape), feldspathic glass crystals, and crystalline silicates (Treiman, 2010). Allan Hills 84001 is of igneous origin and underwent multiple shock events before spallation from Mars (Eugster et al., 2002; Mittlefehldt, 1994; Treiman, 2010; Udry et al., 2020). Originally formed from basaltic magma, this sample shows evidence that four or five major crater-forming events have effected the rock (Treiman, 2010). The first impact is recorded by intense shear activity and potentially represents excavation. The second impact created fractures in which carbonate pancakes and globules were deposited. The third impact had distinct melting effects along with micro-faulting, intense fracturing, and shearing. During the fourth impact, there was fracturing but not major heating. There is some debate as to whether Allan Hills 84001 was ejected during the fourth impact or if there was an additional fifth impact forming similar features to the fourth impact (Treiman, 2010).

2.3.4.2. NWA 7034 and Pairs

NWA 7034, a single 320g stone, and 18 additional meteorites with nearly identical texture and mineralogy are often referred to collectively as “NWA 7034 and pairs”(Ruzicka et al., 2014). The term “pairs” is assigned to samples that are believed to be from the same meteorite but were collected as separate stones. NWA 7034 and its pairs contain igneous clasts with a range of compositions including basalt, mugearite, trachyandesite, norite, gabbro, and monzonite (Santos et al., 2015; Hewins et al., 2017). NWA 7034 contains

zircons in its igneous clasts, which are dated as the oldest Martian minerals with ages as old as ~4.4Ga (McCubbin et al., 2016).

NWA 7034 has been identified as a polymict regolith breccia, and alteration of its clasts suggests that it originated from an area that underwent hydrothermal activity. There are many lithologies and compositions within the samples, ranging from igneous to sedimentary clasts. The brecciation is most likely the result of a pyroclastic eruption, or an impact event followed by a thermal event that caused lithification (Bridges et al., 2017). The zircons found in NWA 7034 suggest that an enriched, andesitic primordial crust may have been present at the last stage before crystallization (Baziotis et al., 2018). Growth textures of these zircons also provide documentation of low-shock events, suggesting a period of distinct impact events on the Martian surface (Moser et al., 2019).

The mineral compositions of clasts within individual samples provide evidence that the clasts within the parent meteorite originated from distinct parent melts. This is consistent with spectral data of the Martian surface, which indicates that the Martian regolith contains brecciated material as a result of intense bombardment of the Martian surface (Cannon et al., 2015)

2.4. Shock Metamorphism

2.4.1. Shock Mechanisms

Shock metamorphism is commonly seen in Martian meteorites and can provide insight into a sample's post-crystallization formation history. Shock metamorphism is the characteristic transformation in minerals caused by shock-induced increases in pressure

and/or temperature (Fritz et al., 2017). The following information is taken from Stöffler et al. (1988) and Bischoff and Stöffler (1992) which are used as core references for the effects of shock metamorphism as they are considered the seminal works on this topic. Shock in meteorites can occur through two mechanisms. The first is through classic shock metamorphism, defined as the mechanical deformation and transformation of rocks below or above the solidus by shock compression. The second is by ballistic or non-ballistic transport to form breccias through the relative movement of rock fragments and melt displacement. Shock compression can occur due to impacts and creates distinct combinations of shock metamorphism and brecciation. It is important to note that while brecciation is seen in some ungrouped Martian meteorites, such as basaltic breccia NWA 7034 (described in Section 2.3.4.2 above), brecciation is not seen within the SNC meteorites.

Shock metamorphism in meteorites is proposed to have happened during the five major phases of meteorite evolution (Bischoff and Stöffler, 1992):

1. Collision of particles within the accretionary disc in the solar nebula.
2. Collision of particles during the accretion of planetesimals.
3. Collision of planetesimals during the accretion of the meteorite parent body.
4. Interplanetary collisions of the meteorite parent bodies immediately after accretion.
5. Late collisions of the meteorite parent bodies and formation of Earth-crossing meteorites.

These five major phases all carry signatures of shock metamorphism that can be interpreted through the study of minerals and textures of the host rock.

2.4.2. Shock minerals and features

Shock metamorphism affects the petrographic characteristics, chemical properties, and isotopic properties of the parent rock. Shock effects are classified into five categories based on the presence of the following characteristics (Bischoff and Stöffler, 1992):

1. Fracturing
2. Plastic deformation
3. Phase transformations
4. Melting or chemical dissociation
5. Vaporization and condensation

There are two categories of metamorphic effects in shock metamorphism, destructive and constructive effects. Destructive effects represent an increase in disorder of the crystal lattice and material volume, caused by compression and decompression of the shock wave (Fritz et al., 2017). For example, olivine in the deconstructive low-pressure phase shows fractures, dislocations, undulatory extinction, mosaicism, and planar deformation features. In the deconstructive mixed phase regime, the crystal lattice of the olivine collapses, producing brown staining caused by Fe-nanoparticles forming (Van de Moortèle et al., 2007). This process is called shock-darkening (Takenouchi et al., 2018). In the deconstructive high-pressure phase, the collapse of the olivine's crystal lattice into a more dense phase is complete and produces brown-stained olivine. If the shock pressures are even greater, the crystal will be melted or vaporized (Fritz et al., 2017). All of these deconstructive shock features can be seen in Martian meteorites. These features are of importance as meteorites with shock features are assigned a shock classification based on the shock phase. The two

most highly referenced shock classification schemes are Fritz et al. (2017) and Stöffler et al. (2018). In both these schemes, the presence of certain destructive shock features are diagnostic of shock phase and, therefore, shock classification. Destructive shock events can also record the approximate maximum shock pressure, local-pressure spikes, and short-pressure spikes due to their brief formation period (Fritz et al., 2017).

Constructive shock events are characterized by an increase in crystal lattice order and density of the mineral and can also be diagnostic in determining the shock phase (Fritz et al. 2017). The presence of high-pressure phases is evidence of constructive shock and provides an indicator of the maximum temperature, which can in turn help in interpreting the maximum shock pressure limit (Fritz et al., 2017). One of the most notable high-pressure phases in Martian meteorites is maskelynite, the high-pressure glass phase of plagioclase. The presence of maskelynite is diagnostic of high shock pressure because maskelynitization occurs at a minimum pressure of 20 GPa (Fritz et al., 2017). Both destructive and constructive shock features can provide valuable insight to a meteorite's shock history.

3. METHODS

3.1. Preservation

3.1.1. 3D Scanner

3D scans of NWA 14904 were completed using an EinScan SP-Desktop 3D scanner. The 3D scanner was calibrated using EinScan's calibration board according to Shining 3D's Quick Start Guide (Shining 3D, 2019). NWA 14904 was placed on the scanner's turntable and imaged at multiple orientations, to ensure all sides of NWA 14904 were captured. The

EinScan software was then used to combine these scans to create a composite model of the meteorite's surface. Composites can be saved as either an editable non-watertight file or a watertight file to be used for 3D printing replicas.

3.1.2. Photogrammetry

Photogrammetry is the process of creating 3D data from 2D images by making a composite model (Haines, 2022). NWA 14904 was placed inside a photography lightbox on an automated turntable, which was covered with black fleece to eliminate glare. A Canon EOS 5Ds with a 24-70mm ultrasonic lens was attached to a tripod outside the lightbox. Photographs were then taken, rotating the stage by a 1/32 turn (11.25°) for each photograph until the full 360 degrees of the sample had been imaged. These photographs were then loaded into the Agisoft Metashape program. The 3D rendering was then completed using the workflow outlined in *3D model reconstruction* (Agisoft, 2020). Two separate models were created to image both the top and bottom of NWA 14904. These models were then combined to create a complete 3D composite of the sample.

3.1.3. Computed Tomography (CT)

Computed Tomography (CT) is a non-destructive imaging method that allows samples to be internally examined without cutting into the sample. The CT scanner produces a set of images (slices) in grayscale. The grayscale value produced is distinct for each mineral, as the gray value is representative of x-ray attenuation, a product of a minerals' density and mean atomic number (Ketcham and Carlson, 2001; Hanna et al., 2015). The image slices are compiled to provide 3D context of textural and mineralogical relations.

CT imaging of NWA 14904 was performed at the University of Texas High-Resolution X-ray CT Facility (UTCT) at the University of Texas, Austin. Scans were taken of the whole 800g rock prior to cutting, and of a smaller 174.97g mass after cutting to obtain higher-resolution scan slices. Both scans were performed using an NSI scanner with a Fein Focus High Power source, aluminum filter, and a Perkin Elmer detector. The samples were prepared by mounting the stones on study foam contained in a plexiglass cylinder (**Figure 3**). The CT was calibrated by measuring the empty plexiglass cylinder prior to the samples being mounted. Based on calibration each sample scan had corrections applied.



Figure 3. NSI Scanner at UTCT with the complete 800 g stone of NWA 14904 loaded into the plexiglass cylinder.

The whole rock scan settings were 210 kV, 0.09 mA, 2700 projections, 4 frames averaged, source to object 218.818 mm, and source to detector 731.485 mm. Corrections were made for 4 grain calibration, a 5mm calibration phantom, a 0.425 beam hardening correction, and a post-reconstruction ring correction of 2. The final data set after reconstruction had a voxel size of 59.8 mm. After post-reconstruction, a total of 1785 slices were produced.

The smaller mass scan settings were 160 kV, 0.17 mA, 5400 projections, 4 frames averaged, source to object 133.483 mm, and source to detector 730.94 mm. Corrections were made for 4 grain calibrations, a 5 mm calibration phantom, a 0.275 beam hardening correction, and a post-reconstruction ring correction of 2. The final data set after reconstruction had a voxel size of 36.5 mm. After post-reconstruction, a total of 1781 slices were produced.

After the slices were produced for both samples, 16-bit TIFFs and 8-bit JPGs (for viewing only) image files were created for each slice. These images were then compiled in ImageJ to create a GIF of the images, starting at the base and moving upwards through the scan until the top. These GIFs allow for the quick toggling between slices to examine textural and mineralogical relations.

3.2. Analysis

3.2.1. Classification

The naming and classification of meteorites is organized by the Nomenclature Committee (NomCom), a subcommittee within The Meteoritical Society. Each meteorite is

assigned an official name following an approved submission to NomCom. To request the official classification of new meteorites NomCom requires the following information (The Meteoritical Society and Meteorite Nomenclature Committee, 2015):

- a) The location, preferably as geographic coordinates, of the fall or find;
- b) The circumstances of the fall or find (narrative);
- c) The total known mass and number of pieces recovered;
- d) An authoritative classification;
- e) The location of the main mass;
- f) The location of a type specimen. Type specimens must be deposited in approved institutions that have well-curated meteorite collections and long-standing commitments to such curation. At the time of submission of the meteorite to NomCom, the type specimen must be in the permanent custody of the institution that is the type specimen repository;
- g) The type specimen mass. The minimum mass of a type specimen should be 20% of the total mass or 20 g, whichever is the lesser amount. For newly paired meteorites from dense collection areas (§4.2b), the minimum required mass shall be whatever is needed to bring the aggregate mass of existing type specimens (if any) to 20% of the aggregate mass of the entire pairing group or 20 g, whichever is less.

The request is submitted using an Excel template, provided by NomCom. The Excel template can be found on the Meteoritical Societies Meteoritical Bulletin website linked in the NomCom Resources section under “obtaining meteorite names” (The Meteoritical Society). This Excel template is filled out, containing the minimum information listed above, and emailed to the NomCom editor. Upon receiving submission, NomCom will review the request and notify the submitter via email of the approval decision. If the new meteorite is approved, it will receive a unique name and be added to the Meteoritical Bulletin Database (MetBase). Meteorites are named after the town closest to the location in which they were discovered (The Meteoritical Society). However, in dense collection areas where numerous

meteorites are found a generic prefix is used with a unique numeric suffix. Meteorites found in Northwest Africa are an example of this; they are given the prefix NWA, and NomCom assigns the numeric suffix upon accepting a submitted classification. All the data collected in the methods that follow (3.2.3 Petrographic Analysis; 3.2.4 Scanning Electron Microscope; 3.2.5 Electron Microprobe) were used in the classification submission for NWA 14904.

3.2.2. Thin Sections

Following the collection of non-destructive data, a total of nine thin sections were produced from NWA 14904. Through initial petrographic analysis it became clear that NWA 14904 was more complex in texture and mineralogy than originally anticipated (4. Results). To complete this study in a timely manner, one thin section was selected to be the focus of this study. Section 01 was selected, as it was the most complex texturally and mineralogically of all nine thin sections, with the hopes that it would be the most representative of the bulk rock.

3.2.3. Petrographic Analysis

All petrographic analysis was performed using an Olympus BX51 Microscope. NWA 14904 thin section 01 was photographed in plane-polarized light (PPL), cross-polarized light (XPL), and reflected light at a 4x magnification using a Meiji Techno HD1500MET Color HD camera. Photographs were taken systematically in rows moving from the top left-hand side of the section towards the right, and then down to the next row. This was repeated for each successive row until the entire thin section had been photographed. Photographs were taken at intervals to ensure there was ~40% overlap between the photo edges of one section

to the next. Photographs were then loaded into Adobe Photoshop to create a larger composite photograph by automating a Photomerge using a reposition layout. This process was done to create 3 composite photographs of the section in PPL, XPL, and reflected light.

3.2.4. Scanning Electron Microprobe (SEM)

SEM work was completed at Texas Christian University's Monnig Meteorite Lab using a Hitachi TM4000Plus Tabletop Microscope fitted with an Oxford Instruments AZtec Energy Dispersive Spectrometer (EDS). NWA 14904 thin section 01 was imaged at 30 times magnification using an accelerating voltage of 15 kV on the Analysis setting (mode 4). 50 frames were collected for each individual elemental map, and 5 frames for each BSE image. A coordinate system was used to map the section, starting at the lower left-hand corner of the thin section, labeled position (0,0) for row 0 column 0. The SEM scans the defined area, then moves across the section to the right producing tiles of increasing column number (0,0; 0,1; 0,2 etc.). When the row is complete and reaches the edge of the thin section the SEM moves up to the next row, starting on the left-hand side with tile (1,0) (**Figure 4**). This process continues until the entire thin section is mapped. This mapping produces a back-scattered electron (BSE) image and elemental x-ray images, for each tile.

(3,0)			
(2,0)			
(1,0)			
(0,0)	(0,1)	(0,2)	(0,3)

Figure 4. Mapping Grid Coordinate system used for both Backscattered Electron Images (BSE) and elemental x-ray maps.

The SEM data were processed using the Fiji imaging processing package for ImageJ (Schindelin et al., 2012). Fiji is an open-source program which contains plugins designed for material analysis. Here, the image stitching plugin was utilized to merge the individual BSE and x-ray tiles into maps of the section (Preibisch et al., 2009). Initially, the BSE tiles were entered into Fiji as an unknown configuration and the resulting coordinate output (those used to produce the BSE map) was then utilized to stitch together all elemental maps so that all sample maps are co-referenced. This process resulted in a BSE map and elemental maps for S, Ti, Cr, C, P, Al, Mg, Ca, Si, Na, Co, Mn, Ni, and Fe.

A high magnification (100X) BSE image was taken of the section using the Zigzag function on the Hitachi TM4000Plus Tabletop Microscope. Zigzag enables automatic acquisition of a continuous field of view; it maps out the number of tiles necessary to capture the defined area at the specified magnification. Once all the tiles are collected, Zigzag then automates their compilation into one coherent image.

3.2.5. Electron Microprobe (EMP)

The mineral chemistry of olivine, pyroxene, maskelynite, calcite, merrillite, and other carbonate and opaque phases within NWA 14904 was measured using the JEOL JXA-8530F Field Emission Electron Probe Microanalyzer at Fayetteville State University (FSU), North Carolina. The facility at FSU was funded by the U.S. Department of Defense grant W911NF-09-1-0011. Operating conditions for olivine, pyroxene, maskelynite, and merrillite were set to a current of 20 nA, accelerating voltage energy of 15 keV, and a focused beam. Operating conditions for calcite and other carbonates were set to a current of 10 nA, accelerating voltage energy of 15keV, and a $5\mu\text{m}$ beam, to lessen the effects of burns on the sample from

the probe. All probed sample locations were plotted on a composite photograph of NWA 14904 Section 01. In addition, photographs were taken using the probe's camera at each probe location and can be correlated to the composite photograph locations. Minerals used for the standardization of olivine included albite (Si, Al, Na), rutile (Ti), chromite (Cr), almandine (Fe), rhodonite (Mn), olivine (Mg), chrome diopside (Ca), monazite (P), and Ni-metal (Ni). Minerals used for standardization of pyroxenes included albite (Na, Al, Si), sanidine (K), rutile (Ti), olivine (Mg), chrome-diopside (Ca, Si), chromium oxide (Cr), almandine (Fe), and bustamite (Mn) from an Astimex standardization plate. Minerals used for the standardization of maskelynite included sanidine (Si, K), albite (Na, Al), and chrome diopside (Ca) from an Astimex standardization plate. Minerals used for the standardization of carbonates included calcite (Ca), rhodonite (Mn), and dolomite (Mg) from an Astimex standardization plate and siderite (Fe) from a Smithsonian standardization plate. Minerals used for the standardization of phosphates included albite (Al, Na), olivine (Si, Mg, Fe), apatite (P), monazite (Ce), tugtupite (Cl), chrome diopside (Ca), rutile (Ti), sanidine (K), chromite (Cr), and rhodonite (Mn) from an Astimex standardization plate. Minerals used for the standardization of oxides and sulfides included albite (Al), olivine (Si, Mg, Fe), apatite (P), chrome diopside (Ca), rutile (Ti), galena (Pb), chromite (Cr), rhodonite (Mn), and sphalerite (Zn) from an Astimex standardization plate. Recipes used for the analysis of each phase can be found in Appendix 7.1.1.

3.2.6. Modal Abundance Calculation

ImageJ was used to calculate modal abundances in the thin section. In this method, a map of the section is chosen for each phase present and imported into ImageJ. These maps

are chosen based on how well they highlight the selected phase; for example, the P elemental map was chosen for the phosphates in NWA 14904. Threshold limits are then applied to each image so that only the pixels for that phase are highlighted. All images used must be the same size and the same resolution. ImageJ can then calculate the number of pixels for each phase and these values are used to calculate modal abundances.

All maps used to calculate the modal abundance of NWA 14904 Section 01 are given in **Table 1**. As melt is such a large proportion of NWA 14904 Section 01, melt was included as one of the phases that needed to be quantified. However, the melt has a composition that overlaps with both the olivine and some of the pyroxene in x-ray elemental maps used for these phases. This made it impossible to distinguish the melt using only the BSE and x-ray maps collected. The PPL images of the thin section, which clearly delineate the melt pockets, were instead used to define the limits of the melt and calculate its abundance. The resulting melt phase map (**Figure 5**) was then subtracted from all other phase maps to ensure that these pixels were not counted twice. This was achieved using the image math function in ImageJ. Similarly, due to subtle changes in contrast over the entire section map, low-Ca pyroxene was hard to define with the threshold method alone as there was some overlap with other phases. Low-Ca pyroxene was defined by thresholding all pyroxene and olivine phases in the BSE and subtracting both olivine and high-Ca pyroxene from the resulting threshold image.

Table 1. Image Thresholding for Phase Maps

Phase	Image used for thresholding*
Melt	PPL image
Maskelynite	Al x-ray map
Phosphates	P x-ray map
Chromite	Cr x-ray map
Ilmenite	Ti x-ray map
Olivine	BSE image
Low-Ca Pyroxene	BSE image
High-Ca Pyroxene	BSE image
Carbonates	C x-ray map
Sulfide	S x-ray map

* This column reflects the dominant image used to produce all phase maps used for modal abundance calculations; however, additional image processing was required as described in the text.

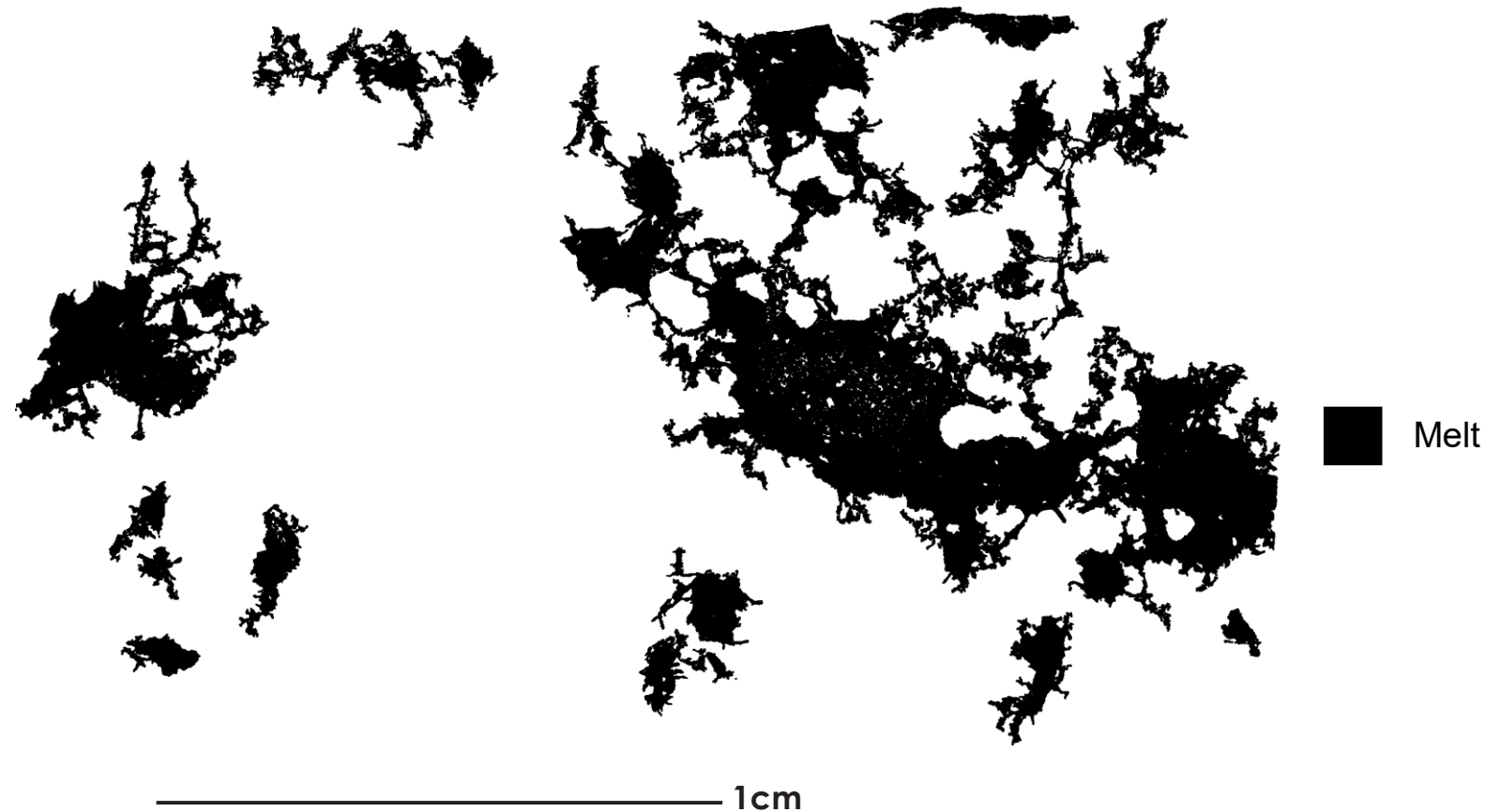


Figure 5. Phase Map that shows the extent of the melt (black) within section 01 of NWA 14904.

3.2.7. Modal Mineralogy

As shock melt accounts for nearly 20% of the calculated modal abundance of NWA 14904, the presence of the melt phase has a notable impact on the overall modal mineralogy. High magnification BSE images and elemental maps show that the melt areas are dominated by zoned microlites of olivine in a matrix of glass (**Figure 6**).

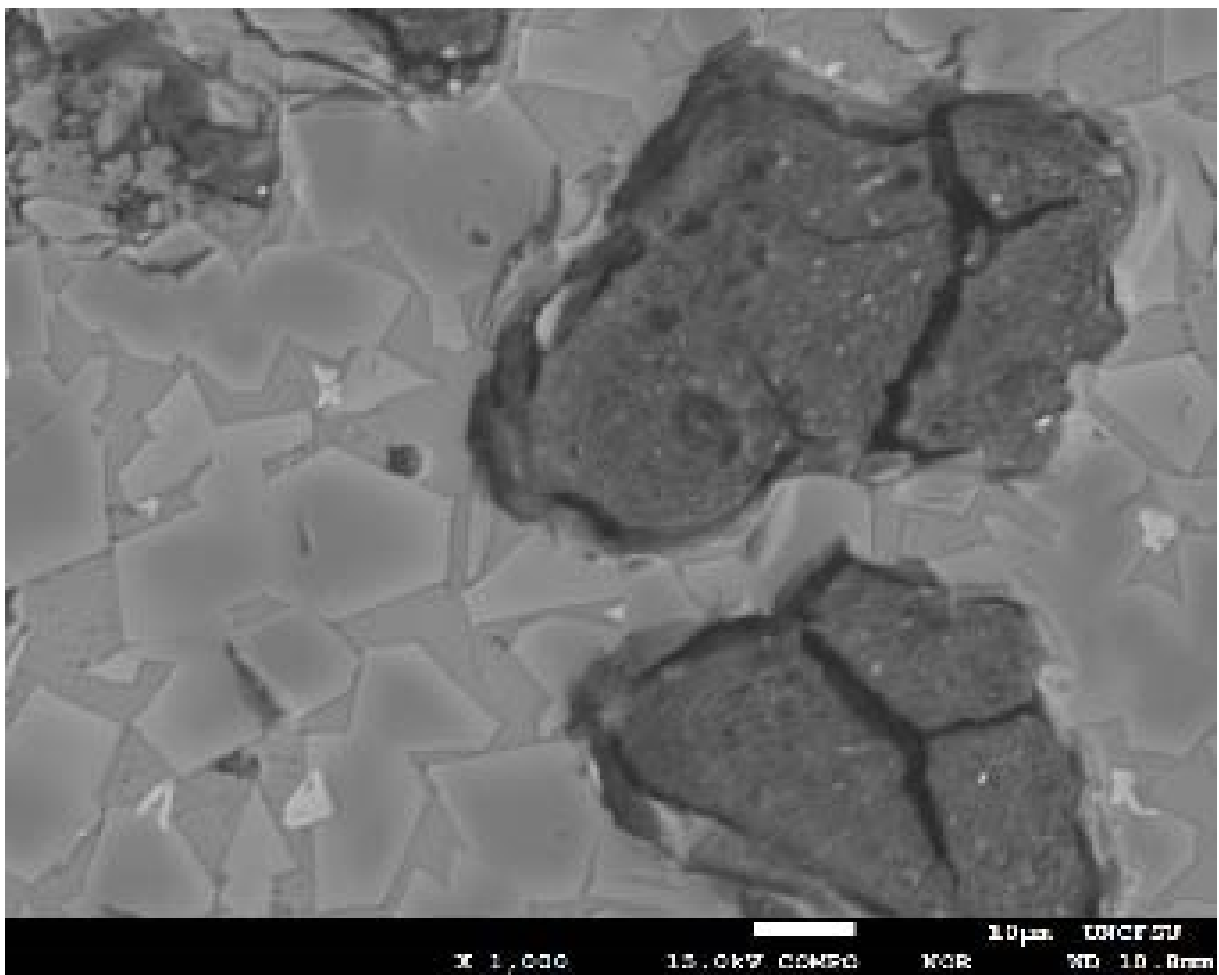


Figure 6. BSE of Melt showing zoned olivine microlites (light gray getting darker in gray scale value moving from rim to core). Shock melt glass matrix (medium gray) surrounds the zoned olivine microlites. Carbonate alteration of shock melt (dark gray with cracks) is also present and can be seen throughout the melt. White scale bar represents 10 μm .

Therefore, any calculated modal mineralogy that includes the melt as a component must underestimate the amount of olivine in the original pre-shocked sample, as this phase was preferentially melted during the shock event or events. While petrographic observations can be made of the melt phase, calculating the modal abundance for the melt phase itself was outside the scope of this study. Therefore, the modal mineralogy was calculated in three ways to provide potential ranges for NWA 14904:

1. with melt: with the melt component as a separate phase
2. bulk melt removed: with the melt component removed from the calculation
3. melt assumed to be 100% olivine: with the melt component removed and the assumption that all melt was olivine.

Modal mineralogy calculation 1 includes the melt as its own separate phase, or component, in the calculation of the overall modal mineralogy. This gives the relative abundance of all phases including the melt phase.

Modal mineralogy calculation 2 removes the melt from the modal mineralogy calculations and normalizes all other components to 100%. The melt phase is removed under the assumption that the melt contains the same modal proportions as the whole sample. However, based on petrographic observation it is understood that the melt is not representative of the whole rock mineralogy. This calculated mode likely results in a minimum value for olivine within the sample, as the removed melt is dominated by olivine microlites, and a maximum value for all other phases. While calculation 2 is the preferred standard when determining modal mineralogy for a sample, it is not particularly

representative of the whole rock sample in the presence of high volumes of melt components such as in NWA 14904.

Modal mineralogy calculation 3 assumes that the melt is composed entirely of olivine and, therefore, adds the calculated melt value to that calculated for olivine. This calculation yields a potential maximum value for the modal abundance of olivine and a minimum modal value for all other phases.

3.2.8. Bulk Composition

The bulk chemical composition of NWA 14904 was calculated using the method outlined in Gross et al. (2020), using the sum of average mineral compositions. This calculation assumes that the modal mineralogy, which accounts for the area proportions of minerals, is equal to the volume proportion of the minerals. Due to the high modal percentage of melt within NWA 14904, the melt-removed modal mineralogy (#2 in section 3.2.7) was used in this calculation. This is discussed further in section 5.2.2. To obtain a volume measurement for NWA 14904, the whole rock 3D model created by the Einscan 3D scanner was imported to the Autodesk Meshmixer 3D computing software which calculated the total volume of NWA 14904 to be 254,796 mm³. Volume proportions for each mineral were then converted to mass proportions using mineral densities. These mineral densities were interpolated from past works (Gross et al., 2020 and references therein) and provided via personal communication with Julianne Gross, and are shown in the **Table 2**, with the exception of the density of merrillite which was provided by the Hudson Institute of Mineralogy (1993-2022).

Table 2. Mineral Densities used in bulk composition calculation.

Mineral	Density (g/cm ³)
Forsterite	3.22
Fayalite	4.39
Wollastonite	2.84
Enstatite	3.21
Ferrosilite	3.96
Anorthite	2.76
Albite	2.63
Orthoclase	2.55
Chromite	4.79*
Ilmenite	4.79
Merrillite**	3.10

*ranges from 5.09 to 4.5 with an average of 4.79 (Gross et al., 2020)

**(Hudson Institute of Mineralogy, 1993-2022)

4. RESULTS

4.1. Whole-rock description



Figure 7. NWA 14904 as a whole rock 800g single stone. Sample is ~95mm across in this orientation.

NWA 14904 was an 800g single stone measuring ~95mm x ~50mm x ~55mm (**Figure 7**). It is red-brown to tan in color with a brown-black fusion crust (**Figure 8A**). Some terrestrial alteration represented by light tan caliche is present as well (**Figure 8 B**). The outer surface contains vesicles ranging in size and shape, from subrounded to angular, and from moderate to elongate in sphericity (**Figure 8C**). Vesicles can be found on all surfaces of the rock but are concentrated on one of the concave sides. Areas of tan-green glassy melt (**Figure 8D**) are apparent on one of the concave sides but can be found all over the sample.

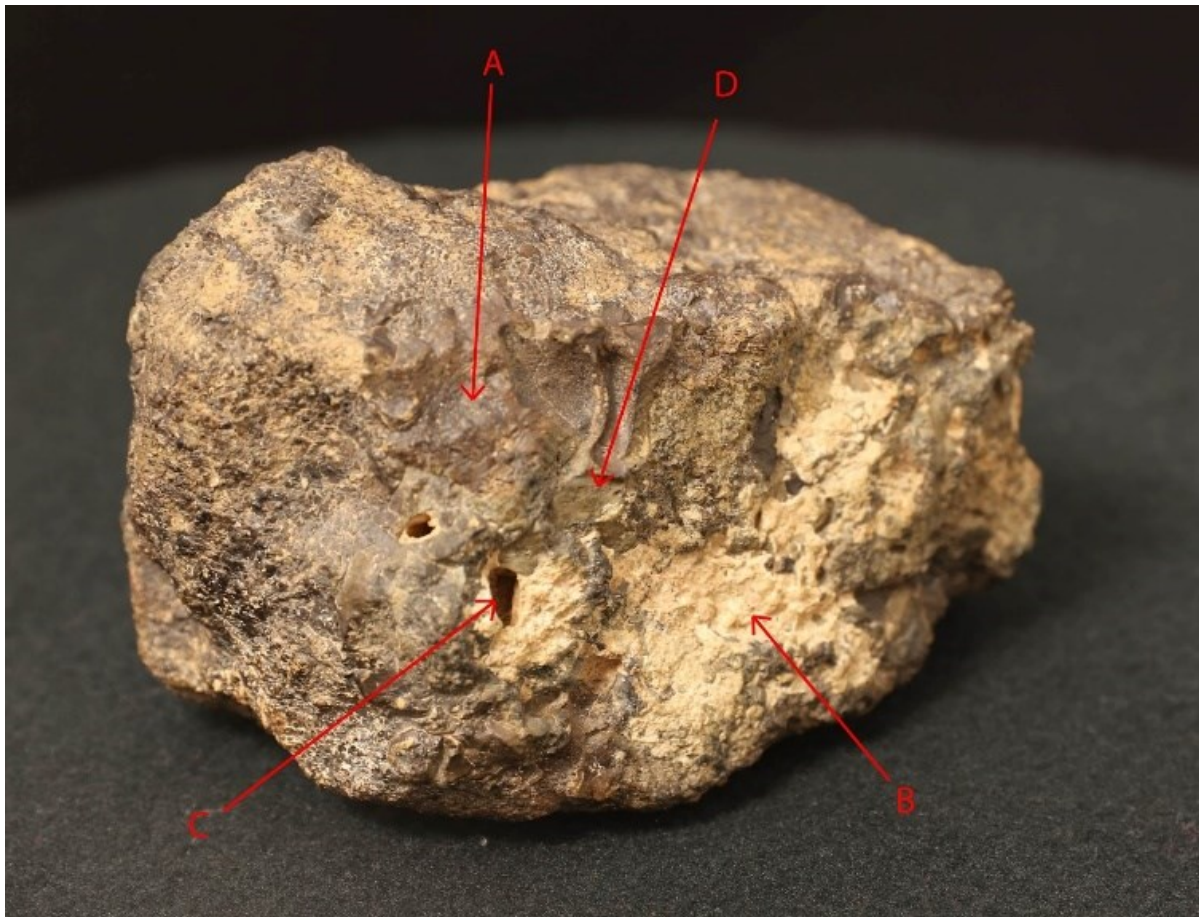


Figure 8. NWA 14904 Whole Rock Features. Sample is ~95mm from front to back in this orientation. Image exposure has been increased to highlight color and textural differences between features. A. fusion crust; B. terrestrial alteration; C. vesicles; D. glass melt.

4.2. CT Results

The goal of the CT portion of this work was to produce a 3-D digital model of the interior of NWA 14904 that allowed interpretation of the overall texture of the sample, and analysis of the grain shapes and mineral relationships within it. Scans of the entire 800g stone of NWA 14904 were not of sufficient resolution to achieve the goal of this portion of the study (**Figure 9**).

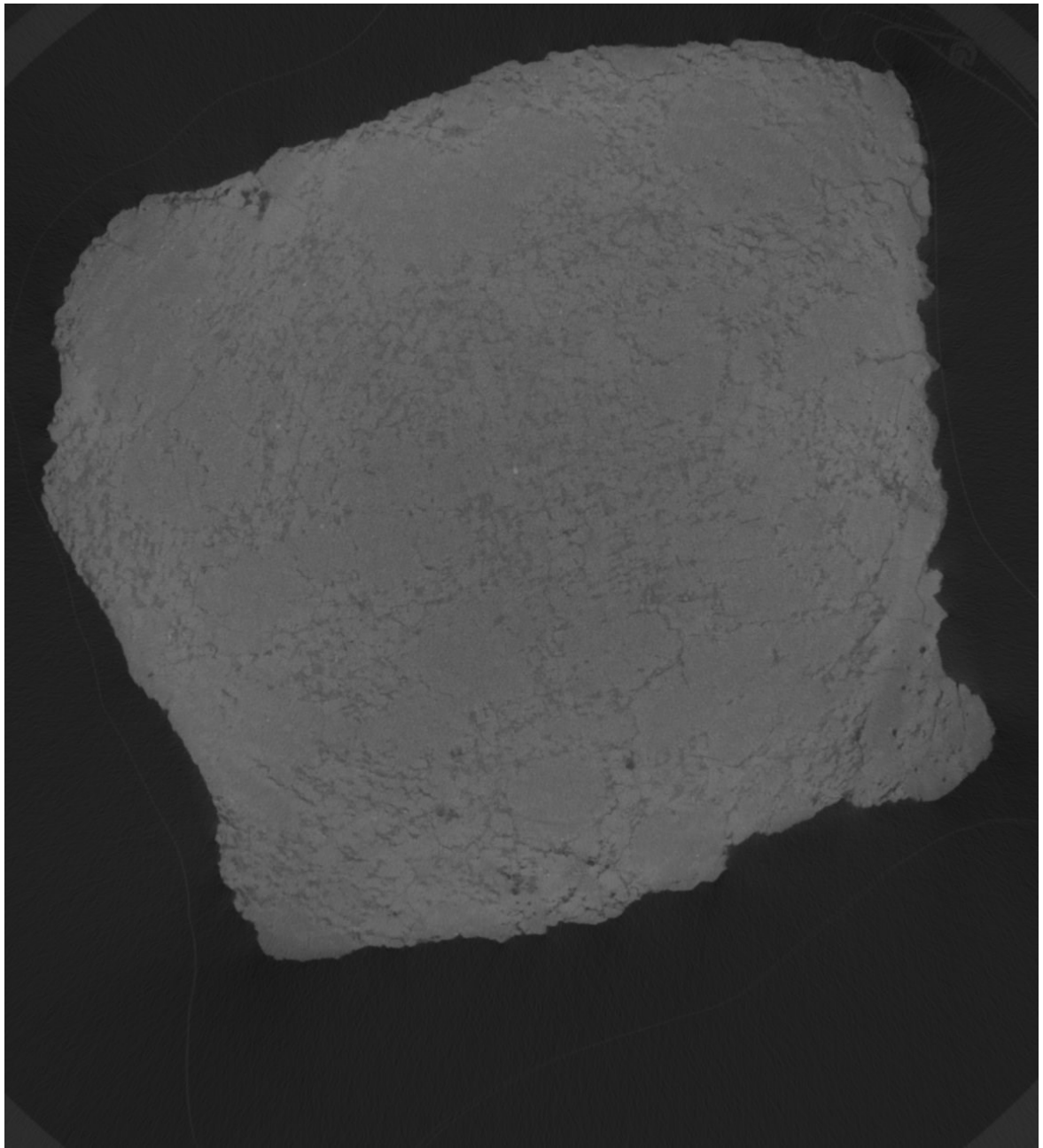


Figure 9. CT slice of NWA 14904 whole rock. Slice is 60mm across.

As a result, after the whole rock was cut to produce a 174.97g stone. This smaller piece was imaged to see if higher-resolution images could be collected. However, it was still not possible to isolate and produce a 3D rendering of the main mineral phases due to the fine-grained nature of the sample, and the relatively large size of the masses available for scanning. Olivine and pyroxene, the two most abundant minerals, are similar enough in composition that in a large, fine-grained sample, the contrast differences between them within the CT data are too small to allow them to be accurately distinguished from one another. It was decided that the scientific value of these data was not worth cutting the specimen further to achieve a scan that could resolve these two phases. However, an overall bimodal texture can clearly be distinguished within the second CT dataset. Both poikilitic and non-poikilitic textures can be seen throughout the slices as demonstrated in **Figure 10**. These two textural regions are heterogeneously distributed throughout the sample with poikilitic and non-poikilitic areas up to 40cm and 60cm across, respectively.

Areas of melt containing infilled vesicles can be seen at the higher CT scan resolution as clusters throughout the sample. While vesicles are hard to distinguish by themselves, these clusters are easily identifiable due to their dark-speckled appearance (**Figure 11**).

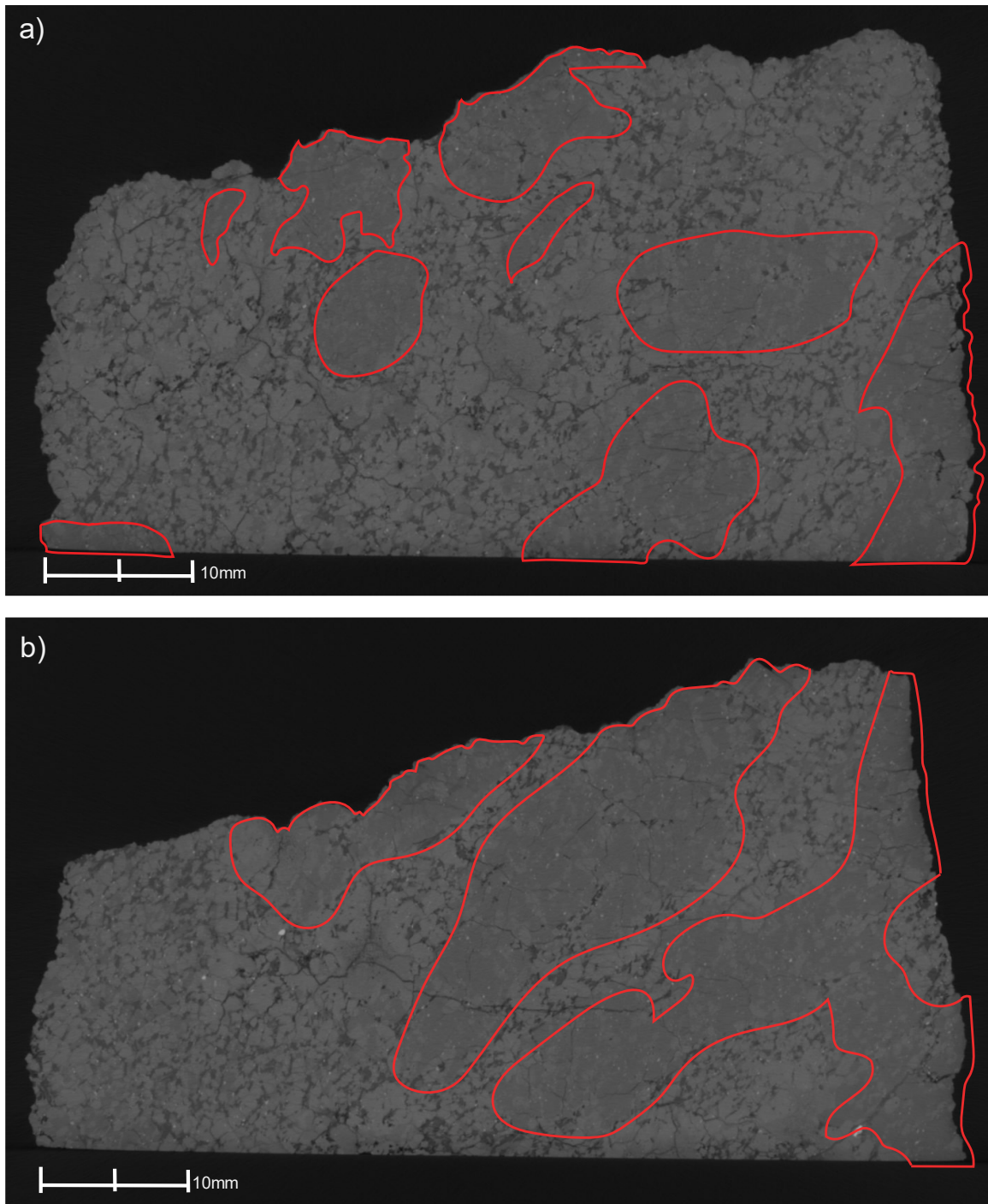


Figure 10. CT slices of NWA 14904 174.97 g end cut displaying bimodal texture: poikilitic texture (outlined in red), and non-poikilitic texture. (a) Slice is 64mm across and contains poikilitic areas ~15 mm in length. In comparison (b) Slice is 64 mm across and only contains poikilitic areas ~35mm in length. This demonstrates the different size and shape of the poikilitic and non-poikilitic areas throughout the sample.

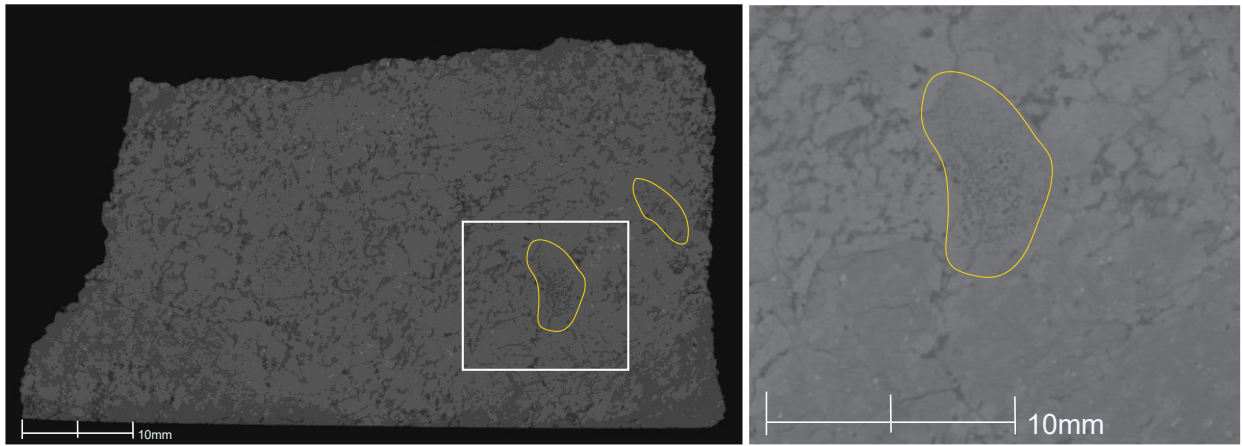


Figure 11. CT slice of NWA 14904 174.97 g end cut showing evidence for vesicles in melt glass (outlined in yellow)

4.3. Modal Mineralogy

A mineral map (**Figure 12**) was produced to display mineral phase positions in relation to one another in Section 01 and to calculate the modal mineralogy (**Table 3**), following the procedures as discussed in section 3.2.7.

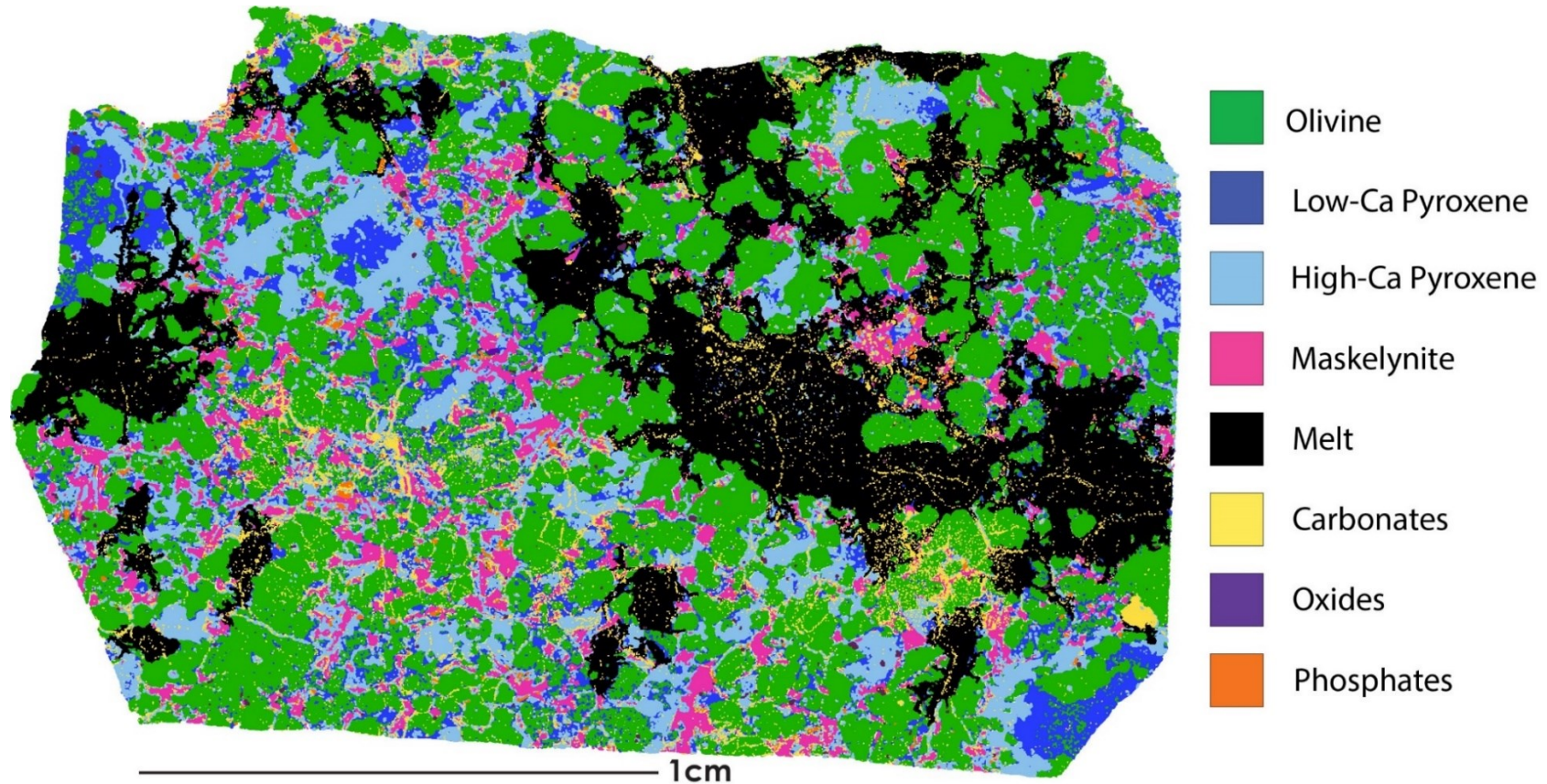


Figure 12. Section 01 Phase Map. Different colors represent the presence of different mineral phases in NWA 1409, thin section 01.

Modal Abundances

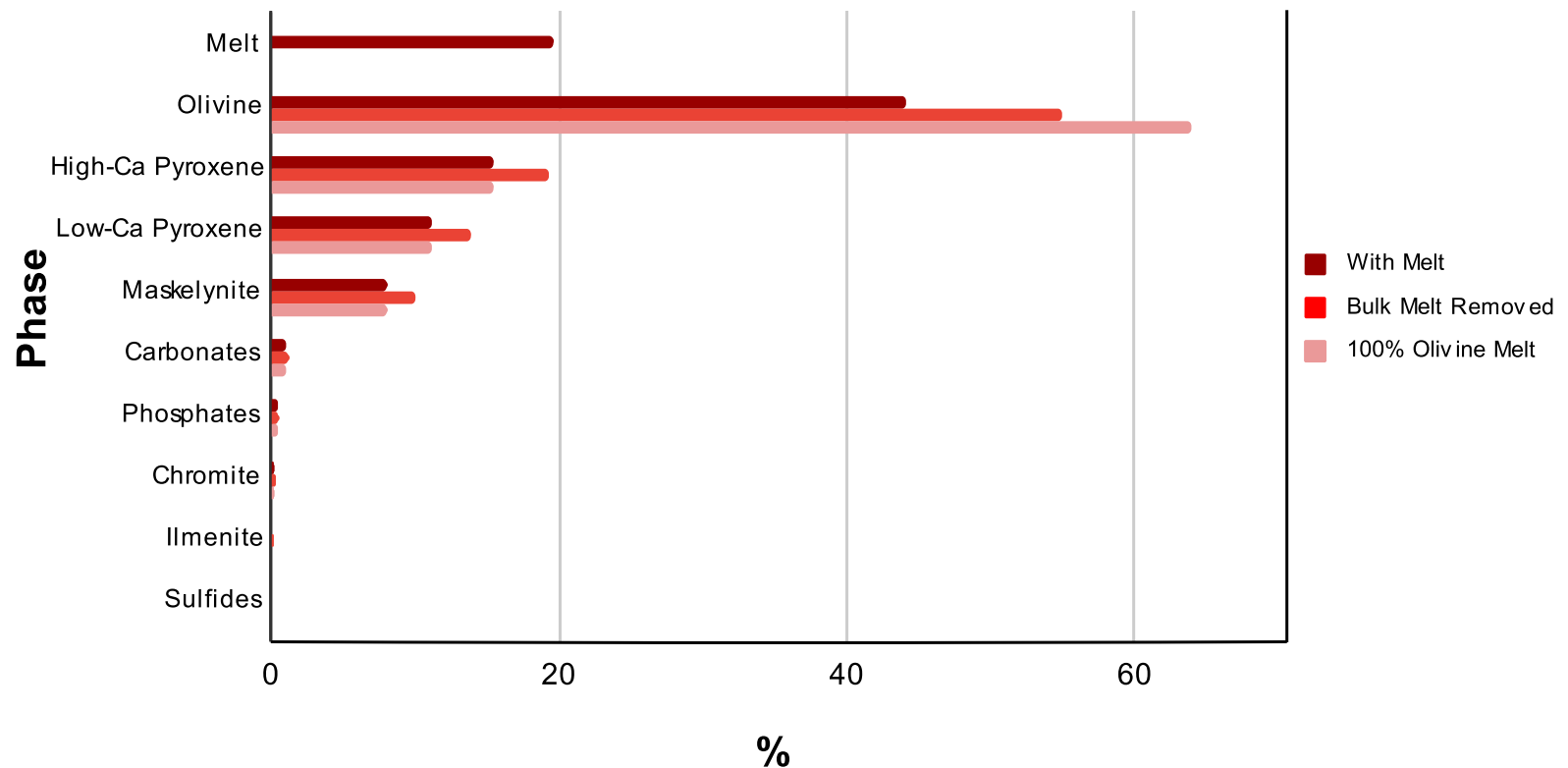


Figure 13. Modal Abundance Plot. Displays the modal mineralogy calculated three different ways. 1) with the melt as a separate phase; 2) with the melt removed under the assumption that the melt has the same modal abundances as the whole sample; 3) with the melt included under the assumption that its composition is 100% olivine.

Table 3. Modal Mineralogy Calculations

Phase	With Melt (%)	Bulk Melt Removed (%)*	100% Olivine Melt (%)
Melt	19.67	n/a	n/a
Olivine	43.98	54.75	63.65
High-Ca Pyroxene	15.43	19.20	15.43
Low-Ca Pyroxene	11.09	13.80	11.09
Maskelynite	8.05	10.20	8.05
Carbonates	0.99	1.23	0.99
Phosphates	0.43	0.53	0.43
Chromite	0.24	0.30	0.24
Ilmenite	0.13	0.17	0.13
Sulfides	0.07	0.09	0.07

*where the modal mineralogy of the melt is assumed equal to that in the whole rock

4.4. Bulk Composition

The bulk composition was calculated using the method outlined in Gross et al., (2020). The modal mineralogy calculation for “bulk melt removed” and “100% olivine melt” was used to calculate the bulk composition. This was done in order to provide a potential range for the bulk composition.

Table 4. Bulk Composition

	<i>Bulk Melt Removed</i>	<i>100% Olivine Melt</i>
Oxide	wt%	wt%
SiO ₂	43.84	42.59
TiO ₂	0.23	0.18
Al ₂ O ₃	2.68	2.12
Cr ₂ O ₃	0.52	0.42
FeO _T	20.74	22.39
MnO	0.45	0.47
MgO	25.91	27.30
CaO	4.86	3.90
Na ₂ O	0.50	0.40
K ₂ O	0.03	0.03
P ₂ O ₅	0.24	0.20
Total	100.00	100.00

Bulk composition calculated two separate ways based on the modal mineralogy calculation 1)with the melt as a separate phase; 2) with the melt included under the assumption that its composition is 100% olivine

4.5. Petrography

The CT data described above shows a distinct bimodal texture, with poikilitic and non-poikilitic regions up to 60mm in size present throughout the main mass. In this study, one 1-inch round thin section of NWA 14904 was used for petrographic characterization and, therefore, the description here may not be fully reflective of NWA 14904 as a whole. NWA 14904 Section 01 is dominated by the non-poikilitic texture. Composite photographs of Section 01 in PPL, XPL, and reflected light, and BSE composite maps were produced during the petrographic study.

Along with the poikilitic and non-poikilitic areas NWA 14901 Section 01 contains large melt pockets distributed throughout the section (**Figure 14-Figure 17**). Poikilitic areas contain large pyroxene oikocrysts up to 4 mm in size that completely or partially enclose chadacrysts of olivine, which range from 0.35–0.7 mm across (**Figure 18**). The oikocrysts are cut off at the edge of the thin section, so their actual size is larger than given here (**Figure 18**). Olivine chadacrysts tend to be more rounded than olivine grains outside of poikilitic regions, and they do not touch other olivine grains, as opposed to non-poikilitic olivine where the olivine grains are in contact with each other (**Figure 18**). Smaller-scale poikilitic areas contain pyroxene oikocrysts up to 2 mm enclosing olivine chadacrysts which range from 0.1–0.3 mm in size (**Figure 18**).

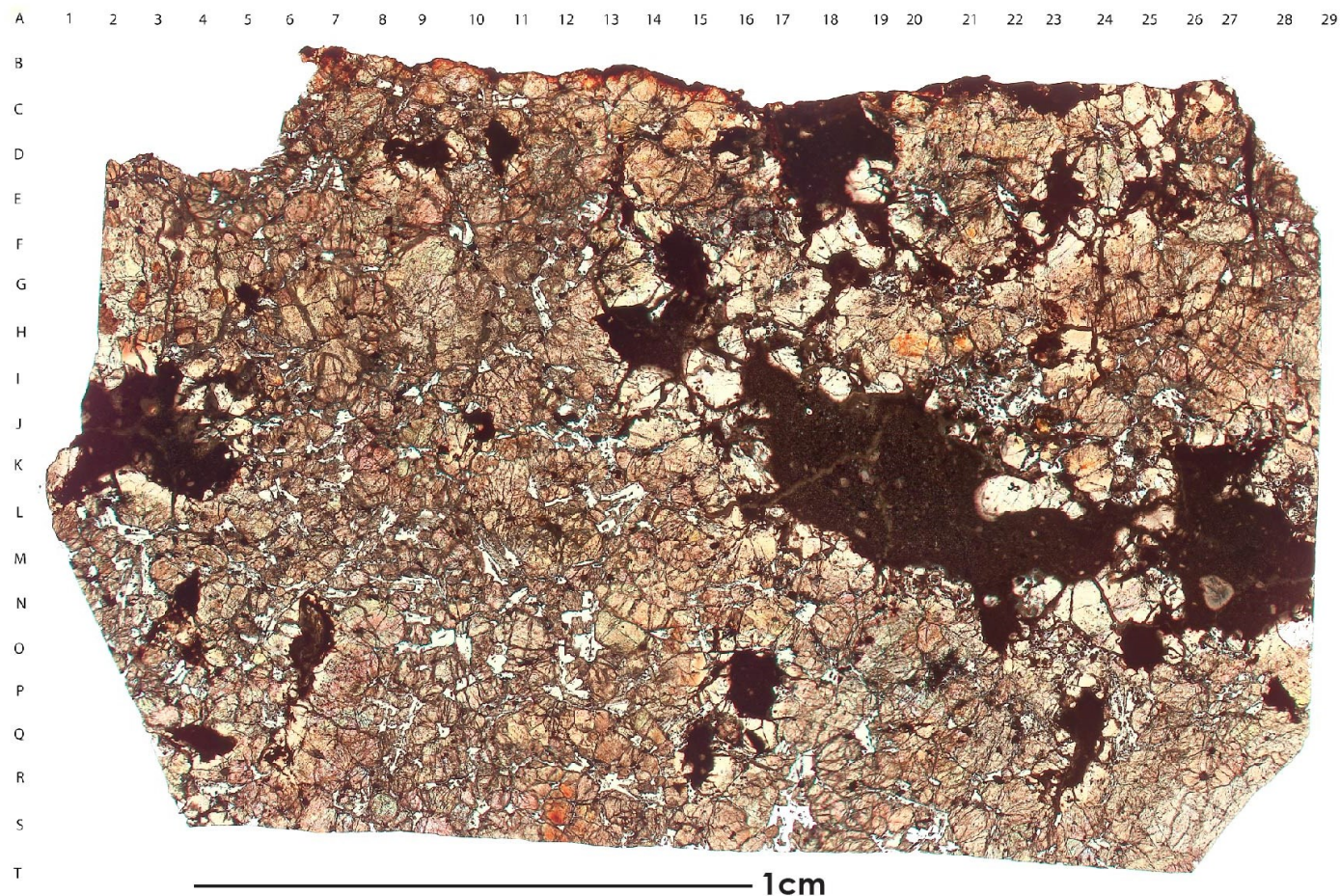


Figure 14. Plane Polarized Light (PPL) Composite Image, showing shock melt pockets (black).

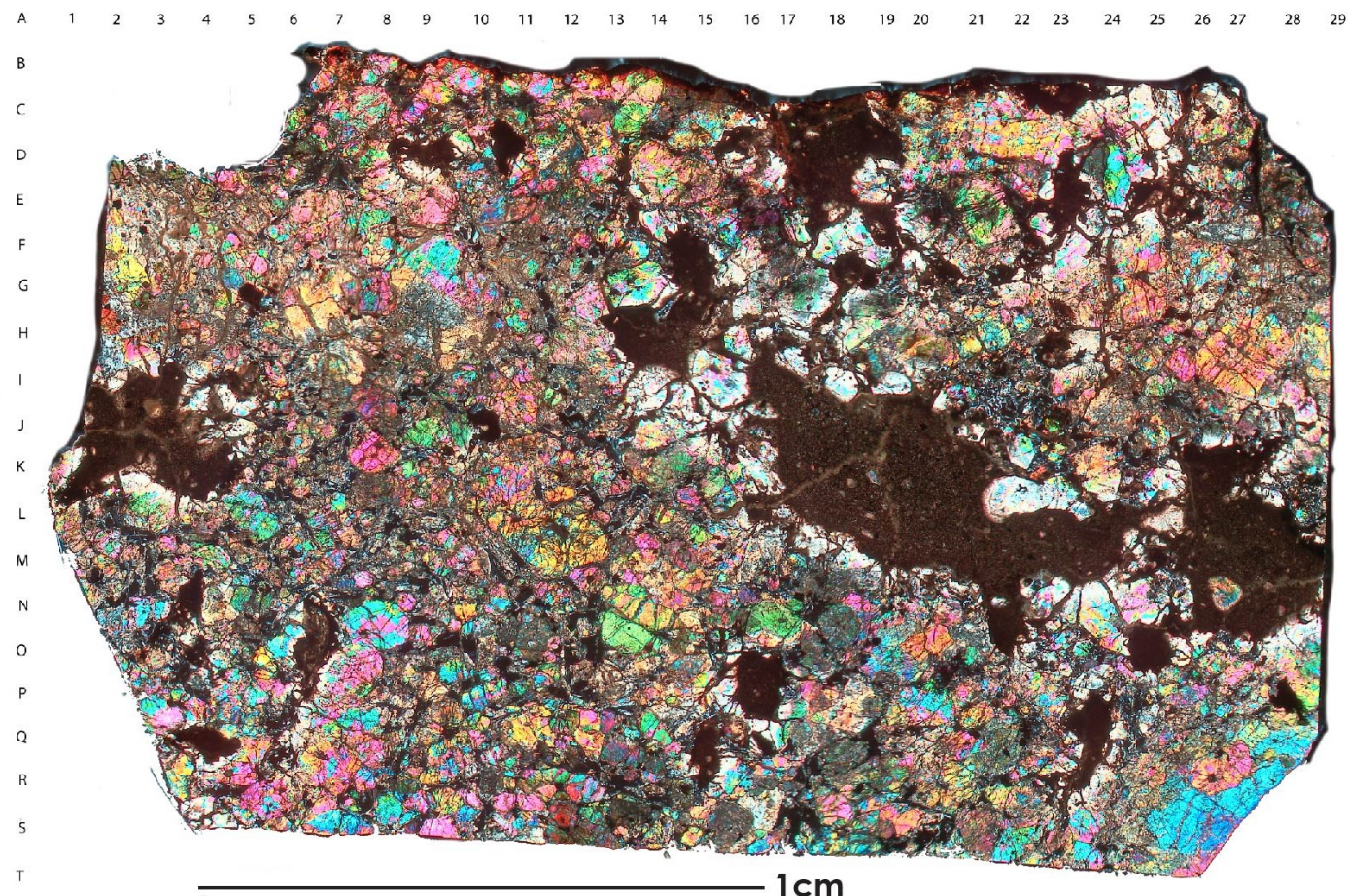


Figure 15. Cross Polarized Light (XPL) Composite Image.

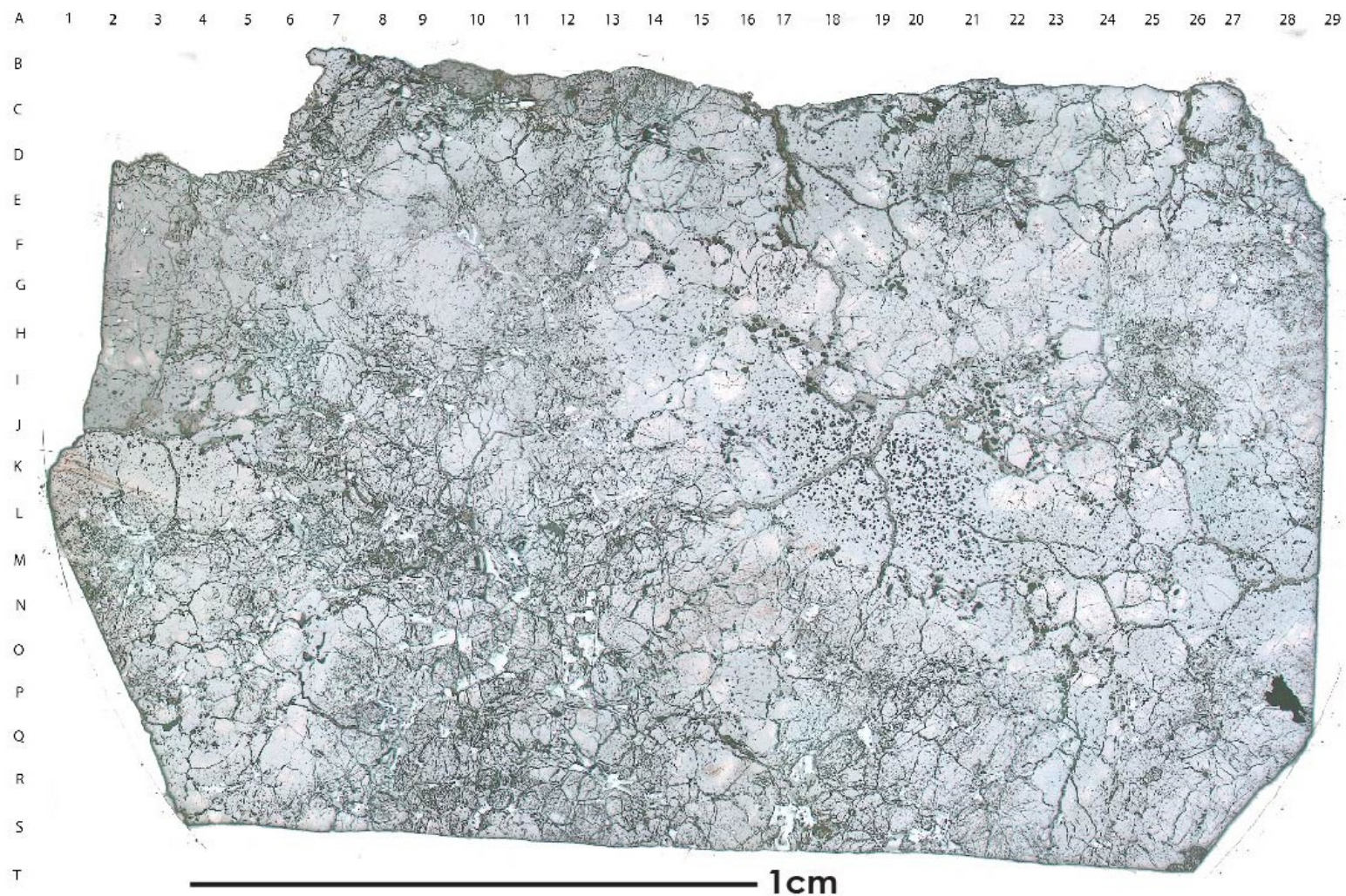


Figure 16. Reflected Light Composite Image.

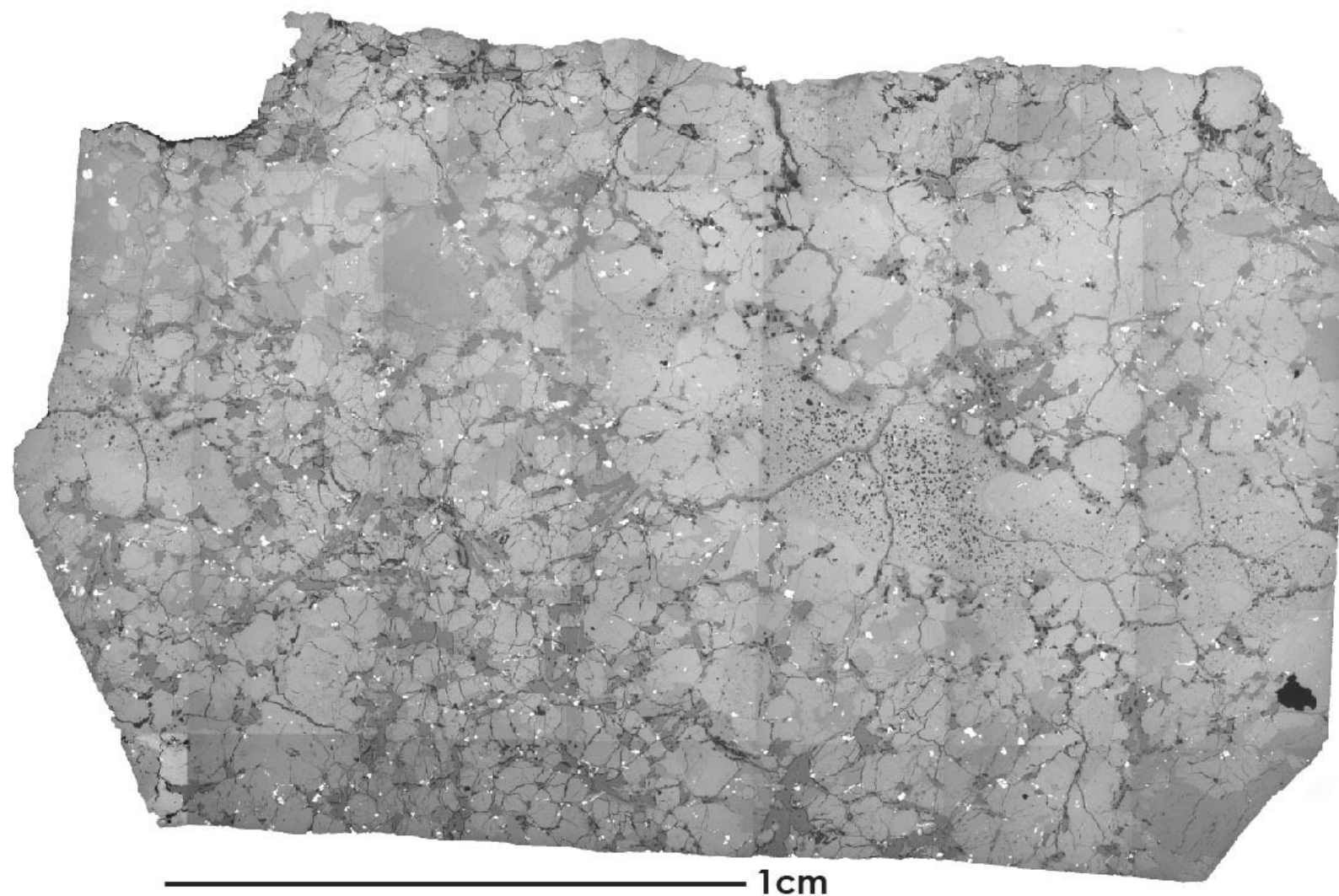


Figure 17. Backscatter Electron (BSE) Composite Map.

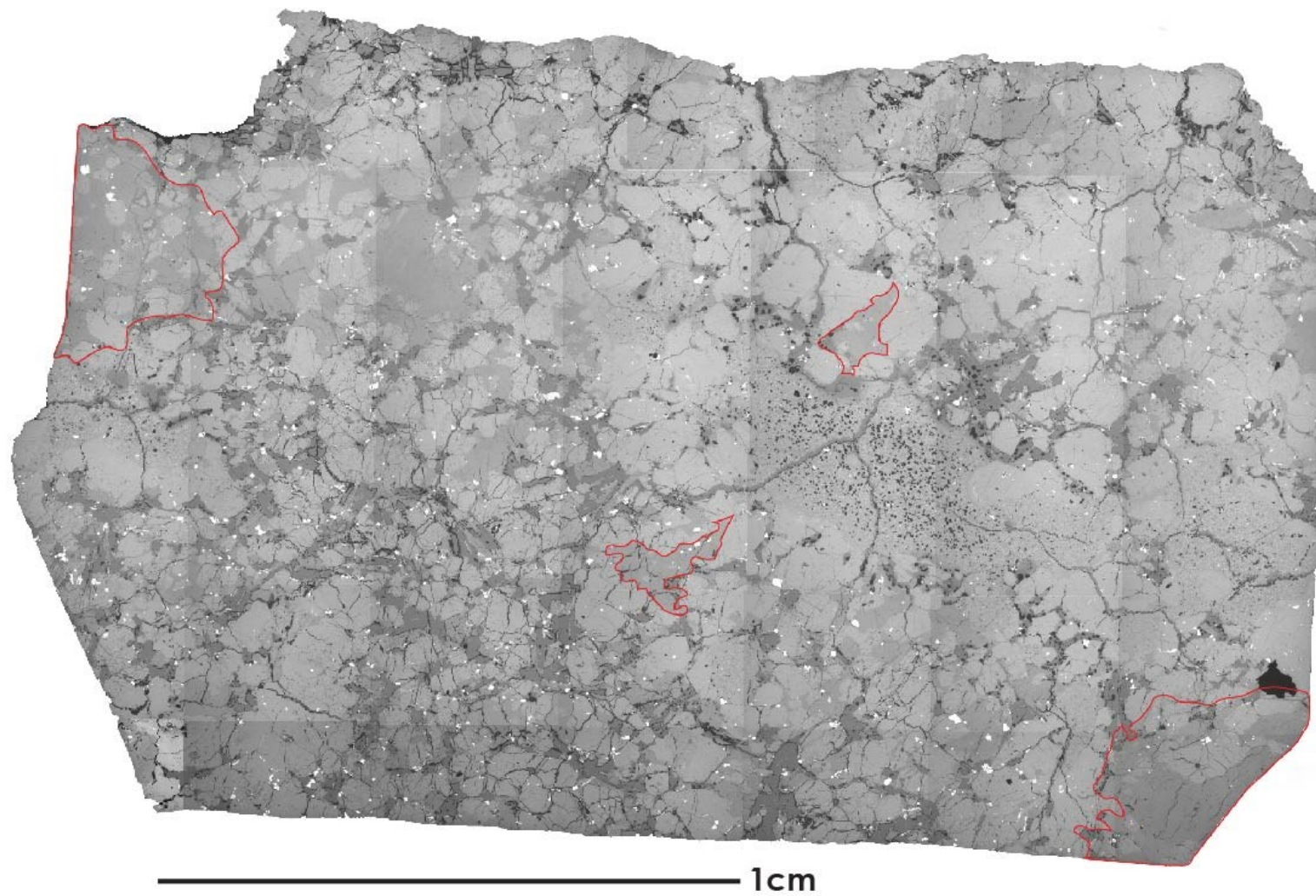


Figure 18. BSE Composite Map Showing Poikilitic texture outlined in red, with two different sizes of pyroxene oikocrysts. This highlights the size difference observed between large- and small-scale poikilitic texture.

Non-poikilitic areas contain high- and low-Ca pyroxene (~0.5-2mm), maskelynite laths (up to 1mm) and angular grains (~0.5-2mm) and bimodal size populations of anhedral olivines; larger olivines (~4-5 mm) are volumetrically more abundant than smaller (~0.5-1mm) anhedral olivine grains. Melt pockets and veins can be found throughout the section.

Melt pockets show pervasive carbonate alteration (**Figure 26**). Carbonate-filled vesicles are found in the melt, and within maskelynite (**Figure 22c-d**). Vesicles filled with carbonates range from completely filled, to partially filled, and there are a few in the section that contain no carbonates. Carbonate veins are also found throughout the sample (**Figure 24**). Accessory phases include merrillite, chromite, ilmenite, and sulfides and are found in both poikilitic and non-poikilitic areas. Significant evidence of shock is seen; pockets of dark brown shock melt and shock veins are prevalent (**Figure 23a**) and are discussed further below.

4.5.1. Textural Descriptions

As mentioned above, NWA 14904 has a bimodal texture and contains both poikilitic and non-poikilitic areas. Textures within non-poikilitic areas vary and can be examined in three locations: (1) inside mineral grains, (2) at grain boundaries with other mineral phases, (3) at grain boundaries with the melt. These textural variations are discussed in detail, for each mineral below.

4.5.2. Olivine

Olivine shows many shock features, which will be detailed further in Section 4.6.3. In BSE imaging, olivine often shows reaction textures with other minerals. Evidence for

reaction zones, particularly where olivine is in contact with carbonate veins, can be seen as grainy texture on the edge of olivine grains (**Figure 19a**). In some cases, olivine displays vermicular growth with pyroxene (**Figure 19a**). Olivine near melt pockets occasionally shows melt banding inside olive grains as the melt becomes entrained within the olivine (**Figure 19b**). Olivine grains also display melt features with a variety of textures, including leopard and granular olivine textures, along with elongated olivine dendrites (**Figure 19c**), similar to those observed by Walton and Shaw (2009) in other meteorites. Olivine is commonly cross-cut by carbonate veins (**Figure 19d**).

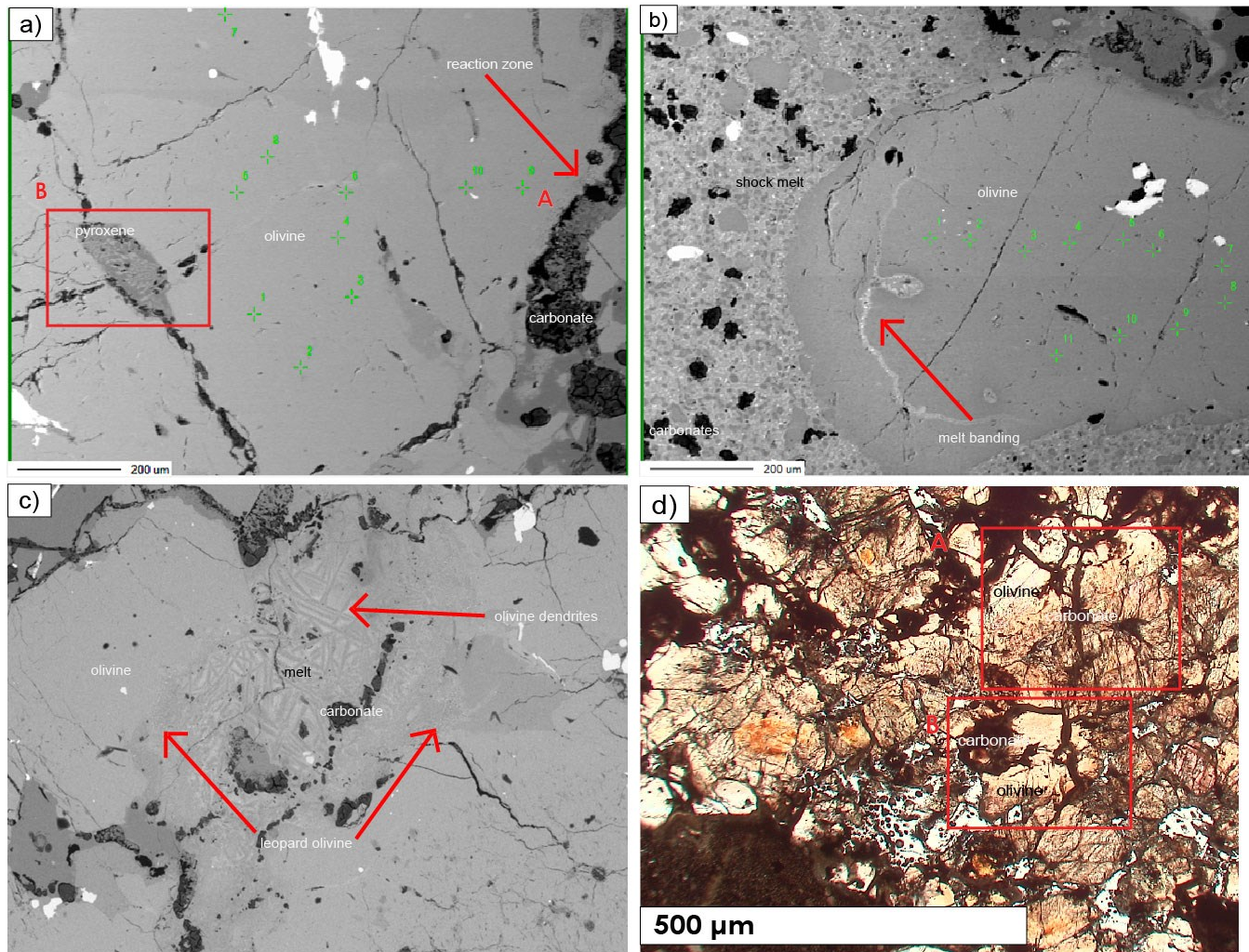


Figure 19. A variety of olivine textures seen in NWA 14904 a) BSE image of olivine reaction textures next to carbonate veins (A) and pyroxene (dark gray) melt inclusion of with vermicular intergrowth (B); b) BSE image showing melt band inclusion from shock melt in olivine; c) BSE image of shock melted olivine with evidence of olivine dendrites, and leopard olivine; d) PPL image of terrestrial alteration of carbonate veins cross cutting olivine grains.

4.5.3. Pyroxene

Poikilitic pyroxene is found throughout the section, mostly as a larger-scale oikocryst 4-5 mm in size. The best example of this is seen in the upper left-hand side of the thin section (**Figure 17**). These larger-scale oikocrysts go beyond the edge of the thin section, obscuring the total size of the larger poikilitic area (**Figure 20a**). Smaller scale oikocrysts can be found throughout the sample, containing only 1-4 olivine grains (**Figure 20b**). Non-poikilitic pyroxenes are scattered throughout the thin section as interstitial material between olivine, maskelynite, and the accessory phases. Non-poikilitic pyroxenes show evidence for sieve texture with olivine (**Figure 20c**). Pyroxene oikocrysts in NWA 14904 show evidence for zoning, with low-Ca pyroxene at the core and high-Ca pyroxene at the rim (**Figure 21a-b**). The Ca composite map (Appendix 1.1). shows evidence for a sharp compositional transition rather than a gradual one, which is suggestive of a high-Ca overgrowth onto the oikocryst (Orr et al., 2022).

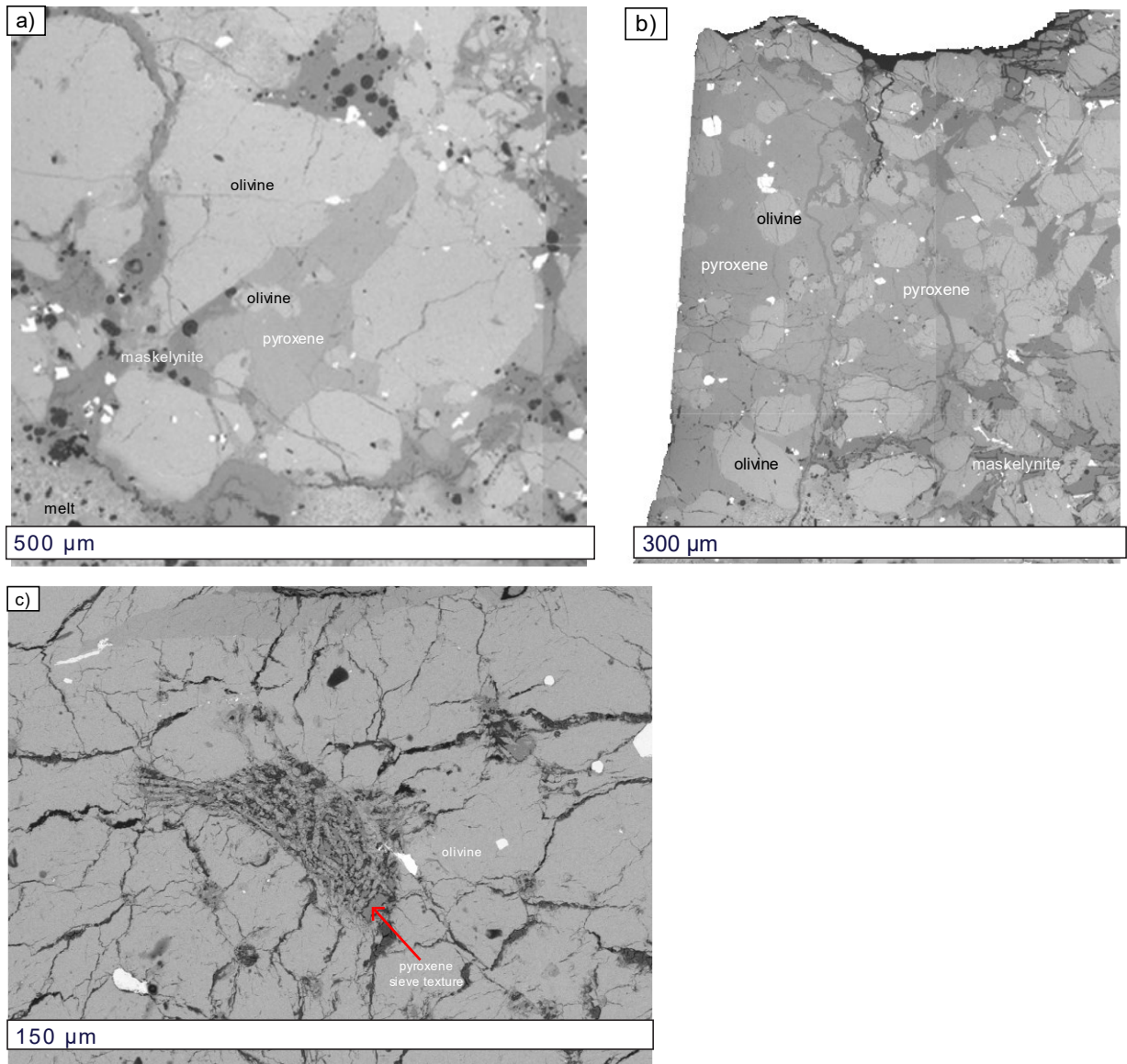


Figure 20. Pyroxene Textures a) BSE image of small-scale poikilitic texture; b) BSE image of large-scale poikilitic texture; c) BSE image of melt inclusion in olivine showing sieve texture

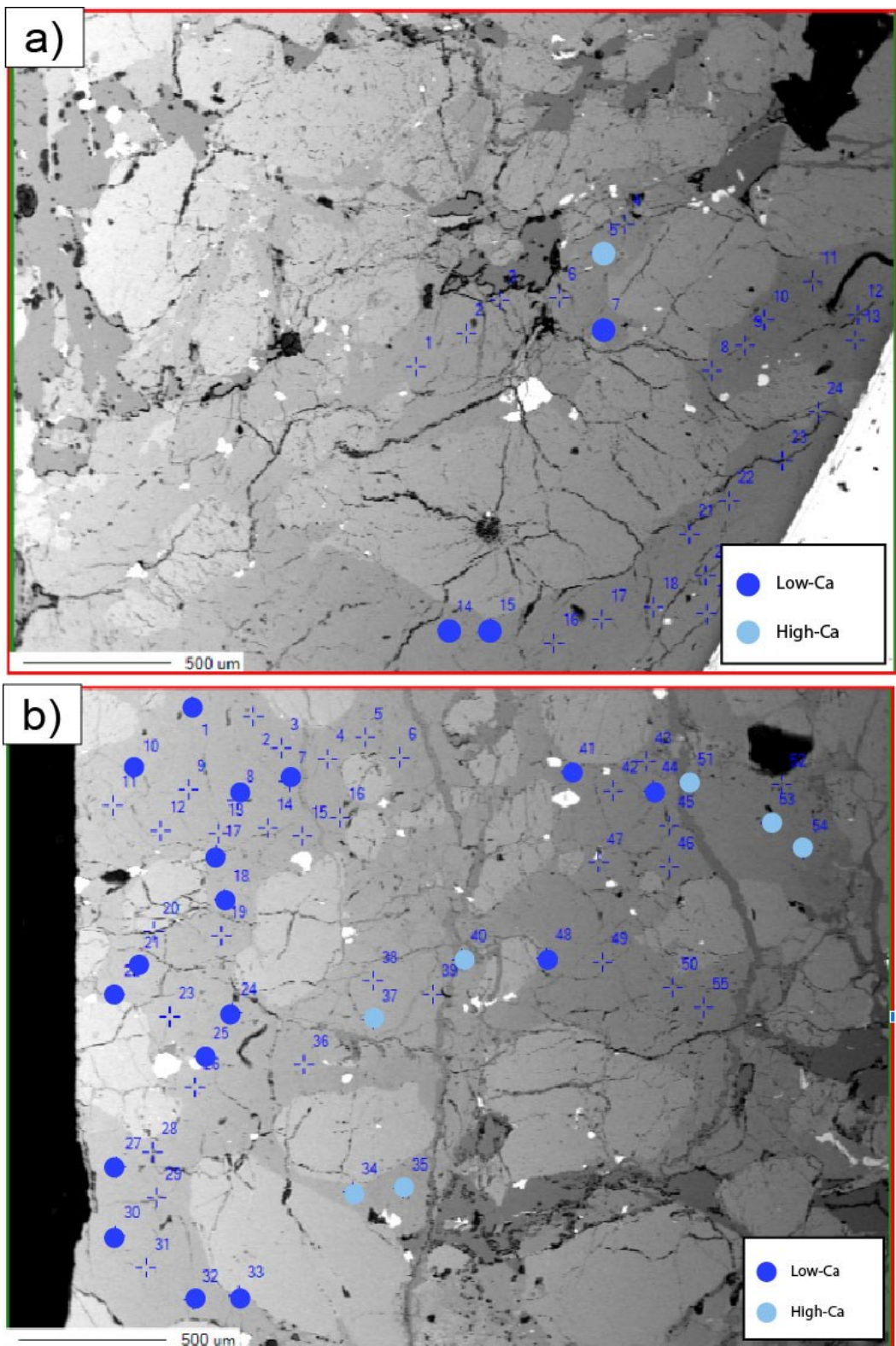


Figure 21. BSE images of two large-scale pyroxene oikocrysts. Cross hairs indicate probe locations from EMP. Cross hairs with circles indicate probe data used for this study, whereas cross hairs without circles indicate a probe analysis where the totals were too low to be used here. In both (a) and (b) the high-Ca analyses lie towards the rim of the pyroxene oikocryst.

4.5.4. Maskelynite

Maskelynite typically occurs as laths (**Figure 22a**) up to ~1 mm in size or as angular grains (**Figure 22b**) ranging from 0.5-2mm in size. In section 01, maskelynite can be found throughout the sample but is more heavily concentrated on the lower left-hand side of the section. Here, maskelynite surrounds the interstitial space between olivine grains in the non-poikilitic area. Maskelynite can also be found rimming pyroxene oikocrysts. Maskelynite is often highly vesiculated and vesicles were later infilled with carbonates to create carbonate amygdales (**Figure 22c**), and this is particularly true for maskelynite located close to regions of shock melt (**Figure 22d**). Maskelynite is also found to be cross-cut by carbonate veins (**Figure 22e**), but on a smaller scale than olivine grains. The phosphates (merrillite and apatite) present in the section are found in direct association with maskelynite.

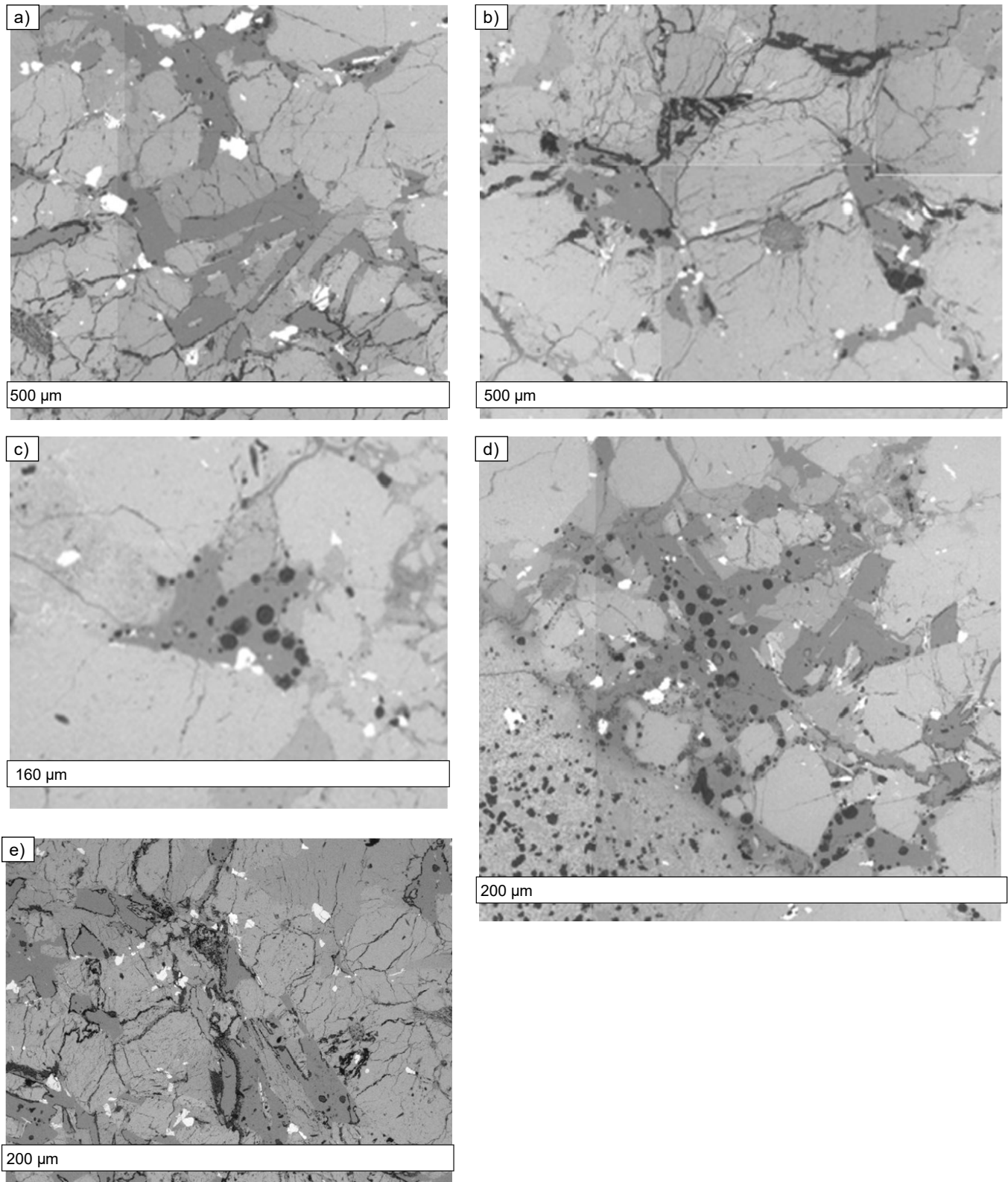


Figure 22. BSE images of maskelynite a) maskelynite laths; b) angular maskelynite grains; c) carbonate vesicles in maskelynite; d) carbonate vesicles in maskelynite near shock melt pocket; e) carbonate veins cross cutting maskelynite.

4.6. Shock Features

4.6.1. *Introduction*

NWA 14904 shows mineralogic, and textural evidence of shock. Shock effects are seen through the presence of shock melt, and in olivine and maskelynite, which are the two dominant mineral phases within the sample.

4.6.2. *Shock Melt*

Shock melt accounts for 19.67% of section 01, and appears primarily in pockets throughout the sample. The melt is dark brown to black in color (**Figure 23a**). It contains olivine microlites set in a matrix of isotropic shock glass, and vesicles that are often partially or completely infilled with carbonates, which are described in section 4.8. Shock veins are present radiating out from areas of shock melt and can connect shock melt pockets (**Figure 23a**) or terminate in surrounding mineral grains. The shock veins are found throughout the entire sample but are seen primarily originating from shock melt pockets; they range in width from ~2mm to ~15mm, being wider closer to melt pockets, and narrowing out further away from melt pockets before terminating.

4.6.3. *Olivine*

Olivine shows effects of shock darkening, where olivine grains are a deeper brown color than unshocked grains (Takenouchi et al., 2018) (**Figure 23b**). Shock-darkened grains can be found directly adjacent to non-shock-darkened grains and show no preference for poikilitic or non-poikilitic texture. Olivine grains surrounding the melt pockets show high levels of shock, with abnormally high birefringence color up to fifth-order blue (Ogilvie et al., 2011). Gradational shock

features can be seen in some grains, where the birefringence is higher closer to the melt and transitions to a more normal birefringence moving away from the melt (**Figure 23d**). In areas close to melt pockets, post-shock annealing of olivine has occurred, where high temperatures have overwritten other shock features that may have initially been present, such as original fracturing and planar deformation features (**Figure 23c**). Olivine grains next to shock melt pockets can also be found either partially destroyed or vaporized (**Figure 23e**).

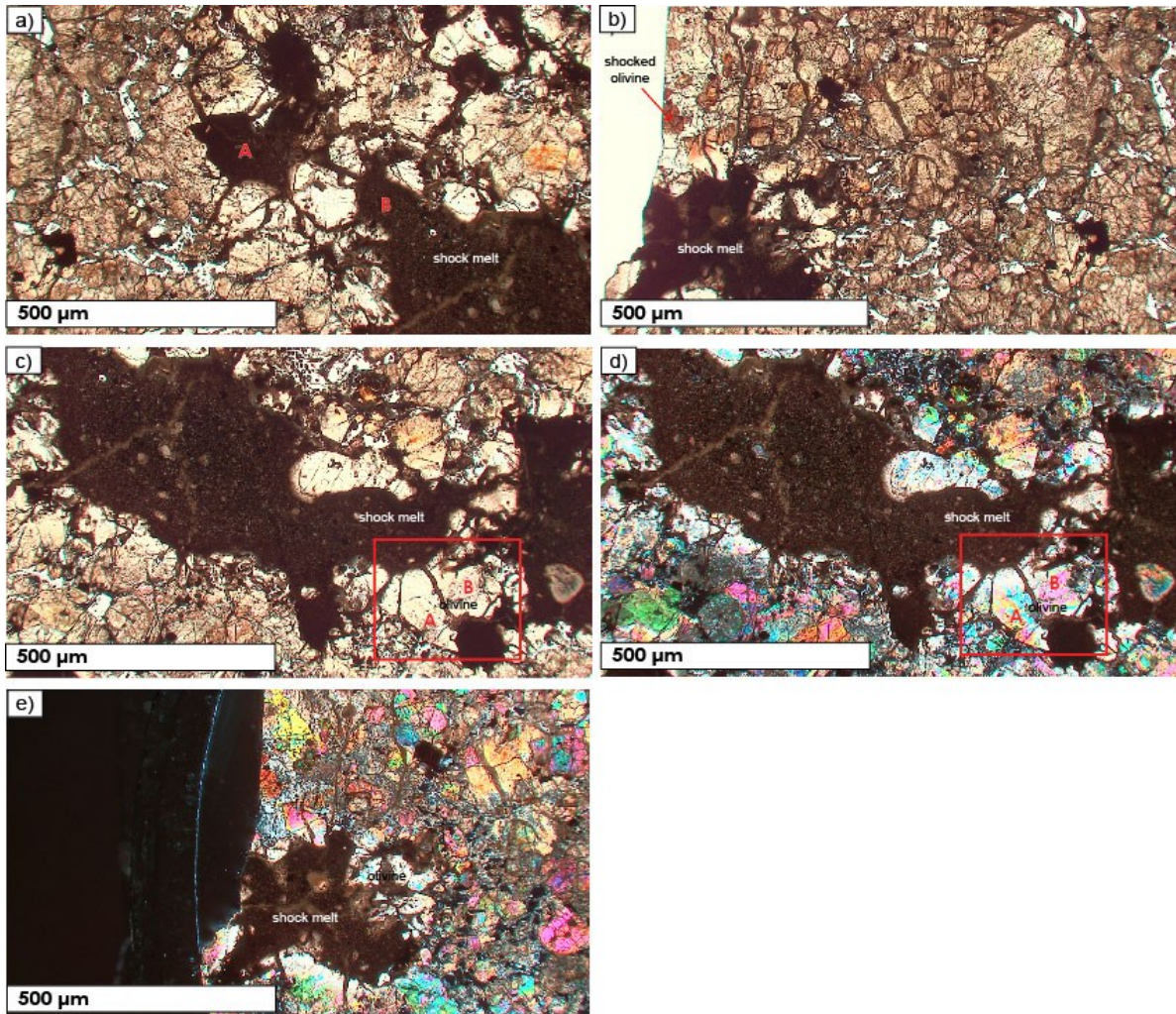


Figure 23. Shock Effects a) PPL image, shock melt pockets and shock melt veins (black); b) PPL image, shock darkened olivine; c) PPL image, Grain A and Grain B both showing lack of fracture; d) XPL image, Grain A displays an abnormally high birefringence interference color; e) XPL image, olivine grains near shock melt edge show partial destruction or complete vaporization.

4.6.4. Maskelynite

Maskelynite is a form of dialethic plagioclase glass that forms from high shock temperatures and pressures in a process referred to as maskelynitization (Milton and de Carli, 1963). The very presence of maskelynite is evidence that the sample has undergone shock and it is an almost ubiquitous phase in shergottites (Chen and El Goresy, 2000).

4.7. Shock Classification

In addition to classification based on mineralogy and textures as discussed in previous sections, meteorites are also assigned a shock classification. Shock classification ranks the shock effects in a sample from no evidence of shock to completely shocked that its 100% shock melted. As discussed above in Section 4.6., NWA 14904 is highly shocked and shows many shock features such as shock melt pockets, shock veins, shock darkening, abnormal birefringence in olivine, alteration of mineral phase grains, and maskelynitization. Using the shock classification scheme outlined in Fritz et al. (2017) and Stöffler et al. (2018), NWA 14904 has a shock classification of S6- very strongly shocked. Implications for the petrogenic conditions during formation based on the S6-very strongly shocked, classification will be discussed in section 5.3.4.

4.8. Terrestrial Alteration

The carbonates found in this sample are attributed here to terrestrial alteration. They are present as either carbonate vesicles or carbonate veins, which are common in desert

meteorites like NWA 14904 (Crozaz et al., 2003). The carbonate veins are predominantly calcite and originate at the outer edge of the sample and radiate inwards, cross-cutting the shock melt, or infilling cracks (**Figure 24a-b**). This relationship supports a terrestrial origin, as all veins come from the outside of the sample and penetrate inwards. Some carbonate veins show a dendritic texture, with darker features lining one side of the vein (**Figure 24c-d**).

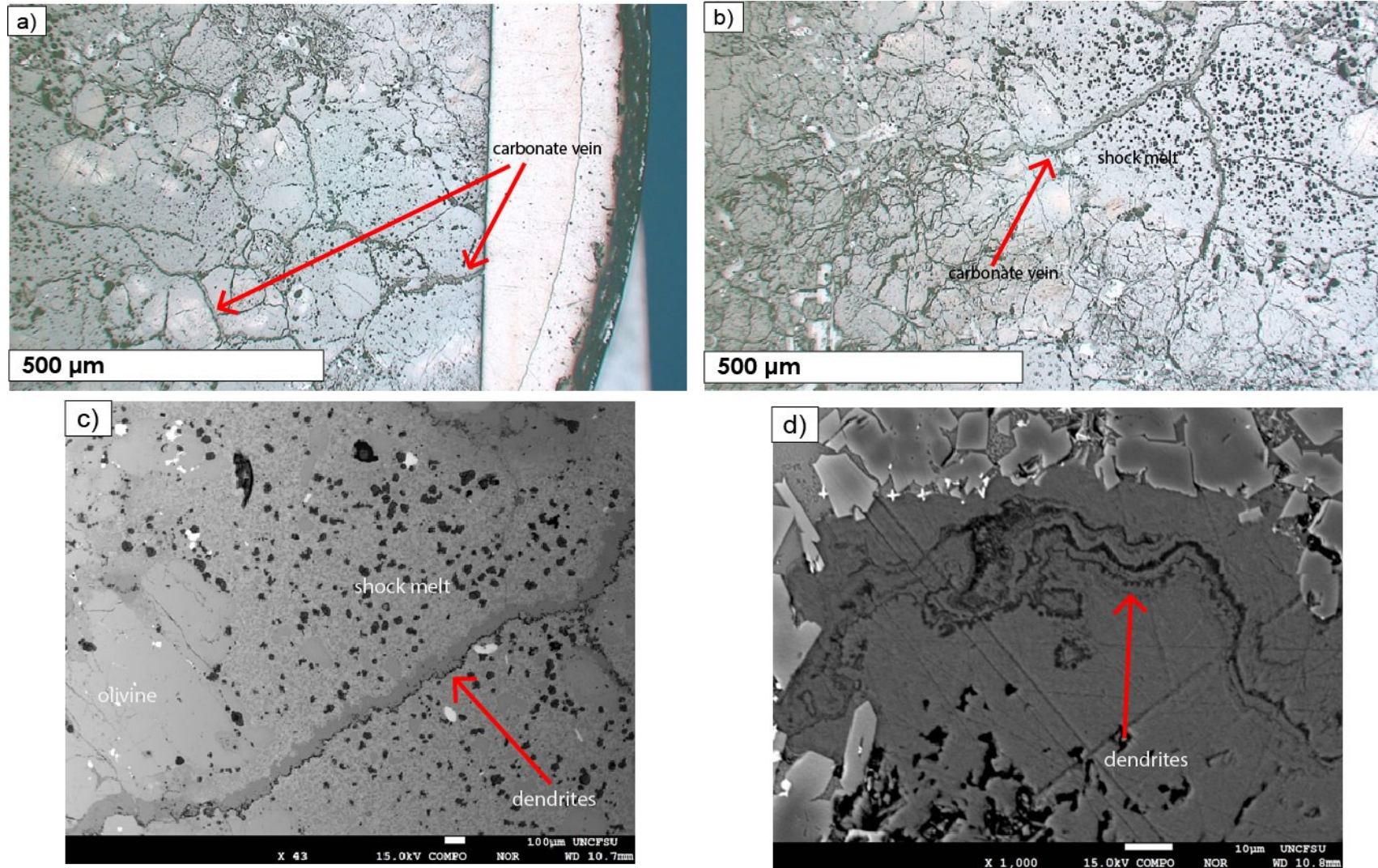


Figure 24. Carbonate Veins a-b) Reflected light image of carbonate veins; c-d) BSE images of dendritic textures in carbonate veins.

Carbonate-filled vesicles are also present in Section 01 and contain many different compositions of carbonates in a single vesicle. (**Figure 25**). Vesicles are seen primarily in maskelynite and shock melt but can also be found in other minerals such as pyroxenes. Most vesicles are completely to partially filled with carbonates, with a small percentage containing no carbonate fill. Additionally, pervasive carbonate alteration is seen in the melt. Carbonates replacing the melt are round to oblong area with few displaying irregular or globular shapes (**Figure 26**). Where maskelynite in close contact with the melt, the carbonate alteration in the melt often times rims maskelynite, as it is more easily altered. All carbonates show irregular fracturing and all range in carbonate composition (**Table 5**).

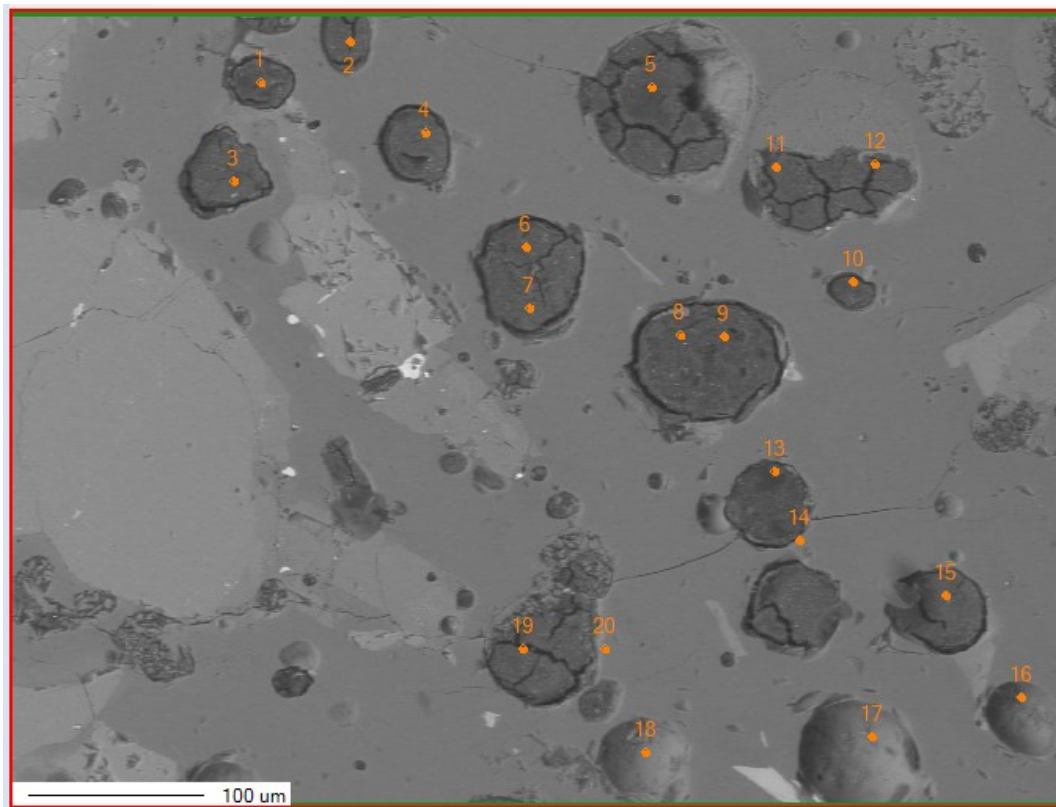


Figure 25. BSE image of carbonate filled vesicles in maskelynite

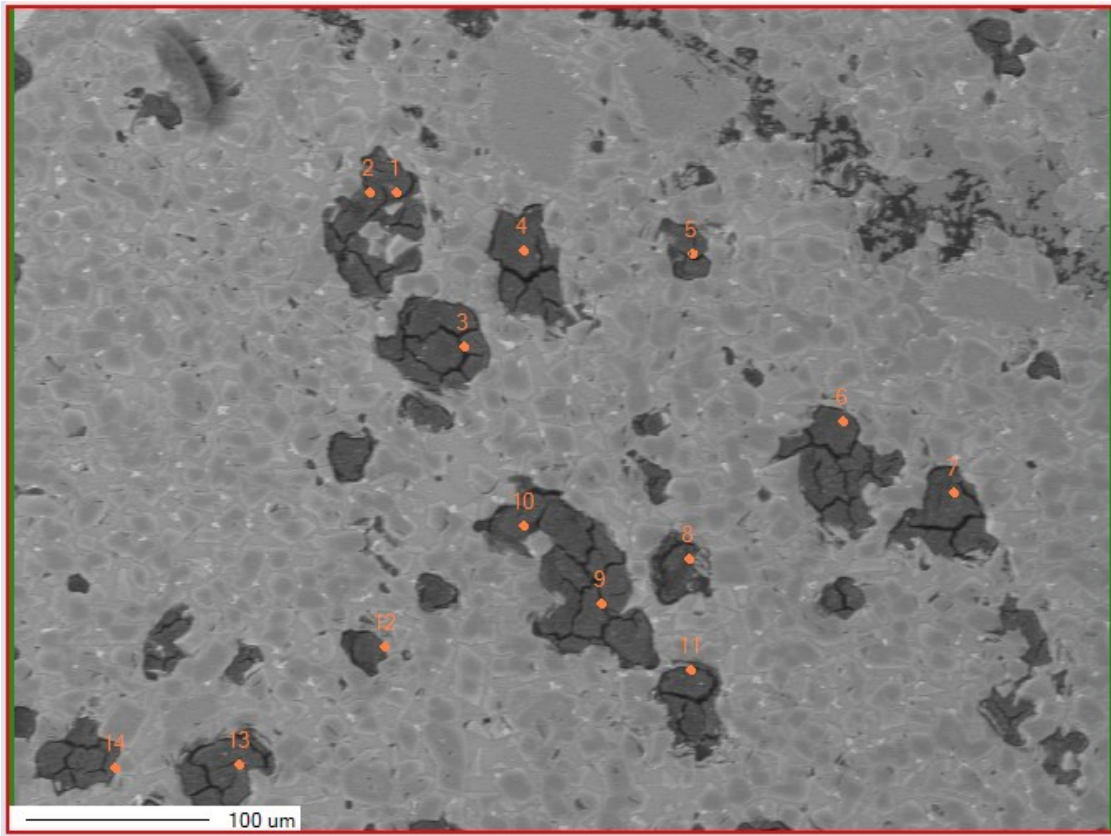


Figure 26. BSE image showing carbonates altering shock melt. Olivine microlites dominate the melt and are zoned. Their brighter edges suggest that they are more Fe-rich at their rims.

4.9. Electron Microprobe

Table 5. Summary of EMP Mineral Compositions for all major phases

Mineral	Average	Range Min	Range Max
Olivine	Fo _{66.94} -Fa _{33.06}	Fo _{65.15} -Fa _{33.85}	Fo _{69.12} -Fa _{34.85}
High-Ca Pyroxene	Wo _{34.00} En _{51.04} Fs _{14.96}	Wo _{30.01} En _{48.23} Fs _{13.10}	Wo _{38.20} En _{54.23} Fs _{17.05}
Low-Ca Pyroxene	Wo _{8.67} En _{69.40} Fs _{21.93}	Wo _{2.93} En _{60.57} Fs _{19.59}	Wo _{17.85} En _{77.48} Fs _{25.24}
Maskelynite	An _{51.69} Ab _{46.49} Or _{1.82}	An _{48.33} Ab _{43.97} Or _{0.07}	An _{54.72} Ab _{48.99} Or _{2.92}
Carbonate veins	Cal _{91.11} Mag _{6.59} Sid _{2.29}	Cal _{0.48} Mag _{1.23} Sid _{0.00}	Cal _{98.42} Mag _{81.03} Sid _{39.07}
Carbonate vesicles	Cal _{40.86} Mag _{38.05} Sid _{21.09}	Cal _{0.42} Mag _{1.47} Sid _{2.33}	Cal _{95.49} Mag _{74.90} Sid _{51.08}
Chromite	Chr _{61.38} Spn _{6.56} Ulv _{32.07}	Chr _{57.46} Spn _{5.17} Ulv _{29.85}	Chr _{62.76} Spn _{8.45} Ulv _{35.95}
Ilmenite	Chr _{1.94} Spn _{14.85} Ulv _{83.21}	Chr _{1.45} Spn _{13.80} Ulv _{82.13}	Chr _{2.62} Spn _{16.11} Ulv _{84.13}

Analysis from EMP data shows both high- and low-calcium pyroxenes are present. The low-Ca pyroxene is enstatite-pigeonite in composition and has a range of $\text{Fs}_{19.59\text{-}25.24}\text{Wo}_{2.93\text{-}17.85}$. The high-Ca pyroxene phase is augite, with a composition of $\text{Fs}_{13.10\text{-}17}\text{Wo}_{30.01\text{-}38.20}$. The FeO/MnO of all pyroxenes ranges from 17.68 to 31.07, with an average of 24.22. Pyroxene oikocrysts are predominantly low-Ca pyroxene, but have higher-Ca at the rim (**Figure 21**). Poikilitic areas have low-Ca pyroxenes with compositions ranging from $\text{Fs}_{19.59\text{-}23.12}\text{Wo}_{2.93\text{-}12.23}\text{En}_{65.43\text{-}77.48}$, and high-Ca pyroxenes ranging from $\text{Fs}_{13.88\text{-}15.24}\text{Wo}_{31.49\text{-}37.12}\text{En}_{48.23\text{-}53.26}$. Mg#s for pyroxene oikocrysts in poikilitic areas average 77.16 and 77.70, for low-Ca and high-Ca pyroxenes, respectively.

Non-poikilitic pyroxenes have Mg#s averaging 74.12 for low-Ca pyroxene and 77.30 for high-Ca pyroxene. In poikilitic low-Ca pyroxenes as Mg# increases, Al_2O_3 , CaO , and TiO_2 decrease; whereas, for their high-Ca pyroxene counterparts, only TiO_2 decreases with Mg# increase. In the non-poikilitic zones, in low-Ca pyroxene, Cr_2O_3 , and CaO show a positive correlation with Mg#, and in high-Ca pyroxene only CaO increases with Mg#, with a corresponding decrease in both Al_2O_3 , and TiO_2 (**Figure 27**).

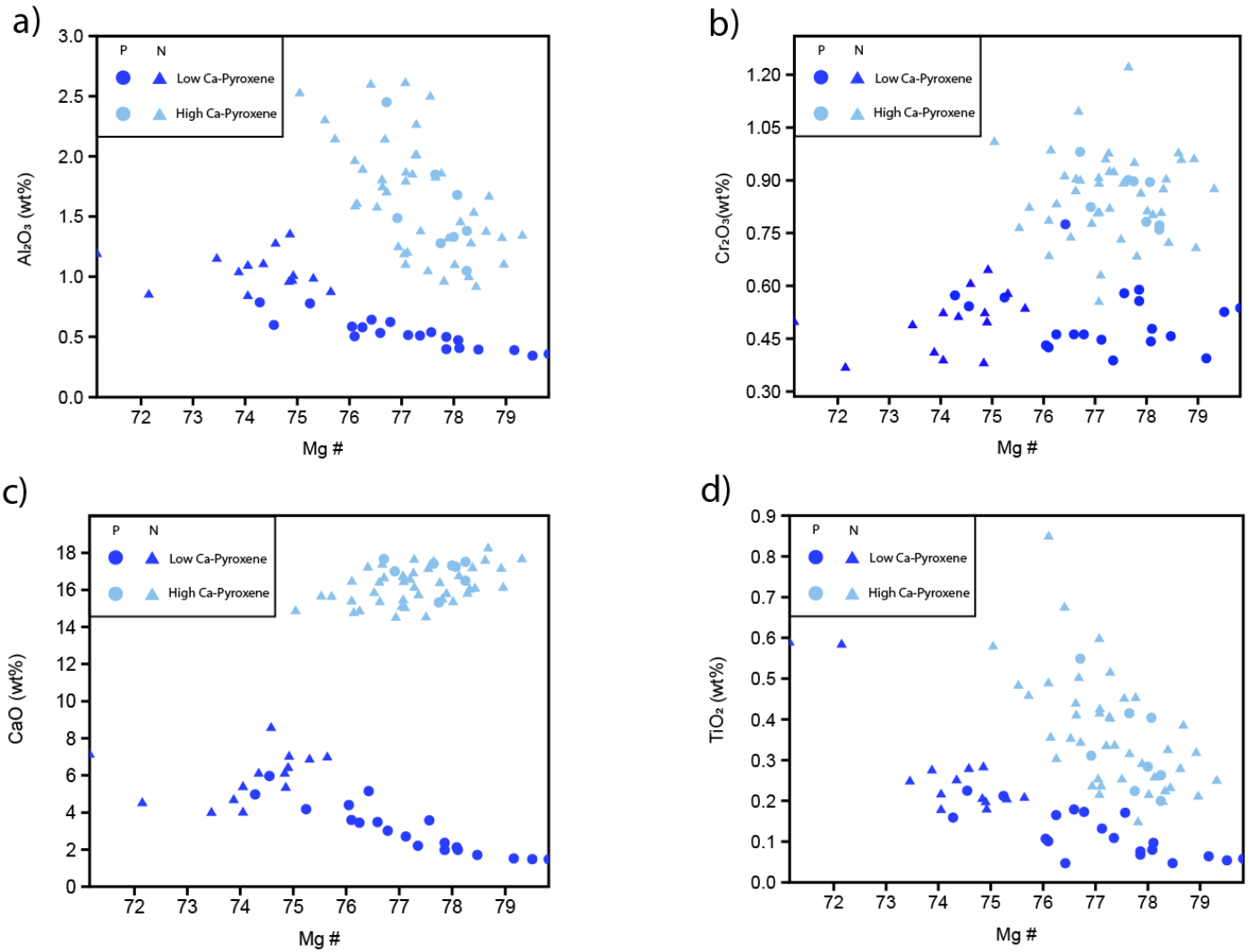


Figure 27. Mg# plotted vs. (a) Al_2O_3 (b) Cr_2O_3 (c) CaO (d) TiO_2 . Low-Ca poikilitic pyroxenes are richer in Mg than their poikilitic counterparts, as reflected by their higher Mg#. High-Ca pyroxenes are higher in Al_2O_3 , Cr_2O_3 , CaO , and TiO_2 as compared to low-Ca pyroxenes. P=poikilitic, NP=non-poikilitic.

EMP analysis was only obtained for non-poikilitic olivine. Olivine has a compositional range of $\text{Fo}_{65.15-69.12}\text{-}\text{Fa}_{30.88-34.85}$ with an average of $\text{Fo}_{66.94}\text{Fa}_{34.84}$. Olivine has a FeO/MnO range of 46.49-66.14 with an average FeO/MnO of 54.44. Olivine has a Mg# ranging from 65.15-69.12 with an average Mg# of 66.94.

Maskelynite has a compositional range between $\text{An}_{48.33-54}\text{Ab}_{43.97-48.99}\text{Or}_{0.07-2.92}$ with an average of $\text{An}_{51.69}\text{Ab}_{46.49}\text{Or}_{1.82}$.

Carbonate veins are predominantly calcite with an average of $\text{Ca}_{91.11}\text{Mag}_{6.59}\text{Sid}_{2.29}$ and a range in composition of $\text{Ca}_{0.48-98.42}\text{Mag}_{1.23-81.03}\text{Sid}_{0.00-39.07}$.

Carbonates vesicles show a wide range in compositions of $\text{Ca}_{0.42-95.49}\text{Mag}_{1.47-74.90}\text{Sid}_{2.33-51.08}$ with an average composition of $\text{Ca}_{40.86}\text{Mag}_{38.04}\text{Sid}_{21.09}$. BSE imaging shows that the vesicles are made up of many different compositional domains, where a single carbonate vesicle contains multiple carbonate compositions (**Figure 25**). However, the compositional domains are too small to be measured separately by the EMP.

Oxides and phosphates are present as accessory minerals in NWA 14904. The oxides in NWA 14904 are chromite and ilmenite. Chromite has a range in compositions from $\text{Chr}_{57.46-62.76}\text{Spn}_{5.17-8.45}\text{Ulv}_{29.85-35.95}$ with an average of $\text{Chr}_{61.38}\text{Spn}_{6.56}\text{Ulv}_{32.07}$. Ilmenite has a compositional range of $\text{Chr}_{1.45-2.62}\text{Spn}_{13.80-16.11}\text{Ulv}_{82.13-84.13}$. The phosphate in NWA 14904 is merrillite. Tables of all EMP measurements can be found in Appendix **Error! Reference source not found.**

4.10. Classification

The data collected were summarized and submitted to NomCom, with a classification of poikilitic shergottite. This was accepted and the official name for this meteorite was given as NWA 14904 (MetBase et al., 2022).

5. DISCUSSION

Here, the full details of the classification of NWA 14904 are discussed, followed by a comparison to other poikilitic shergottites, and a petrogenetic model for its formation.

5.1. Confirming Martian Origin

While Martian meteorites can be identified using oxygen isotopes and the composition of trapped gas bubbles, as discussed in section 2.3.1., Martian samples contain other signatures that are distinct from Earth as a result of their different bulk composition; in other words, the two planets formed from different materials. Many previous studies have demonstrated how this has impacted their planetary evolution (e.g. Drake and Righter, 2002; Taylor et al., 2006); for example, terrestrial minerals have different chemical compositions than their Martian counterparts and these differences allow us to distinguish Martian meteorites from terrestrial samples without the need for more complex isotopic analysis (Agee and Draper, 2004). Olivine, a key mineral in the mantle of both bodies, demonstrates this well as terrestrial mantle olivine has a composition of ~Fo₈₉₋₉₁ (Filiberto and Dasgupta, 2011), whereas olivine found on Mars and, therefore, within Martian meteorites has an

average composition of \sim Fo₆₀₋₉₀ (Koeppen and Hamilton, 2008). McSween et al., (2004) further states that Rover measurements have been as low as Fo₅₁, suggesting that Martian meteorites may not provide the full scope of Martian olivine compositions. Regardless, the difference in olivine composition between Earth and Mars is the result of the mantles of both bodies containing different iron and magnesium contents as a result of their differing bulk compositions (e.g., Agee and Draper, 2004; Bertka and Fei, 1996; Filiberto and Dasgupta, 2011). Martian basalts contain higher amounts of FeO than terrestrial basalts (Dreibus and Wänke, 1987; McSween, 1994; Treiman et al., 2000; Filiberto and Dasgupta, 2011), which results in lower Fo contents and Mg# within Martian samples, where Mg# = Mg/(Mg+Fe) mol%. The Fo-content of olivine, and the Mg# of a sample can, therefore, be used as one of the parameters to classify meteorites and infer a Martian origin.

The compositional range of olivine in NWA 14904 is Fo₆₅₋₆₉ (**Table 5**) which is closer to the range measured in olivine compositions in Martian meteorites, Fo \sim 60-90, (Koeppen and Hamilton, 2008) than those from terrestrial sources, Fo \sim 89-91 (Filiberto and Dasgupta, 2011). While the comparatively low Fo value of NWA 14904 olivine does lie within the range measured for Martian meteorites, it is affected by a measurement bias in the data presented here. Studies of previously classified Martian meteorites have shown that there is a compositional difference in olivine measured within samples that contain both poikilitic and non-poikilitic olivine (Rahib et al., 2019 and references therein). This is because poikilitic regions crystallize first, incorporating more magnesium into their silicates than the later forming non-poikilitic regions, which are more iron-rich. As a result, non-poikilitic Martian olivine has lower Fo-contents than their poikilitic counterparts. In this

study, we were only able to measure non-poikilitic olivine, which resulted in a precise, but inaccurately low average Fo value for the sample.

The Mg# for olivine was calculated for NWA 14904 and ranges from 55.15-69.12, with an average of 66.94, which falls within the average for Martian meteorites and is too low to be terrestrial. As with the average olivine content, the measurement bias (only analyzing non-poikilitic olivine) results in a low bulk Mg# of 55.54 for NWA 14904 when compared to other Martian samples(**Table 6**) The bulk Mg# for NWA 14904 is likely higher than is currently reported here, and will be recalculated when poikilitic olivine data are available after this work is complete.

Table 6. Different Bulk Mg# reported for Martian samples in the literature

NWA 14904	Morgan and Anders (1979)	Dreibus and Wänke (1997)	Lodders and Fegley (1997)	Sanloup (1999)	Taylor (2013)
55.54	65.26	65.27	63.32	60.66	62.76

The bulk Mg# for NWA 14904 and comparative samples listed in

Table 6 were calculated using the bulk wt% values of Mg and Fe.(Morgan and Anders, 1979; Dreibus and Wänke, 1997; Lodders and Fegley, 1997; Sanloup, 1999; Taylor, 2013).

In addition to the parameters discussed above, the Mn and Fe ratios in olivine, and potentially pyroxene, can also be used to determine the parent body of a meteorite. Fe and Mn behave similarly during differentiation and their primordial values remain relatively constant throughout the differentiation process. Mn/Fe ratios are directly attributed to the initial accretional abundances as well as a planetary body's accretional position in the solar

system at the time of formation (Papike et al., 2009). As a result, the Mn/Fe ratio for Mars is unique and can be used to link samples with similar ratios to that planet.

The Mn/Fe ratio was examined in NWA 14904 using olivine and compared to other similar trends for Mars, Earth, and the Moon (Papike et al., 2009) (**Figure 27**). The Mn/Fe ratio for NWA 14904 lies close to or on the Martian trend line (Dymek et al., 1976; Drake et al., 1989; Papike et al., 2009).

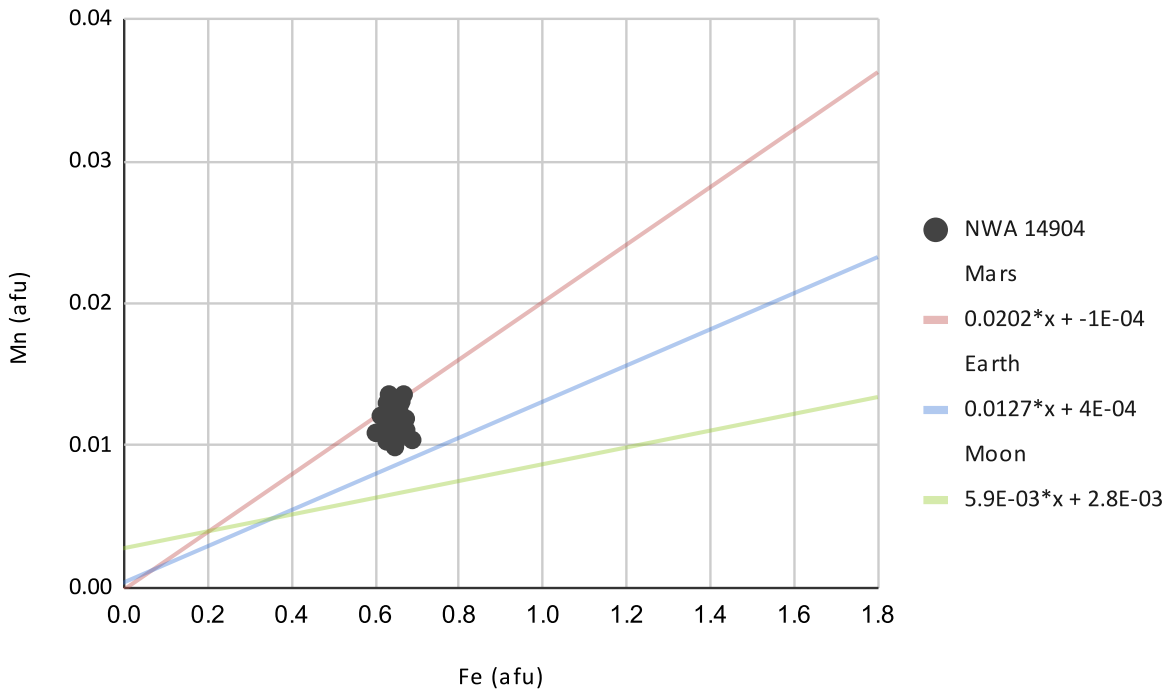


Figure 28. Mn vs Fe plotted for NWA 14904 olivine and compared to reported Mn/Fe trends for Mars, Earth, and the Moon (Papike et al., 2009)

5.2. Poikilitic Shergottites

As discussed in section 2.3 above, the Martian meteorite clan can be subdivided into four different groups based on their mineralogy, texture, and bulk composition: the shergottites, nakhlites, and chassignites (the SNCs), and ungrouped, with the latter containing those samples with characteristics that do not fit in the SNC groups.

Shergottites are igneous meteorites whose classification is broken into four groups (basaltic, olivine-phyric, poikilitic, and gabbroic) based on their mineralogy and texture. Poikilitic shergottites can be identified by their bimodal texture of pyroxene oikocrysts enclosing olivine chadacrysts.

NWA 14904 is classified as a poikilitic shergottite due to its bimodal texture and mineralogy. In order to place NWA 14904 within the current suite of poikilitic shergottites and understand its petrogenesis, it is necessary to first compare NWA 14904 to the existing dataset. Here, we compare NWA 14904 to eight other poikilitic shergottites described in Combs et al. (2019) and Rahib et al. (2019)(**Table 7**). While shergottites are broken into three main geochemical groups: enriched, intermediate, and depleted, poikilitic shergottites have thus far only been found to be geochemically enriched or intermediate. In order to constrain a possible geochemical group for NWA 14904, the following data were analyzed and compared to other poikilitic shergottites in the intermediate and enriched geochemical group.

Table 7. Comparative Suite of Poikilitic Shergottites

Meteorite Name	Geochemical Group
NWA 11065 ¹	intermediate
NWA 10961 ¹	intermediate
ALHA 77005 ¹	intermediate
LEW 88516 ¹	intermediate
NWA 11043 ¹	enriched
NWA 4468 ¹	enriched
NWA 10618 ¹	enriched
NWA 10169 ²	enriched

Rahib et al., (2019)¹; Combs et al., (2019)²

5.2.1. Olivine Sampling Bias

As discussed in section 5.1, only non-poikilitic olivine grains were sampled by EMP analysis due to probe availability. Lack of poikilitic olivine grain sampling causes NWA 14904 to appear lower in Mg and richer in Fe than it likely is, producing biased values for olivine averages. This error is then propagated into the bulk composition and Mg# of the bulk rock presented here, as the average olivine composition was used to calculate these values. In order to offset this bias, only non-poikilitic olivine will be used here for comparisons, when possible.

5.2.2. Bulk Composition

It is important to note that when calculating bulk composition based on modal abundances derived from thin sections, the bulk composition is only representative if the thin-section (a 1-inch round) contains the same mineral proportions as the bulk rock. In poikilitic shergottites, thin sections can display disproportionately large or small areas of poikilitic or non-poikilitic texture that are not representative of the whole rock (Orr et al., 2022). It is, therefore, challenging to compare the bulk composition calculated for NWA 14904 to measured values for the comparison suite used here. Indeed, when examining trends in bulk compositions for the major oxides vs. Mg# in NWA 14904 relative to the comparative suite, there do not appear to be significant correlations between bulk compositions and geochemical group (**Figure 29**).

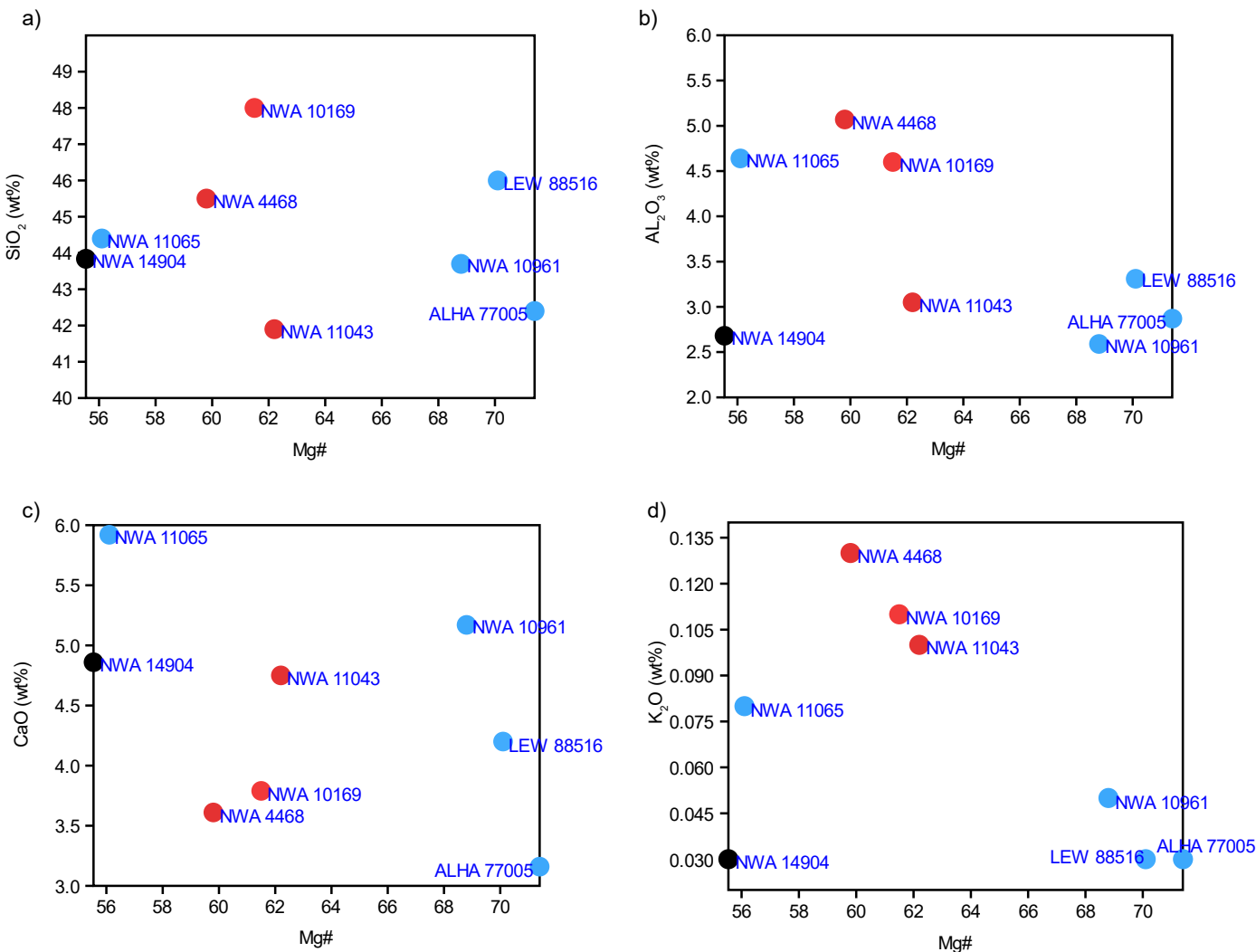


Figure 29. Bulk Oxides vs Mg# NWA 14904 (black), intermediate samples (blue), and enriched samples (red). The Mg# for NWA 14904 is anomalously low due to a data collection bias.

5.2.3. Modal Mineralogy

While modal mineralogy does not appear to be a diagnostic tool to distinguish intermediate and enriched samples, NWA 14904 contains more melt than any of the poikilitic shergottites used here for comparison (Appendix 7.2). Of the comparative suite, only NWA 10961 contains a significant amount of melt (14%) which, similarly to NWA 14904, contains olivine as the dominant phase (Rahib et al. 2019). If the modal abundances of melt for both of these samples are recalculated assuming that all melt is olivine, then they both contain approximately 63% olivine. However, CT scans of NWA 14904 show that the modal mineralogy varies significantly on a scale larger than the one-inch section used for this study and this is likely true for most poikilitic shergottites. As a result, to produce truly comparable modal abundances, a larger representative area would have to be analyzed for each sample.

5.2.4. Textures and composition

5.2.4.1. Olivine

Non-poikilitic olivine¹ in NWA 14904 has a compositional range of Fo₆₅₋₆₉, which is consistent with intermediate poikilitic shergottites (**Figure 30**) and is most similar to NWA 10961, with a compositional range of Fo₆₈₋₇₁ (Rahib et al., 2019) (Section **Error! Reference source not found.**). All the enriched shergottites here have Fo ranges below NWA 14904;

¹ As discussed earlier, only comparisons with non-poikilitic olivines are presented here due to the lack of data for poikilitic olivine.

however, the upper range of NWA 11043 does slightly overlap the lower end of the range for NWA 14904 (**Figure 30**).

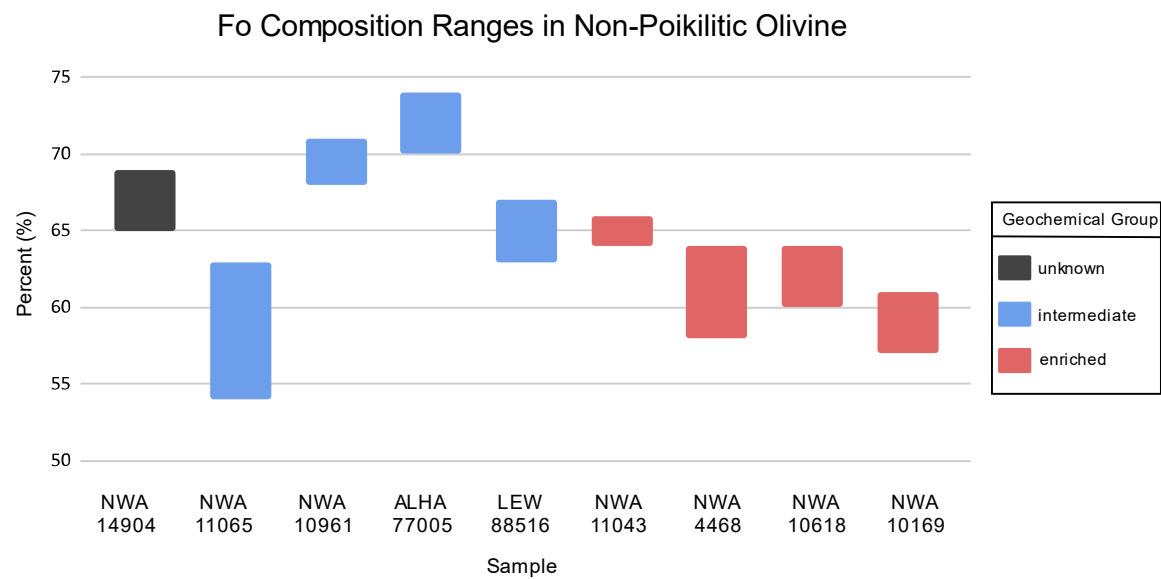


Figure 30. Comparison of Fo compositional ranges within the non-poikilitic olivine of NWA 14904 and other poikilitic shergottites (both intermediate and enriched). NWA 14904 overlaps the range given for the intermediate shergottites.

5.2.4.2. Pyroxene

In NWA 14904 the non-poikilitic high-Ca pyroxene has an average of $\text{Wo}_{31}\text{En}_{53}\text{Fs}_{16}$ (**Figure 31**) with an Mg# between 76-79 and an average of 77 (**Figure 32**). Non-poikilitic low-Ca pyroxenes have an average composition of $\text{Wo}_{12}\text{En}_{65}\text{Fs}_{23}$ (**Figure 31**) and Mg# from 71-76, with an average of 74 (**Figure 33**). These values are more Fe-rich than the poikilitic oikocrysts, which is typical for both geochemical groups; however, NWA 14904 non-poikilitic pyroxenes are more similar to those found in other intermediate samples (**Figure 31**) and are most similar to intermediate poikilitic shergottites NWA 10961 and ALHA

77005, which both have an average composition of $\text{Wo}_{10}\text{En}_{66}\text{Fs}_{24}$ for low-Ca pyroxene, and high-Ca pyroxene compositions of $\text{Wo}_{32}\text{En}_{52}\text{Fs}_{16}$ and $\text{Wo}_{36}\text{En}_{50}\text{Fs}_{15}$ respectively (**Error! Reference source not found.**) (Rahib et al., 2019). The Mg# values for the low-Ca pyroxenes are consistent with all other intermediate poikilitic shergottites in the comparative suite, which have an average Mg# of 73, as opposed to enriched shergottites whose Mg#s for non-poikilitic low-Ca pyroxene averages much lower at 63 (**Figure 33**) (Rahib et al., 2019).

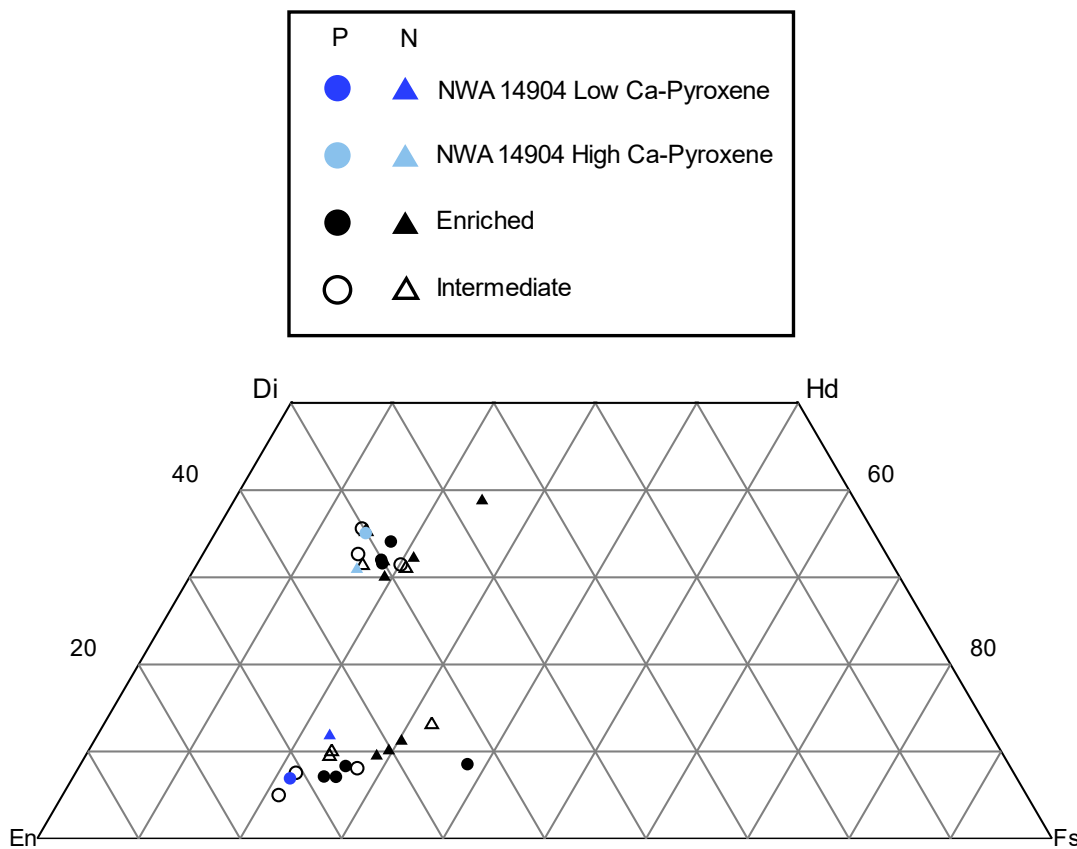


Figure 31. Pyroxene quadrilateral with NWA 14904 pyroxene compositions compared to other poikilitic shergottites of both the enriched and intermediate geochemical groups. NWA 10169 is not included in this plot as its compositions are not comparable to other specimens due to zonation.

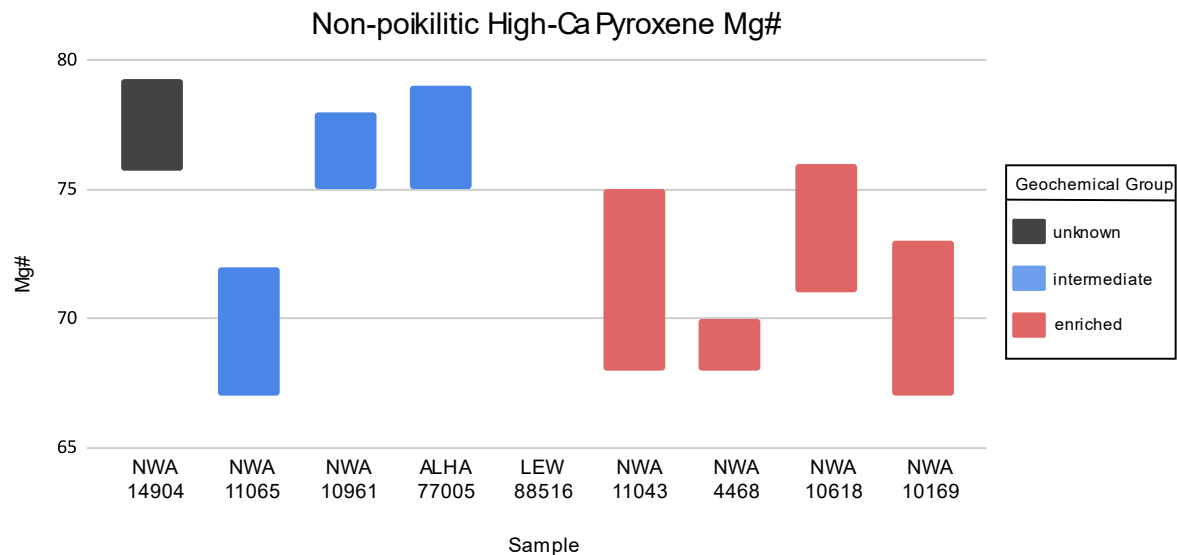


Figure 32. Comparison of the range of Mg# in non-poikilitic high-Ca pyroxene within NWA 14904 and the comparative suite of poikilitic shergottites.

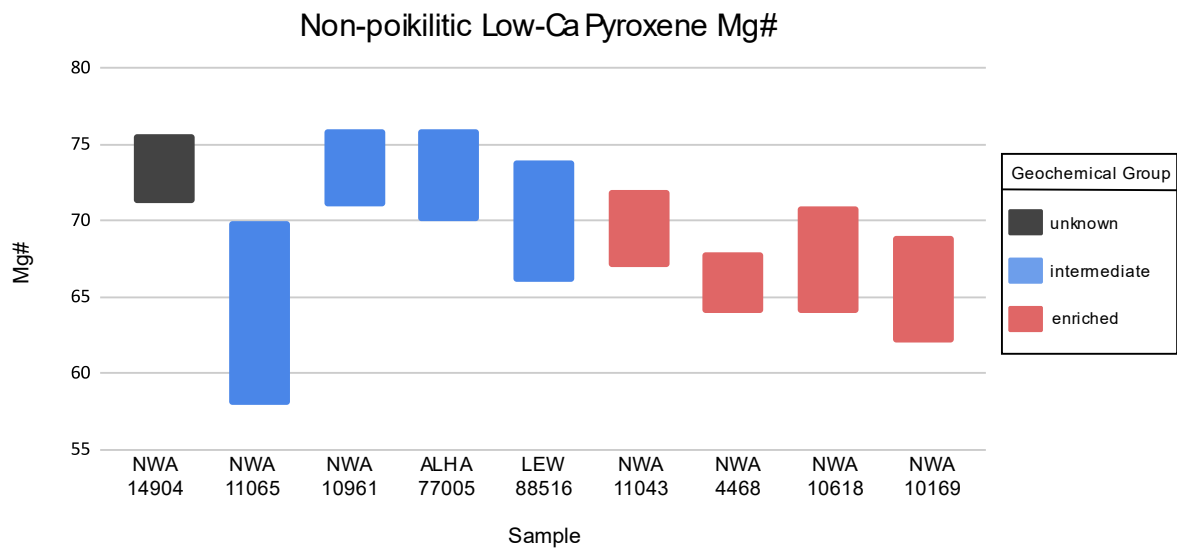


Figure 33. Comparison of the range of Mg# in non-poikilitic low-Ca pyroxene within NWA 14904 and the comparative suite of poikilitic shergottites.

In NWA 14904 the average composition for poikilitic high-Ca pyroxene is $\text{Wo}_{35}\text{En}_{50}\text{Fs}_{15}$, with a Mg# ranging from 75-78 (**Figure 34**). The average composition for poikilitic low-Ca pyroxene is $\text{Wo}_7\text{En}_{72}\text{Fs}_{21}$, with a Mg# ranging from 78-80 (**Figure 35**). NWA 14904's poikilitic pyroxenes (both low and high-Ca) have an Mg# of 77. The intermediate poikilitic shergottites NWA 10961 and ALHA 77005 are most similar to NWA 14904 in this regard, as their poikilitic pyroxenes have an Mg# of 77 (NWA 10961) and 78 (ALHA 77005) for both pyroxene compositions. (Rahib et al., 2019).

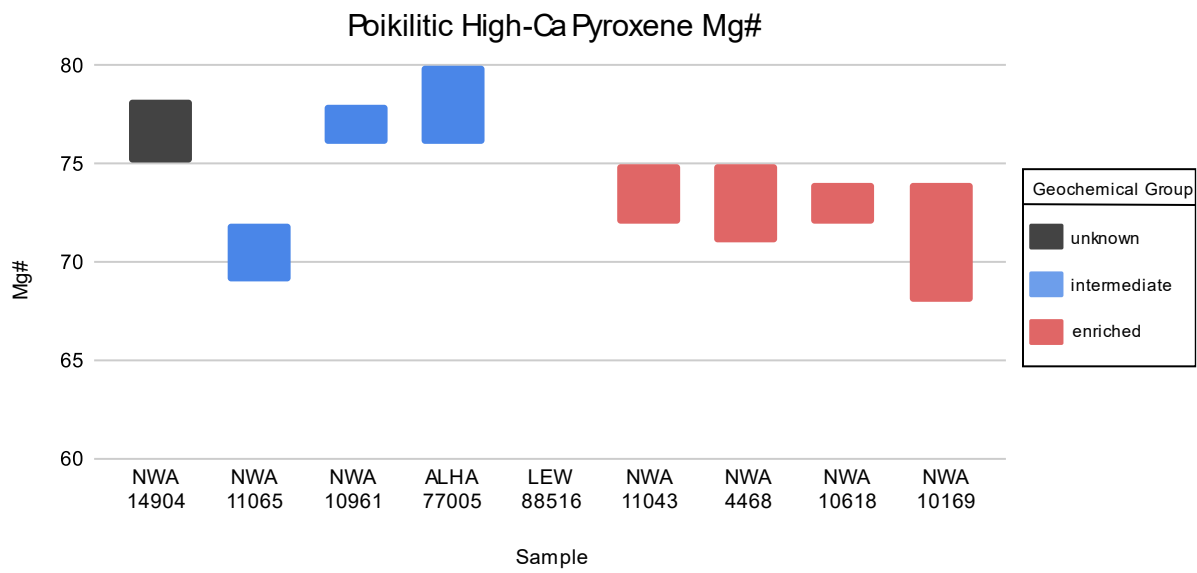


Figure 34. Comparison of the range of Mg# in poikilitic high-Ca pyroxene within NWA 14904 and the comparative suite of poikilitic shergottites.

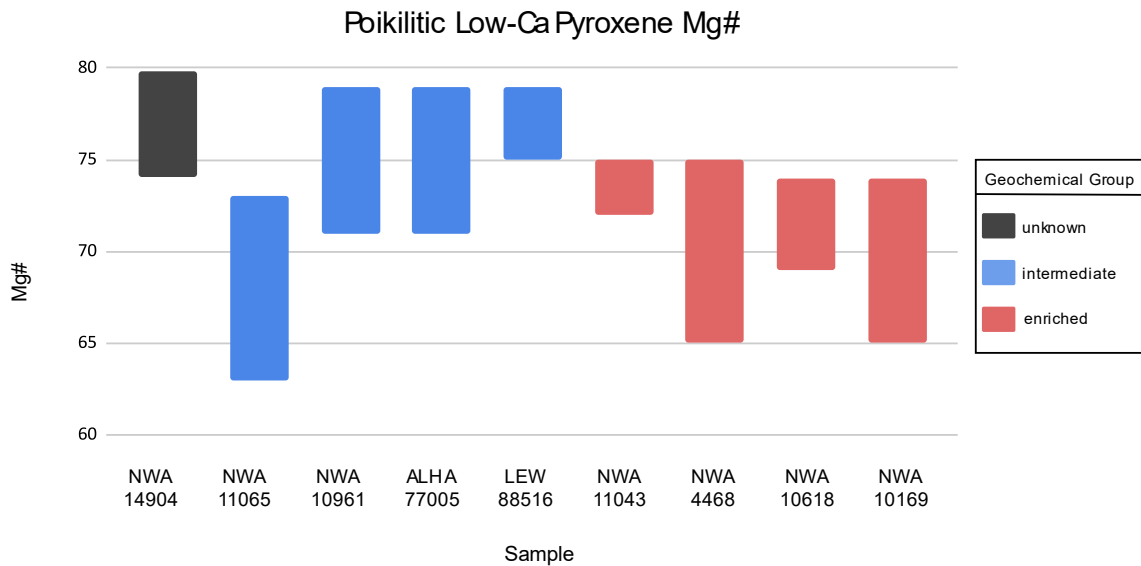


Figure 35. Comparison of the range of Mg# in poikilitic low-Ca pyroxene within NWA 14904 and the comparative suite of poikilitic shergottites.

5.2.4.3. Crustal Regime

The Ti/Al ratios in NWA 14904 pyroxenes were examined using poikilitic and non-poikilitic pyroxene grains. The Ti/Al ratio plots within the ~lower crust regime, with a few analyses suggesting higher emplacement close or at the surface, which is consistent with both enriched and intermediate poikilitic shergottites (**Figure 36**). While there is an overall statistical trend for enriched samples to plot at consistently lower emplacement depths than intermediate ones, there are multiple examples of both geochemical groups that do not fit this generalization. Therefore, these data can be used to understand the emplacement history of NWA 14904, but not its geochemical grouping.

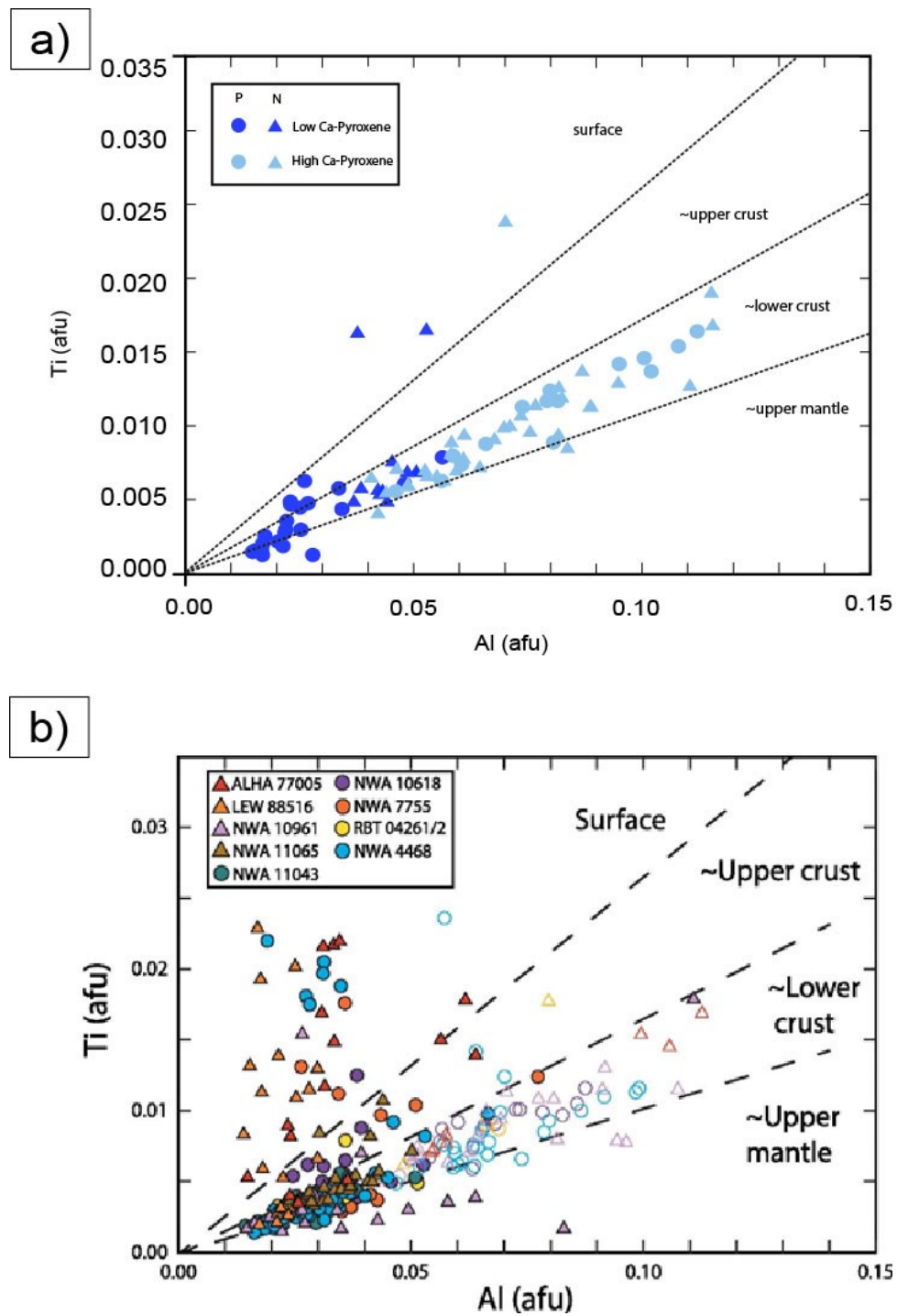


Figure 36. Ti vs Al of pyroxenes within a) NWA 14904 and ;b) from Rahib et al., (2019) “enriched (circle) and intermediate (triangle) poikilitic pyroxenes, including low-Ca (solid symbols) and high-Ca (open symbols). Isobars are calibrated experimentally from Nekvasil et al. (2004) and Filiberto et al. (2010). Most poikilitic pyroxenes have crystallized at the martian lower crust. Exact pressures were not included here as Nekvasil et al. (2004) barometry was calibrated for terrestrial conditions.”

5.2.4.4. Maskelynite

Maskelynite compositions in NWA 14904 range from $\text{An}_{48-55}\text{Ab}_{44-49}\text{Or}_{0.07-3}$ with an average of $\text{An}_{52}\text{Ab}_{47}\text{Or}_2$. These values overlap members of both the intermediate (NWA 11065 and NWA 10961) and enriched (NWA 11043 and NWA 4468) poikilitic shergottite suite (**Figure 37**). These compositions are, therefore, not a useful indicator of the geochemical grouping.

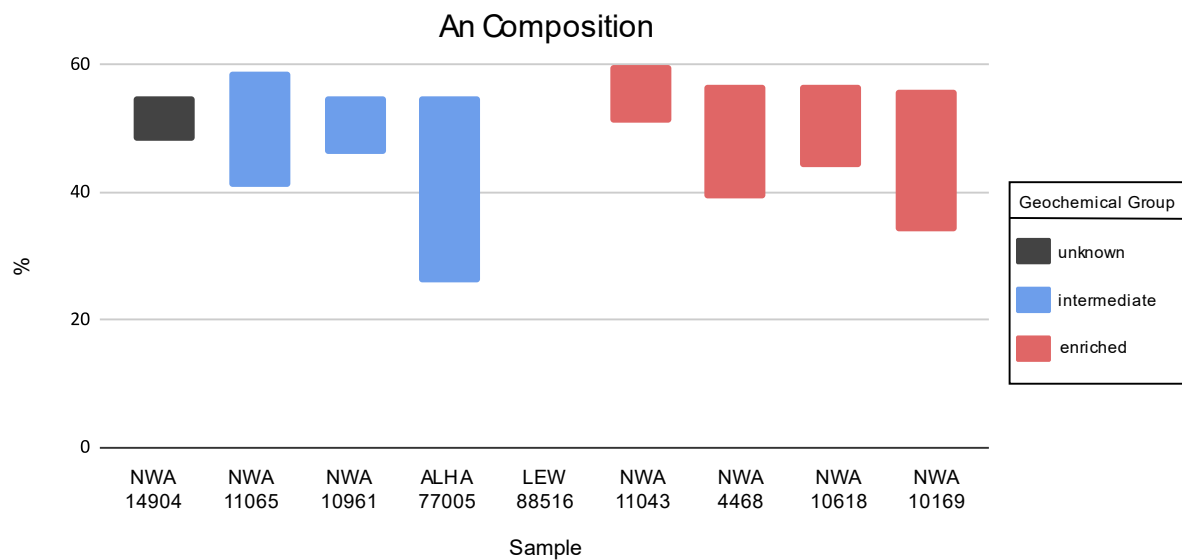


Figure 37. Comparison of An-value in maskelynite within NWA 14904 and the comparative suite of poikilitic shergottites.

5.2.4.5. Oxides

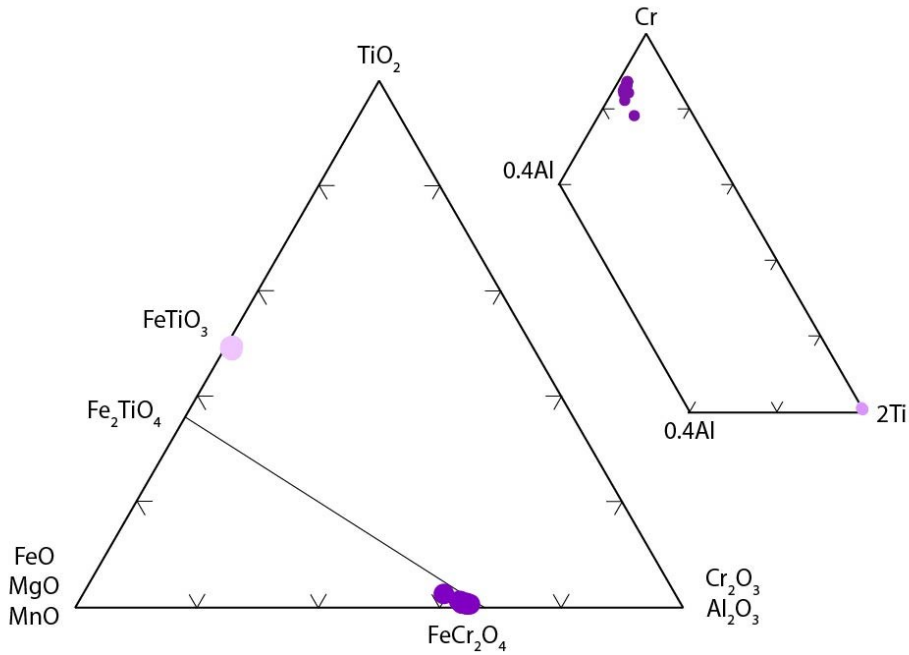


Figure 38. NWA 14904 Oxide Compositions: chromite (dark purple) and ilmenite (light purple).

In both enriched and intermediate poikilitic shergottites, spinel chadacrysts tend to be more Cr-rich in the poikilitic textural regions, whereas those within the non-poikilitic texture are more Ti-rich (Rahib et al., 2019). However, the spinel within the non-poikilitic regions of enriched poikilitic shergottites has a higher Ti composition than that within intermediate samples, with an average TiO_2 content of 9.5 wt% (enriched) compared to 6.4% (intermediate) (Rahib et al., 2019). NWA 14904 contains chromite, with an average TiO_2 content of 1.34 wt% (**Figure 38**). This value for non-poikilitic chromite is consistent with that of the intermediate geochemical group. Only one poikilitic chromite was measured and, therefore, does not provide an ample sample size for comparison. Ilmenite compositions were

not reported for the comparative suite and so cannot be discussed further here, though it has been identified as a phase in other poikilitic shergottites (Combs et al., 2019).

Based on all the factors examined above, NWA 14904 most closely fits in the intermediate geochemical group.

5.3. Petrogenesis of NWA 14904

It is theorized that early in its history, Mars had a global magma ocean which underwent differentiation as it cooled to produce the shergottite source region (Halliday et al., 2001). Shergottites are divided into three different geochemical groups: enriched, intermediate, and depleted, as noted previously. These geochemical groups are defined by their incompatible trace elements (ITE), abundance of rare earth elements (REE), and $^{147}\text{Sm}/^{144}\text{Nd}$ and $^{176}\text{Lu}/^{177}\text{Hf}$ isotopic ratios (Borg and Draper, 2003). Their differences are hypothesized to be a result of formation in different magma reservoirs or crustal contamination (Borg and Draper, 2003), where each geochemical group is sourced from a distinct magma reservoir or source. In this model, enriched shergottites originate from a geochemically enriched magma reservoir and depleted shergottites from a geochemically depleted source; however, the source of NWA 14904, which is an intermediate shergottite, is more complex. The intermediate shergottites are believed to derive from either (1) mixing of an enriched and depleted source, or (2) a separate mantle source formed during the crystallization of the magma ocean (Borg et al., 2002; Bridges and Warren, 2006; Howarth et al., 2014; Rahib et al., 2019 and references therein).

5.3.1. Two-Stage Crystallization

NWA 14904, like other poikilitic shergottites, has a bimodal texture, which is believed to form as a result of two separate crystallization events, with the poikilitic texture forming first, followed by the non-poikilitic. As discussed above, Mg# is higher in poikilitic silicates. This occurs because MgO is highly compatible in the early crystallizing phases, like olivine and pyroxene, and, as a result, it decreases with higher degrees of crystal fractionation and there is a corresponding increase in FeO. Non-poikilitic areas are formed during later stage crystallization as a more evolved parent melt is transported to the Martian surface. These areas are characterized by lower Mg#, as well as higher TiO₂ values. Similar to Mg#, higher TiO₂ values are the result of the parental magma for non-poikilitic areas being more evolved. This trend is illustrated well in NWA 14904 (**Figure 27d**).

5.3.2. Crystallization Sequence

Crystallization sequence also plays an important role in the formation of minerals for the poikilitic vs non-poikilitic zones in NWA 14904. In intermediate poikilitic shergottites, olivine is the primary liquidus phase, whereas for evolved poikilitic shergottites it is spinel (Rahib et al., 2019). The primary liquidus phase in NWA 14904 is olivine, and as a result the olivine within NWA 14904 crystallized first, followed by spinel. This results in a poikilitic texture that contains no spinel inclusions within olivine, only as individual grains detached or adjacent to it. This is due to the low $f\text{O}_2$ of poikilitic zones in intermediate shergottites where the magmatic environment is too reduced, so spinel growth is inhibited. This allows for olivine to form first, followed by spinel and, as a result, spinel grows sequentially with olivine rather than as inclusions within it (Castle and Herd, 2018; Rahib et

al., 2019). As the magma begins to ascend, the formation of the non-poikilitic texture is initiated. As the melt continues to crystallize it becomes highly fractionated and accessory phases such as merrillite, sulfides, and ilmenite are able to crystalize more readily in non-poikilitic zones (Combs et al., 2019). Additionally, maskelynite in NWA 14904 is only present in non-poikilitic areas, which fits with observations of other poikilitic shergottites and is suggestive of plagioclase forming after oikocryst formation, most likely from an interstitial melt (Combs et al., 2019).

5.3.3. *Crystallization Depth*

The two-stage crystallization of poikilitic vs non-poikilitic pyroxene in NWA 14904 can be used to infer crystallization depth through the Ti-Al pyroxene geobarometer. While this geobarometer is calibrated for terrestrial planets and cannot determine an exact depth for shergottites (Filiberto et al., 2010), relative depth can be inferred. Ti/Al ratios in pyroxenes decrease with increasing pressure (Combs et al., 2019). The low Ti-Al ratios seen in NWA 14904, and other intermediate poikilitic shergottites, indicate that the poikilitic pyroxenes likely formed within the lower crust, whereas the non-poikilitic pyroxenes formed at shallower depths, likely near the Martian surface (**Figure 36**). However, Ti/Al ratios of non-poikilitic pyroxenes cannot be used as a crystallization pressure estimate because maskelynite formation occurred in the non-poikilitic texture as well, skewing the Ti/Al ratio (Comb et al., 2019). This trend suggests magma ponding occurred at the base of the Martian crust as the majority of the poikilitic textures have Ti/Al ratios that plot at this depth.

5.3.4. Shock History

NWA 14904 contains many features that can be attributed to shock: shock melt, shock-darkened olivine, abnormal birefringence of olivine, lack of fracture in olivine, vaporization of olivine, and maskelynite. The shock features of Martian meteorites are most likely related to their spallation from the surface of Mars. In order for a rock fragment to escape the Martian atmosphere, it must have an escape velocity of 5 kms^{-1} or greater (Artemieva and Ivanov, 2004; Orr et al., 2022). Evidence of large-scale impacts that are capable of accelerating ejecta to this velocity is recorded in meteorites as shock deformation features. It is suggested that impact craters of 3 km are the minimum size needed to result in ejecta traveling at or above Martian escape velocity (Herd et al., 2002).

NWA 14904, like most shergottites, contains maskelynite, which is formed when plagioclase undergoes shock metamorphism and is converted to a diaplectic glass in a process called maskelynitization. Maskelynitization of plagioclase occurs under pressures of 24-34 GPa (depending on the compositional range from anorthite to albite) to ~ 45 GPa (Stöffler et al., 2018). In addition to maskelynite, NWA 14904 contains shock melt, brown olivine, and textures indicative of olivine recrystallization. As stated above in section 4.7 this puts NWA 14904 in the S6 shock classification group, which is defined by shock pressures over 60 GPa and post-shock temperatures of 1500-1700 °C (Fritz et al., 2017)(**Table 8**). This also correlates with the Stöffler et al. (2018) M-S6 shock classification (**Table 9**) which is described as experiencing shock pressures of 55-60 GPa with post-shock temperatures greater than ~ 1000 °C. The combination of these two schemes provides an estimate of shock

pressures greater than 55 GPa and a post-shock temperature around \sim 1500 °C for NWA 14904. Additionally, NWA 14904 contains a notable amount of vesicles. These vesicles are highly concentrated in the melt and maskelynite in NWA 14904, and are common in other highly shocked samples as well.

Table 8. Fritz et al. (2017) Shock Classification Scheme

Shock stage	<i>P</i> (GPa)	<i>T</i> (°C) (postshock)	Destructive shock effects in rock-forming minerals		Mineralogy of localized polymineralic melt zones including constructive shock effects
			Olivine	Plagioclase	
S1 Unshocked	<4–5	10–20	Sharp optical extinction with $<2^\circ$ angular variation	Sharp optical extinction (for chemically unzoned plagioclase)	
S2 Very weakly shocked	5–10	20–50	Undulatory extinction with $>2^\circ$ angular variation	Undulatory extinction	
S3 Weakly shocked	15–20	100–150	Undulatory extinction, Planar fractures (PF)	Undulatory extinction	Glass, low pressure (LP), and possibly high-pressure (HP) minerals such as Wadsleyite (Wds), ringwoodite (Rwd), majorite (Maj)
S4 Moderately shocked	25–35	200–300	Weak mosaicism and PF	Low grade: undulatory extinction; High grade: partially isotropic, PDF	Glass, LP, and possibly HP minerals such as Wds, Rwd, Maj, bridgemanite (Bdm), ferropericlase (Fpc)
S5 Strongly shocked	45–60	600–900	Strong mosaicism, planar deformation features (PDF) and PF	Maskelynite; Note: minimum pressure for maskelynitization (20–35 GPa) falls with rising Ca-content	Glass, LP, and possibly HP minerals such as Wds, Rwd, Maj, Fpc; back reaction of bdm
S6 Very strongly shocked		1500–1700	Strong mosaicism, PDF, recrystallization, brown staining	Shock melted glass with flow structures, vesicles and fusing of adjacent minerals; recrystallization	Glass, devitrified glass, LP minerals; bleaching of brown stained olivine, recrystallization
Shock melted	Whole rock melting and formation of melt rock				

Table 9. Stöffler et al. (2018) Shock Classification Scheme

Shock stage Present proposal	Shock stage IUGS 2007	Equilibration shock pressure (GPa)	Post-shock temperature (°C)	Diagnostic shock effects in plagioclase, pyroxene, olivine, amphibole, and mica	Accompanying disequilibrium shock effects
M—S1	0			Sharp optical extinction of all minerals Irregular fracturing	None
M—S2	1	~1–5	~0	Fractured silicates; mechanical twinning of pyroxene; kink bands in mica	None
M—S3	2a	~20–22	~50–150	Plagioclase with pdf and partially converted to diaplectic glass; mosaicism in plagioclase and mafic minerals; pf in olivine	Incipient formation of localized “mixed melt” and glassy melt veins
M—S4	2b	~28–34	~200–250	Diaplectic plagioclase glass; mechanical twinning in pyroxene; mosaicism in mafic minerals; pf in olivine	Localized “mixed melt” and melt veins (glassy or microcrystalline)
M—S5	3	~42–45	~900 (?)	Melted plagioclase glass with incipient flow structure and vesicles; mosaicism in mafic minerals; pdf in pyroxene and amphibole; loss of pleochroism in mafic minerals	Melt veins and melt pockets
M—S6	4	~55–60	~1100 (?)	Melted plagioclase glass with vesicles and flow structure; incipient and increasing contact melting of pyroxene and olivine and (re) crystallization of olivine	Pervasive melt veins and melt pockets
M—S7	5	>~60–65	~1500 (?)	Whole rock melt	

5.4. Future work

5.4.1. Age Dating

Currently, radiometric ages between 180-570 Ma have been measured for shergottites (Nyquist et al., 2001; Bridges and Warren, 2006; Kiefer and Qingsong, 2016). These ages are considerably younger than those of chassignites and nakhlites at ~1.3 Ga. Because the shergottites are so young compared to other Martian meteorites, they can be a powerful tool for constraining recent Martian processes. Obtaining age data for NWA 14904 would further constrain its formation history. The analysis of isotopic decay schemes can also be used to constrain active volcanism ages (Kiefer and Qingsong, 2016), trace assimilation and magma mixing, correlate strata with isotope chemostratigraphy, provide lithification and ejection ages, and date major thermal disturbances (Dauphas et al., 2022).

Furthermore, isotopic ages can be used to constrain information about the Martian mantle and the mantle potential temperature (T_p). The mantle potential temperature represents the temperature of the mantle, regardless of depth, if the mantle was adiabatically decompressed to the surface (Filiberto, 2017). The mantle potential temperature is calculated using a regression equation dependent on age. While this equation has yet to be precisely constrained for shergottite sources, it has potential for further study.

5.4.2. Bulk Composition

While the bulk composition was calculated using modal mineralogy for the scope of this thesis, the bulk composition will additionally be measured using MC-ICP-MS to produce

a more accurate composition. This should allow us to more accurately constrain the petrogenetic history, but could not be completed within the scope of this study.

5.4.3. Oxygen fugacity

Oxygen fugacity, $f\text{O}_2$, is the measurement of how oxidizing or reducing a magmatic environment was during rock formation (Doyle et al., 2019). Oxygen fugacity provides insight into the magmatic environment, relative position in the mantle, and crystallization sequence. Oxygen fugacity data indicate that the shergottite group source mantle formed under redox conditions (Rahib et al., 2019 and references therein). The source for depleted shergottites displays evidence of a reduced magmatic environment, whereas the source for enriched shergottites displays an oxidized magmatic environment. However, when referring specifically to poikilitic shergottites, only enriched and intermediate poikilitic shergottites have been classified to date. Oxygen fugacity data for intermediate poikilitic shergottites show they originated from a more reduced magmatic source, which is indicative of a reservoir that resides in the mantle (Rahib et al., 2019 and references therein). Oxygen fugacity data further support the concept that the poikilitic texture is formed prior to the non-poikilitic texture, as $f\text{O}_2$ is higher in poikilitic areas than in non-poikilitic. This is attributed to different factors during magma ascent and crystallization. Fe^{3+} becomes more enriched in the melt and, therefore, during crystallization Fe^{3+} is more highly concentrated in late-stage phases resulting in higher $f\text{O}_2$ values for late-stage melts in a process known as auto-oxidation. The disparity between $f\text{O}_2$ levels for early and late-stage crystallization (poikilitic and non-poikilitic textures) supports the suggestion that shergottite magma sources of all geochemical groups have undergone large degrees of crystallization (Rahib et al., 2019 and

references therein). Oxygen fugacity was not measured in NWA 14904, as this was beyond the scope of this thesis, and this is another area where future work is required.

5.4.4. Crystal Size Distribution

Intermediate poikilitic shergottites originated from different magmatic systems or an isolated magmatic system but it is also theorized that the intermediate poikilitic shergottites come from at least two separate locations on Mars. The theory for multiple locations is based on the presence of two different ejection ages. Additionally, while Ti/Al ratios suggest a formation model involving ponding at the base of the Martian crust, cooling rates of different intermediate poikilitic samples suggest an additional spatial variation of emplacement in various sills (Mikouchi, 2010). Crystal size distribution (CSD) results are used to help determine relative magma residence time (Rahib et al., 2019). Longer magma residence time is represented by larger grain size and is suggestive of deeper emplacement. Using this information, the literature suggests that intermediate poikilitic shergottites did not all crystallize in the same shallow sill (Borg et al., 2002). While obtaining CSD would potentially allow NWA 14904 to be grouped with meteorites with similar magma residence times and further constrain its original location, it is likely that this is not possible for this sample due to its high degree of shock. Highly shocked samples do not preserve their original crystallization grain sizes and, therefore, CSD analysis does not yield an accurate result.

5.4.5. Sm-Nd Crystallization Ages and Cosmic Ray Exposure

While it is not possible to precisely determine which shallow sill or other igneous body a meteorite came from, it is possible to determine if the origin is from the same

magmatic complex due to similarities in Sm-Nd crystallization ages and cosmic ray exposure (CRE) ages (Nyquist et al., 2001). Additionally, poikilitic olivine compositions can also be used to determine if samples originated from the same magmatic complex. Utilizing these methods applied to other samples, Rahib et al. (2019) proposed the existence of at least three different magmatic bodies for the intermediate poikilitic shergottites. Sm-Nd, and CRE ages, and compositions of poikilitic olivine were not analyzed in NWA 14904, and therefore it cannot be placed with context to a distinct magma body, but such work should be done in the future.

5.4.6. Other thin sections

While nine thin sections were produced, the scope of this study only focused on section 01 due to the time available. While section 01 was the most complex of the sections in texture and mineralogy, it is far from representative of the whole rock sample. The shock features, textures, and modal mineralogy vary between all nine sections, suggesting these differences continue throughout the whole rock sample. NWA 14904 section 01 contains only a small portion of the poikilitic texture; CT scans of the whole rock sample show large areas of poikilitic texture (**Figure 10**). Due to the fact that only a small portion of the poikilitic texture is seen in section 01, only small-scale poikilitic pyroxene or incomplete grains of the large-scale poikilitic grains are seen (**Figure 18**). Further study of thin sections would hopefully yield a more comprehensive analysis of poikilitic textures through the capture of complete poikilitic grains, both large- and small-scale. It is imperative to study the other sections to obtain a better understanding of the differences in texture and modal mineralogy represented in the remaining sections.

6. CONCLUSION

6.1. Classification

NWA 14904 is classified as a poikilitic shergottite that most likely belongs to the intermediate geochemical group. Additionally, NWA 14904 has a shock classification of S6- very strongly shocked.

6.2. Formation model for NWA 14904

Using the above information discussed in section 5.3 and in combination with all the data collected during my study, I conclude that NWA 14904 has the following petrogenetic history:

1. The parental magma for NWA 14904 is most likely intermediate in composition and formed either from the mixing of enriched and depleted source reservoirs or from a distinct intermediate reservoir.
2. Fractional crystallization of the parent magma resulted in olivine chadacrysts and poikilitic pyroxenes crystallizing first, to produce the poikilitic textures observed
3. Pyroxene oikocrysts were transported to the surface, or close to it, during magma ascent.
4. Non-poikilitic minerals crystallized from a more evolved melt during magma ascent
5. The remaining highly fractioned melt crystallizes accessory minerals to form sulfides, merrillite, and ilmenite.

6. NWA 14904 was emplaced in the crust.
7. NWA 14904 underwent a large shock event, likely resulting in its ejection from the Martian surface.

These conclusions can be further strengthened with the additional analysis described in section 5.4.

7. APPENDIX

7.1. EMP

7.1.1. *Probe Recipes*

Table 10. Olivine EMP recipe

1	2	3	4	5
TAP	PETJ	TAP	PETJ	LIFH
Al	P	Na	K	Ni
Si	Cl	Mg	Ca	Fe
	Ce		Ti	Cr
				Mn

Table 11. Pyroxene EMP recipe

1	2	3	4	5
TAP	TAP		LiFH	PETH
Si	Na		Fe	K
Mg	Al		Mn	Ca
			Cr	Ti

Table 12. Maskelynite EMP recipe

1	2	3	4	5
TAP	TAP			PETH
Si	Na			K
	Al			Ca

Table 13. Carbonates EMP recipe

1	2	3	4	5
TAP	TAP	TAP	LIF	PETH
Mg	Al	Si	Fe	Ca

Table 14. Phosphates EMP recipe

1	2	3	4	5
TAP				
Al	P	Mg	Ca	Fe
Si	Ce	Na	Ti	Cr
	Cl		K	Mn

Table 15. Oxides EMP recipe

1	2	3	4	5
TAP	PETJ	TAP	PETJ	LIFH
Al	P	Mg	Ca	Fe
Si			Ti	Cr
			Pb	Mn
				Zn

Table 16. Sulfides EMP recipe

1	2	3	4	5
TAP	PETJ	TAP	PETJ	LIFH
Al	P	Mg	Ca	Fe
Si			Ti	Cr
			Pb	Mn
				Zn

7.1.2. Probe Site Locations

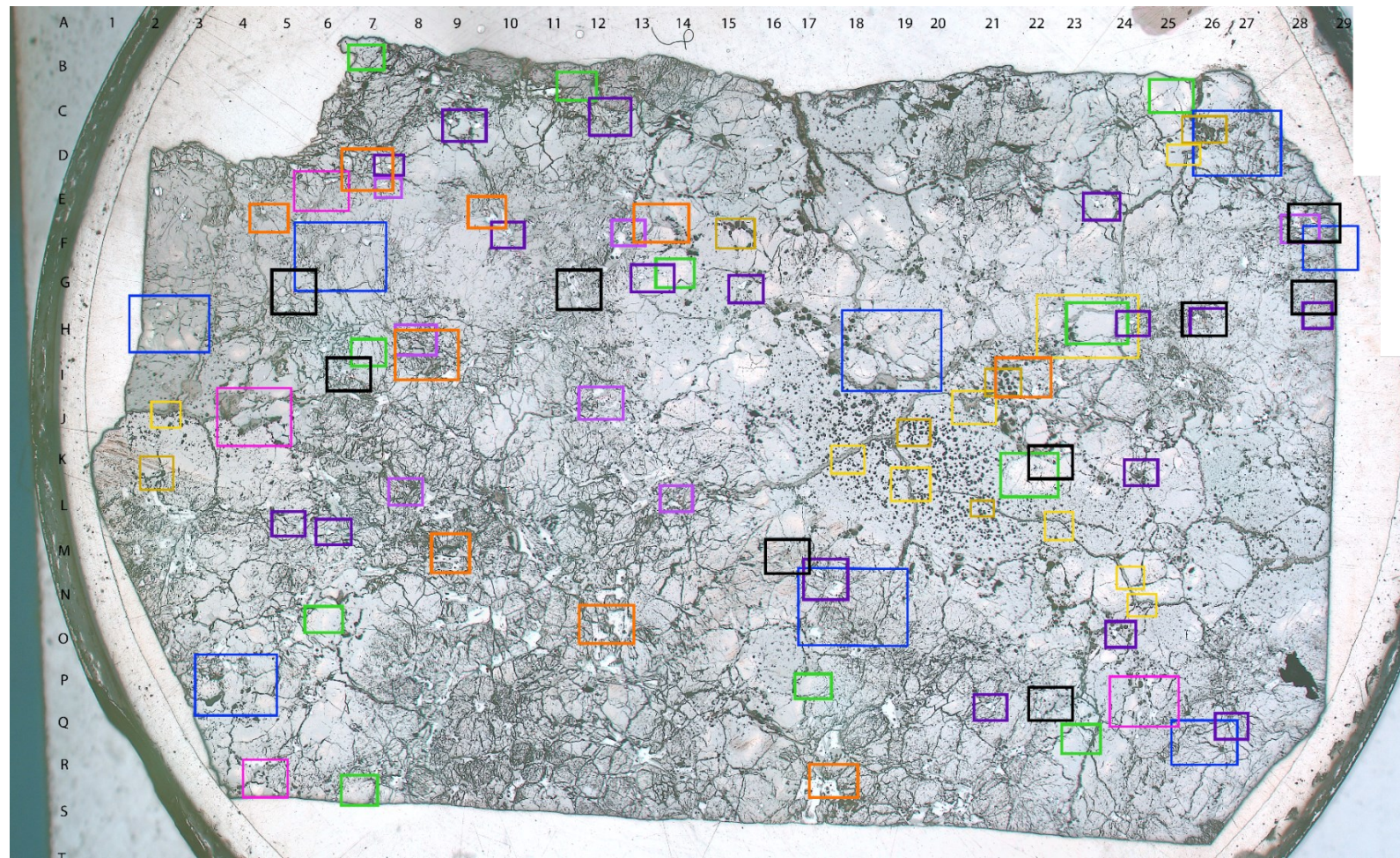


Figure 39. EMP Probe Site Locations

7.1.3. Probe Data

Table 17. NWA 14904 Olivine Compositions

Slide Point	c25 2	B11 3	c25 3	K22 3	G14 2	B11 1	c25 6	c25 7
SiO ₂	37.90	37.45	37.94	38.10	37.63	37.54	37.62	37.66
TiO ₂	0.00	0.03	0.00	0.00	0.03	0.00	0.00	0.00
Al ₂ O ₃	0.05	0.03	0.00	0.00	0.00	0.00	0.00	0.00
Cr ₂ O ₃	0.05	0.02	0.02	0.04	0.04	0.02	0.06	0.04
FeO	28.36	28.95	28.44	27.41	28.10	29.29	28.51	28.72
MnO	0.56	0.54	0.53	0.53	0.53	0.57	0.47	0.52
MgO	32.73	32.42	32.63	33.37	33.10	31.92	32.72	32.32
CaO	0.26	0.30	0.29	0.20	0.26	0.26	0.17	0.25
P ₂ O ₅	0.03	0.07	0.03	0.00	0.00	0.03	0.00	0.00
NiO	0.07	0.03	0.00	0.02	0.05	0.05	0.08	0.09
Ce ₂ O ₃	0.00	0.10	0.02	0.04	0.00	0.00	0.02	0.00
Na ₂ O	0.02	0.02	0.01	0.03	0.00	0.03	0.00	0.00
K ₂ O	0.01	0.00	0.00	0.00	0.00	0.00	0.01	0.01
Cl	0.01	0.00	0.00	0.03	0.01	0.00	0.00	0.01
Total	100.04	99.96	99.90	99.78	99.76	99.70	99.66	99.61
Si	1.00	1.01	1.01	1.01	1.01	1.01	1.01	1.01
Ti	0.00	0.00	0.00	0.00	0.00	0.00	0.00	0.00
Al	0.00	0.00	0.00	0.00	0.00	0.00	0.00	0.00
Cr	0.00	0.00	0.00	0.00	0.00	0.00	0.00	0.00
Fe	0.69	0.65	0.64	0.66	0.66	0.64	0.63	0.64
Mn	0.01	0.01	0.01	0.01	0.01	0.01	0.01	0.01
Mg	1.29	1.31	1.32	1.30	1.30	1.32	1.33	1.31
Ca	0.01	0.01	0.01	0.01	0.01	0.01	0.01	0.01
P	0.00	0.00	0.00	0.00	0.00	0.00	0.00	0.00
Ni	0.00	0.00	0.00	0.00	0.00	0.00	0.00	0.00
Ce	0.00	0.00	0.00	0.00	0.00	0.00	0.00	0.00
Na	0.00	0.00	0.00	0.00	0.00	0.00	0.00	0.00
K	0.00	0.00	0.00	0.00	0.00	0.00	0.00	0.00
Cl	0.00	0.00	0.00	0.00	0.00	0.00	0.00	0.00
Total	3.00	2.99	2.99	2.99	2.99	2.99	2.99	2.99
Fo	65.15	66.70	67.40	66.34	66.35	67.27	67.74	67.09

Slide Point	H23 3	G14 8	H23 5	C25 7	c25 1	G14 4	H23 7	c25 4
SiO ₂	37.72	37.54	37.61	37.24	37.77	37.55	37.39	37.77
TiO ₂	0.00	0.05	0.01	0.00	0.01	0.00	0.00	0.02
Al ₂ O ₃	0.03	0.02	0.01	0.00	0.02	0.00	0.02	0.03
Cr ₂ O ₃	0.01	0.02	0.05	0.04	0.04	0.08	0.05	0.04
FeO	28.75	28.48	28.46	28.88	28.15	27.88	28.38	28.36
MnO	0.45	0.52	0.57	0.52	0.52	0.50	0.52	0.55
MgO	32.30	32.63	32.31	32.45	32.43	32.88	32.72	32.19
CaO	0.23	0.26	0.26	0.26	0.29	0.30	0.23	0.28
P ₂ O ₅	0.00	0.01	0.03	0.00	0.02	0.07	0.00	0.00
NiO	0.08	0.01	0.07	0.05	0.07	0.08	0.04	0.03
Ce ₂ O ₃	0.00	0.00	0.00	0.00	0.10	0.00	0.00	0.00
Na ₂ O	0.00	0.00	0.04	0.01	0.00	0.03	0.00	0.04
K ₂ O	0.00	0.00	0.02	0.00	0.00	0.00	0.00	0.02
Cl	0.00	0.00	0.01	0.00	0.01	0.00	0.00	0.00
Total	99.57	99.52	99.46	99.44	99.41	99.36	99.34	99.33
Si	1.01	1.01	1.01	1.01	1.01	1.01	1.01	1.01
Ti	0.00	0.00	0.00	0.00	0.00	0.00	0.00	0.00
Al	0.00	0.00	0.00	0.00	0.00	0.00	0.00	0.00
Cr	0.00	0.00	0.00	0.00	0.00	0.00	0.00	0.00
Fe	0.64	0.63	0.64	0.64	0.65	0.65	0.63	0.63
Mn	0.01	0.01	0.01	0.01	0.01	0.01	0.01	0.01
Mg	1.32	1.32	1.32	1.31	1.30	1.30	1.32	1.32
Ca	0.00	0.01	0.00	0.01	0.01	0.01	0.01	0.01
P	0.00	0.00	0.00	0.00	0.00	0.00	0.00	0.00
Ni	0.00	0.00	0.00	0.00	0.00	0.00	0.00	0.00
Ce	0.00	0.00	0.00	0.00	0.00	0.00	0.00	0.00
Na	0.00	0.00	0.00	0.00	0.00	0.00	0.00	0.00
K	0.00	0.00	0.00	0.00	0.00	0.00	0.00	0.00
Cl	0.00	0.00	0.00	0.00	0.00	0.00	0.00	0.00
Total	2.99	2.99	2.99	2.99	2.99	2.99	2.99	2.99
Fo	67.17	67.85	67.46	67.23	66.62	66.91	67.49	67.60

Slide Point	H23 1	B11 5	H23 2	C25 6	C25 4	K22 11	P17 4	C25 1
SiO ₂	37.67	37.48	37.58	37.62	37.34	37.79	36.62	37.40
TiO ₂	0.06	0.03	0.00	0.00	0.01	0.00	0.00	0.06
Al ₂ O ₃	0.02	0.03	0.00	0.01	0.01	0.03	0.02	0.02
Cr ₂ O ₃	0.08	0.05	0.00	0.03	0.06	0.11	0.01	0.04
FeO	28.21	28.63	28.46	28.28	28.17	26.78	30.08	28.35
MnO	0.53	0.51	0.54	0.54	0.54	0.48	0.45	0.51
MgO	32.44	32.08	32.40	32.27	32.67	33.62	31.56	32.34
CaO	0.24	0.28	0.17	0.33	0.28	0.21	0.24	0.35
P ₂ O ₅	0.01	0.09	0.01	0.03	0.00	0.04	0.03	0.04
NiO	0.06	0.03	0.06	0.05	0.04	0.05	0.17	0.01
Ce ₂ O ₃	0.00	0.02	0.02	0.00	0.00	0.02	0.00	0.00
Na ₂ O	0.00	0.00	0.00	0.02	0.05	0.04	0.00	0.01
K ₂ O	0.00	0.03	0.00	0.00	0.02	0.02	0.00	0.00
Cl	0.00	0.01	0.00	0.03	0.02	0.01	0.01	0.00
Total	99.32	99.25	99.24	99.21	99.20	99.19	99.18	99.14
Si	1.01	1.01	1.01	1.01	1.01	1.01	1.02	1.01
Ti	0.00	0.00	0.00	0.00	0.00	0.00	0.00	0.00
Al	0.00	0.00	0.00	0.00	0.00	0.00	0.00	0.00
Cr	0.00	0.00	0.00	0.00	0.00	0.00	0.00	0.00
Fe	0.64	0.63	0.64	0.64	0.63	0.66	0.64	0.60
Mn	0.01	0.01	0.01	0.01	0.01	0.01	0.01	0.01
Mg	1.31	1.31	1.31	1.31	1.32	1.29	1.30	1.34
Ca	0.01	0.01	0.00	0.01	0.01	0.01	0.01	0.01
P	0.00	0.00	0.00	0.00	0.00	0.00	0.00	0.00
Ni	0.00	0.00	0.00	0.00	0.00	0.00	0.00	0.00
Ce	0.00	0.00	0.00	0.00	0.00	0.00	0.00	0.00
Na	0.00	0.00	0.00	0.00	0.00	0.00	0.00	0.00
K	0.00	0.00	0.00	0.00	0.00	0.00	0.00	0.00
Cl	0.00	0.00	0.00	0.00	0.00	0.00	0.00	0.00
Total	2.99	2.99	2.99	2.99	2.99	2.99	2.99	2.98
Fo	67.15	67.48	67.17	67.12	67.76	66.01	66.92	69.12

Slide Point	G14 6	c25 8	H7 5	C25 2	K22 5	C25 8	C25 9	C25 6
SiO ₂	37.41	37.61	37.56	37.50	37.55	37.57	37.45	37.24
TiO ₂	0.02	0.02	0.00	0.00	0.04	0.00	0.00	0.01
Al ₂ O ₃	0.00	0.03	0.01	0.02	0.02	0.01	0.00	0.02
Cr ₂ O ₃	0.07	0.05	0.02	0.04	0.10	0.07	0.02	0.06
FeO	27.97	28.41	28.49	28.30	27.75	28.15	28.98	28.41
MnO	0.52	0.53	0.51	0.51	0.45	0.48	0.49	0.53
MgO	32.74	32.10	32.15	32.42	32.67	32.37	31.77	32.60
CaO	0.28	0.26	0.27	0.17	0.28	0.26	0.19	0.13
P ₂ O ₅	0.00	0.02	0.03	0.01	0.06	0.07	0.02	0.02
NiO	0.04	0.07	0.00	0.05	0.02	0.03	0.07	0.00
Ce ₂ O ₃	0.06	0.00	0.00	0.05	0.03	0.00	0.00	0.00
Na ₂ O	0.00	0.00	0.03	0.00	0.04	0.03	0.03	0.00
K ₂ O	0.01	0.00	0.00	0.00	0.01	0.00	0.00	0.00
Cl	0.00	0.00	0.00	0.00	0.00	0.00	0.01	0.00
Total	99.12	99.10	99.08	99.07	99.03	99.02	99.02	99.02
Si	1.01	1.02	1.01	1.01	1.02	1.01	1.02	1.02
Ti	0.00	0.00	0.00	0.00	0.00	0.00	0.00	0.00
Al	0.00	0.00	0.00	0.00	0.00	0.00	0.00	0.00
Cr	0.00	0.00	0.00	0.00	0.00	0.00	0.00	0.00
Fe	0.64	0.65	0.65	0.67	0.64	0.66	0.63	0.64
Mn	0.01	0.01	0.01	0.01	0.01	0.01	0.01	0.01
Mg	1.30	1.30	1.30	1.28	1.31	1.29	1.31	1.31
Ca	0.01	0.01	0.01	0.01	0.00	0.01	0.01	0.01
P	0.00	0.00	0.00	0.00	0.00	0.00	0.00	0.00
Ni	0.00	0.00	0.00	0.00	0.00	0.00	0.00	0.00
Ce	0.00	0.00	0.00	0.00	0.00	0.00	0.00	0.00
Na	0.00	0.00	0.00	0.00	0.00	0.00	0.01	0.00
K	0.00	0.00	0.00	0.00	0.00	0.00	0.00	0.00
Cl	0.00	0.00	0.00	0.00	0.00	0.00	0.00	0.00
Total	2.98	2.98	2.98	2.98	2.98	2.98	2.98	2.98
Fo	67.03	66.73	66.71	65.46	67.13	66.18	67.47	67.29

Slide Point	H7 1	N6 3	H23 10	P17 7	H23 8	C25 5	K22 2	C25 2
SiO ₂	37.16	37.56	37.36	37.28	37.33	37.24	37.59	37.51
TiO ₂	0.02	0.00	0.02	0.00	0.00	0.00	0.02	0.00
Al ₂ O ₃	0.00	0.01	0.02	0.02	0.04	0.00	0.03	0.02
Cr ₂ O ₃	0.04	0.04	0.03	0.04	0.02	0.06	0.06	0.07
FeO	28.95	28.24	28.67	29.26	28.44	28.34	27.86	28.24
MnO	0.56	0.55	0.46	0.59	0.50	0.47	0.52	0.56
MgO	31.78	32.18	32.04	31.28	32.26	32.41	32.42	32.22
CaO	0.21	0.26	0.28	0.21	0.30	0.29	0.23	0.26
P ₂ O ₅	0.17	0.04	0.05	0.01	0.00	0.04	0.01	0.02
NiO	0.06	0.04	0.04	0.07	0.02	0.04	0.09	0.01
Ce ₂ O ₃	0.04	0.08	0.02	0.15	0.00	0.01	0.00	0.00
Na ₂ O	0.02	0.01	0.00	0.03	0.03	0.01	0.10	0.00
K ₂ O	0.00	0.00	0.01	0.03	0.01	0.02	0.00	0.01
Cl	0.02	0.00	0.00	0.02	0.02	0.02	0.00	0.03
Total	99.01	99.00	98.99	98.97	98.96	98.94	98.93	98.93
Si	1.02	1.01	1.02	1.02	1.02	1.01	1.02	1.02
Ti	0.00	0.00	0.00	0.00	0.00	0.00	0.00	0.00
Al	0.00	0.00	0.00	0.00	0.00	0.00	0.00	0.00
Cr	0.00	0.00	0.00	0.00	0.00	0.00	0.00	0.00
Fe	0.64	0.65	0.63	0.67	0.65	0.66	0.61	0.64
Mn	0.01	0.01	0.01	0.01	0.01	0.01	0.01	0.01
Mg	1.31	1.30	1.31	1.27	1.30	1.28	1.33	1.30
Ca	0.00	0.01	0.01	0.01	0.01	0.01	0.01	0.01
P	0.00	0.00	0.00	0.00	0.00	0.00	0.00	0.00
Ni	0.00	0.00	0.00	0.00	0.00	0.00	0.00	0.00
Ce	0.00	0.00	0.00	0.00	0.00	0.00	0.00	0.00
Na	0.00	0.00	0.00	0.00	0.00	0.00	0.00	0.00
K	0.00	0.00	0.00	0.00	0.00	0.00	0.00	0.00
Cl	0.00	0.00	0.00	0.00	0.00	0.00	0.00	0.00
Total	2.98	2.98	2.98	2.98	2.98	2.98	2.98	2.98
Fo	66.98	66.57	67.49	65.58	66.57	66.10	68.45	67.04

Slide Point	G14 3	c25 5	H23 9	K22 8	G14 7	G14 9	H23 4	Q23 5
SiO ₂	37.30	37.41	37.39	37.70	37.29	37.22	37.31	37.63
TiO ₂	0.00	0.00	0.00	0.02	0.00	0.05	0.00	0.04
Al ₂ O ₃	0.02	0.02	0.02	0.03	0.02	0.01	0.03	0.01
Cr ₂ O ₃	0.04	0.01	0.00	0.05	0.03	0.12	0.07	0.08
FeO	27.72	28.49	28.66	27.66	28.27	28.02	28.53	27.74
MnO	0.57	0.43	0.49	0.48	0.53	0.55	0.52	0.52
MgO	32.82	32.14	32.02	32.62	32.43	32.59	32.08	32.43
CaO	0.29	0.28	0.19	0.30	0.26	0.17	0.26	0.25
P ₂ O ₅	0.07	0.03	0.06	0.01	0.01	0.03	0.02	0.03
NiO	0.06	0.07	0.07	0.01	0.03	0.05	0.00	0.00
Ce ₂ O ₃	0.00	0.02	0.00	0.00	0.00	0.00	0.01	0.00
Na ₂ O	0.03	0.00	0.01	0.01	0.00	0.05	0.00	0.05
K ₂ O	0.01	0.00	0.00	0.01	0.00	0.00	0.01	0.01
Cl	0.00	0.00	0.01	0.00	0.00	0.00	0.00	0.02
Total	98.93	98.92	98.92	98.90	98.88	98.84	98.83	98.80
Si	1.02	1.01	1.02	1.02	1.02	1.02	1.02	1.02
Ti	0.00	0.00	0.00	0.00	0.00	0.00	0.00	0.00
Al	0.00	0.00	0.00	0.00	0.00	0.00	0.00	0.00
Cr	0.00	0.00	0.00	0.00	0.00	0.00	0.00	0.00
Fe	0.65	0.65	0.66	0.64	0.66	0.66	0.65	0.65
Mn	0.01	0.01	0.01	0.01	0.01	0.01	0.01	0.01
Mg	1.30	1.29	1.29	1.30	1.28	1.28	1.30	1.30
Ca	0.01	0.01	0.01	0.01	0.01	0.01	0.01	0.01
P	0.00	0.00	0.00	0.00	0.00	0.00	0.00	0.00
Ni	0.00	0.00	0.00	0.00	0.00	0.00	0.00	0.00
Ce	0.00	0.00	0.00	0.00	0.00	0.00	0.00	0.00
Na	0.00	0.00	0.00	0.00	0.00	0.00	0.00	0.00
K	0.00	0.00	0.00	0.00	0.00	0.00	0.00	0.00
Cl	0.00	0.00	0.00	0.00	0.00	0.00	0.00	0.00
Total	2.98	2.98	2.98	2.98	2.98	2.98	2.98	2.98
Fo	66.79	66.46	66.14	67.03	65.95	66.15	66.79	66.69

Slide Point	R7 3	C25 3	P17 10	C25 10	P17 1	G14 5	C25 9	G14 10
SiO ₂	37.31	37.28	37.12	37.41	37.21	37.27	36.97	37.45
TiO ₂	0.00	0.01	0.02	0.01	0.00	0.00	0.00	0.00
Al ₂ O ₃	0.02	0.00	0.02	0.01	0.00	0.00	0.00	0.00
Cr ₂ O ₃	0.03	0.00	0.01	0.03	0.16	0.04	0.05	0.03
FeO	28.98	28.16	29.48	28.75	28.63	27.96	28.80	27.82
MnO	0.52	0.54	0.48	0.50	0.56	0.49	0.51	0.50
MgO	31.48	32.41	31.35	31.69	31.83	32.57	31.86	32.39
CaO	0.25	0.29	0.19	0.25	0.25	0.30	0.26	0.27
P ₂ O ₅	0.02	0.00	0.04	0.03	0.05	0.01	0.02	0.04
NiO	0.09	0.06	0.06	0.03	0.03	0.02	0.09	0.06
Ce ₂ O ₃	0.05	0.00	0.00	0.03	0.00	0.00	0.06	0.00
Na ₂ O	0.04	0.03	0.01	0.01	0.01	0.02	0.02	0.04
K ₂ O	0.02	0.02	0.00	0.02	0.00	0.00	0.01	0.02
Cl	0.00	0.00	0.00	0.00	0.00	0.00	0.02	0.00
Total	98.80	98.78	98.77	98.74	98.72	98.69	98.66	98.63
Si	1.01	1.01	1.02	1.02	1.02	1.02	1.02	1.02
Ti	0.00	0.00	0.00	0.00	0.00	0.00	0.00	0.00
Al	0.00	0.00	0.00	0.00	0.00	0.00	0.00	0.00
Cr	0.00	0.00	0.00	0.00	0.00	0.00	0.00	0.00
Fe	0.63	0.65	0.67	0.64	0.64	0.63	0.64	0.63
Mn	0.01	0.01	0.01	0.01	0.01	0.01	0.01	0.01
Mg	1.32	1.29	1.27	1.30	1.30	1.31	1.30	1.31
Ca	0.01	0.01	0.01	0.01	0.01	0.01	0.01	0.01
P	0.00	0.00	0.00	0.00	0.00	0.00	0.00	0.00
Ni	0.00	0.00	0.00	0.00	0.00	0.00	0.00	0.00
Ce	0.00	0.00	0.00	0.00	0.00	0.00	0.00	0.00
Na	0.00	0.00	0.00	0.00	0.00	0.00	0.00	0.00
K	0.00	0.00	0.00	0.00	0.00	0.00	0.00	0.00
Cl	0.00	0.00	0.00	0.00	0.00	0.00	0.00	0.00
Total	2.98	2.98	2.98	2.98	2.98	2.98	2.98	2.98
Fo	67.73	66.64	65.36	67.20	67.16	67.44	67.21	67.57

Slide Point	Q23 1	H23 6	H7 6	UNKWN 8	B11 2	P17 6
SiO ₂	37.45	37.29	37.16	37.23	36.93	37.18
TiO ₂	0.01	0.02	0.02	0.01	0.00	0.02
Al ₂ O ₃	0.02	0.01	0.05	0.01	0.04	0.01
Cr ₂ O ₃	0.08	0.04	0.06	0.04	0.04	0.02
FeO	27.84	27.83	28.85	28.78	28.76	29.37
MnO	0.52	0.59	0.50	0.54	0.55	0.52
MgO	32.36	32.40	31.56	31.55	31.81	31.09
CaO	0.22	0.32	0.27	0.17	0.27	0.25
P ₂ O ₅	0.04	0.04	0.00	0.08	0.05	0.00
NiO	0.05	0.02	0.11	0.05	0.02	0.03
Ce ₂ O ₃	0.00	0.00	0.00	0.00	0.00	0.00
Na ₂ O	0.03	0.03	0.00	0.07	0.04	0.02
K ₂ O	0.00	0.02	0.00	0.02	0.02	0.00
Cl	0.00	0.02	0.00	0.01	0.02	0.00
Total	98.63	98.62	98.58	98.55	98.55	98.50
Si	1.02	1.02	1.02	1.02	1.02	1.02
Ti	0.00	0.00	0.00	0.00	0.00	0.00
Al	0.00	0.00	0.00	0.00	0.00	0.00
Cr	0.00	0.00	0.00	0.00	0.00	0.00
Fe	0.65	0.64	0.64	0.64	0.63	0.62
Mn	0.01	0.01	0.01	0.01	0.01	0.01
Mg	1.29	1.30	1.30	1.30	1.30	1.31
Ca	0.01	0.01	0.01	0.01	0.01	0.01
P	0.00	0.00	0.00	0.00	0.00	0.00
Ni	0.00	0.00	0.00	0.00	0.00	0.00
Ce	0.00	0.00	0.00	0.00	0.00	0.00
Na	0.00	0.00	0.00	0.00	0.00	0.00
K	0.00	0.00	0.00	0.00	0.00	0.00
Cl	0.00	0.00	0.00	0.00	0.00	0.00
Total	2.98	2.98	2.98	2.98	2.98	2.98
Fo	66.26	67.01	66.92	66.83	67.25	67.77

Table 18. NWA 14904 Low-Ca Pyroxene Compositions

Slide Point	H2 10	H2 1	H2 8	H2 7	H2 30	Q26 15	Q26 14	H2 18
SiO ₂	55.12	54.92	54.70	54.47	54.80	54.65	54.38	54.36
TiO ₂	0.06	0.05	0.06	0.05	0.08	0.10	0.08	0.11
Al ₂ O ₃	0.36	0.34	0.39	0.40	0.40	0.41	0.47	0.51
Cr ₂ O ₃	0.54	0.53	0.39	0.46	0.56	0.48	0.44	0.39
MgO	27.96	28.16	27.91	27.47	27.07	27.22	26.94	26.65
CaO	1.48	1.49	1.52	1.71	1.98	1.99	2.12	2.21
MnO	0.41	0.39	0.46	0.58	0.43	0.39	0.54	0.48
FeO	12.60	12.93	13.10	13.43	13.72	13.60	13.48	13.91
Na ₂ O	0.03	0.04	0.04	0.03	0.03	0.10	0.09	0.04
K ₂ O	0.00	0.00	0.01	0.00	0.01	0.02	0.00	0.02
Total	98.54	98.84	98.60	98.60	99.07	98.94	98.54	98.67
Si	2.00	1.99	1.99	1.98	1.99	1.98	1.98	1.98
Ti	0.00	0.00	0.00	0.00	0.00	0.00	0.00	0.00
Al	0.02	0.01	0.02	0.02	0.02	0.02	0.02	0.02
Cr	0.02	0.02	0.01	0.01	0.02	0.01	0.01	0.01
Mg	1.51	1.52	1.51	1.49	1.46	1.47	1.46	1.45
Ca	0.06	0.06	0.06	0.07	0.08	0.08	0.08	0.09
Mn	0.01	0.01	0.01	0.02	0.01	0.01	0.02	0.02
Fe	0.38	0.39	0.40	0.41	0.42	0.41	0.41	0.42
Na	0.00	0.00	0.00	0.00	0.00	0.01	0.01	0.00
K	0.00	0.00	0.00	0.00	0.00	0.00	0.00	0.00
Total	3.99	4.00	4.00	4.00	4.00	4.00	4.00	4.00
Wo	2.94	2.93	3.01	3.40	3.94	3.93	4.24	4.40
En	77.48	77.18	76.78	75.81	74.79	75.04	74.78	73.95
Fs	19.59	19.89	20.21	20.80	21.27	21.03	20.99	21.65

Slide Point	H2 17	H2 32	H2 21	H2 33	H2 41	H2 27	H2 48	D26 17
SiO ₂	54.74	54.33	53.99	53.87	54.16	54.45	54.05	53.17
TiO ₂	0.07	0.13	0.17	0.17	0.18	0.17	0.10	0.25
Al ₂ O ₃	0.50	0.52	0.62	0.58	0.53	0.54	0.51	1.16
Cr ₂ O ₃	0.59	0.45	0.46	0.46	0.46	0.58	0.43	0.49
MgO	26.77	26.18	25.88	25.51	25.38	25.83	25.27	23.59
CaO	2.36	2.71	3.02	3.45	3.49	3.58	3.60	4.06
MnO	0.42	0.48	0.42	0.52	0.49	0.44	0.46	0.54
FeO	13.57	13.84	13.95	14.16	13.83	13.32	14.14	15.20
Na ₂ O	0.07	0.06	0.07	0.07	0.07	0.07	0.05	0.07
K ₂ O	0.00	0.00	0.00	0.00	0.00	0.00	0.01	0.01
Total	99.10	98.69	98.59	98.79	98.59	98.97	98.61	98.54
Si	1.99	1.98	1.98	1.98	1.99	1.98	1.98	1.97
Ti	0.00	0.00	0.00	0.00	0.00	0.00	0.00	0.01
Al	0.02	0.02	0.03	0.03	0.02	0.02	0.02	0.05
Cr	0.02	0.01	0.01	0.01	0.01	0.02	0.01	0.01
Mg	1.45	1.43	1.41	1.39	1.39	1.40	1.38	1.30
Ca	0.09	0.11	0.12	0.14	0.14	0.14	0.14	0.16
Mn	0.01	0.02	0.01	0.02	0.02	0.01	0.01	0.02
Fe	0.41	0.42	0.43	0.43	0.42	0.41	0.43	0.47
Na	0.01	0.00	0.00	0.00	0.00	0.00	0.00	0.00
K	0.00	0.00	0.00	0.00	0.00	0.00	0.00	0.00
Total	4.00	4.00	4.00	4.00	3.99	3.99	4.00	4.00
Wo	4.71	5.42	6.05	6.90	7.03	7.17	7.22	8.33
En	74.19	72.94	72.14	70.98	71.21	72.01	70.60	67.34
Fs	21.10	21.63	21.81	22.11	21.76	20.82	22.18	24.33

Slide Point	F6 13	H2 44	H2 24	D26 19	F6 11	Q26 7	H2 22	F6 8
SiO ₂	53.46	54.07	53.91	52.88	53.49	53.26	53.84	53.09
TiO ₂	0.18	0.21	0.11	0.59	0.28	0.16	0.05	0.29
Al ₂ O ₃	0.85	0.78	0.59	0.86	1.05	0.79	0.64	1.36
Cr ₂ O ₃	0.39	0.57	0.43	0.37	0.41	0.57	0.78	0.53
MgO	24.28	24.44	24.84	22.96	23.83	23.62	24.24	23.35
CaO	4.08	4.18	4.40	4.58	4.75	4.98	5.16	5.41
MnO	0.55	0.52	0.55	0.55	0.48	0.47	0.58	0.52
FeO	15.17	14.33	13.95	15.80	15.02	14.58	13.33	13.98
Na ₂ O	0.02	0.08	0.06	0.07	0.07	0.09	0.09	0.06
K ₂ O	0.00	0.02	0.01	0.00	0.01	0.05	0.00	0.00
Total	98.98	99.18	98.84	98.67	99.39	98.56	98.70	98.59
Si	1.97	1.98	1.98	1.96	1.96	1.97	1.98	1.96
Ti	0.01	0.01	0.00	0.02	0.01	0.00	0.00	0.01
Al	0.04	0.03	0.03	0.04	0.05	0.03	0.03	0.06
Cr	0.01	0.02	0.01	0.01	0.01	0.02	0.02	0.02
Mg	1.33	1.33	1.36	1.27	1.30	1.30	1.33	1.29
Ca	0.16	0.16	0.17	0.18	0.19	0.20	0.20	0.21
Mn	0.02	0.02	0.02	0.02	0.01	0.01	0.02	0.02
Fe	0.47	0.44	0.43	0.49	0.46	0.45	0.41	0.43
Na	0.00	0.01	0.00	0.01	0.00	0.01	0.01	0.00
K	0.00	0.00	0.00	0.00	0.00	0.00	0.00	0.00
Total	4.00	3.99	4.00	4.00	4.00	4.00	4.00	4.00
Wo	8.20	8.47	8.83	9.38	9.57	10.11	10.46	11.09
En	67.98	68.87	69.33	65.38	66.80	66.77	68.43	66.56
Fs	23.82	22.66	21.84	25.24	23.62	23.12	21.11	22.35

Slide Point	H18 11	H2 25	F6 4	D26 12	F6 1	D26 5	D26 6	D26 3
SiO ₂	53.10	53.56	53.18	53.18	53.29	53.46	53.26	53.40
TiO ₂	0.22	0.23	0.25	0.21	0.20	0.21	0.21	0.18
Al ₂ O ₃	1.10	0.60	1.12	0.97	0.98	1.00	0.88	1.02
Cr ₂ O ₃	0.53	0.54	0.52	0.38	0.50	0.58	0.54	0.65
MgO	23.30	22.95	22.92	23.13	23.10	22.89	22.87	22.66
CaO	5.45	5.97	6.17	6.17	6.48	6.93	7.04	7.08
MnO	0.58	0.55	0.53	0.51	0.56	0.54	0.52	0.56
FeO	14.56	13.97	14.10	13.86	13.80	13.38	13.13	13.52
Na ₂ O	0.06	0.15	0.08	0.09	0.05	0.10	0.11	0.11
K ₂ O	0.00	0.01	0.03	0.01	0.00	0.01	0.00	0.00
Total	98.90	98.51	98.89	98.52	98.96	99.08	98.56	99.18
Si	1.96	1.98	1.96	1.97	1.97	1.97	1.97	1.97
Ti	0.01	0.01	0.01	0.01	0.01	0.01	0.01	0.01
Al	0.05	0.03	0.05	0.04	0.04	0.04	0.04	0.04
Cr	0.02	0.02	0.02	0.01	0.01	0.02	0.02	0.02
Mg	1.28	1.27	1.26	1.28	1.27	1.26	1.26	1.24
Ca	0.22	0.24	0.24	0.24	0.26	0.27	0.28	0.28
Mn	0.02	0.02	0.02	0.02	0.02	0.02	0.02	0.02
Fe	0.45	0.43	0.44	0.43	0.43	0.41	0.41	0.42
Na	0.00	0.01	0.01	0.01	0.00	0.01	0.01	0.01
K	0.00	0.00	0.00	0.00	0.00	0.00	0.00	0.00
Total	4.00	4.00	4.00	4.00	4.00	4.00	4.00	4.00
Wo	11.07	12.23	12.58	12.55	13.12	14.08	14.34	14.41
En	65.85	65.43	65.00	65.45	65.07	64.71	64.79	64.12
Fs	23.08	22.34	22.43	22.00	21.80	21.22	20.86	21.46

Slide Point	P4 6	H18 19
SiO ₂	52.30	52.84
TiO ₂	0.59	0.28
Al ₂ O ₃	1.20	1.29
Cr ₂ O ₃	0.50	0.61
MgO	21.07	21.30
CaO	7.20	8.63
MnO	0.53	0.55
FeO	15.23	12.94
Na ₂ O	0.11	0.08
K ₂ O	0.00	0.01
Total	98.73	98.54
Si	1.95	1.96
Ti	0.02	0.01
Al	0.05	0.06
Cr	0.01	0.02
Mg	1.17	1.18
Ca	0.29	0.34
Mn	0.02	0.02
Fe	0.48	0.40
Na	0.01	0.01
K	0.00	0.00
Total	4.00	4.00
Wo	14.88	17.85
En	60.57	61.27
Fs	24.55	20.88

Table 19. NWA 14904 High-Ca Pyroxene Compositions

Slide Point	D26 16	F6 26	H18 5	H2 54	F6 27	H18 10	H2 51	H18 3
SiO ₂	52.39	52.43	51.21	51.31	52.24	51.74	52.66	51.25
TiO ₂	0.39	0.25	0.52	0.55	0.28	0.32	0.26	0.51
Al ₂ O ₃	1.68	1.35	2.27	2.45	1.38	1.84	1.38	2.15
Cr ₂ O ₃	0.96	0.88	0.93	0.98	0.98	1.23	0.77	1.10
MgO	16.75	17.47	16.71	16.50	17.30	17.18	17.36	16.78
CaO	18.31	17.73	17.70	17.66	17.65	17.58	17.51	17.43
MnO	0.26	0.32	0.31	0.36	0.33	0.43	0.31	0.34
FeO	8.09	8.12	8.75	8.93	8.38	8.81	8.60	9.10
Na ₂ O	0.27	0.21	0.26	0.28	0.25	0.25	0.21	0.20
K ₂ O	0.01	0.01	0.00	0.01	0.01	0.00	0.00	0.00
Total	99.09	98.78	98.66	99.03	98.81	99.37	99.06	98.85
Si	1.95	1.95	1.92	1.92	1.95	1.93	1.96	1.92
Ti	0.01	0.01	0.01	0.02	0.01	0.01	0.01	0.01
Al	0.07	0.06	0.10	0.11	0.06	0.08	0.06	0.10
Cr	0.03	0.03	0.03	0.03	0.03	0.04	0.02	0.03
Mg	0.93	0.97	0.93	0.92	0.96	0.95	0.96	0.94
Ca	0.73	0.71	0.71	0.71	0.71	0.70	0.70	0.70
Mn	0.01	0.01	0.01	0.01	0.01	0.01	0.01	0.01
Fe	0.25	0.25	0.27	0.28	0.26	0.27	0.27	0.29
Na	0.02	0.02	0.02	0.02	0.02	0.02	0.02	0.01
K	0.00	0.00	0.00	0.00	0.00	0.00	0.00	0.00
Total	4.00	4.00	4.01	4.01	4.01	4.01	4.00	4.01
Wo	38.20	36.65	37.05	37.12	36.57	36.36	36.20	36.41
En	48.62	50.24	48.65	48.23	49.87	49.42	49.92	48.76
Fs	13.18	13.10	14.30	14.64	13.56	14.22	13.88	14.83

Slide Point	H2 53	H2 40	D26 20	H2 37	D26 13	F6 22	D26 23
SiO ₂	51.82	52.34	51.09	52.27	52.37	52.47	51.63
TiO ₂	0.42	0.28	0.68	0.40	0.33	0.32	0.45
Al ₂ O ₃	1.85	1.33	2.61	1.68	1.54	1.33	2.51
Cr ₂ O ₃	0.90	0.78	0.92	0.90	0.91	0.96	0.90
MgO	16.91	17.41	16.40	17.10	17.46	17.87	16.63
CaO	17.41	17.31	17.28	17.25	17.25	17.22	17.21
MnO	0.36	0.34	0.40	0.36	0.48	0.36	0.40
FeO	8.68	8.76	9.03	8.57	8.58	8.51	8.58
Na ₂ O	0.23	0.22	0.25	0.21	0.18	0.18	0.27
K ₂ O	0.00	0.01	0.01	0.01	0.00	0.02	0.00
Total	98.58	98.79	98.66	98.75	99.09	99.24	98.58
Si	1.94	1.95	1.92	1.95	1.95	1.95	1.93
Ti	0.01	0.01	0.02	0.01	0.01	0.01	0.01
Al	0.08	0.06	0.12	0.07	0.07	0.06	0.11
Cr	0.03	0.02	0.03	0.03	0.03	0.03	0.03
Mg	0.94	0.97	0.92	0.95	0.97	0.99	0.93
Ca	0.70	0.69	0.69	0.69	0.69	0.69	0.69
Mn	0.01	0.01	0.01	0.01	0.02	0.01	0.01
Fe	0.27	0.27	0.28	0.27	0.27	0.26	0.27
Na	0.02	0.02	0.02	0.02	0.01	0.01	0.02
K	0.00	0.00	0.00	0.00	0.00	0.00	0.00
Total	4.00	4.01	4.00	4.00	4.00	4.01	4.00
Wo	36.50	35.79	36.66	36.14	35.76	35.34	36.58
En	49.31	50.08	48.40	49.85	50.36	51.03	49.18
Fs	14.19	14.13	14.94	14.01	13.89	13.63	14.24

Slide Point	Q26 5	D26 1	D26 22	P4 15	H18 6	D26 28	D26 25	D26 21
SiO ₂	51.80	51.92	51.38	52.14	51.95	51.74	52.02	51.92
TiO ₂	0.31	0.41	0.60	0.26	0.42	0.35	0.34	0.85
Al ₂ O ₃	1.49	2.02	2.62	1.46	1.80	1.71	1.86	1.60
Cr ₂ O ₃	0.82	0.98	0.91	0.81	0.89	0.90	0.96	0.69
MgO	17.24	17.26	16.82	17.70	17.30	17.42	17.43	17.31
CaO	17.00	16.96	16.81	16.81	16.76	16.71	16.62	16.53
MnO	0.43	0.40	0.40	0.32	0.40	0.38	0.33	0.34
FeO	9.22	9.05	8.92	8.84	9.17	9.43	9.17	9.69
Na ₂ O	0.22	0.15	0.25	0.23	0.24	0.21	0.22	0.36
K ₂ O	0.00	0.01	0.01	0.00	0.00	0.01	0.00	0.00
Total	98.53	99.17	98.72	98.57	98.92	98.84	98.95	99.29
Si	1.94	1.93	1.92	1.95	1.94	1.94	1.94	1.93
Ti	0.01	0.01	0.02	0.01	0.01	0.01	0.01	0.02
Al	0.07	0.09	0.12	0.06	0.08	0.08	0.08	0.07
Cr	0.02	0.03	0.03	0.02	0.03	0.03	0.03	0.02
Mg	0.96	0.96	0.94	0.99	0.96	0.97	0.97	0.96
Ca	0.68	0.68	0.67	0.67	0.67	0.67	0.66	0.66
Mn	0.01	0.01	0.01	0.01	0.01	0.01	0.01	0.01
Fe	0.29	0.28	0.28	0.28	0.29	0.29	0.29	0.30
Na	0.02	0.01	0.02	0.02	0.02	0.02	0.02	0.03
K	0.00	0.00	0.00	0.00	0.00	0.00	0.00	0.00
Total	4.01	4.00	4.00	4.01	4.00	4.01	4.00	4.01
Wo	35.28	35.31	35.64	34.78	34.93	34.58	34.62	34.31
En	49.78	49.99	49.60	50.96	50.15	50.18	50.48	50.00
Fs	14.94	14.71	14.76	14.27	14.91	15.23	14.90	15.70

Slide Point	D26 27	H2 34	Q26 2	D26 26	F6 17	F6 6	F6 21	N18 17
SiO ₂	51.89	52.64	51.98	52.06	53.00	51.92	52.76	52.33
TiO ₂	0.43	0.20	0.44	0.46	0.21	0.41	0.24	0.23
Al ₂ O ₃	1.88	1.05	1.81	1.87	1.11	2.02	0.93	1.29
Cr ₂ O ₃	0.81	0.76	0.87	0.95	0.71	0.82	0.73	0.88
MgO	17.47	18.08	17.20	17.70	18.46	17.55	18.38	18.19
CaO	16.49	16.49	16.47	16.45	16.19	16.19	16.14	16.09
MnO	0.31	0.32	0.36	0.44	0.46	0.40	0.34	0.37
FeO	9.26	8.96	9.35	9.02	8.77	9.19	9.01	8.97
Na ₂ O	0.23	0.20	0.20	0.21	0.22	0.21	0.15	0.24
K ₂ O	0.01	0.00	0.02	0.01	0.01	0.03	0.01	0.01
Total	98.77	98.69	98.71	99.17	99.15	98.74	98.67	98.60
Si	1.94	1.96	1.94	1.94	1.96	1.94	1.97	1.95
Ti	0.01	0.01	0.01	0.01	0.01	0.01	0.01	0.01
Al	0.08	0.05	0.08	0.08	0.05	0.09	0.04	0.06
Cr	0.02	0.02	0.03	0.03	0.02	0.02	0.02	0.03
Mg	0.97	1.01	0.96	0.98	1.02	0.98	1.02	1.01
Ca	0.66	0.66	0.66	0.66	0.64	0.65	0.64	0.64
Mn	0.01	0.01	0.01	0.01	0.01	0.01	0.01	0.01
Fe	0.29	0.28	0.29	0.28	0.27	0.29	0.28	0.28
Na	0.02	0.01	0.01	0.01	0.02	0.02	0.01	0.02
K	0.00	0.00	0.00	0.00	0.00	0.00	0.00	0.00
Total	4.00	4.00	4.00	4.00	4.00	4.00	4.00	4.01
Wo	34.34	33.90	34.52	34.18	33.24	33.89	33.12	33.25
En	50.61	51.72	50.18	51.18	52.72	51.10	52.45	52.28
Fs	15.05	14.38	15.31	14.63	14.05	15.02	14.43	14.46

Slide Point	D26 29	F6 18	D26 7	H2 52	P4 14	H18 18	D26 4	F6 19
SiO ₂	52.16	52.92	52.64	51.66	52.35	51.20	51.82	53.49
TiO ₂	0.36	0.20	0.29	0.45	0.34	0.49	0.46	0.15
Al ₂ O ₃	1.59	1.01	1.33	2.04	1.39	2.31	2.15	0.97
Cr ₂ O ₃	0.74	0.81	0.87	0.93	0.93	0.77	0.83	0.69
MgO	17.64	18.69	18.24	17.54	17.87	17.52	17.31	18.82
CaO	15.91	15.87	15.86	15.83	15.79	15.72	15.70	15.57
MnO	0.52	0.37	0.37	0.45	0.39	0.41	0.41	0.33
FeO	9.64	9.24	9.23	9.70	9.32	10.12	9.89	9.57
Na ₂ O	0.18	0.16	0.22	0.25	0.15	0.26	0.22	0.18
K ₂ O	0.00	0.00	0.00	0.01	0.00	0.00	0.00	0.00
Total	98.73	99.27	99.05	98.85	98.53	98.80	98.81	99.77
Si	1.95	1.96	1.96	1.93	1.96	1.92	1.94	1.97
Ti	0.01	0.01	0.01	0.01	0.01	0.01	0.01	0.00
Al	0.07	0.04	0.06	0.09	0.06	0.10	0.09	0.04
Cr	0.02	0.02	0.03	0.03	0.03	0.02	0.02	0.02
Mg	0.98	1.03	1.01	0.98	1.00	0.98	0.96	1.03
Ca	0.64	0.63	0.63	0.63	0.63	0.63	0.63	0.61
Mn	0.02	0.01	0.01	0.01	0.01	0.01	0.01	0.01
Fe	0.30	0.29	0.29	0.30	0.29	0.32	0.31	0.29
Na	0.01	0.01	0.02	0.02	0.01	0.02	0.02	0.01
K	0.00	0.00	0.00	0.00	0.00	0.00	0.00	0.00
Total	4.00	4.01	4.00	4.01	4.00	4.02	4.00	4.00
Wo	33.16	32.34	32.73	33.12	32.95	32.76	33.06	31.63
En	51.15	52.97	52.40	51.05	51.88	50.78	50.69	53.20
Fs	15.69	14.69	14.87	15.83	15.18	16.46	16.25	15.17

Slide Point	N18 10	D26 37	F6 20	D26 8	H2 35	N18 15	N18 11	H18 16
SiO ₂	52.63	51.85	52.42	52.19	52.35	52.50	52.90	51.16
TiO ₂	0.22	0.49	0.22	0.41	0.22	0.26	0.24	0.58
Al ₂ O ₃	1.11	1.97	1.11	1.76	1.28	1.20	1.21	2.54
Cr ₂ O ₃	0.56	0.79	0.82	0.91	0.90	0.81	0.63	1.01
MgO	18.35	17.54	18.66	18.27	18.63	18.64	18.61	17.36
CaO	15.52	15.46	15.42	15.41	15.33	15.16	15.09	14.93
MnO	0.43	0.47	0.35	0.42	0.45	0.41	0.41	0.46
FeO	9.73	9.82	9.37	9.93	9.50	9.90	9.85	10.29
Na ₂ O	0.18	0.25	0.16	0.22	0.15	0.20	0.17	0.19
K ₂ O	0.01	0.00	0.00	0.00	0.00	0.01	0.01	0.00
Total	98.73	98.65	98.52	99.50	98.81	99.08	99.13	98.52
SiO ₂								
Si	1.96	1.94	1.96	1.94	1.95	1.95	1.96	1.92
Ti	0.01	0.01	0.01	0.01	0.01	0.01	0.01	0.02
Al	0.05	0.09	0.05	0.08	0.06	0.05	0.05	0.11
Cr	0.02	0.02	0.02	0.03	0.03	0.02	0.02	0.03
Mg	1.02	0.98	1.04	1.01	1.03	1.03	1.03	0.97
Ca	0.62	0.62	0.62	0.61	0.61	0.60	0.60	0.60
Mn	0.01	0.02	0.01	0.01	0.01	0.01	0.01	0.01
Fe	0.30	0.31	0.29	0.31	0.30	0.31	0.31	0.32
Na	0.01	0.02	0.01	0.02	0.01	0.01	0.01	0.01
K	0.00	0.00	0.00	0.00	0.00	0.00	0.00	0.00
Total	4.00	4.00	4.01	4.01	4.01	4.01	4.00	4.00
Wo	31.91	32.53	31.66	31.73	31.49	31.05	31.01	31.68
En	52.48	51.34	53.32	52.32	53.26	53.12	53.20	51.27
Fs	15.61	16.12	15.02	15.95	15.24	15.82	15.79	17.05

Slide Point	D26 36	P4 12	N18 8	P4 10
SiO ₂	52.00	52.08	52.71	52.55
TiO ₂	0.31	0.36	0.26	0.24
Al ₂ O ₃	1.90	1.62	1.06	1.26
Cr ₂ O ₃	0.84	0.99	0.74	0.78
MgO	18.03	18.21	18.94	18.79
CaO	14.93	14.83	14.60	14.57
MnO	0.40	0.36	0.44	0.43
FeO	10.01	10.17	9.80	10.04
Na ₂ O	0.22	0.22	0.22	0.18
K ₂ O	0.01	0.01	0.00	0.00
Total	98.64	98.84	98.75	98.84
Si	1.94	1.94	1.96	1.96
Ti	0.01	0.01	0.01	0.01
Al	0.08	0.07	0.05	0.06
Cr	0.02	0.03	0.02	0.02
Mg	1.00	1.01	1.05	1.04
Ca	0.60	0.59	0.58	0.58
Mn	0.01	0.01	0.01	0.01
Fe	0.31	0.32	0.31	0.31
Na	0.02	0.02	0.02	0.01
K	0.00	0.00	0.00	0.00
Total	4.00	4.00	4.01	4.00
Wo	31.21	30.84	30.04	30.01
En	52.46	52.66	54.23	53.85
Fs	16.34	16.50	15.74	16.14

Table 20. NWA 14904 Maskelynite Compositions

Slide Point	E6 8	D24 37	D24 44	R4 19	D24 24	R4 2	D24 28	R4 10
SiO ₂	54.08	54.07	53.47	54.17	54.02	54.02	53.92	54.42
Al ₂ O ₃	28.66	28.69	28.61	27.96	27.96	28.56	28.11	28.08
CaO	11.30	11.13	11.16	10.64	10.93	11.03	11.05	10.62
Na ₂ O	5.39	5.43	5.30	5.53	5.48	5.48	5.43	5.61
K ₂ O	0.38	0.33	0.32	0.46	0.35	0.26	0.33	0.38
Total	99.81	99.64	98.86	98.76	98.73	99.34	98.85	99.13
Si	2.45	2.45	2.45	2.48	2.47	2.46	2.47	2.48
Al	1.53	1.54	1.54	1.51	1.51	1.53	1.52	1.51
Ca	0.55	0.54	0.55	0.52	0.54	0.54	0.54	0.52
Na	0.47	0.48	0.47	0.49	0.49	0.48	0.48	0.50
K	0.02	0.02	0.02	0.03	0.02	0.01	0.02	0.02
Total	5.03	5.03	5.03	5.03	5.03	5.03	5.03	5.03
An	52.51	52.13	52.82	50.20	51.38	51.91	51.98	50.03
Ab	45.37	46.04	45.40	47.22	46.66	46.66	46.19	47.83
Or	2.12	1.82	1.78	2.58	1.95	1.43	1.83	2.13

Slide Point	D24 43	D24 15	J4 8	R4 5	D24 38	D24 30	D24 35	R4 15
SiO ₂	54.26	54.37	54.58	54.37	54.15	54.69	54.27	54.86
Al ₂ O ₃	28.80	28.44	27.81	27.77	28.46	27.83	27.92	28.18
CaO	11.22	11.13	10.58	10.53	10.96	10.50	11.19	11.04
Na ₂ O	5.38	5.62	5.62	5.61	5.40	5.60	5.32	5.67
K ₂ O	0.30	0.03	0.38	0.35	0.32	0.39	0.37	0.04
Total	99.95	99.60	98.96	98.62	99.29	99.00	99.06	99.79
Si	2.45	2.47	2.49	2.49	2.46	2.49	2.48	2.48
Al	1.54	1.52	1.50	1.50	1.53	1.50	1.50	1.50
Ca	0.54	0.54	0.52	0.52	0.53	0.51	0.55	0.54
Na	0.47	0.49	0.50	0.50	0.48	0.50	0.47	0.50
K	0.02	0.00	0.02	0.02	0.02	0.02	0.02	0.00
Total	5.02	5.02	5.02	5.02	5.02	5.02	5.02	5.02
An	52.64	52.16	49.89	49.94	51.91	49.78	52.64	51.73
Ab	45.69	47.68	48.00	48.11	46.30	48.04	45.29	48.04
Or	1.66	0.16	2.11	1.94	1.79	2.18	2.08	0.23

Slide Point	J4 2	D24 39	R4 18	R4 20	J4 20	R4 4	R4 3	D24 23
SiO ₂	54.00	53.84	54.16	54.53	54.46	54.42	54.22	54.13
Al ₂ O ₃	28.40	28.05	28.38	27.76	27.88	28.13	28.15	28.05
CaO	11.33	11.34	10.94	10.70	10.89	10.97	10.88	11.20
Na ₂ O	5.21	5.23	5.32	5.49	5.43	5.41	5.39	5.26
K ₂ O	0.33	0.27	0.37	0.38	0.34	0.29	0.29	0.32
Total	99.27	98.73	99.17	98.85	98.99	99.23	98.92	98.95
Si	2.46	2.47	2.47	2.49	2.48	2.48	2.47	2.47
Al	1.52	1.51	1.52	1.49	1.50	1.51	1.51	1.51
Ca	0.55	0.56	0.53	0.52	0.53	0.54	0.53	0.55
Na	0.46	0.46	0.47	0.49	0.48	0.48	0.48	0.47
K	0.02	0.02	0.02	0.02	0.02	0.02	0.02	0.02
Total	5.02	5.02	5.02	5.02	5.02	5.02	5.01	5.01
An	53.55	53.66	52.08	50.77	51.58	51.98	51.86	53.10
Ab	44.59	44.82	45.83	47.11	46.53	46.37	46.49	45.10
Or	1.86	1.52	2.09	2.12	1.89	1.65	1.65	1.79
Slide Point	R4 7	J4 4	J4 12	D24 34	J4 14	J4 5	E6 4	D24 33
SiO ₂	54.95	54.63	54.28	53.87	54.76	54.38	55.22	54.59
Al ₂ O ₃	27.95	28.54	28.40	28.05	28.15	28.51	27.81	28.21
CaO	10.32	11.06	11.03	11.44	10.95	11.18	10.81	11.15
Na ₂ O	5.65	5.33	5.28	5.15	5.37	5.18	5.46	5.29
K ₂ O	0.37	0.36	0.35	0.24	0.35	0.38	0.42	0.28
Total	99.23	99.91	99.34	98.76	99.58	99.63	99.71	99.51
Si	2.50	2.47	2.47	2.47	2.48	2.47	2.50	2.48
Al	1.50	1.52	1.52	1.51	1.50	1.52	1.48	1.51
Ca	0.50	0.54	0.54	0.56	0.53	0.54	0.52	0.54
Na	0.50	0.47	0.47	0.46	0.47	0.46	0.48	0.47
K	0.02	0.02	0.02	0.01	0.02	0.02	0.02	0.02
Total	5.01	5.01	5.01	5.01	5.01	5.01	5.01	5.01
An	49.17	52.36	52.54	54.37	51.91	53.24	51.03	52.96
Ab	48.74	45.64	45.50	44.25	46.10	44.61	46.62	45.47
Or	2.09	2.00	1.96	1.38	1.98	2.16	2.35	1.57

Slide Point	E6 10	J4 18	J4 15	J4 17	R4 9	E6 17	J4 10	J4 21
SiO ₂	55.02	54.95	54.98	54.84	55.35	54.90	54.76	54.71
Al ₂ O ₃	28.09	27.97	28.10	28.02	28.09	27.70	28.01	27.90
CaO	10.70	10.60	10.89	10.95	10.25	11.08	10.76	11.59
Na ₂ O	5.46	5.47	5.37	5.35	5.60	5.29	5.33	5.25
K ₂ O	0.34	0.35	0.35	0.31	0.36	0.34	0.36	0.08
Total	99.61	99.33	99.68	99.46	99.65	99.31	99.20	99.54
Si	2.49	2.49	2.49	2.49	2.50	2.50	2.49	2.48
Al	1.50	1.50	1.50	1.50	1.50	1.48	1.50	1.49
Ca	0.52	0.52	0.53	0.53	0.50	0.54	0.52	0.56
Na	0.48	0.48	0.47	0.47	0.49	0.47	0.47	0.46
K	0.02	0.02	0.02	0.02	0.02	0.02	0.02	0.00
Total	5.01	5.01	5.01	5.01	5.01	5.00	5.00	5.00
An	51.01	50.67	51.79	52.13	49.26	52.64	51.68	54.72
Ab	47.06	47.34	46.24	46.09	48.68	45.46	46.28	44.83
Or	1.93	1.99	1.96	1.78	2.06	1.89	2.04	0.45

Slide Point	J4 6	E6 7	J4 3	E6 18	D24 32	J4 7	E6 9	E6 15
SiO ₂	54.94	55.11	54.90	55.13	55.02	54.95	56.14	54.81
Al ₂ O ₃	27.79	27.82	27.90	27.92	27.69	27.45	27.54	28.16
CaO	11.46	10.64	10.72	10.84	10.66	11.10	10.08	10.92
Na ₂ O	5.37	5.37	5.32	5.35	5.38	5.42	5.65	5.21
K ₂ O	0.01	0.41	0.38	0.32	0.31	0.02	0.47	0.31
Total	99.56	99.34	99.23	99.58	99.06	98.94	99.87	99.40
Si	2.49	2.50	2.50	2.50	2.50	2.50	2.53	2.49
Al	1.48	1.49	1.49	1.49	1.48	1.47	1.46	1.51
Ca	0.56	0.52	0.52	0.53	0.52	0.54	0.49	0.53
Na	0.47	0.47	0.47	0.47	0.47	0.48	0.49	0.46
K	0.00	0.02	0.02	0.02	0.02	0.00	0.03	0.02
Total	5.00	5.00	5.00	5.00	5.00	5.00	5.00	5.00
An	54.09	51.03	51.54	51.84	51.37	53.05	48.33	52.69
Ab	45.84	46.65	46.26	46.32	46.88	46.84	48.99	45.51
Or	0.07	2.32	2.20	1.84	1.75	0.11	2.68	1.81

Slide Point	E6 5	E6 14	E6 2	J4 19	J4 13	E6 13
SiO ₂	55.54	55.79	55.80	55.70	54.69	56.21
Al ₂ O ₃	27.16	27.43	27.25	27.62	28.22	27.07
CaO	10.44	10.38	10.06	10.40	10.94	9.93
Na ₂ O	5.42	5.44	5.42	5.34	4.92	5.49
K ₂ O	0.43	0.33	0.50	0.38	0.34	0.36
Total	98.99	99.37	99.03	99.43	99.12	99.06
Si	2.53	2.53	2.53	2.52	2.49	2.55
Al	1.46	1.46	1.46	1.47	1.51	1.45
Ca	0.51	0.50	0.49	0.50	0.53	0.48
Na	0.48	0.48	0.48	0.47	0.43	0.48
K	0.03	0.02	0.03	0.02	0.02	0.02
Total	5.00	4.99	4.99	4.99	4.98	4.98
An	50.31	50.34	49.15	50.68	54.01	48.90
Ab	47.22	47.78	47.93	47.11	43.97	48.98
Or	2.47	1.88	2.92	2.20	2.02	2.12

Table 21. NWA 14904 Carbonate Vein Compositions

Slide Point	I20 4	I20 8	K18 3	K18 5	K18 9	K18 11	K19 2	K19 10
CO ₂	46.9	49.1	49.0	67.7	50.2	48.0	57.7	48.7
CaO	52.4	50.3	50.1	31.6	48.8	51.0	41.0	50.5
MgO	0.7	0.7	0.7	0.4	0.7	0.8	0.7	0.6
FeO	0.0	0.0	0.2	0.2	0.3	0.2	0.5	0.2
MnO	0.0	0.0	0.0	0.1	0.0	0.0	0.0	0.0
Total	100.0	100.0	100.0	100.0	100.0	100.0	100.0	100.0
C	0.3	0.4	0.4	0.4	0.4	0.4	0.4	0.4
Ca	0.3	0.3	0.3	0.2	0.3	0.3	0.2	0.3
Mg	0.0	0.0	0.0	0.0	0.0	0.0	0.0	0.0
Fe	0.0	0.0	0.0	0.0	0.0	0.0	0.0	0.0
Mn	0.0	0.0	0.0	0.0	0.0	0.0	0.0	0.0
Total	0.7	0.6	0.6	0.6	0.6	0.6	0.6	0.6
Cal	98.1	98.1	97.7	97.8	97.6	97.6	96.6	98.1
Mag	1.8	1.8	1.9	1.6	1.9	2.1	2.4	1.5
Sid	0.1	0.0	0.4	0.6	0.5	0.3	0.9	0.3

Slide Point	K19 12	K19 13	N24 9	D25 2	D25 3	D25 6	D25 7	D25 10
CO ₂	50.0	47.6	47.5	49.0	48.6	48.2	48.9	50.6
CaO	49.2	51.6	51.3	49.9	50.3	50.9	50.2	48.3
MgO	0.5	0.5	0.6	0.8	0.7	0.6	0.7	0.8
FeO	0.2	0.3	0.6	0.4	0.4	0.3	0.2	0.4
MnO	0.0	0.0	0.0	0.0	0.0	0.0	0.0	0.0
Total	100.0	100.0	100.0	100.0	100.0	100.0	100.0	100.0
C	0.4	0.3	0.3	0.4	0.4	0.4	0.4	0.4
Ca	0.3	0.3	0.3	0.3	0.3	0.3	0.3	0.3
Mg	0.0	0.0	0.0	0.0	0.0	0.0	0.0	0.0
Fe	0.0	0.0	0.0	0.0	0.0	0.0	0.0	0.0
Mn	0.0	0.0	0.0	0.0	0.0	0.0	0.0	0.0
Total	0.6	0.7	0.7	0.6	0.6	0.6	0.6	0.6
Cal	98.2	98.3	97.4	97.3	97.6	97.9	97.8	97.3
Mag	1.4	1.2	1.7	2.1	1.9	1.6	1.9	2.1
Sid	0.4	0.5	0.9	0.6	0.5	0.4	0.3	0.6

Slide Point	D25 13	D25 14	D25 2	D25 3	D25 4	D25 7	D25 9	H23 1
CO ₂	48.3	60.7	53.8	47.3	46.6	49.4	48.1	46.9
CaO	50.6	26.8	42.4	51.7	52.4	48.0	50.6	51.9
MgO	0.7	6.3	3.2	0.7	0.6	2.0	0.8	0.9
FeO	0.4	6.2	0.7	0.3	0.4	0.5	0.4	0.3
MnO	0.0	0.0	0.0	0.0	0.0	0.0	0.0	0.0
Total	100.0	100.0	100.0	100.0	100.0	100.0	100.0	100.0
C	0.4	0.4	0.4	0.3	0.3	0.4	0.4	0.3
Ca	0.3	0.1	0.2	0.3	0.3	0.3	0.3	0.3
Mg	0.0	0.0	0.0	0.0	0.0	0.0	0.0	0.0
Fe	0.0	0.0	0.0	0.0	0.0	0.0	0.0	0.0
Mn	0.0	0.0	0.0	0.0	0.0	0.0	0.0	0.0
Total	0.6	0.6	0.6	0.7	0.7	0.6	0.6	0.7
Cal	97.5	66.3	89.4	97.7	97.8	93.8	97.1	97.2
Mag	1.9	21.7	9.5	1.8	1.7	5.5	2.2	2.3
Sid	0.6	12.0	1.1	0.4	0.6	0.7	0.6	0.5

Slide Point	H23 3	H23 4	H23 5	H23 7	H23 8	H23 12	I20 2	I20 3
CO ₂	46.2	45.6	55.7	48.6	46.0	89.1	50.1	47.4
CaO	52.7	53.1	41.9	49.9	52.9	10.1	49.0	51.7
MgO	0.9	0.9	1.6	1.2	1.0	0.2	0.8	0.9
FeO	0.2	0.3	0.7	0.2	0.2	0.6	0.1	0.0
MnO	0.0	0.0	0.0	0.0	0.0	0.0	0.0	0.0
Total	100.0	100.0	100.0	100.0	100.0	100.0	100.0	100.0
C	0.3	0.3	0.4	0.4	0.3	0.5	0.4	0.3
Ca	0.3	0.3	0.2	0.3	0.3	0.0	0.3	0.3
Mg	0.0	0.0	0.0	0.0	0.0	0.0	0.0	0.0
Fe	0.0	0.0	0.0	0.0	0.0	0.0	0.0	0.0
Mn	0.0	0.0	0.0	0.0	0.0	0.0	0.0	0.0
Total	0.7	0.7	0.6	0.6	0.7	0.5	0.6	0.7
Cal	97.4	97.2	93.6	96.4	97.3	93.0	97.5	97.6
Mag	2.3	2.4	5.1	3.3	2.5	2.8	2.3	2.3
Sid	0.3	0.5	1.3	0.3	0.3	4.2	0.2	0.0

Slide Point	I20 6	I20 7	I20 10	I20 11	K18 8	K19 3	K19 4	K19 9
CO ₂	47.5	51.4	47.7	51.0	49.0	51.8	50.4	47.8
CaO	51.9	47.8	51.3	47.8	49.9	46.7	48.3	51.2
MgO	0.6	0.8	0.9	0.9	0.9	0.8	0.8	0.5
FeO	0.1	0.1	0.1	0.4	0.2	0.7	0.5	0.4
MnO	0.0	0.0	0.0	0.0	0.0	0.0	0.0	0.0
Total	100.0	100.0	100.0	100.0	100.0	100.0	100.0	100.0
C	0.3	0.4	0.3	0.4	0.4	0.4	0.4	0.3
Ca	0.3	0.3	0.3	0.3	0.3	0.3	0.3	0.3
Mg	0.0	0.0	0.0	0.0	0.0	0.0	0.0	0.0
Fe	0.0	0.0	0.0	0.0	0.0	0.0	0.0	0.0
Mn	0.0	0.0	0.0	0.0	0.0	0.0	0.0	0.0
Total	0.7	0.6	0.7	0.6	0.6	0.6	0.6	0.7
Cal	98.4	97.6	97.4	97.0	97.3	96.5	97.0	98.0
Mag	1.5	2.2	2.4	2.4	2.4	2.4	2.3	1.4
Sid	0.1	0.1	0.2	0.6	0.3	1.1	0.8	0.6

Slide Point	N24 2	N24 4	N24 6	N24 8	N24 10	N24 11	D25 9	D25 12
CO ₂	48.8	48.4	47.4	47.5	40.3	48.6	53.2	49.1
CaO	49.7	49.9	51.3	51.1	0.4	50.1	45.7	49.8
MgO	1.1	1.2	0.8	0.9	42.2	0.8	0.9	0.7
FeO	0.4	0.6	0.4	0.4	17.1	0.5	0.3	0.3
MnO	0.0	0.0	0.0	0.0	0.0	0.0	0.0	0.0
Total	100.0	100.0	100.0	100.0	100.0	100.0	100.0	100.0
C	0.4	0.4	0.3	0.3	0.3	0.4	0.4	0.4
Ca	0.3	0.3	0.3	0.3	0.0	0.3	0.2	0.3
Mg	0.0	0.0	0.0	0.0	0.3	0.0	0.0	0.0
Fe	0.0	0.0	0.0	0.0	0.1	0.0	0.0	0.0
Mn	0.0	0.0	0.0	0.0	0.0	0.0	0.0	0.0
Total	0.6	0.6	0.7	0.7	0.7	0.6	0.6	0.6
Cal	96.5	96.0	97.3	97.0	0.5	97.1	97.0	97.6
Mag	3.0	3.2	2.1	2.3	81.0	2.1	2.5	1.9
Sid	0.5	0.9	0.6	0.6	18.5	0.7	0.5	0.5

Slide Point	D25 15	D25 5	D25 11	D25 12	D25 13	H23 2	H23 6	H23 10
CO ₂	48.0	71.3	45.1	80.7	66.3	46.0	50.0	45.6
CaO	51.0	13.4	54.0	6.0	28.8	52.7	48.3	53.1
MgO	0.7	14.4	0.7	7.6	4.1	1.1	1.2	0.8
FeO	0.3	0.9	0.3	5.7	0.8	0.2	0.5	0.5
MnO	0.0	0.0	0.0	0.0	0.0	0.0	0.0	0.0
Total	100.0	100.0	100.0	100.0	100.0	100.0	100.0	100.0
C	0.4	0.4	0.3	0.5	0.4	0.3	0.4	0.3
Ca	0.3	0.1	0.3	0.0	0.1	0.3	0.3	0.3
Mg	0.0	0.1	0.0	0.0	0.0	0.0	0.0	0.0
Fe	0.0	0.0	0.0	0.0	0.0	0.0	0.0	0.0
Mn	0.0	0.0	0.0	0.0	0.0	0.0	0.0	0.0
Total	0.6	0.6	0.7	0.5	0.6	0.7	0.6	0.7
Cal	97.7	39.3	97.9	28.6	81.9	96.9	95.9	97.2
Mag	1.8	58.6	1.7	50.3	16.4	2.7	3.3	2.1
Sid	0.5	2.1	0.4	21.1	1.7	0.3	0.8	0.7

Slide Point	H23 11	I20 1	I20 5	I20 9	K18 1	K18 2	K18 4	K18 6
CO ₂	46.2	48.4	47.1	48.4	51.0	48.5	46.7	48.5
CaO	52.5	50.6	52.0	50.6	47.6	50.6	52.6	50.8
MgO	0.9	0.8	0.9	0.9	0.9	0.7	0.5	0.6
FeO	0.4	0.2	0.0	0.1	0.4	0.2	0.2	0.1
MnO	0.0	0.0	0.0	0.0	0.0	0.0	0.0	0.0
Total	100.0	100.0	100.0	100.0	100.0	100.0	100.0	100.0
C	0.3	0.4	0.3	0.4	0.4	0.4	0.3	0.4
Ca	0.3	0.3	0.3	0.3	0.3	0.3	0.3	0.3
Mg	0.0	0.0	0.0	0.0	0.0	0.0	0.0	0.0
Fe	0.0	0.0	0.0	0.0	0.0	0.0	0.0	0.0
Mn	0.0	0.0	0.0	0.0	0.0	0.0	0.0	0.0
Total	0.7	0.6	0.7	0.6	0.6	0.6	0.7	0.6
Cal	97.1	97.6	97.7	97.4	96.7	97.7	98.4	98.3
Mag	2.3	2.1	2.3	2.5	2.6	2.0	1.4	1.5
Sid	0.6	0.3	0.0	0.1	0.7	0.3	0.3	0.2

Slide Point	K18 7	K18 10	K19 6	K19 7	K19 8	K19 11	N24 1	N24 3
CO ₂	48.2	49.2	47.7	45.3	48.0	49.9	46.9	50.4
CaO	50.8	49.6	51.0	2.9	51.0	49.0	51.8	48.3
MgO	0.7	0.7	0.8	23.0	0.7	0.6	1.0	0.9
FeO	0.3	0.4	0.5	28.7	0.3	0.4	0.3	0.4
MnO	0.0	0.0	0.0	0.0	0.0	0.0	0.0	0.0
Total	100.0	100.0	100.0	100.0	100.0	100.0	100.0	100.0
C	0.4	0.4	0.3	0.3	0.4	0.4	0.3	0.4
Ca	0.3	0.3	0.3	0.0	0.3	0.3	0.3	0.3
Mg	0.0	0.0	0.0	0.2	0.0	0.0	0.0	0.0
Fe	0.0	0.0	0.0	0.1	0.0	0.0	0.0	0.0
Mn	0.0	0.0	0.0	0.0	0.0	0.0	0.0	0.0
Total	0.6	0.6	0.7	0.7	0.6	0.6	0.7	0.6
Cal	97.7	97.3	97.1	5.1	97.7	97.6	96.9	96.9
Mag	1.8	2.0	2.2	55.8	1.9	1.7	2.6	2.4
Sid	0.5	0.7	0.7	39.1	0.4	0.7	0.5	0.7

Slide Point	N24 5	N24 7	D25 4	D25 5	D25 8	D25 11	D25 1	D25 6
CO ₂	47.2	48.9	49.0	48.8	49.9	49.2	45.6	50.2
CaO	51.6	3.6	50.1	50.0	49.2	49.7	53.2	44.1
MgO	0.9	22.6	0.7	0.7	0.6	0.8	0.8	3.2
FeO	0.4	24.9	0.1	0.4	0.2	0.2	0.4	2.6
MnO	0.0	0.0	0.0	0.1	0.1	0.0	0.0	0.0
Total	100.0	100.0	100.0	100.0	100.0	100.0	100.0	100.0
C	0.3	0.3	0.4	0.4	0.4	0.4	0.3	0.4
Ca	0.3	0.0	0.3	0.3	0.3	0.3	0.3	0.2
Mg	0.0	0.2	0.0	0.0	0.0	0.0	0.0	0.0
Fe	0.0	0.1	0.0	0.0	0.0	0.0	0.0	0.0
Mn	0.0	0.0	0.0	0.0	0.0	0.0	0.0	0.0
Total	0.7	0.7	0.6	0.6	0.6	0.6	0.7	0.6
Cal	97.1	6.7	97.8	97.4	98.0	97.3	97.4	87.3
Mag	2.4	57.7	2.0	2.0	1.6	2.3	2.0	8.7
Sid	0.5	35.6	0.2	0.6	0.4	0.4	0.6	4.0

Slide Point	D25 8	D25 10	H23 9	K19 1	K19 5
CO ₂	43.8	61.8	47.3	52.3	48.6
CaO	55.0	18.6	50.8	46.5	50.3
MgO	0.8	9.5	1.5	0.7	0.9
FeO	0.4	10.0	0.3	0.5	0.2
MnO	0.0	0.0	0.0	0.0	0.0
Total	100.0	100.0	100.0	100.0	100.0
C	0.3	0.4	0.3	0.4	0.4
Ca	0.3	0.1	0.3	0.3	0.3
Mg	0.0	0.1	0.0	0.0	0.0
Fe	0.0	0.0	0.0	0.0	0.0
Mn	0.0	0.0	0.0	0.0	0.0
Total	0.7	0.6	0.7	0.6	0.6
Cal	97.5	46.9	95.5	97.2	97.3
Mag	2.1	33.3	4.0	2.1	2.4
Sid	0.5	19.7	0.5	0.8	0.3

Table 22. NWA 14904 Carbonate Vesicle Compositions

Slides Point	J19 18	J19 19	J19 7	L21 2	K2 2	F15 8	K2 8	L21 1
CO ₂	5.10	6.45	11.71	29.04	46.06	28.68	51.88	41.45
CaO	0.31	0.28	4.93	3.71	3.81	5.54	29.11	5.02
MgO	35.71	36.77	19.36	10.75	16.57	12.85	1.29	9.22
FeO	23.01	21.61	20.86	24.95	15.34	6.33	1.25	15.11
Al ₂ O ₃	0.29	0.31	5.35	1.19	0.79	8.09	2.76	0.98
SiO ₂	35.58	34.56	37.79	30.36	17.43	38.52	13.71	28.22
Total	100.00	100.00	100.00	100.00	100.00	100.00	100.00	100.00
C	0.04	0.05	0.09	0.22	0.31	0.20	0.34	0.28
Ca	0.00	0.00	0.03	0.02	0.02	0.03	0.15	0.03
Mg	0.34	0.34	0.17	0.09	0.12	0.10	0.01	0.07
Fe	0.12	0.11	0.10	0.11	0.06	0.03	0.01	0.06
Al	0.00	0.00	0.04	0.01	0.00	0.05	0.02	0.01
Si	0.22	0.22	0.22	0.17	0.09	0.19	0.07	0.14
Total	0.73	0.73	0.66	0.61	0.60	0.59	0.59	0.58
Cal	0.46	0.42	10.23	9.72	9.83	19.54	91.29	16.94
Mag	73.11	74.90	55.97	39.20	59.34	63.03	5.66	43.29
Sid	26.44	24.69	33.80	51.08	30.82	17.43	3.05	39.77

Slides Point	L21 6	K2 4	F15 20	I21 14	I21 20	C26 3	I21 16	F15 17
CO ₂	50.77	7.41	49.49	16.83	14.44	47.62	24.33	50.61
CaO	2.35	11.18	14.53	11.18	10.62	22.23	6.31	9.30
MgO	12.98	0.21	6.59	0.19	0.12	1.16	3.32	9.00
FeO	13.05	0.68	5.65	0.34	0.44	1.01	3.33	5.52
Al ₂ O ₃	1.10	26.64	2.09	27.00	25.92	4.13	21.56	0.75
SiO ₂	19.75	53.88	21.65	44.46	48.46	23.86	41.17	24.82
Total	100.00	100.00	100.00	100.00	100.00	100.00	100.00	100.00
C	0.33	0.05	0.32	0.12	0.10	0.31	0.16	0.32
Ca	0.01	0.06	0.07	0.06	0.06	0.11	0.03	0.05
Mg	0.09	0.00	0.05	0.00	0.00	0.01	0.02	0.06
Fe	0.05	0.00	0.02	0.00	0.00	0.00	0.01	0.02
Al	0.01	0.17	0.01	0.16	0.16	0.02	0.13	0.00
Si	0.09	0.29	0.10	0.23	0.25	0.11	0.20	0.11
Total	0.58	0.58	0.57	0.57	0.57	0.57	0.57	0.57
Cal	7.66	93.13	51.69	95.49	95.44	90.22	46.73	35.58
Mag	59.03	2.49	32.61	2.18	1.47	6.57	34.08	47.91
Sid	33.31	4.39	15.70	2.33	3.09	3.21	19.19	16.51

Slides Point	C26 12	F15 22	F15 18	J19 2	F15 12	I21 4	F15 4	J19 12
CO ₂	62.45	55.40	43.70	57.28	54.29	60.13	56.69	59.43
CaO	17.14	8.37	5.91	9.78	9.19	10.05	9.38	9.63
MgO	3.48	7.24	7.22	6.94	6.80	4.80	6.24	6.08
FeO	3.52	7.55	6.10	5.73	6.19	8.37	6.14	6.19
Al ₂ O ₃	1.40	0.74	5.01	0.60	0.81	0.97	0.84	0.82
SiO ₂	12.02	20.70	32.07	19.67	22.74	15.68	20.71	17.83
Total	100.00	100.00	100.00	100.00	100.00	100.00	100.00	100.00
C	0.38	0.34	0.28	0.35	0.34	0.37	0.35	0.36
Ca	0.08	0.04	0.03	0.05	0.04	0.05	0.05	0.05
Mg	0.02	0.05	0.05	0.05	0.05	0.03	0.04	0.04
Fe	0.01	0.03	0.02	0.02	0.02	0.03	0.02	0.02
Al	0.01	0.00	0.03	0.00	0.00	0.01	0.00	0.00
Si	0.05	0.09	0.15	0.09	0.10	0.07	0.09	0.08
Total	0.56	0.56	0.56	0.56	0.56	0.56	0.56	0.56
Cal	69.31	34.43	28.50	40.92	39.14	43.23	41.02	42.02
Mag	19.56	41.35	48.50	40.40	40.28	28.70	38.02	36.92
Sid	11.13	24.22	23.00	18.68	20.58	28.07	20.96	21.06

Slides Point	L21 13	C26 4	K2 5	J19 17	J19 3	J19 15	F15 14	J19 14
CO ₂	58.25	61.88	49.75	57.14	56.41	61.72	61.89	56.18
CaO	9.91	15.05	5.75	10.83	9.39	7.79	7.48	11.42
MgO	5.96	3.41	8.28	5.22	5.67	7.08	6.69	4.79
FeO	6.06	4.24	6.12	5.90	6.23	6.10	6.61	4.57
Al ₂ O ₃	0.57	0.52	1.47	0.61	1.15	0.59	1.16	0.57
SiO ₂	19.25	14.90	28.64	20.31	21.15	16.73	16.17	22.47
Total	100.00	100.00	100.00	100.00	100.00	100.00	100.00	100.00
C	0.36	0.38	0.31	0.35	0.35	0.37	0.37	0.34
Ca	0.05	0.07	0.03	0.05	0.05	0.04	0.04	0.06
Mg	0.04	0.02	0.06	0.04	0.04	0.05	0.04	0.03
Fe	0.02	0.02	0.02	0.02	0.02	0.02	0.02	0.02
Al	0.00	0.00	0.01	0.00	0.01	0.00	0.01	0.00
Si	0.09	0.07	0.13	0.09	0.10	0.07	0.07	0.10
Total	0.56	0.56	0.56	0.56	0.55	0.55	0.55	0.55
Cal	43.23	65.19	26.12	47.71	42.42	34.72	34.11	52.73
Mag	36.15	20.49	52.23	31.99	35.58	43.99	42.42	30.78
Sid	20.62	14.32	21.65	20.29	22.00	21.29	23.48	16.49

Slides Point	J19 9	F15 3	I21 6	L21 10	L21 9	J19 20	F15 21	L21 3
CO ₂	59.45	58.60	63.26	58.79	60.62	57.94	60.77	61.70
CaO	6.24	9.46	8.11	6.00	10.53	9.50	10.86	9.56
MgO	7.07	5.93	7.66	7.40	4.93	4.79	4.75	5.33
FeO	7.05	5.12	4.30	6.66	5.00	4.82	4.63	5.29
Al ₂ O ₃	0.99	0.68	0.54	0.65	0.60	2.50	0.56	0.48
SiO ₂	19.19	20.22	16.13	20.51	18.32	20.45	18.44	17.64
Total	100.00	100.00	100.00	100.00	100.00	100.00	100.00	100.00
C	0.36	0.36	0.38	0.36	0.37	0.35	0.37	0.37
Ca	0.03	0.05	0.04	0.03	0.05	0.05	0.05	0.05
Mg	0.05	0.04	0.05	0.05	0.03	0.03	0.03	0.04
Fe	0.03	0.02	0.02	0.02	0.02	0.02	0.02	0.02
Al	0.01	0.00	0.00	0.00	0.00	0.01	0.00	0.00
Si	0.09	0.09	0.07	0.09	0.08	0.09	0.08	0.08
Total	0.55	0.55	0.55	0.55	0.55	0.55	0.55	0.55
Cal	28.98	43.62	36.66	27.91	49.45	47.73	51.50	45.28
Mag	45.56	38.01	48.21	47.89	32.21	33.40	31.36	35.14
Sid	25.46	18.38	15.13	24.19	18.33	18.86	17.13	19.58

Slides Point	I21 12	J19 1	I21 19	J19 8	L21 14	I21 7	I21 11	F15 13
CO ₂	63.44	62.94	64.56	64.06	62.37	64.20	65.23	60.30
CaO	9.94	8.13	12.07	8.01	9.86	10.95	9.53	6.73
MgO	5.58	5.39	4.17	5.61	5.10	4.70	4.82	6.10
FeO	4.09	6.52	3.62	5.71	4.70	3.93	5.36	5.77
Al ₂ O ₃	0.61	0.57	0.63	1.26	0.51	0.68	0.59	1.21
SiO ₂	16.34	16.45	14.95	15.35	17.47	15.54	14.48	19.88
Total	100.00	100.00	100.00	100.00	100.00	100.00	100.00	100.00
C	0.38	0.38	0.38	0.38	0.37	0.38	0.39	0.36
Ca	0.05	0.04	0.06	0.04	0.05	0.05	0.04	0.03
Mg	0.04	0.04	0.03	0.04	0.03	0.03	0.03	0.04
Fe	0.01	0.02	0.01	0.02	0.02	0.01	0.02	0.02
Al	0.00	0.00	0.00	0.01	0.00	0.00	0.00	0.01
Si	0.07	0.07	0.07	0.07	0.08	0.07	0.06	0.09
Total	0.55	0.55	0.55	0.55	0.55	0.55	0.55	0.55
Cal	47.59	39.26	58.32	39.53	47.83	53.28	46.69	34.12
Mag	37.15	36.18	28.02	38.48	34.40	31.80	32.81	43.06
Sid	15.25	24.56	13.65	21.99	17.77	14.91	20.50	22.82

Slides Point	J19 10	L21 12	I21 10	L21 11	F15 1	F15 9	J19 6	I21 17
CO ₂	60.01	61.20	57.31	62.02	60.91	62.08	61.57	41.88
CaO	6.49	8.78	6.21	6.99	8.57	9.09	6.65	2.62
MgO	5.80	5.06	5.44	6.04	4.49	4.95	6.06	0.26
FeO	6.52	5.36	5.18	5.35	5.67	4.49	5.61	0.47
Al ₂ O ₃	1.24	0.64	4.15	0.70	0.96	0.83	0.66	28.36
SiO ₂	19.94	18.96	21.72	18.89	19.41	18.56	19.45	26.41
Total	100.00	100.00	100.00	100.00	100.00	100.00	100.00	100.00
C	0.36	0.37	0.35	0.37	0.37	0.37	0.37	0.26
Ca	0.03	0.04	0.03	0.03	0.04	0.04	0.03	0.01
Mg	0.04	0.03	0.04	0.04	0.03	0.03	0.04	0.00
Fe	0.02	0.02	0.02	0.02	0.02	0.02	0.02	0.00
Al	0.01	0.00	0.02	0.00	0.01	0.00	0.00	0.15
Si	0.09	0.08	0.10	0.08	0.09	0.08	0.08	0.12
Total	0.55	0.55	0.55	0.55	0.55	0.55	0.55	0.55
Cal	33.01	43.89	34.83	35.74	44.54	46.65	34.18	77.91
Mag	41.10	35.18	42.54	42.95	32.41	35.35	43.30	11.04
Sid	25.89	20.94	22.63	21.31	23.04	18.00	22.53	11.04

Slides Point	I21 15	J19 5	L21 4	F15 2	J19 13	L21 5	I21 3	J19 4
CO ₂	65.14	60.52	62.46	63.97	64.16	69.11	65.91	54.00
CaO	7.10	8.23	5.13	8.18	10.82	3.96	10.39	9.07
MgO	6.27	5.05	6.87	4.98	3.42	6.67	3.94	3.99
FeO	4.64	4.51	5.67	4.90	4.30	7.87	3.87	4.60
Al ₂ O ₃	0.59	1.05	0.48	0.64	0.48	0.46	0.63	0.53
SiO ₂	16.25	20.64	19.39	17.33	16.83	11.94	15.26	27.82
Total	100.00	100.00	100.00	100.00	100.00	100.00	100.00	100.00
C	0.38	0.36	0.37	0.38	0.38	0.40	0.39	0.33
Ca	0.03	0.04	0.02	0.04	0.05	0.02	0.05	0.04
Mg	0.04	0.03	0.04	0.03	0.02	0.04	0.03	0.03
Fe	0.02	0.02	0.02	0.02	0.02	0.03	0.01	0.02
Al	0.00	0.01	0.00	0.00	0.00	0.00	0.00	0.00
Si	0.07	0.09	0.08	0.08	0.07	0.05	0.07	0.12
Total	0.55	0.55	0.54	0.54	0.54	0.54	0.54	0.54
Cal	36.57	43.81	26.83	43.18	57.14	20.43	54.98	49.83
Mag	44.82	37.46	50.06	36.59	25.17	47.86	28.98	30.47
Sid	18.62	18.73	23.11	20.23	17.69	31.72	16.04	19.70

Slides Point	L21 7	C26 15	F15 19	F15 5	I21 1	C26 17	C26 2	L21 8
CO ₂	64.04	61.82	64.14	62.26	66.81	65.47	65.06	66.26
CaO	8.58	7.52	7.94	9.26	7.81	9.71	7.84	6.32
MgO	4.50	5.24	4.84	4.53	4.89	3.98	4.82	5.31
FeO	4.79	4.61	4.86	3.60	4.87	3.59	4.20	5.10
Al ₂ O ₃	0.59	0.60	0.56	0.62	0.78	0.49	0.85	1.16
SiO ₂	17.50	20.21	17.68	19.73	14.84	16.77	17.24	15.85
Total	100.00	100.00	100.00	100.00	100.00	100.00	100.00	100.00
C	0.38	0.37	0.38	0.37	0.39	0.38	0.38	0.39
Ca	0.04	0.04	0.04	0.04	0.04	0.04	0.04	0.03
Mg	0.03	0.03	0.03	0.03	0.03	0.03	0.03	0.03
Fe	0.02	0.02	0.02	0.01	0.02	0.01	0.02	0.02
Al	0.00	0.00	0.00	0.00	0.00	0.00	0.00	0.01
Si	0.08	0.09	0.08	0.09	0.06	0.07	0.07	0.07
Total	0.54	0.54	0.54	0.54	0.54	0.54	0.54	0.54
Cal	46.12	40.79	42.99	50.41	42.49	53.85	43.97	35.71
Mag	33.72	39.63	36.45	34.27	36.92	30.65	37.64	41.75
Sid	20.16	19.58	20.56	15.32	20.59	15.50	18.39	22.54

Slides Point	I21 2	I21 5	C26 14	C26 7	F15 11	K2 1	C26 11	K2 6
CO ₂	66.94	68.66	66.23	63.25	55.88	64.88	68.46	64.92
CaO	8.80	9.17	6.69	6.53	2.86	5.68	8.05	5.93
MgO	3.72	4.03	5.30	4.88	5.82	5.34	4.12	5.05
FeO	4.73	3.98	4.43	4.56	6.51	4.78	3.75	4.75
Al ₂ O ₃	0.81	0.68	0.62	1.14	1.23	0.58	0.90	0.76
SiO ₂	15.00	13.48	16.74	19.64	27.70	18.75	14.72	18.60
Total	100.00	100.00	100.00	100.00	100.00	100.00	100.00	100.00
C	0.39	0.40	0.39	0.37	0.34	0.38	0.40	0.38
Ca	0.04	0.04	0.03	0.03	0.01	0.03	0.04	0.03
Mg	0.02	0.03	0.03	0.03	0.04	0.03	0.03	0.03
Fe	0.02	0.01	0.02	0.02	0.02	0.02	0.01	0.02
Al	0.00	0.00	0.00	0.01	0.01	0.00	0.00	0.00
Si	0.06	0.06	0.07	0.08	0.12	0.08	0.06	0.08
Total	0.54	0.54	0.54	0.54	0.54	0.54	0.54	0.54
Cal	49.82	51.23	38.15	38.64	17.86	33.81	48.22	35.60
Mag	29.27	31.37	42.14	40.31	50.53	44.04	34.26	42.15
Sid	20.91	17.40	19.70	21.05	31.61	22.15	17.52	22.25

Slides Point	C26 10	K2 3	C26 16	C26 5	C26 13	J19 11	C26 8	C26 9
CO ₂	64.11	63.99	49.31	67.13	64.13	61.06	71.47	74.00
CaO	6.97	6.53	3.69	7.83	3.28	2.26	7.36	7.97
MgO	4.14	4.65	4.10	3.99	4.86	5.14	3.23	3.12
FeO	4.47	3.92	2.56	3.40	5.38	5.21	3.57	3.08
Al ₂ O ₃	0.81	0.69	8.13	0.55	1.20	2.16	0.41	0.43
SiO ₂	19.50	20.22	32.22	17.11	21.15	24.17	13.96	11.40
Total	100.00	100.00	100.00	100.00	100.00	100.00	100.00	100.00
C	0.38	0.37	0.30	0.39	0.37	0.36	0.41	0.42
Ca	0.03	0.03	0.02	0.04	0.01	0.01	0.03	0.04
Mg	0.03	0.03	0.03	0.03	0.03	0.03	0.02	0.02
Fe	0.02	0.01	0.01	0.01	0.02	0.02	0.01	0.01
Al	0.00	0.00	0.04	0.00	0.01	0.01	0.00	0.00
Si	0.08	0.09	0.14	0.07	0.09	0.10	0.06	0.05
Total	0.54	0.54	0.54	0.54	0.53	0.53	0.53	0.53
Cal	42.97	40.71	32.35	48.83	22.92	16.77	50.23	54.13
Mag	35.48	40.30	50.09	34.71	47.54	53.06	30.69	29.51
Sid	21.55	19.00	17.56	16.46	29.54	30.16	19.08	16.36

Slides Point	F15 7	C26 18	C26 6	K2 7	F15 6	F15 15	I21 9	I21 8
CO ₂	69.80	66.48	68.25	63.22	81.51	68.19	66.71	66.46
CaO	1.92	5.12	5.64	3.87	8.15	3.40	3.44	2.21
MgO	5.21	3.69	3.67	3.43	1.95	3.86	2.60	3.26
FeO	5.73	3.90	3.56	3.31	2.11	3.79	4.06	4.75
Al ₂ O ₃	1.03	0.99	0.42	2.84	0.36	0.55	2.76	2.31
SiO ₂	16.31	19.83	18.45	23.33	5.93	20.22	20.44	21.01
Total	100.00	100.00	100.00	100.00	100.00	100.00	100.00	100.00
C	0.40	0.38	0.39	0.37	0.45	0.39	0.38	0.38
Ca	0.01	0.02	0.03	0.02	0.04	0.02	0.02	0.01
Mg	0.03	0.02	0.02	0.02	0.01	0.02	0.02	0.02
Fe	0.02	0.01	0.01	0.01	0.01	0.01	0.01	0.02
Al	0.01	0.00	0.00	0.01	0.00	0.00	0.01	0.01
Si	0.07	0.08	0.08	0.10	0.02	0.08	0.09	0.09
Total	0.53	0.53	0.53	0.53	0.53	0.53	0.53	0.53
Cal	14.10	38.44	41.61	34.38	65.12	28.87	33.62	21.11
Mag	53.11	38.60	37.83	42.63	21.71	45.89	35.37	43.50
Sid	32.79	22.96	20.56	22.99	13.17	25.24	31.00	35.39

Slides Point	C26 1	J19 16	F15 16	I21 13	F15 10
CO ₂	81.73	73.99	80.23	75.20	84.36
CaO	6.32	1.76	1.23	1.66	1.06
MgO	1.69	3.19	3.90	2.14	2.86
FeO	2.75	3.61	3.40	2.95	2.30
Al ₂ O ₃	0.32	1.69	0.65	1.79	0.55
SiO ₂	7.19	15.76	10.59	16.26	8.87
Total	100.00	100.00	100.00	100.00	100.00
C	0.45	0.41	0.44	0.41	0.45
Ca	0.03	0.01	0.01	0.01	0.00
Mg	0.01	0.02	0.02	0.01	0.02
Fe	0.01	0.01	0.01	0.01	0.01
Al	0.00	0.01	0.00	0.01	0.00
Si	0.03	0.06	0.04	0.07	0.03
Total	0.52	0.52	0.52	0.52	0.51
Cal	58.41	19.59	13.13	24.00	15.44
Mag	21.77	49.11	58.33	43.00	58.25
Sid	19.83	31.30	28.54	33.00	26.32

Table 23. NWA 149404 Chromite Compositions

Slide Point	H26 2	O24 2	P21 2	H26 1	M17 1	G13 2	P21 1	E23 1
SiO ₂	0.11	0.18	0.08	0.08	0.08	0.10	0.12	0.12
TiO ₂	0.89	2.99	0.79	0.89	0.73	0.92	0.75	0.92
Al ₂ O ₃	5.61	6.38	5.06	5.47	5.13	5.77	5.06	5.31
Cr ₂ O ₃	60.18	54.97	61.69	60.13	61.55	59.58	61.94	60.09
FeO	30.51	32.51	29.24	30.17	28.92	30.19	28.66	30.20
MnO	0.59	0.61	0.53	0.58	0.67	0.57	0.56	0.67
MgO	3.00	3.34	3.50	3.16	3.37	3.34	3.41	2.66
CaO	0.03	0.02	0.00	0.02	0.00	0.00	0.00	0.02
PbO	0.16	0.12	0.00	0.29	0.16	0.16	0.08	0.45
ZnO	0.03	0.00	0.06	0.00	0.11	0.07	0.02	0.06
P ₂ O ₅	0.01	0.00	0.00	0.00	0.01	0.02	0.01	0.01
Total	101.12	101.12	100.96	100.78	100.73	100.71	100.61	100.50
Si	0.02	0.04	0.02	0.02	0.02	0.02	0.03	0.03
Ti	0.14	0.47	0.13	0.14	0.12	0.15	0.12	0.15
Al	1.40	1.58	1.26	1.37	1.28	1.44	1.26	1.34
Cr	10.06	9.14	10.30	10.10	10.31	9.98	10.37	10.16
Fe	5.40	5.72	5.17	5.36	5.13	5.35	5.08	5.40
Mn	0.11	0.11	0.09	0.10	0.12	0.10	0.10	0.12
Mg	0.95	1.05	1.10	1.00	1.06	1.06	1.08	0.85
Ca	0.01	0.00	0.00	0.00	0.00	0.00	0.00	0.01
Pb	0.01	0.01	0.00	0.02	0.01	0.01	0.00	0.03
Zn	0.01	0.00	0.01	0.00	0.02	0.01	0.00	0.01
P	0.00	0.00	0.00	0.00	0.00	0.00	0.00	0.00
Total	18.10	18.13	18.08	18.11	18.07	18.12	18.04	18.08
Recalc								
Total	3.02	3.02	3.01	3.02	3.01	3.02	3.01	3.01
Chr	61.34	57.46	62.17	61.36	62.50	60.91	62.76	61.92
Spn	5.76	6.59	6.66	6.08	6.44	6.45	6.51	5.17
Ulv	32.90	35.95	31.17	32.56	31.06	32.64	30.72	32.91

Slide Point	K24 1	C12 1	M17 2	O24 1	L6 2	H28 1	H24 1	Q26 1
SiO ₂	0.13	0.11	0.06	0.14	0.14	0.11	0.13	0.44
TiO ₂	1.45	0.93	0.78	0.96	0.92	0.86	0.83	1.14
Al ₂ O ₃	6.48	5.61	4.98	5.48	5.83	6.06	5.14	5.70
Cr ₂ O ₃	57.93	59.72	61.29	59.61	59.85	60.27	60.44	58.53
FeO	30.11	29.68	29.08	30.23	29.12	27.57	29.53	29.89
MnO	0.63	0.54	0.57	0.66	0.56	0.58	0.59	0.58
MgO	3.50	3.27	3.29	3.01	3.27	4.38	3.09	3.26
CaO	0.00	0.00	0.00	0.00	0.00	0.01	0.00	0.06
PbO	0.00	0.25	0.00	0.00	0.21	0.17	0.00	0.00
ZnO	0.10	0.09	0.12	0.10	0.17	0.07	0.10	0.10
P ₂ O ₅	0.00	0.00	0.00	0.00	0.05	0.02	0.00	0.00
Total	100.33	100.19	100.18	100.17	100.10	100.08	99.85	99.69
Si	0.03	0.02	0.01	0.03	0.03	0.02	0.03	0.09
Ti	0.23	0.15	0.12	0.15	0.15	0.14	0.13	0.18
Al	1.61	1.41	1.25	1.38	1.46	1.50	1.30	1.43
Cr	9.68	10.06	10.33	10.06	10.06	10.04	10.23	9.87
Fe	5.32	5.29	5.18	5.39	5.18	4.86	5.29	5.33
Mn	0.11	0.10	0.10	0.12	0.10	0.10	0.11	0.10
Mg	1.10	1.04	1.04	0.96	1.04	1.37	0.99	1.03
Ca	0.00	0.00	0.00	0.00	0.00	0.00	0.00	0.01
Pb	0.00	0.01	0.00	0.00	0.01	0.01	0.00	0.00
Zn	0.02	0.01	0.02	0.02	0.03	0.01	0.02	0.02
P	0.00	0.00	0.00	0.00	0.01	0.00	0.00	0.00
Total	18.10	18.09	18.07	18.10	18.05	18.06	18.08	18.07
Recalc Total	3.02	3.02	3.01	3.02	3.01	3.01	3.01	3.01
Chr	60.10	61.39	62.39	61.29	61.81	61.70	61.98	60.79
Spn	6.85	6.34	6.31	5.83	6.38	8.45	5.98	6.37
Ulv	33.05	32.27	31.30	32.88	31.81	29.85	32.04	32.84

Slide Point	G15 2	G15 1	G15 3	C9 1
SiO ₂	0.14	0.11	0.13	0.15
TiO ₂	1.04	0.83	0.81	1.38
Al ₂ O ₃	6.15	5.47	5.68	5.49
Cr ₂ O ₃	59.34	60.18	59.40	58.34
FeO	28.32	27.96	28.50	29.68
MnO	0.54	0.55	0.61	0.59
MgO	3.86	3.99	3.80	3.22
CaO	0.02	0.00	0.08	0.01
PbO	0.00	0.00	0.00	0.12
ZnO	0.12	0.06	0.07	0.09
P ₂ O ₅	0.01	0.04	0.00	0.00
Total	99.52	99.20	99.08	99.08
Si	0.03	0.02	0.03	0.03
Ti	0.17	0.13	0.13	0.22
Al	1.54	1.38	1.43	1.39
Cr	9.96	10.16	10.05	9.93
Fe	5.03	4.99	5.10	5.34
Mn	0.10	0.10	0.11	0.11
Mg	1.22	1.27	1.21	1.03
Ca	0.00	0.00	0.02	0.00
Pb	0.00	0.00	0.00	0.01
Zn	0.02	0.01	0.01	0.01
P	0.00	0.01	0.00	0.00
Total	18.05	18.07	18.10	18.08
Recalc Total	3.01	3.01	3.02	3.01
Chr	61.45	61.87	61.42	60.89
Spn	7.53	7.73	7.42	6.34
Ulv	31.02	30.40	31.17	32.77

Table 24. NWA 14904 Ilmenite Compositions

Slide Point	E7 1	F13 1	L14 1	H8 1	F28 1	K8 1	I12 1
SiO ₂	0.07	0.06	0.03	0.05	0.09	0.04	0.02
TiO ₂	53.90	54.34	53.52	53.12	52.87	53.45	53.09
Al ₂ O ₃	0.03	0.04	0.06	0.09	0.05	0.10	0.02
Cr ₂ O ₃	0.75	0.90	0.91	1.13	1.36	1.02	0.93
FeO	40.28	40.04	40.89	41.06	40.92	39.98	40.08
MnO	0.71	0.72	0.74	0.66	0.75	0.66	0.71
MgO	4.29	4.41	3.85	3.82	3.79	3.91	4.30
CaO	0.13	0.05	0.15	0.22	0.04	0.11	0.01
PbO	0.69	0.00	0.28	0.00	0.00	0.00	0.00
ZnO	0.07	0.06	0.00	0.06	0.05	0.02	0.04
P ₂ O ₅	0.02	0.08	0.01	0.02	0.05	0.01	0.02
Total	100.92	100.69	100.42	100.23	99.96	99.32	99.21
Si	0.01	0.01	0.01	0.01	0.02	0.01	0.00
Ti	7.89	7.92	7.88	7.83	7.82	7.92	7.88
Al	0.01	0.01	0.01	0.02	0.01	0.02	0.00
Cr	0.12	0.14	0.14	0.18	0.21	0.16	0.14
Fe	6.56	6.49	6.70	6.73	6.73	6.59	6.61
Mn	0.12	0.12	0.12	0.11	0.13	0.11	0.12
Mg	1.25	1.27	1.12	1.12	1.11	1.15	1.26
Ca	0.03	0.01	0.03	0.05	0.01	0.02	0.00
Pb	0.04	0.00	0.01	0.00	0.00	0.00	0.00
Zn	0.01	0.01	0.00	0.01	0.01	0.00	0.01
P	0.00	0.01	0.00	0.00	0.01	0.00	0.00
Total	16.03	15.98	16.03	16.06	16.04	15.98	16.04
Recalc Total	2.00	2.00	2.00	2.01	2.01	2.00	2.00
Chr	1.45	1.75	1.76	2.19	2.62	2.01	1.80
Spn	15.72	16.11	14.11	13.92	13.80	14.56	15.76
Ulv	82.83	82.13	84.13	83.90	83.58	83.43	82.44

Table 25. NWA 14904 Merrillite Compositions

Slide Point	R17 2	R17 1	M8 5	E13 5	D7 1	E13 3	M8 1	H8 1
Al ₂ O ₃	0.00	0.01	0.02	0.04	0.00	0.01	0.00	0.00
SiO ₂	0.00	0.00	0.00	0.04	0.03	0.02	0.01	0.00
P ₂ O ₅	46.60	46.74	46.31	46.00	46.71	45.70	46.33	46.06
Ce ₂ O ₃	0.00	0.00	0.07	0.00	0.00	0.00	0.00	0.00
Cl	0.02	0.00	0.01	0.00	0.00	0.00	0.00	0.00
MgO	2.52	2.66	2.61	2.69	2.49	2.48	2.57	2.53
Na ₂ O	1.31	1.42	1.50	1.57	1.58	1.23	1.45	1.53
CaO	49.65	49.45	49.72	49.65	49.24	49.35	49.36	49.61
TiO ₂	0.04	0.01	0.00	0.00	0.01	0.00	0.00	0.00
K ₂ O	0.02	0.02	0.05	0.02	0.02	0.02	0.04	0.03
FeO	1.03	0.65	0.56	0.82	0.72	1.52	0.67	0.60
Cr ₂ O ₃	0.00	0.00	0.01	0.01	0.00	0.02	0.01	0.00
MnO	0.05	0.01	0.03	0.04	0.05	0.09	0.00	0.04
Total	101.24	100.99	100.88	100.87	100.85	100.44	100.44	100.40
Al	0.00	0.00	0.00	0.01	0.00	0.00	0.00	0.00
Si	0.00	0.00	0.00	0.01	0.00	0.00	0.00	0.00
P	6.00	6.02	5.98	5.95	6.02	5.95	6.00	5.98
Ce	0.00	0.00	0.00	0.00	0.00	0.00	0.00	0.00
Cl	0.01	0.00	0.00	0.00	0.00	0.00	0.00	0.00
Mg	0.57	0.60	0.59	0.61	0.57	0.57	0.59	0.58
Na	0.38	0.42	0.44	0.46	0.47	0.37	0.43	0.45
Ca	8.09	8.05	8.13	8.13	8.03	8.14	8.09	8.15
Ti	0.00	0.00	0.00	0.00	0.00	0.00	0.00	0.00
K	0.00	0.00	0.01	0.00	0.00	0.00	0.01	0.01
Fe	0.13	0.08	0.07	0.10	0.09	0.20	0.09	0.08
Cr	0.00	0.00	0.00	0.00	0.00	0.00	0.00	0.00
Mn	0.01	0.00	0.00	0.01	0.01	0.01	0.00	0.01
Total	15.20	15.19	15.25	15.29	15.20	15.25	15.21	15.26
Recal								
Total	17.72	17.71	17.78	17.84	17.73	17.79	17.74	17.80

Slide Point	O12 3	E13 1	E9 1	R17 3	O12 1	H8 2	E13 2	D7 4
Al ₂ O ₃	0.01	0.00	0.09	0.02	0.03	0.13	0.01	0.04
SiO ₂	0.00	0.00	0.47	0.00	0.02	0.19	0.04	0.00
P ₂ O ₅	46.04	45.80	45.95	45.50	45.73	45.29	45.84	46.35
Ce ₂ O ₃	0.03	0.18	0.12	0.00	0.03	0.07	0.04	0.00
Cl	0.01	0.01	0.00	0.00	0.02	0.00	0.01	0.00
MgO	2.59	2.64	2.59	2.62	2.55	2.59	2.54	2.53
Na ₂ O	1.54	1.56	1.43	1.63	1.44	1.26	1.66	1.51
CaO	49.16	49.01	48.54	49.93	49.60	49.55	49.22	48.86
TiO ₂	0.05	0.06	0.00	0.00	0.03	0.03	0.00	0.00
K ₂ O	0.02	0.02	0.01	0.03	0.03	0.04	0.02	0.05
FeO	0.87	1.01	1.09	0.57	0.81	1.00	0.78	0.73
Cr ₂ O ₃	0.00	0.00	0.02	0.00	0.00	0.01	0.01	0.01
MnO	0.04	0.05	0.02	0.02	0.04	0.07	0.03	0.02
Total	100.35	100.34	100.33	100.32	100.31	100.22	100.19	100.10
Al	0.00	0.00	0.02	0.00	0.01	0.02	0.00	0.01
Si	0.00	0.00	0.07	0.00	0.00	0.03	0.01	0.00
P	5.98	5.97	5.96	5.93	5.96	5.91	5.97	6.02
Ce	0.00	0.01	0.01	0.00	0.00	0.00	0.00	0.00
Cl	0.00	0.00	0.00	0.00	0.00	0.00	0.00	0.00
Mg	0.59	0.61	0.59	0.60	0.58	0.59	0.58	0.58
Na	0.46	0.47	0.42	0.49	0.43	0.38	0.50	0.45
Ca	8.09	8.08	7.97	8.24	8.18	8.19	8.12	8.03
Ti	0.01	0.01	0.00	0.00	0.00	0.00	0.00	0.00
K	0.00	0.00	0.00	0.01	0.01	0.01	0.00	0.01
Fe	0.11	0.13	0.14	0.07	0.10	0.13	0.10	0.09
Cr	0.00	0.00	0.00	0.00	0.00	0.00	0.00	0.00
Mn	0.01	0.01	0.00	0.00	0.00	0.01	0.00	0.00
Total	15.25	15.28	15.19	15.35	15.28	15.28	15.29	15.20
Recal Total	17.79	17.82	17.72	17.90	17.82	17.82	17.83	17.72

Slide Point	H8 4	E4 1	I22 1	M8 2	I22 2	H8 3	E9 2	D7 2	M8 3
Al ₂ O ₃	0.01	0.01	0.03	0.84	0.21	0.04	0.01	0.00	1.43
SiO ₂	0.00	0.00	0.02	1.27	0.47	0.11	0.01	0.00	2.40
P ₂ O ₅	45.72	45.98	45.92	44.41	45.33	45.48	45.70	45.33	43.58
Ce ₂ O ₃	0.00	0.00	0.00	0.00	0.03	0.00	0.06	0.00	0.01
Cl	0.00	0.01	0.00	0.01	0.01	0.00	0.01	0.00	0.01
MgO	2.54	2.54	2.57	2.65	2.53	2.52	2.52	2.52	2.34
Na ₂ O	1.56	1.37	1.31	1.33	1.35	1.25	1.27	1.45	1.30
CaO	49.23	49.16	48.78	48.50	48.66	49.54	48.63	48.88	47.13
TiO ₂	0.00	0.00	0.00	0.02	0.00	0.00	0.00	0.00	0.00
K ₂ O	0.02	0.02	0.02	0.02	0.06	0.04	0.00	0.03	0.04
FeO	0.86	0.84	1.23	0.57	0.91	0.59	1.25	0.87	0.71
Cr ₂ O ₃	0.00	0.00	0.02	0.00	0.00	0.02	0.04	0.01	0.00
MnO	0.03	0.05	0.06	0.05	0.07	0.02	0.07	0.05	0.01
Total	99.99	99.99	99.95	99.67	99.63	99.62	99.56	99.14	98.96
Al	0.00	0.00	0.01	0.15	0.04	0.01	0.00	0.00	0.26
Si	0.00	0.00	0.00	0.20	0.07	0.02	0.00	0.00	0.37
P	5.97	5.99	5.99	5.79	5.93	5.96	5.99	5.97	5.70
Ce	0.00	0.00	0.00	0.00	0.00	0.00	0.00	0.00	0.00
Cl	0.00	0.00	0.00	0.00	0.00	0.00	0.00	0.00	0.00
Mg	0.58	0.58	0.59	0.61	0.58	0.58	0.58	0.58	0.54
Na	0.47	0.41	0.39	0.40	0.40	0.38	0.38	0.44	0.39
Ca	8.13	8.11	8.05	8.01	8.06	8.21	8.07	8.15	7.80
Ti	0.00	0.00	0.00	0.00	0.00	0.00	0.00	0.00	0.00
K	0.00	0.00	0.00	0.00	0.01	0.01	0.00	0.01	0.01
Fe	0.11	0.11	0.16	0.07	0.12	0.08	0.16	0.11	0.09
Cr	0.00	0.00	0.00	0.00	0.00	0.00	0.01	0.00	0.00
Mn	0.00	0.01	0.01	0.01	0.01	0.00	0.01	0.01	0.00
Total	15.28	15.22	15.21	15.24	15.22	15.24	15.20	15.27	15.16
Recal Total	17.82	17.75	17.74	17.78	17.75	17.77	17.73	17.81	17.67

7.2. Comparison Data Tables

Table 26. Modal Mineralogy Comparisons

vol%	NWA 14904		NWA 11065(I)	NWA 10961 (I)	ALHA 77005 (I)	NWA 11043 (E)	NWA 4468 (E)	LEW 88516 (I)	NWA 10169 (E)
Olivine	43.98	54.75	33	49	53	63	36	52	37
Low-Ca pyroxene	11.09	3.80	30	21	23	13	37	21	34
High-Ca pyroxene	15.43	19.20	16	11	8.4	15	15	9.1	12
Total pyroxene	26.52	33.00	46	32	31	28	52	30	46
Maskelynite	8.05	10.20	17	2.6	8.3	7.5	10	10	15
Phosphate	0.43	0.53	2.1	1.5	0.7	1.0	0.9	1.3	trace
Spinels	0.24	0.30	1.5	0.8	0.5	0.8	1.0	1.2	2.0
Ilmenite + Sulfides	0.20	0.26	0.2	0.1	trace	0.1	0.2	0.3	trace
Carbonates	0.99	1.23	n.a.	n.a.	n.a.	n.a.	n.a.	n.a.	n.a.
Glass	-	-	n.a.	n.a.	n.a.	n.a.	n.a.	n.a.	-
Shock melt	19.67	-	n.a.	14	n.a.	n.a.	n.a.	4.4	-

(E)= enriched | (I)= intermediate | trace=<0.01% volume | n.a.= not analyzed | - = data not available

Table 27. Bulk Composition Comparisons

wt%	NWA 14904		NWA 11065 (I)	NWA 10961 (I)	ALHA 77005 (I)	NWA 11043 (E)	NWA 4468 (E)	LEW 88516 (I)	NWA 10169 (E)
SiO ₂	43.84	42.59	44.40	43.7	42.4	41.9	45.5	46.0	48.0
TiO ₂	0.23	0.18	0.75	0.39	0.39	0.52	0.69	0.39	0.54
Al ₂ O ₃	2.68	2.12	4.64	2.59	2.87	3.05	5.07	3.31	4.60
Cr ₂ O ₃	0.52	0.42	0.08	0.46	0.98	0.97	n.a.	0.86	n.a.
FeO	20.74	22.39	24.3	20.5	20.1	24.6	23.4	19.0	21.6
MnO	0.45	0.47	0.49	0.43	0.45	0.50	0.51	0.49	0.50
MgO	25.91	27.30	17.4	25.4	28.2	22.8	19.5	25.0	19.3
CaO	4.86	3.90	5.92	5.17	3.16	4.75	3.61	4.20	3.97
Na ₂ O	0.50	0.40	0.81	0.37	0.47	0.22	1.03	0.56	0.96
K ₂ O	0.03	0.03	0.08	0.05	0.03	0.10	0.13	0.03	0.11
P ₂ O ₅	0.24	0.20	0.89	0.48	0.4	0.58	0.50	0.39	0.40
SO ₃	n.a.	n.a.	n.a.	n.a.	0.05	n.a.	n.a.	0.10	n.a.
Total	100.0	100.00	99.4	99.6	99.5	100.0	100.0	100.3	100.0
Mg#	55.54	54.94	56.1	68.8	71.4	62.2	59.8	70.1	61.5

(E)= enriched | (I)= intermediate | n.a.= not analyzed | b.d.= below detection

Table 28. Olivine Comparisons

*	NWA 14904		NWA 11065 (I)		NWA 10961 (I)		ALHA 77005 (I)		NWA 11043 (E)	
	avg	SD	avg	SD	avg	SD	avg	SD	avg	SD
n	62		29		56		53		23	
wt%										
SiO ₂	37.44	0.25	35.3	0.40	37.4	0.28	37.5	0.21	36.2	0.24
TiO ₂	0.01	0.02	0.03	0.03	0.03	0.03	0.02	0.01	0.03	0.02
Al ₂ O ₃	0.02	0.01	0.02	0.04	0.04	0.08	b.d	-	0.12	0.21
Cr ₂ O ₃	0.05	0.03	0.03	0.04	0.05	0.05	0.06	0.05	0.06	0.05
FeO	28.41	0.53	35.4	1.68	26.7	0.64	25.4	0.69	30.9	0.50
MnO	0.52	0.03	0.77	0.05	0.59	0.04	0.55	0.02	0.69	0.03
MgO	32.30	0.47	28.2	1.30	34.4	0.53	36.5	0.59	31.9	0.60
CaO	0.25	0.04	0.21	0.04	0.19	0.04	0.17	0.04	0.21	0.06
P ₂ O ₅	0.03	0.03	0.07	0.09	0.05	0.07	0.05	0.05	0.10	0.12
NiO	0.05	0.03	0.03	0.02	0.04	0.03	0.04	0.02	0.05	0.02
Na ₂ O	n.a.	n.a.	n.a.	n.a.	n.a.	n.a.	n.a.	n.a.	n.a.	n.a.
Total	99.10	0.37	100.1	0.52	99.4	0.44	100.3	0.42	100.2	0.052
Fo	66.94	0.71	58.7	2.23	69.7	0.79	71.9	0.84	64.8	0.61

(E)= enriched | (I)= intermediate | P= poikilitic | NP= non-poikilitic | Avg= average | SD= standard deviation | n= number of analyses | n.a.= not analyzed | b.d.= below detection | Fo= forsterite

*	NWA 4468 (E)		NWA 10618 (E)		LEW 88516 (I)		NWA 10169 (E)	
	avg	SD	avg	SD	avg	SD	avg	SD
<i>n</i>	84		53		30		60	
<i>wt%</i>								
SiO ₂	36.2	0.33	35.8	0.35	36.7	0.31	36.72	0.64
TiO ₂	0.03	0.02	0.03	0.02	0.06	0.09	0.02	0.02
Al ₂ O ₃	0.02	0.02	0.05	0.14	0.04	0.09	0.03	0.02
Cr ₂ O ₃	b.d.	-	0.04	0.04	0.04	0.04	0.02	0.07
FeO	34.1	0.79	33.0	0.84	30.0	0.83	34.57	1.03
MnO	0.71	0.03	0.69	0.02	0.63	0.04	0.63	0.05
MgO	28.8	0.74	29.8	0.62	31.6	0.85	31.21	1.01
CaO	0.19	0.04	0.18	0.05	0.24	0.16	0.17	0.09
P ₂ O ₅	n.a.	-	0.09	0.12	0.08	0.10	0.03	0.06
NiO	0.03	0.02	0.05	0.02	0.05	0.02	0.06	0.02
Na ₂ O	n.a.	n.a.	n.a.	n.a.	n.a.	n.a.	0.01	0.02
Total	100.1	0.45	99.7	0.61	99.5	0.47	100.9	0.45
Fo	60.0	1.14	61.7	1.01	65.3	1.12	59.5	1.45

(E)= enriched | (I)= intermediate | P= poikilitic | NP= non-poikilitic | Avg= average | SD= standard deviation | *n*= number of analyses | n.a.= not analyzed | b.d.= below detection | Fo= forsterite | *all compositions shown are for non-poikilitic olivine

Table 29. Pyroxene Comparisons

	NWA 14904								NWA11065 (I)								
	Low-Ca Pyroxene				High-Ca pyroxene				Low-Ca Pyroxene				High-Ca pyroxene				
	P	SD	NP	SD	P	SD	NP		SD	P	SD	NP	SD	P	SD	NP	SD
n	22		12		15		35		30		18		15		9		
wt%																	
SiO ₂	54.16	0.59	53.18	0.33	51.85	0.53	52.35	0.48	53.2	0.72	51.9	0.73	51.9	0.77	51.8	0.43	
TiO ₂	0.13	0.07	0.29	0.15	0.39	0.12	0.31	0.14	0.17	0.06	0.48	0.19	0.36	0.14	0.41	0.11	
Al ₂ O ₃	0.58	0.23	1.04	0.15	1.81	0.46	1.45	0.46	0.75	0.16	1.07	0.28	1.69	0.56	1.83	0.32	
Cr ₂ O ₃	0.51	0.09	0.49	0.08	0.91	0.13	0.81	0.11	0.44	0.09	0.33	0.12	0.74	0.11	0.78	0.15	
FeO	13.69	0.52	14.35	0.88	9.12	0.52	9.87	0.56	17.6	1.34	20.0	1.65	12.3	0.72	12.8	1.38	
MnO	0.49	0.06	0.53	0.02	0.38	0.05	0.41	0.05	0.64	0.07	0.71	0.10	0.46	0.07	0.50	0.06	
MgO	25.68	1.81	23.05	0.78	17.29	0.53	18.41	0.67	23.1	1.67	19.0	1.08	16.7	0.84	16.6	0.92	
CaO	3.43	1.80	5.83	1.20	16.84	0.89	15.05	0.93	4.03	1.39	6.46	1.62	15.1	1.31	15.0	1.93	
Na ₂ O	0.06	0.03	0.08	0.03	0.22	0.03	0.21	0.04	0.07	0.03	0.10	0.04	0.16	0.04	0.20	0.03	
Total	98.74	0.21	98.84	0.28	9.80	0.22	98.88	0.29	100.0	0.46	100.1	0.53	99.6	0.43	99.9	0.39	
Wo	6.92	3.73	11.88	2.47	35.08	1.85	31.12	2.09	8.09	2.86	13.3	3.36	31.5	2.89	31.2	4.15	
En	71.63	4.27	65.31	1.90	50.09	1.29	52.94	1.50	64.4	3.94	54.4	2.94	48.5	2.06	48.0	2.32	
Fs	21.45	0.94	22.81	1.45	14.83	0.90	15.94	0.90	27.5	2.35	32.2	2.65	20.1	1.07	20.7	2.19	
Mg#	77		74		77		77		70	2.8	63	2.6	71	0.8	70	54.0	

(E)= enriched | (I)= intermediate | P= poikilitic | NP= non-poikilitic | Avg= average | SD= standard deviation | n= number of analyses | n.a.= not analyzed | b.d.= below detection | Wo= wollastonite | En= enstatite | Fs= ferrosillite

	NWA 10961 (I)								ALHA77005 (I)							
	Low-Ca Pyroxene				High-Ca pyroxene				Low-Ca Pyroxene				High-Ca pyroxene			
	P	SD	NP	SD	P	SD	NP	SD	P	SD	NP	SD	P	SD	NP	SD
n	24		32		20		18		40		15		8		16	
wt%																
SiO ₂	54.7	0.77	54.3	0.48	53.0	0.41	52.5	0.57	55.0	0.63	53.9	0.63	52.4	0.61	52.1	0.73
TiO ₂	0.16	0.15	0.31	0.16	0.31	0.08	0.38	0.10	0.11	0.09	0.36	0.23	0.37	0.16	0.44	0.17
Al ₂ O ₃	0.87	0.52	0.94	0.24	1.62	0.44	1.99	0.40	0.49	0.19	0.94	0.25	1.68	0.64	1.88	0.54
Cr ₂ O ₃	0.47	0.09	0.44	0.12	0.80	0.06	0.84	0.07	0.47	0.08	0.43	0.11	0.87	0.06	0.88	0.09
FeO	14.0	0.81	15.2	1.26	9.48	0.51	10.1	0.62	14.1	0.41	15.5	0.90	8.95	0.56	9.21	0.59
MnO	0.49	0.05	0.54	0.05	0.41	0.10	0.41	0.05	0.49	0.04	0.57	0.04	0.37	0.03	0.39	0.03
MgO	25.6	1.83	23.6	0.70	18.1	0.74	18.1	0.83	27.4	1.49	24.0	1.07	17.7	0.74	17.5	0.66
CaO	3.79	1.93	5.10	1.25	15.8	1.17	15.2	1.12	2.58	1.24	4.87	0.88	17.5	0.87	17.4	1.05
Na ₂ O	0.05	0.03	0.07	0.02	0.16	0.03	0.18	0.03	0.04	0.03	0.09	0.04	0.21	0.02	0.21	0.03
Total	100.2	0.58	100.4	0.52	99.7	0.39	99.7	0.30	100.6	0.52	100.7	0.42	100.1	0.64	100.0	0.43
Wo	7.56	3.93	10.2	2.53	32.7	2.44	31.6	2.54	5.01	2.49	9.66	1.80	35.6	1.99	35.5	2.12
En	70.7	4.33	65.8	1.37	52.1	1.82	52.2	1.90	73.7	3.20	66.4	2.41	50.2	1.64	49.9	1.56
Fs	21.7	1.30	23.9	2.04	15.3	0.81	16.3	0.90	21.3	0.86	24.0	1.51	14.2	0.90	14.7	1.00
Mg#	77	1.9	73	1.7	77	0.7	76	0.8	77	1.5	73	1.6	78	1.1	77	1.1

(E)= enriched | (I)= intermediate | P= poikilitic | NP= non-poikilitic | Avg= average | SD= standard deviation | n= number of analyses | n.a.= not analyzed | b.d.= below detection | Wo= wollastonite | En= enstatite | Fs= ferrosillite

	NWA 11043 (E)								NWA 4468 (E)							
	Low-Ca Pyroxene				High-Ca pyroxene				Low-Ca Pyroxene				High-Ca pyroxene			
	P	SD	NP	SD	P	SD	NP	SD	P	SD	NP	SD	P	SD	NP	SD
n	23		22		4		20		62		17		25		5	
wt%																
SiO ₂	53.9	0.53	53.0	0.37	52.5	0.58	52.1	0.36	54.2	0.66	52.8	0.44	52.6	0.45	52.0	0.81
TiO ₂	0.13	0.04	0.42	0.14	0.38	0.18	0.41	0.13	0.18	0.18	0.55	0.24	0.32	0.14	0.69	0.14
Al ₂ O ₃	0.67	0.19	0.96	0.28	1.51	0.29	1.85	0.29	0.67	0.20	0.93	0.25	1.56	0.31	1.45	0.12
Cr ₂ O ₃	0.48	0.09	0.38	0.09	0.76	0.13	0.75	0.13	0.38	0.06	0.32	0.11	0.73	0.07	0.55	0.07
FeO	16.1	0.40	18.3	0.98	11.3	0.69	11.9	1.20	16.4	0.06	18.7	0.90	11.0	0.55	12.8	0.84
MnO	0.63	0.03	0.72	0.04	0.50	0.04	0.52	0.05	0.58	0.04	0.68	0.04	0.46	0.03	0.48	0.04
MgO	24.9	0.89	22.1	0.68	17.7	1.00	17.7	0.74	23.7	1.45	20.3	0.61	16.6	0.65	16.0	0.43
CaO	3.62	1.09	4.82	0.89	15.7	1.58	14.7	1.77	3.49	1.20	5.51	1.20	16.4	1.01	15.5	0.99
Na ₂ O	0.05	0.02	0.09	0.02	0.18	0.04	0.21	0.03	0.07	0.02	0.11	0.03	0.21	0.03	0.25	0.04
P ₂ O ₅	n.a.	n.a.	n.a.	n.a.	n.a.	n.a.	n.a.	n.a.	n.a.	n.a.	n.a.	n.a.	n.a.	n.a.	n.a.	n.a.
NiO	n.a.	n.a.	n.a.	n.a.	n.a.	n.a.	n.a.	n.a.	n.a.	n.a.	n.a.	n.a.	n.a.	n.a.	n.a.	n.a.
Total	100.5	0.57	100.7	0.45	100.7	0.46	100.2	0.51	99.6	0.49	99.8	0.48	99.8	0.33	99.4	0.53
Wo	7.14	2.17	9.70	1.85	32.0	3.28	30.2	3.67	7.10	2.51	11.4	2.48	34.1	2.13	32.4	2.20
En	68.2	2.13	61.7	1.50	50.1	2.64	50.6	2.00	67.0	3.37	58.4	1.54	48.1	1.77	46.7	1.08
Fs	24.7	0.56	28.6	1.49	17.9	1.11	19.1	1.93	25.9	1.24	30.2	1.44	17.8	0.90	20.9	1.24
Mg#	73	0.8	68	1.4	74	1.2	73	1.5	72	1.9	66	1.0	73	1.1	69	0.9

(E)= enriched | (I)= intermediate | P= poikilitic | NP= non-poikilitic | Avg= average | SD= standard deviation | n= number of analyses | n.a.= not analyzed | b.d.= below detection | Wo= wollastonite | En= enstatite | Fs= ferrosillite

	NWA 10618 (E)								NWA 10169 (E)							
	Low-Ca Pyroxene				High-Ca pyroxene				Low-Ca Pyroxene				High-Ca pyroxene			
	P	SD	NP	SD	P	SD	NP	SD	P	SD	NP	SD	P	SD	NP	SD
n	19		36		3		7		57		50		20		9	
wt%																
SiO ₂	53.2	0.57	52.5	0.41	52.1	0.56	52.0	0.57	54.22	0.71	53.08	0.69	52.84	0.53	52.32	0.60
TiO ₂	0.18	0.08	0.33	0.13	0.26	0.05	0.42	0.17	0.13	0.07	0.34	0.12	0.32	0.11	0.45	0.28
Al ₂ O ₃	0.79	0.15	0.94	0.28	1.39	0.08	1.75	0.11	0.69	0.21	0.85	0.22	1.59	0.28	1.48	0.32
Cr ₂ O ₃	0.43	0.10	0.35	0.12	0.70	-	0.75	0.07	0.38	0.06	0.30	0.09	0.71	0.10	0.62	0.12
FeO	16.8	0.73	18.5	1.28	11.4	0.71	11.3	1.25	16.85	0.71	19.37	1.00	11.06	0.88	12.13	0.73
MnO	0.59	0.03	0.64	0.04	0.44	0.03	0.45	0.04	0.49	0.07	0.54	0.09	0.39	0.05	0.36	0.07
MgO	23.5	0.92	21.3	0.58	17.6	0.27	17.3	0.59	23.00	1.30	20.28	0.81	16.10	0.63	15.99	1.03
CaO	4.16	0.97	5.07	1.03	15.4	0.59	15.5	1.66	4.14	1.40	5.03	1.07	16.44	1.25	15.51	0.92
Na ₂ O	0.07	0.02	0.10	0.03	0.21	0.02	0.23	0.04	0.06	0.03	0.10	0.04	0.20	0.03	0.22	0.06
P ₂ O ₅	n.a.	n.a.	n.a.	n.a.	n.a.	n.a.	n.a.	n.a.	0.00	0.02	0.01	0.02	0.00	0.01	0.01	0.01
NiO	n.a.	n.a.	n.a.	n.a.	n.a.	n.a.	n.a.	n.a.	0.02	0.02	0.02	0.02	0.02	0.02	0.02	0.02
Total	99.6	0.64	99.7	0.44	99.2	0.46	99.5	0.91	99.98	0.47	99.93	0.48	99.7	0.73	99.1	0.82
Wo	8.34	2.00	10.3	2.13	31.6	1.29	32.0	3.40	8.42	2.93	10.4	2.27	34.6	2.64	32.9	2.20
En	65.4	2.10	60.2	1.39	50.2	0.68	49.8	1.52	64.9	3.19	58.3	1.88	47.2	1.68	47.1	2.61
Fs	26.2	1.07	29.5	2.00	18.2	1.10	18.2	2.02	26.7	1.14	31.3	1.60	18.2	1.45	20.0	1.26

(E)= enriched | (I)= intermediate | P= poikilitic | NP= non-poikilitic | Avg= average | SD= standard deviation | n= number of analyses | n.a.= not analyzed | b.d.= below detection | Wo= wollastonite | En= enstatite | Fs= ferrosilllite

Table 30. Maskelynite Comparisons

	NWA 14904		NWA 11065 (I)		NWA 10961 (I)		NWA 11043 (E)		NWA 4468 (E)		NWA 10618 (E)		NWA 10169 (E)	
	Avg	SD	Avg	SD	Avg	SD	Avg	SD	Avg	SD	Avg	SD	Avg	SD
<i>n</i>	54		32		36		28		28		31		53	
<i>wt%</i>														
SiO ₂	55.46	0.59	53.8	0.89	54.3	0.50	54.0	0.62	55.8	1.71	54.3	0.74	56.10	3.33
TiO ₂	n.a.	n.a.	0.05	0.02	0.08	0.03	0.08	0.03	0.07	0.03	0.06	0.02	0.08	0.06
Al ₂ O ₃	27.56	0.38	29.0	0.54	28.4	0.42	29.1	0.38	27.9	1.05	28.4	0.45	27.51	2.39
FeO	n.a.	n.a.	0.49	0.08	0.34	0.07	0.52	0.10	0.46	0.11	0.47	0.06	0.50	0.10
MnO	n.a.	n.a.	n.a.	n.a.	n.a.	n.a.	n.a.	n.a.	n.a.	n.a.	n.a.	n.a.	0.01	0.02
MgO	n.a.	n.a.	0.11	0.03	0.14	0.03	0.13	0.03	0.07	0.02	0.10	0.02	0.09	0.03
CaO	10.49	0.37	11.5	0.67	10.9	0.41	11.6	0.32	10.2	1.27	10.9	0.54	9.94	1.79
Na ₂ O	5.37	0.14	4.83	0.33	5.20	0.20	4.75	0.25	5.37	0.61	4.97	0.29	5.39	0.67
K ₂ O	0.35	0.10	0.18	0.08	0.26	0.05	0.24	0.03	0.49	0.15	0.32	0.05	0.60	0.73
P ₂ O ₅	n.a.	n.a.	0.04	0.02	0.05	0.02	0.06	0.06	n.a.	n.a.	0.03	0.02	0.02	0.05
BaO	n.a.	n.a.	n.a.	n.a.	n.a.	n.a.	n.a.	n.a.	n.a.	n.a.	n.a.	n.a.	0.02	0.04
Cl	n.a.	n.a.	n.a.	n.a.	n.a.	n.a.	n.a.	n.a.	n.a.	n.a.	n.a.	n.a.	0.00	0.00
F	n.a.	n.a.	n.a.	n.a.	n.a.	n.a.	n.a.	n.a.	n.a.	n.a.	n.a.	n.a.	0.03	0.05
Total	99.23	0.34	100.0	0.66	99.6	0.32	100.5	0.56	100.4	0.35	99.7	0.47	100.3	0.65
An	50.88	1.45	59.5	3.25	52.8	1.90	56.6	1.82	49.7	6.16	53.9	2.61	48.42	8.41

(E)= enriched | (I)= intermediate | P= poikilitic | NP= non-poikilitic | Avg= average | SD= standard deviation | *n*= number of analyses | n.a.= not analyzed | b.d.= below detection | An= anorthite

Table 31. Oxide Comparisons

	NWA 14904					
	P		NP			
	Chr Avg	SD	Chr Avg	SD	Ilm Avg	SD
<i>n</i>	<i>1</i>		<i>19</i>		<i>6</i>	
<i>wt%</i>						
SiO ₂	0.44	-	0.12	0.03	0.05	0.03
TiO ₂	1.14	-	1.04	0.50	53.47	0.51
Al ₂ O ₃	5.70	-	5.59	0.43	0.05	0.03
Cr ₂ O ₃	58.53	-	59.81	1.52	1.00	0.20
Fe ₂ O ₃	n.a.	-	n.a.	n.a.	n.a.	n.a.
FeO	29.89	-	29.48	1.09	40.46	0.47
MnO	0.578	-	0.59	0.04	0.71	0.03
MgO	3.26	-	3.39	0.38	4.05	0.27
CaO	0.06	-	0.01	0.02	0.10	0.07
ZnO	0.10	-	0.08	0.04	0.04	0.02
PbO	b.d.	-	0.11	0.12	0.14	0.26
P ₂ O ₅	b.d.	-	0.01	0.01	0.03	0.02
Total	99.69	-	100.23	0.63	100.12	0.65
Chr	60.79	-	61.41	1.14	1.83	0.25
Spn	6.37	-	6.57	0.77	15.03	0.95
Ulv	32.84	-	32.03	1.35	83.14	0.81

(E)= enriched | (I)= intermediate | P= poikilitic | NP= non-poikilitic | Avg= average | SD= standard deviation | *n*= number of analyses | n.a.= not analyzed | b.d.= below detection | Chr= chromite | Spn= spinel | Ulv= ulvöspinel | Ilm= ilmenite

	NWA 11065 (I)						NWA 10961 (I)					
	P			NP			P			NP		
	Avg	SD	Chr-rich Avg	SD	Ulv-rich Avg	SD	Avg	SD	Chr-rich Avg	SD	Ulv-rich Avg	SD
<i>n</i>	8		8		8		5		11		6	
<i>wt%</i>												
SiO ₂	0.16	0.04	0.08	0.06	0.04	0.02	0.22	0.11	0.61	0.02	0.08	0.02
TiO ₂	0.93	0.17	13.7	1.00	17.2	1.24	1.00	0.14	1.20	0.36	11.2	1.08
Al ₂ O ₃	4.78	0.71	4.28	0.70	3.56	1.04	6.82	0.70	6.40	0.69	6.11	0.35
Cr ₂ O ₃	58.0	0.94	25.4	3.25	16.5	2.08	58.2	1.36	57.5	1.35	34.4	2.49
Fe ₂ O ₃	3.80	0.91	12.7	1.79	15.9	2.47	0.89	0.46	1.40	0.26	6.25	0.88
FeO	27.1	1.23	40.5	0.84	43.7	1.01	25.4	0.73	27.1	0.85	36.1	1.24
MnO	0.68	0.03	0.71	0.07	0.75	0.04	0.56	0.04	0.66	0.03	0.73	0.05
MgO	4.29	0.63	2.73	0.19	2.48	0.28	5.76	0.25	4.42	0.52	4.10	0.29
CaO	0.02	0.01	0.04	0.04	0.02	0.01	0.03	0.01	0.03	0.02	0.03	0.01
Na ₂ O	n.a.	n.a.	n.a.	n.a.	n.a.	n.a.	n.a.	n.a.	n.a.	n.a.	n.a.	n.a.
K ₂ O	n.a.	n.a.	n.a.	n.a.	n.a.	n.a.	n.a.	n.a.	n.a.	n.a.	n.a.	n.a.
NiO	n.a.	n.a.	n.a.	n.a.	n.a.	n.a.	n.a.	n.a.	n.a.	n.a.	n.a.	n.a.
Total	99.8	0.72	100.3	0.92	100.1	0.76	98.9	0.21	98.9	0.27	99.0	0.48
Chr	86.7	1.64	43.8	4.31	30.2	2.81	82.9	1.80	82.9	1.96	53.1	3.16
Sp	10.6	1.42	11.0	1.61	9.78	3.10	14.4	1.47	13.8	1.48	14.1	0.82
Ulv	2.64	0.48	45.2	4.53	60.0	3.76	2.70	0.39	3.30	0.99	32.9	3.52

(E)= enriched | (I)= intermediate | P= poikilitic | NP= non-poikilitic | Avg= average | SD= standard deviation | n= number of analyses | n.a.= not analyzed | b.d.= below detection | Chr= chromite | Spn= spinel | Ulv= ulvöspinel | Ilm= ilmenite

	NWA 11043 (E)						NWA 4468 (E)					
	P			NP			P			NP		
	Avg	SD	Chr-rich Avg	SD	Ulv-rich Avg	SD	Avg	SD	Chr-rich Avg	SD	Ulv-rich Avg	SD
<i>n</i>	14		5		19		12		3		10	
<i>wt%</i>												
SiO ₂	0.16	0.19	0.16	0.06	0.15	0.18	0.29	0.24	0.34	0.19	0.10	0.06
TiO ₂	1.47	0.49	2.68	1.47	12.9	3.01	1.39	0.56	1.16	0.27	11.4	5.21
Al ₂ O ₃	6.06	1.36	6.31	0.84	4.92	1.06	7.81	1.21	6.32	0.59	5.67	1.35
Cr ₂ O ₃	55.1	2.72	51.6	3.68	30.2	6.33	54.2	2.41	55.0	1.56	31.8	11.1
Fe ₂ O ₃	4.38	1.29	5.21	1.78	8.55	1.82	4.17	0.65	4.78	0.58	9.50	2.50
FeO	27.0	1.35	29.0	1.65	39.0	2.77	27.3	1.37	28.8	0.39	38.3	5.03
MnO	0.66	0.03	0.68	0.03	0.77	0.04	0.70	0.05	0.72	0.04	0.71	0.03
MgO	4.91	0.75	4.41	0.68	3.46	0.24	4.44	0.64	3.10	0.28	2.97	0.41
CaO	0.07	0.04	0.08	0.10	0.03	0.02	0.02	0.02	b.d.	-	b.d.	-
Na ₂ O	n.a	n.a	n.a	n.a	n.a	n.a	n.a	n.a	n.a	n.a	n.a	n.a
K ₂ O	n.a	n.a	n.a	n.a	n.a	n.a	n.a	n.a	n.a	n.a	n.a	n.a
NiO	n.a	n.a	n.a	n.a	n.a	n.a	n.a	n.a	n.a	n.a	n.a	n.a
Total	99.8	0.57	100.1	0.85	100	0.74	100.3	0.44	100.2	0.66	100.4	0.47
Chr	82.3	3.91	78.0	3.91	48.5	8.76	79.1	3.49	82.6	1.50	50.7	15.6
Sp	13.5	2.89	14.2	1.87	11.8	2.20	17.0	2.59	14.1	1.44	13.6	2.68
Ulv	4.18	1.44	7.76	4.33	39.7	10.2	3.86	1.56	3.30	0.78	35.8	18.0

(E)= enriched | (I)= intermediate | P= poikilitic | NP= non-poikilitic | Avg= average | SD= standard deviation | n= number of analyses | n.a.= not analyzed | b.d.= below detection | Chr= chromite | Spn= spinel | Ulv= ulvöspinel | Ilm= ilmenite

	NWA 10618 (E)						NWA 10169 (E)			
	P			NP			P		NP	
	Avg	SD	Chr-rich Avg	SD	Ulv-rich Avg	SD	Avg	SD	Avg	SD
<i>n</i>	19		15		13		40		33	
<i>wt%</i>										
SiO ₂	0.10	0.07	0.13	0.10	0.05	0.02	0.20	0.07	0.14	0.07
TiO ₂	3.42	3.34	1.84	1.07	13.1	3.54	1.72	2.15	10.78	5.95
Al ₂ O ₃	8.80	2.53	7.61	1.15	5.35	1.51	7.34	1.02	5.35	1.41
Cr ₂ O ₃	47.0	9.23	51.5	3.85	26.1	7.13	53.4	5.70	32.3	13.0
Fe ₂ O ₃	5.25	1.89	4.68	0.97	11.2	2.48	3.68	1.69	9.44	3.39
FeO	29.9	3.65	29.4	1.07	39.5	2.90	28.9	2.50	38.0	5.1
MnO	0.65	0.03	0.65	0.03	0.71	0.05	0.67	0.05	0.71	0.04
MgO	4.12	0.77	3.47	0.57	2.81	0.29	4.04	0.77	2.84	0.48
CaO	0.06	0.04	0.04	0.03	0.03	0.01	0.01	0.03	0.01	0.03
Na ₂ O	n.a	n.a	n.a	n.a	n.a	n.a	0.02	0.02	0.02	0.03
K ₂ O	n.a	n.a	n.a	n.a	n.a	n.a	0.00	0.00	0.00	0.00
NiO	n.a	n.a	n.a	n.a	n.a	n.a	0.03	0.02	0.04	0.03
Total	99.2	0.62	99.3	0.43	98.9	0.4	100.0	0.65	99.7	0.54
Chr	70.4	12.9	77.6	5.26	43.9	10.1	78.8	7.12	52.2	18.1
Sp	19.7	5.33	17.1	2.66	13.4	3.25	16.2	2.27	13.0	2.93
Ulv	9.97	10.0	5.29	3.13	42.7	13.1	5.0	6.64	34.80	20.10

(E)= enriched | (I)= intermediate | P= poikilitic | NP= non-poikilitic | Avg= average | SD= standard deviation | n= number of analyses | n.a.= not analyzed | b.d.= below detection | Chr= chromite | Spn= spinel | Ulv= ulvöspinel | Ilm= ilmenite

7.3. Elemental Maps

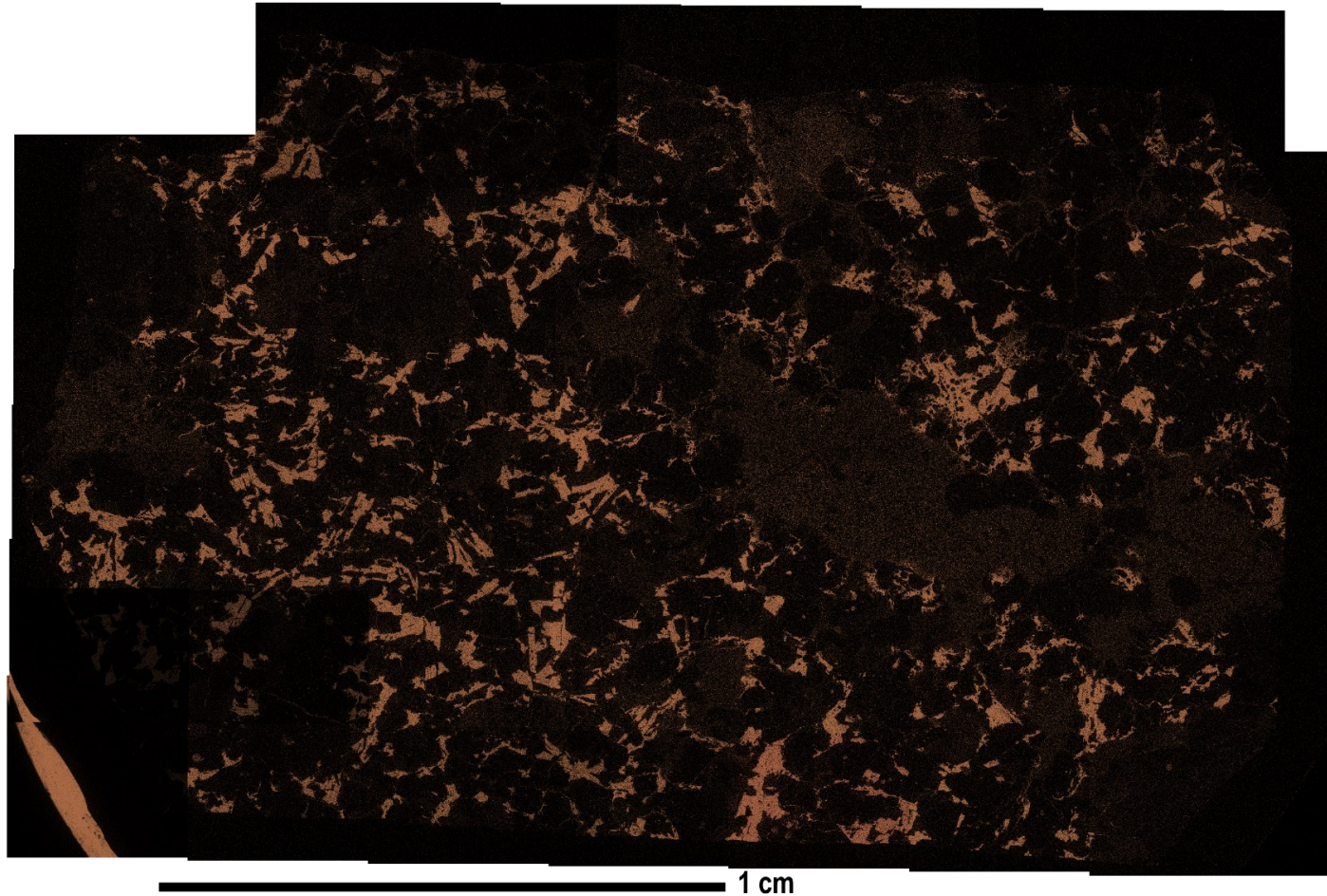


Figure 40. Al elemental map

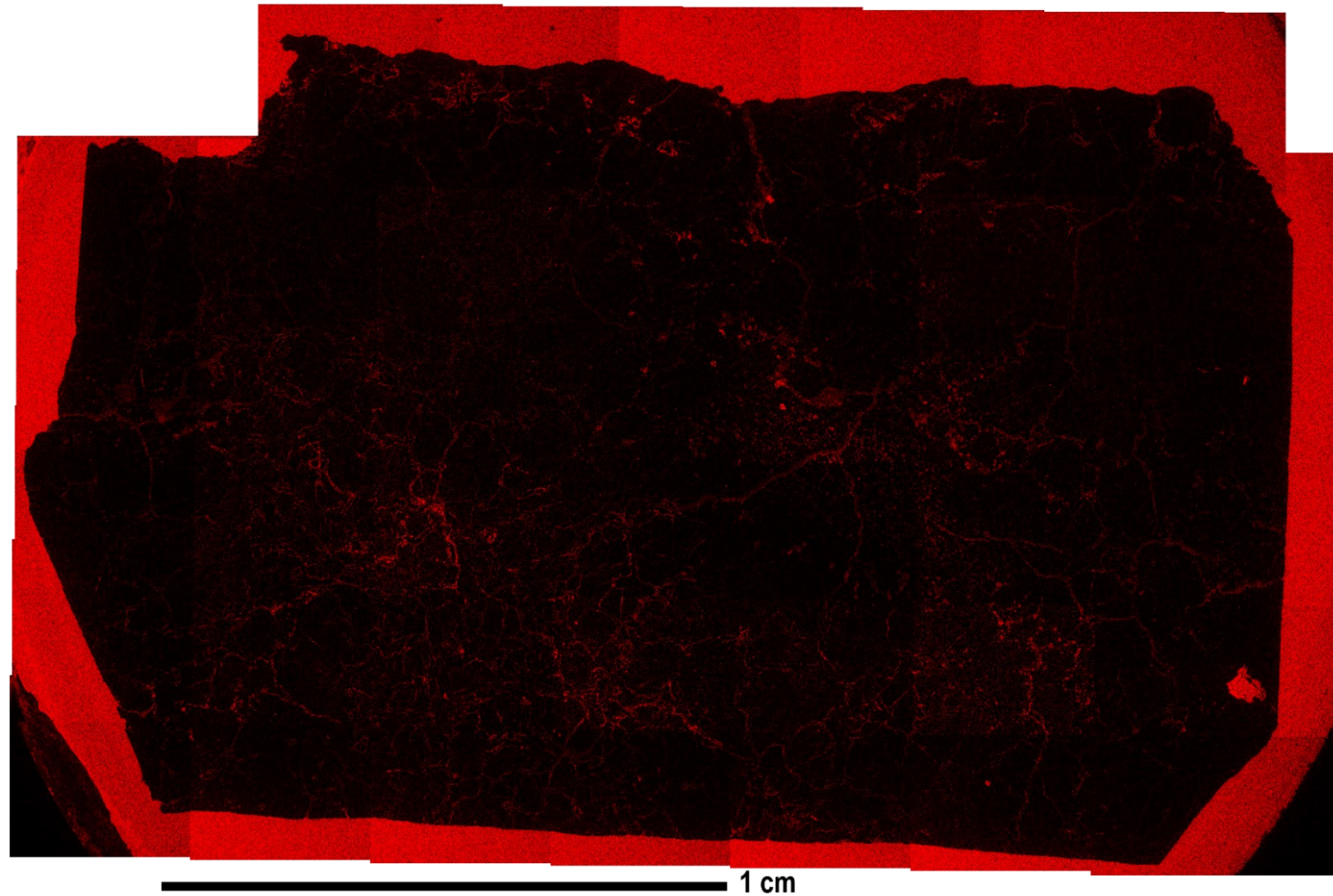


Figure 41. C elemental map

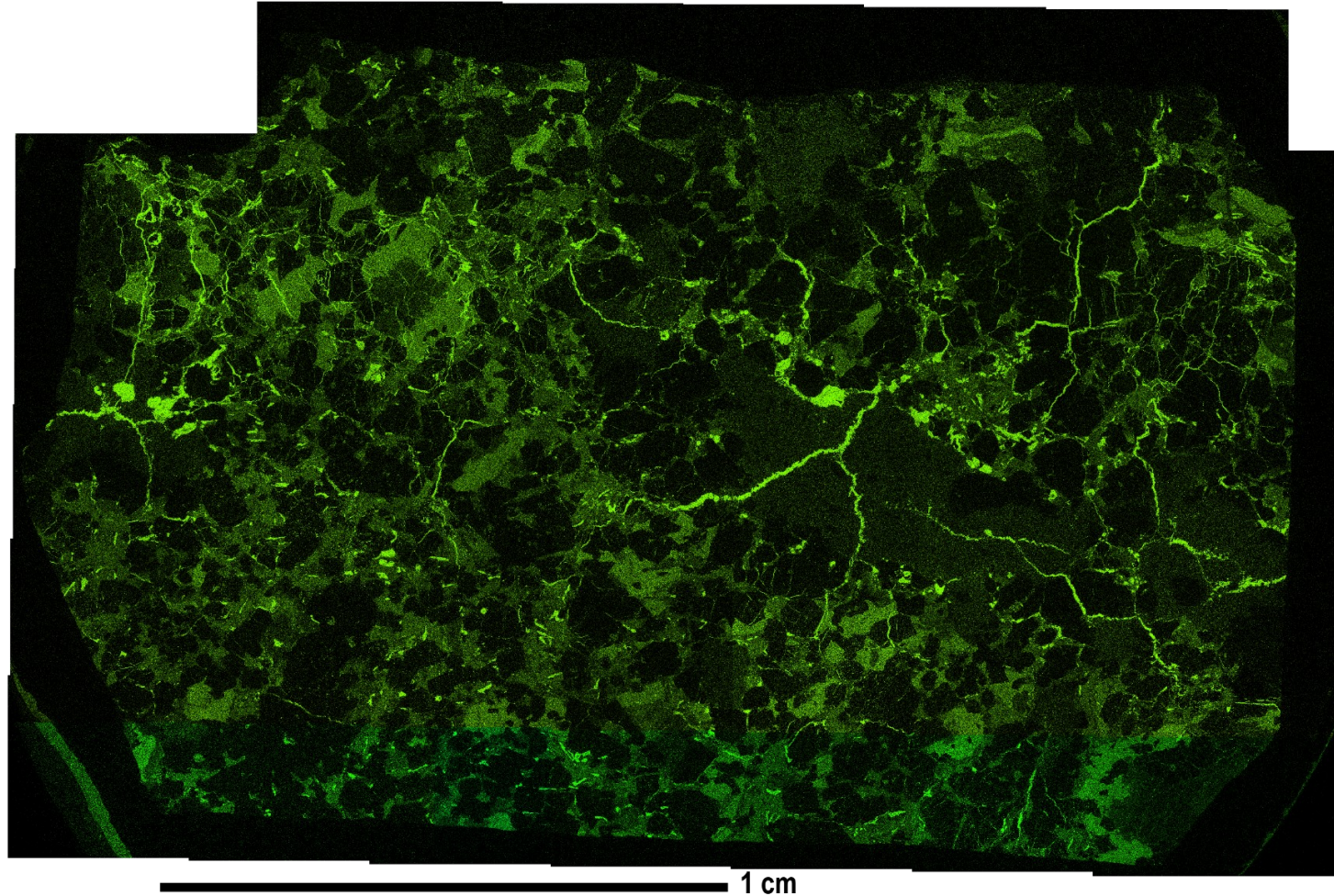


Figure 42. Ca elemental map

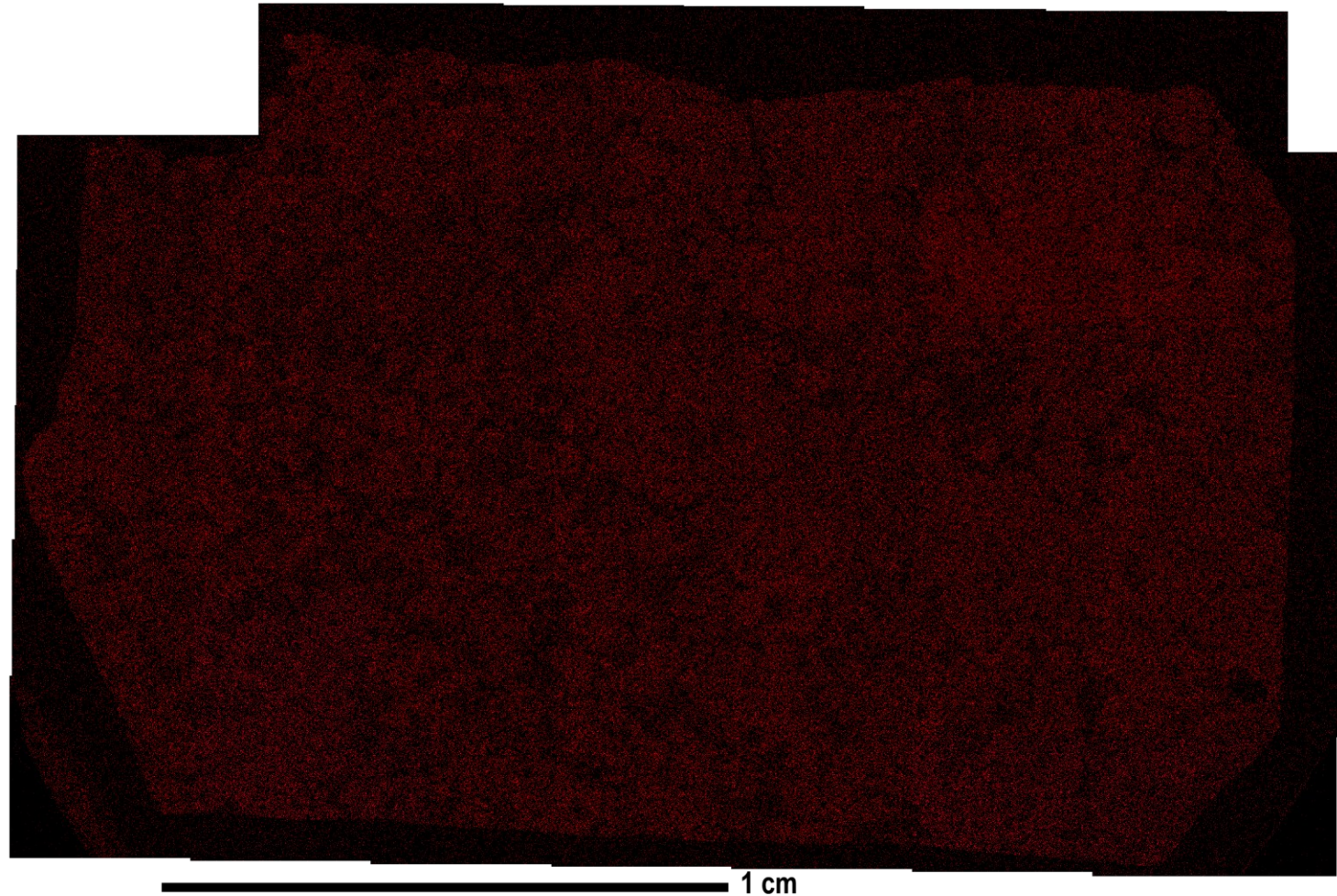


Figure 43. Co elemental map

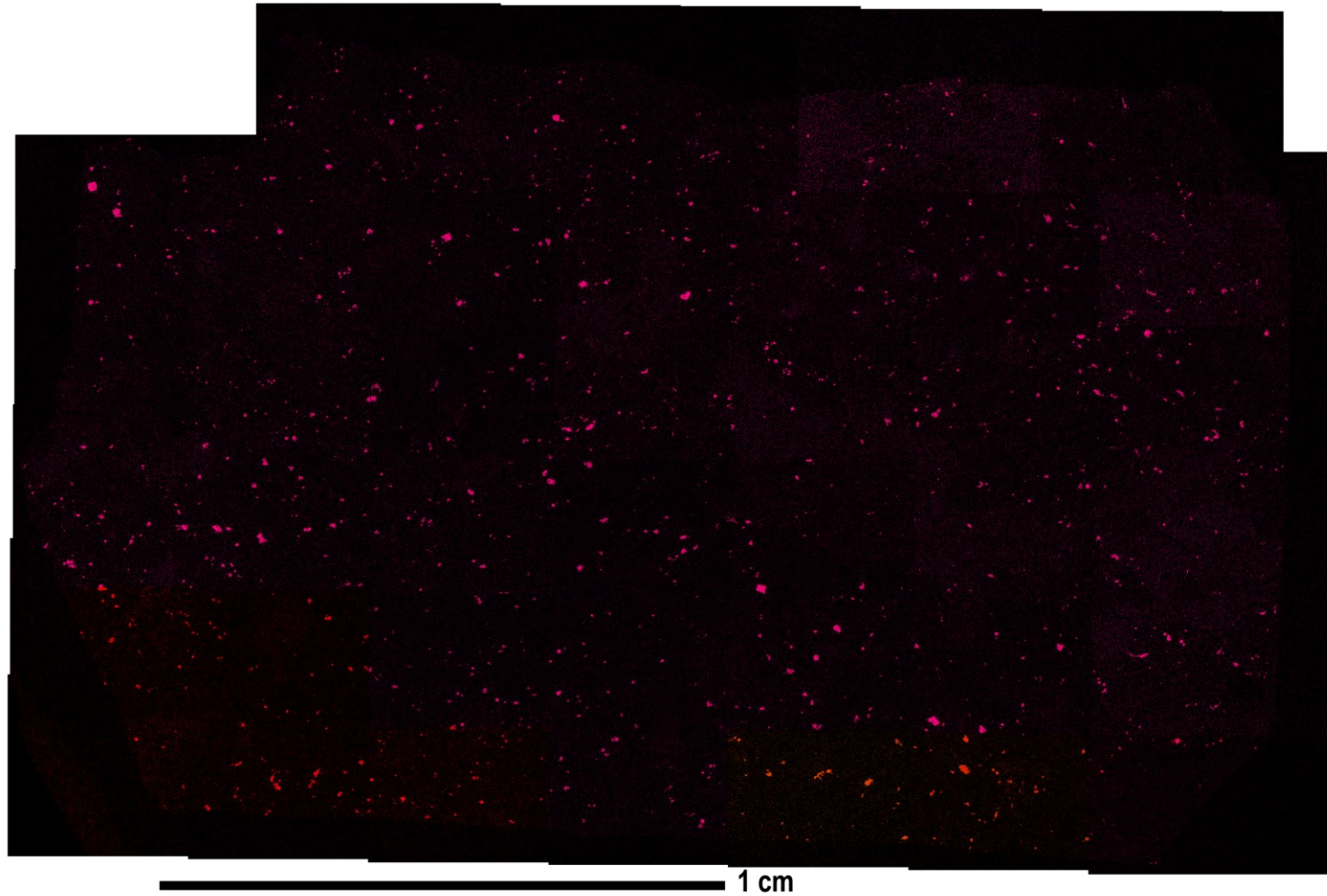


Figure 44. Cr elemental map

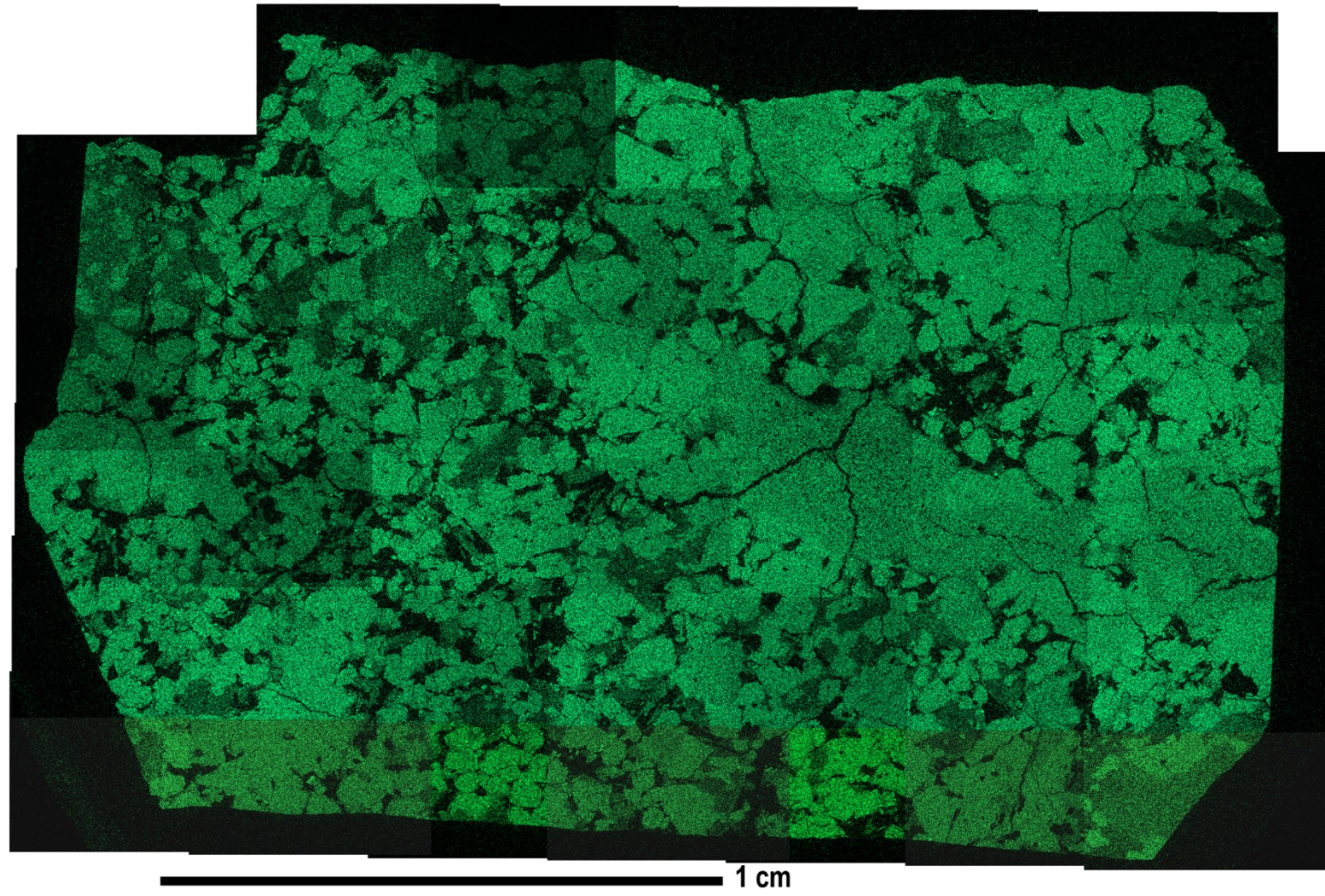


Figure 45. Fe elemental map

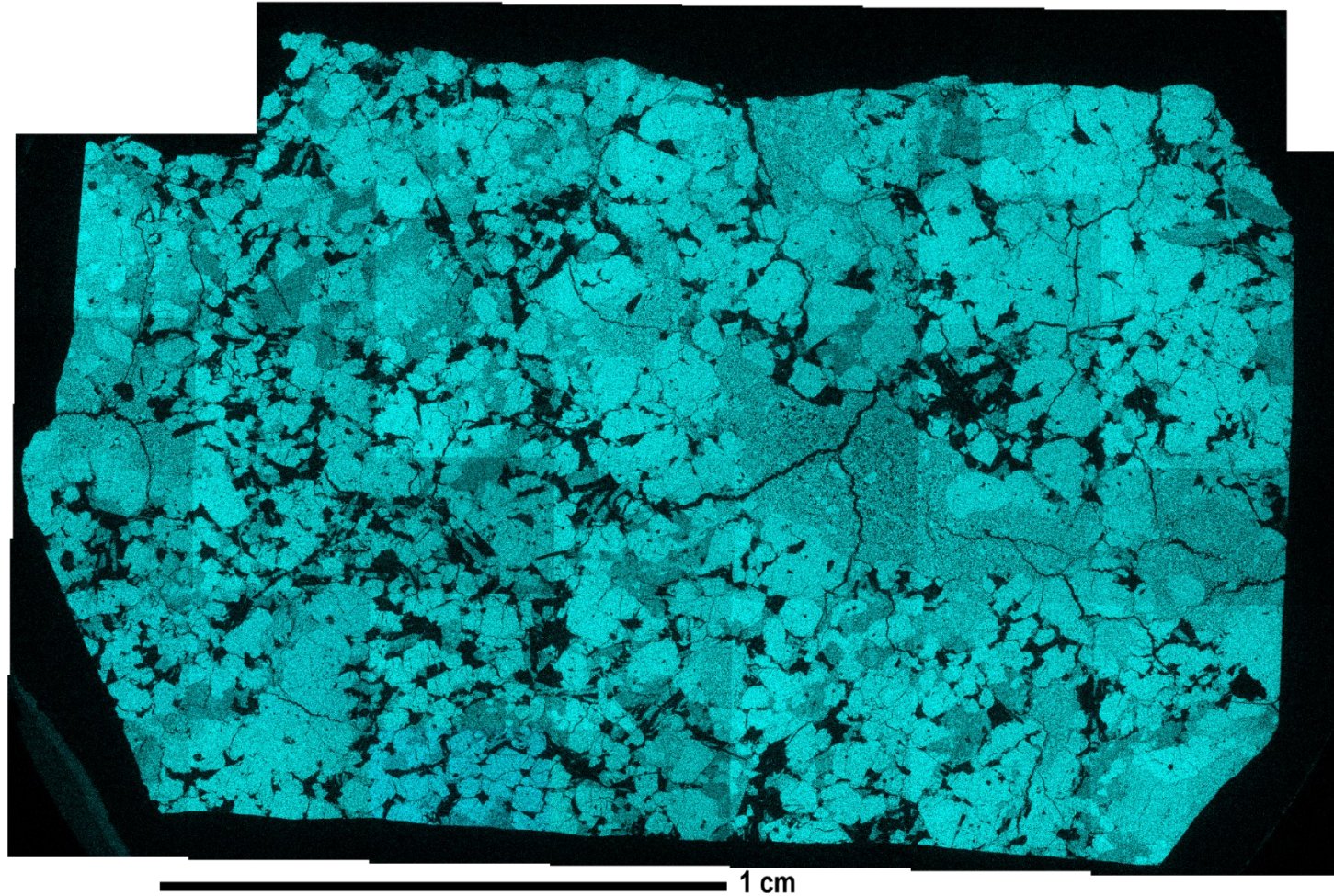


Figure 46. Mg elemental map

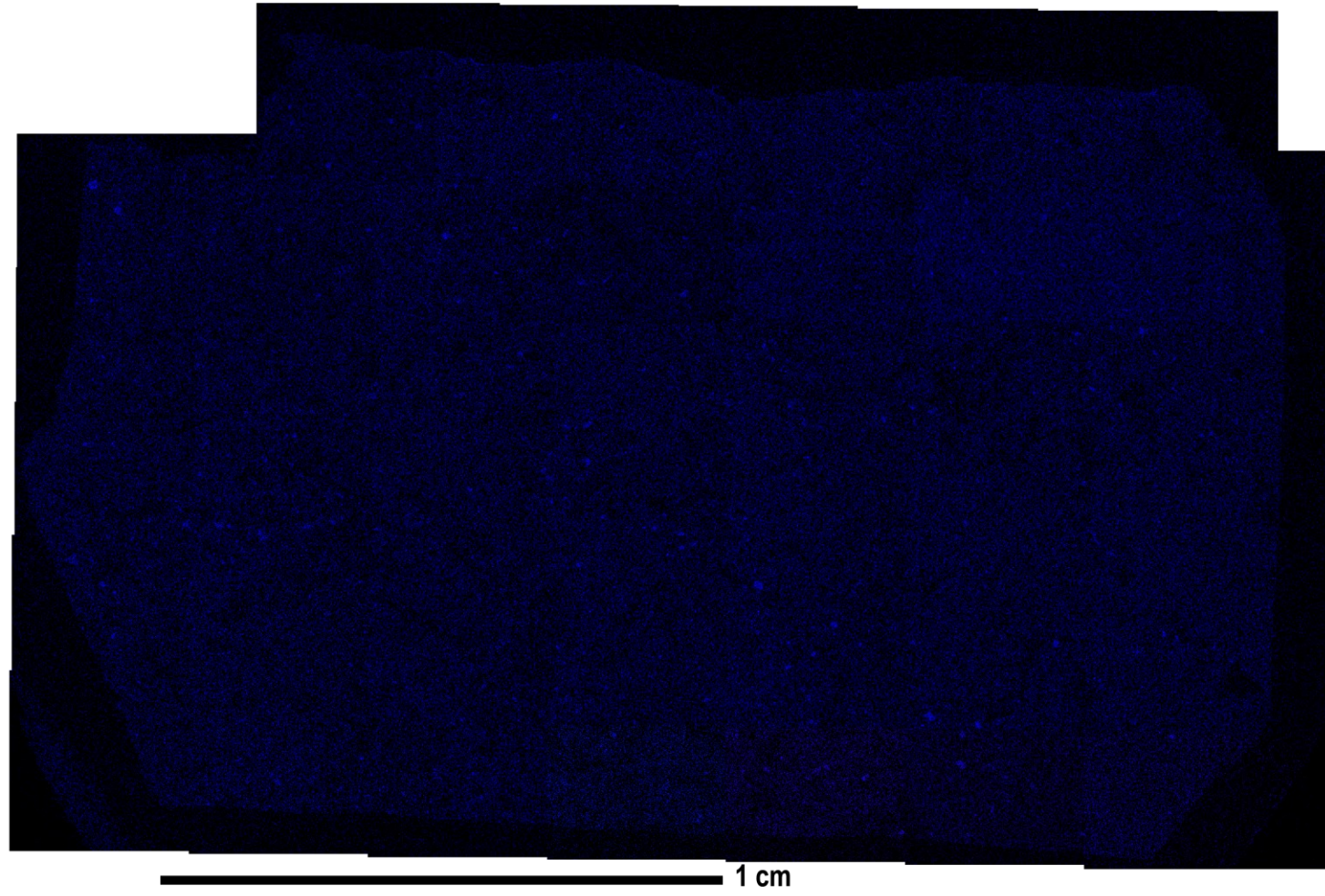


Figure 47. Mn elemental map

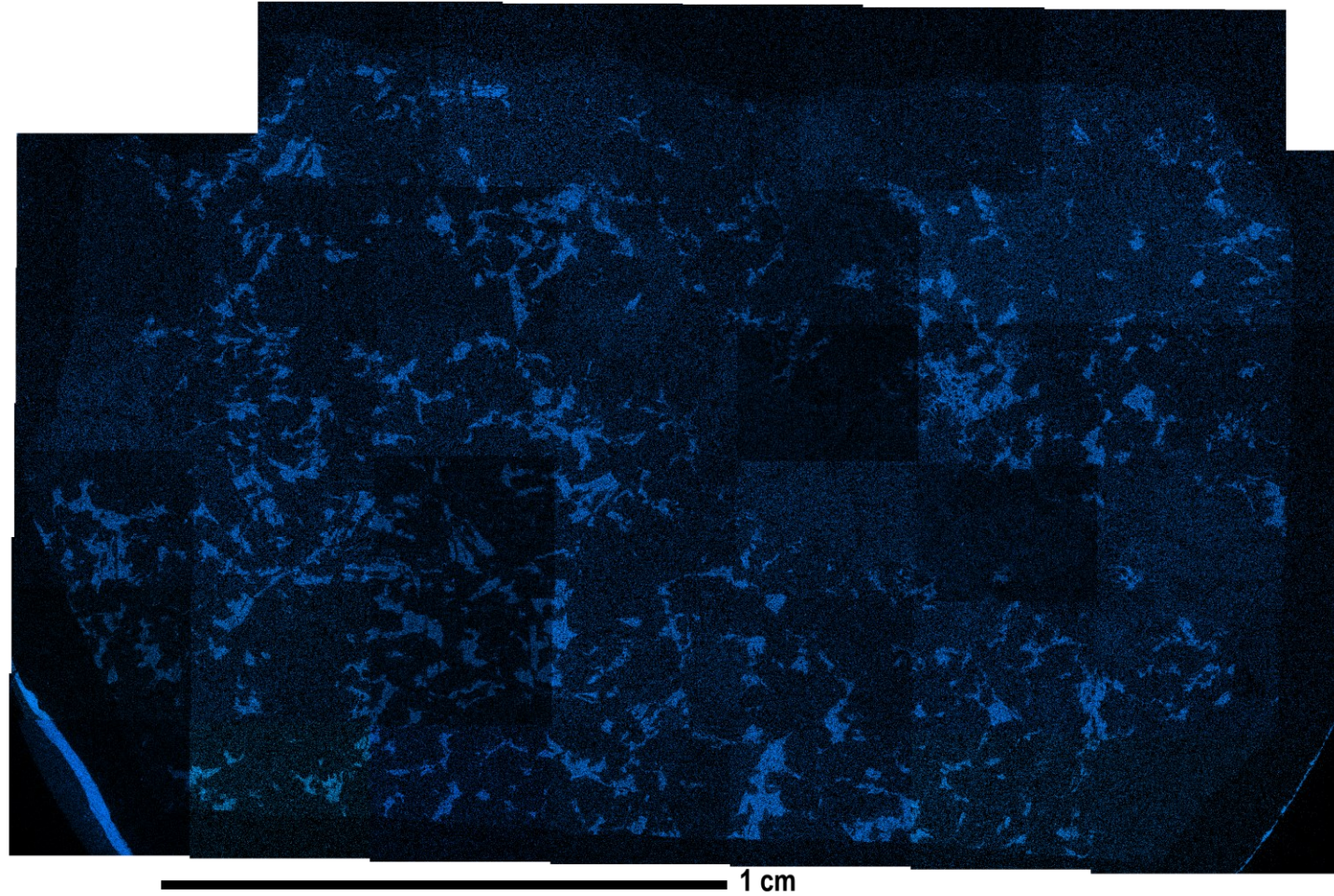


Figure 48. Na elemental map



Figure 49. Ni elemental map

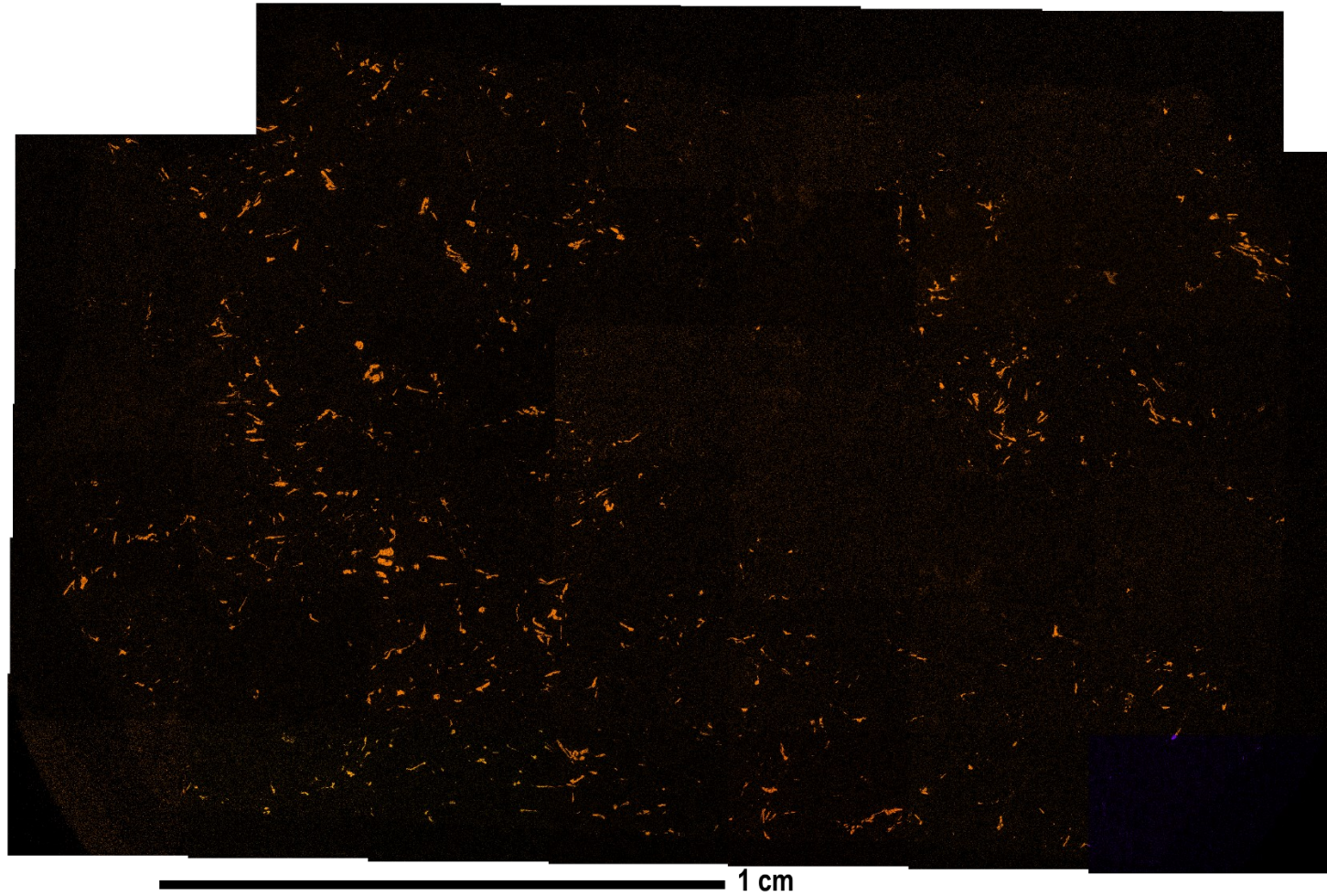


Figure 50. P elemental map

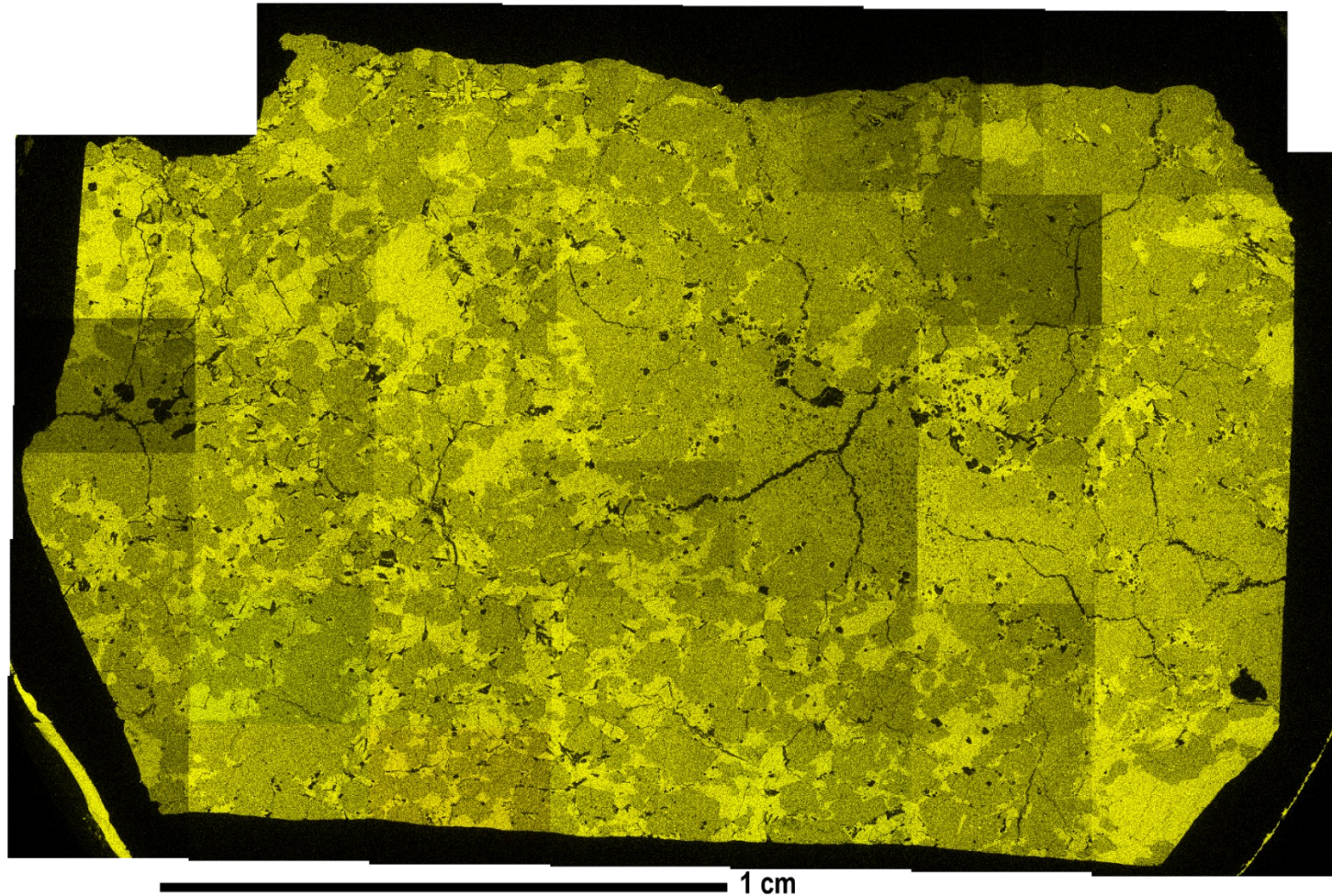


Figure 51. Si elemental map

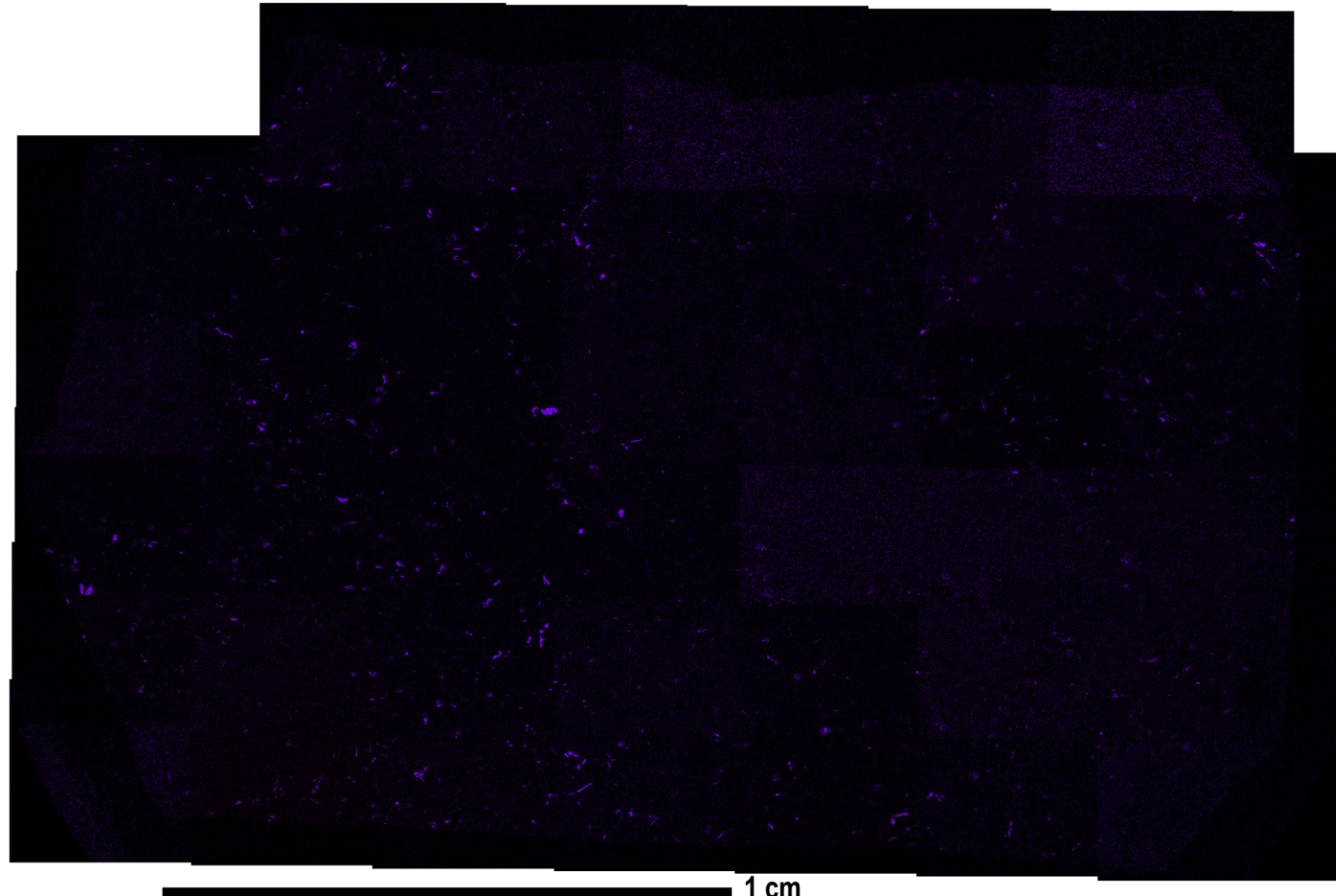


Figure 52. Ti elemental map

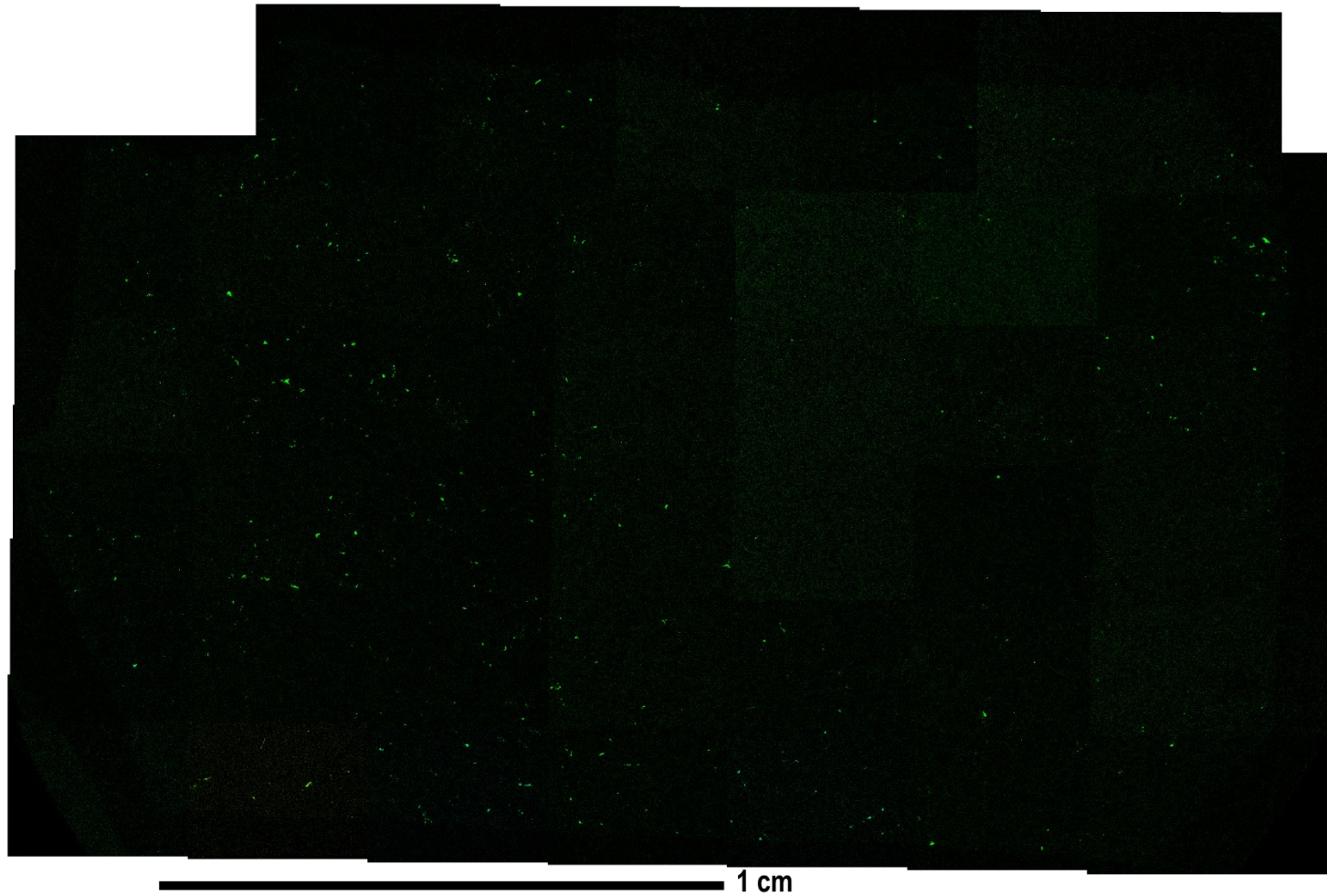


Figure 53. S elemental map

8. REFERENCES

- Agisoft. "3D Model Reconstruction.", <https://agisoft.freshdesk.com/support/solutions/articles/31000152092-3d-model-reconstruction> <https://agisoft.freshdesk.com/support/solutions/articles/31000152092>.
- Agee, Carl B. and David S. Draper. 2004. "Experimental Constraints on the Origin of Martian Meteorites and the Composition of the Martian Mantle." *Earth and Planetary Sciences Letters* 224 (3-4): 415-429. <https://www.sciencedirect.com/science/article/abs/pii/S0012821X04003437>.
- Anders, Edward, C. K. Shearer, J. J. Papike, Jeffrey F. Bell, Simon J. Clemett, Richard N. Zare, David S. McKay, et al. 1996. "Evaluating the Evidence for Past Life on Mars." *Science* 274 (5295): 2119-2125. <https://www.jstor.org/stable/2891374>.
- Artemieva, Natalia and Boris Ivanov. 2004. "Launch of Martian Meteorites in Oblique Impacts." *Icarus* 171 (1): 84-101. <https://www.sciencedirect.com/science/article/abs/pii/S0019103504001459>.
- Baziotis, Ioannis, Paul D. Asimow, Jinping Hu, Ludovic Ferrière, Chi Ma, Ana Cernok, Mahesh Anand, and Dan Topa. 2018. "High Pressure Minerals in the Château-Renard (L6) Ordinary Chondrite: Implications for Collisions on its Parent Body." *Scientific Reports* 8 (1): 9851. doi:10.1038/s41598-018-28191-6. <https://www.nature.com/articles/s41598-018-28191-6> <https://www.nature.com/articles/s41598-018-28191-6.pdf>
- Beard, Brian L., James M. Ludois, Thomas J. Lapen, and Clark M. Johnson. 2013. "Pre-4.0 Billion Year Weathering on Mars Constrained by Rb-Sr Geochronology on Meteorite ALH84001." *Earth and Planetary Science Letters* 361: 173-182. doi:10.1016/j.epsl.2012.10.021. <https://www.sciencedirect.com/science/article/abs/pii/S0012821X12005821> <https://www.sciencedirect.com/science/article/abs/pii/S0012821X12005821?via%3Dihub>.
- Becker and Pepin. 1984. "The Case for a Martian Origin of the Shergottites: Nitrogen and Noble Gases in EETA 79001." *Earth and Planetary Science Letters* 69 (2): 225-242. doi:10.1016/0012-821X(84)90183-3. [https://dx.doi.org/10.1016/0012-821X\(84\)90183-3](https://dx.doi.org/10.1016/0012-821X(84)90183-3).
- Berkley, J. L., K. Keil, and M. Prinz. 1980. "Comparative Petrology and Origin of Governador Valadares and Other Nakhrites." <https://adsabs.harvard.edu/full/1980LPSC...11.1089B>.
- Bertka, Constance M. and Yingwei Fei. 1996. "Constraints on the Mineralogy of an Iron-Rich Martian Mantle from High-Pressure Experiments." *Planetary and Space*

Science 44 (11): 1269-1276. <https://www.sciencedirect.com/science/article/abs/pii/S0032063396000347>.

Bischoff, Addi and Dieter Stöffler. 1992. "Shock Metamorphism as a Fundamental Process in the Evolution of Planetary Bodies: Information from M." *European Journal of Mineralogy* 4 (4): 707-755. doi:10.1127/ejm/4/4/0707. <https://pubs-geoscienceworld-org.ezproxy.tcu.edu/eurjmin/article/4/4/707/70053>.

Bogard, D. D. and P. Johnson. 1983. "Martian Gases in an Antarctic Meteorite?" *Science* 221 (4611): 651-654. doi:10.1126/science.221.4611.651. <http://www.sciencemag.org/cgi/content/abstract/221/4611/651>.

Borg, Lars E. and David S. Draper. 2003. "A Petrogenetic Model for the Origin and Compositional Variation of the Martian Basaltic Meteorites." *Meteoritics & Planetary Science* 38 (12): 1713-1731. doi:10.1111/j.1945-5100.2003.tb00011.x. <https://onlinelibrary.wiley.com/doi/10.1111/j.1945-5100.2003.tb00011.x>.

Borg, Lars E., Larry E. Nyquist, Henry Weismann, and Young Reese. 2002. "Constraints on the Petrogenesis of Martian Meteorites from the Rb-Sr and Sm-Nd Isotopic Systematics of the Lherzolitic Shergottites ALH77005 and LEW88516." *Geochimica Et Cosmochimica Acta* 66 (11): 2037-2053. <https://www.sciencedirect.com/science/article/abs/pii/S0016703702008359>.

Bridges, J. C., L. J. Hicks, C. Bedford, S. P. Schwenzer, J. MacArthur, and P. H. Edwards. 2017. "Igneous Differentiation of the Martian Crust." 12; 2021/09/03. <http://oro.open.ac.uk/52920/> <http://oro.open.ac.uk/52920/>.

Bridges, J. C. and S. P. Schwenzer. 2012. "The Nakhelite Hydrothermal Brine on Mars." *Earth and Planetary Science Letters* 359-360: 117-123. doi:10.1016/j.epsl.2012.09.044. <https://www.sciencedirect.com/science/article/pii/S0012821X12005407> <https://www.sciencedirect.com/science/article/abs/pii/S0012821X12005407>.

Bridges, J. C. and P. H. Warren. 2006. "The SNC Meteorites: Basaltic Igneous Processes on Mars." *Journal of the Geological Society* 163 (2): 229-251. doi:10.1144/0016-764904-501. <https://jgs.lyellcollection.org/content/163/2/229> https://oro.open.ac.uk/71/1/Bridges-Warren-revised_Jour_of_geo_soc_spec_iss.pdf <https://jgs.lyellcollection.org/content/163/2/229.short>

Cannon, K., J. Mustard, and C. Agee. 2015. "Evidence for a Widespread Basaltic Breccia Component in the Martian Low-Albedo Regions from the Reflectance Spectrum of Northwest Africa 7034." doi:10.1016/J.ICARUS.2015.01.016. <https://www.semanticscholar.org/paper/Evidence-for-a->

widespread-basaltic-breccia-in-the-Cannon-Mustard/1756bff89355dcd5af7ec73c2f0422a4d531b3a9.

Carlson, Richard W. and Maud Boyet. 2009. "Short-Lived Radionuclides as Monitors of Early Crust–mantle Differentiation on the Terrestrial Planets." *Earth and Planetary Science Letters* 279 (3): 147-156.
doi:10.1016/j.epsl.2009.01.017. <https://www.sciencedirect.com/science/article/pii/S0012821X09000272> <https://www.sciencedirect.com/science/article/pii/S0012821X09000272/pdf?md5=ff083c7e0f54a52b0afe0fee14c7f357&pid=1-s2.0-S0012821X09000272-main.pdf&isDTMRedir=Y>.

Castle, Nicholas and Christopher D. K. Herd. 2018. "Experimental Investigation into the Effects of Oxidation during Petrogenesis of the Tissint Meteorite." *Meteoritics & Planetary Science* 53 (7): 1341-1363.
doi:10.1111/maps.13083. <https://onlinelibrary.wiley.com/doi/abs/10.1111/maps.13083>.

Chen, Ming and Ahmed El Goresy. 2000. "The Nature of Maskelynite in Shocked Meteorites: Not Diaplectic Glass but a Glass Quenched from Shock-Induced Dense Melt at High Pressures." *Earth and Planetary Science Letters* 179 (3): 489-502. doi:10.1016/S0012-821X(00)00130-8. [https://dx.doi.org/10.1016/S0012-821X\(00\)00130-8](https://dx.doi.org/10.1016/S0012-821X(00)00130-8).

Clayton, Robert N. 2006. "Meteorites and their Parent Asteroids." *Science (American Association for the Advancement of Science)* 313 (5794): 1743-1744.
doi:10.1126/science.1133137. <https://www.jstor.org/stable/20031346>.

Clayton, Robert N. and Toshiko K. Mayeda. 1983. "Oxygen Isotopes in Eucrites, Shergottites, Nakhlites, and Chassignites." *Earth and Planetary Science Letters* 62 (1): 1-6.
doi:10.1016/0012-821X(83)90066-3. [https://dx.doi.org/10.1016/0012-821X\(83\)90066-3](https://dx.doi.org/10.1016/0012-821X(83)90066-3).

———. 1986. "Oxygen Isotopes in Shergotty." *Geochimica Et Cosmochimica Acta* 50 (6): 979-982. doi:10.1016/0016-7037(86)90378-9. [https://dx.doi.org/10.1016/0016-7037\(86\)90378-9](https://dx.doi.org/10.1016/0016-7037(86)90378-9).

Clayton, Robert N., Lawrence Grossman, and Toshiko K. Mayeda. 1973. "A Component of Primitive Nuclear Composition in Carbonaceous Meteorites." *Science* 182 (4111): 485-488.
doi:10.1126/science.182.4111.485. <http://www.sciencemag.org/cgi/content/abstract/182/4111/485>.

Combs, Logan M., Arya Udry, Geoffrey H. Howarth, Minako Righter, Thomas J. Lapen, Juliane Gross, Daniel K. Ross, Rachel R. Rahib, and James M. D. Day. 2019. "Petrology of the Enriched Poikilitic Shergottite Northwest Africa 10169: Insight into the Martian Interior." *Geochimica Et Cosmochimica Acta* 266: 435-462.
doi:<https://doi.org/10.1016/j.gca.2019.07.001>. <https://www.sciencedirect.com/science/article/pii/S0016703719304119>.

Corrigan, Catherine M., Michael A. Velbel, and Edward P. Vicenzi. 2015. "Modal Abundances of Pyroxene, Olivine, and Mesostasis in Nakhrites: Heterogeneity, Variation, and Implications for Nakhrite Emplacement." *Meteoritics & Planetary Science* 50, Nr 9, 1497–1511 (2015). https://repository.si.edu/bitstream/handle/10088/27258/Corrigan_et_al-2015-Meteoritics_%20&%20Planetary%20Science.pdf?isAllowed=y&sequence=1.

Crozaz, Ghislaine, Christine Floss, and Meenakshi Wadhwa. 2003. "Chemical Alteration and REE Mobilization in Meteorites from Hot and Cold Deserts." *Geochimica Et Cosmochimica Acta* 67 (24): 4727-4741.
doi:10.1016/j.gca.2003.08.008. <https://dx.doi.org/10.1016/j.gca.2003.08.008>.

Dauphas, Nicolas, Timo Hopp, Grant Craig, Zhe J. Zhang, Maria C. Valdes, Philipp R. Heck, Bruce L. A. Charlier, et al. 2022. "In Situ ^{87}Rb – ^{87}Sr Analyses of Terrestrial and Extraterrestrial Samples by LA-MC-ICP-MS/MS with Double Wien Filter and Collision Cell Technologies." *Journal of Analytical Atomic Spectrometry*.

Doyle, Alexandra E., Edward D. Young, Beth Klein, Ben Zuckerman, and Hilke Schlichting. 2019. "Oxygen Fugacities of Extrasolar Rocks: Evidence for an Earth-Like Geochemistry of Exoplanets." *Science* 366 (6463): 356-359.
doi:10.1126/science.aax3901. <https://www.science.org/doi/10.1126/science.aax3901#:~:text=The%20oxygen%20fugacity%20of%20a,exoplanet%20depends%20on%20this%20value>.

Drake, Michael J., Horton E. Newsom, and Christopher J. Capobianco. 1989. "V, Cr, and Mn in the Earth, Moon, EPB, and SPB and the Origin of the Moon: Experimental Studies ." *Geochimica Et Cosmochimica Acta* 53 (8): 2101-2111. <https://www-sciencedirect-com.ezproxy.tcu.edu/science/article/pii/0016703789903281?via%3Dihub>.

Drake, Michael J. and Kevin Righter. 2002. "Determining the Composition of the Earth." *Nature (London)* 416 (6876): 39-44.
doi:10.1038/416039a. <http://dx.doi.org/10.1038/416039a>.

Dreibus, G. and H. Wänke. 1987. "Accretion of the Earth and Inner Plants." *Geochemistry and Cosmochemistry*: 3-11.

Dymek, R. F., A. L. Albee, A. A. Chodos, and G. J. Wasserburg. 1976. "Petrography of Isotopically-Dated Clasts in the Kapoeta Howardite and Petrologic Constraints on the Evolution of its Parent Body." *Geochimica Et Cosmochimica Acta* 40 (9): 1115-1116.

Elkins-Tanton, Linda, E. M. Parmentier, and P. C. Hess. 2003. "Magma Ocean Fractional Crystallization and Cumulate Overturn in Terrestrial Planets: Implications for Mars." *Meteoritics & Planetary Science* 38 (12): 1753-1771. doi:10.1111/j.1945-5100.2003.tb00013.x. <https://onlinelibrary.wiley.com/doi/abs/10.1111/j.1945-5100.2003.tb00013.x>

Eugster, Otto. "Ejection Ages from Krypton-81-Krypton-83 Dating and Pre-Atmospheric Sizes of Martian Meteorites | Request PDF.", <https://onlinelibrary.wiley.com/doi/10.1111/j.1945-5100.2002.tb01033.x> https://www.researchgate.net/publication/227758190_Ejection_ages_from_krypton-81-krypton-83_dating_and_pre-atmospheric_sizes_of_Martian_meteorites.

Filiberto, Justin. 2017. "Geochemistry of Martian Basalts with Constraints on Magma Genesis." *Chemical Geology* 466: 1-14. doi:10.1016/j.chemgeo.2017.06.009. <https://www.sciencedirect.com/science/article/pii/S009254117303662>.

Filiberto, Justin and Rajdeep Dasgupta. 2011. "Fe²⁺-Mg Partitioning between Olivine and Basaltic Melts: Applications to Genesis of Olivine-Phryic Shergottites and Conditions of Melting in the Martian Interior." *Earth and Planetary Science Letters* 304 (3): 527-537. doi:10.1016/j.epsl.2011.02.029. <https://www.sciencedirect.com/science/article/pii/S0012821X11001002>.

Filiberto, Justin, Donald S. Musselwhite, Julianne Gross, Katherine Burgess, Loan Le, and Allan H. Treiman. 2010. "Experimental Petrology, Crystallization History, and Parental Magma Characteristics of Olivine-Phryic Shergottite NWA 1068: Implications for the Petrogenesis of "enriched" Olivine-Phryic Shergottites." *Meteoritics & Planetary Science* 45 (8): 1258-1270. <https://onlinelibrary.wiley.com/doi/10.1111/j.1945-5100.2010.01080.x>.

Foley, C. N., M. Wadhwa, L. E. Borg, P. E. Janney, R. Hines, and T. L. Grove. 2005. "The Early Differentiation History of Mars from 182W-142Nd Isotope Systematics in the SNC Meteorites." *Geochimica Et Cosmochimica Acta* 69 (18): 4557-4571. doi:10.1016/j.gca.2005.05.009. <https://www.sciencedirect.com/science/article/pii/S0016703705004321>.

Fritz, Jörg, Ansgar Greshake, and Vera A. Fernandes. 2017. "Revising the Shock Classification of Meteorites." *Meteoritics & Planetary Science* 52 (6): 1216-1232. doi:10.1111/maps.12845. <https://onlinelibrary.wiley.com/doi/abs/10.1111/maps.12845>.

Gooding, James L., Susan J. Wentworth, and Michael E. Zolensky. 1991. "Aqueous Alteration of the Nakhla Meteorite." *Meteoritics* 26 (2): 135-143. doi:10.1111/j.1945-5100.1991.tb01029.x. <https://onlinelibrary.wiley.com/doi/abs/10.1111/j.1945-5100.1991.tb01029.x>

Goodrich, Cyrena Anne. 2002. "Olivine-Phryic Martian Basalts: A New Type of Shergottite." *Meteoritics & Planetary Science* 37: B31-B34. doi:10.1111/j.1945-5100.2002.tb00901.x. <https://onlinelibrary.wiley.com/doi/10.1111/j.1945-5100.2002.tb00901.x>

Gross, Julianne, Annette Hilton, Tabb C. Prissel, Jacob B. Setera, Randy L. Korotev, and Abigail Calzada-Diaz. 2020. "Geochemistry and Petrogenesis of Northwest Africa

10401: A New Type of the mg-Suite Rocks." *Journal of Geophysical Research: Planets* 125 (5). <https://agupubs.onlinelibrary.wiley.com/doi/10.1029/2019JE006225>.

Haines, Julia. "Photogrammetry Workflow using a DSLR Camera." Scholars' Lab., accessed Jan 31, 2022, <https://scholarslab.lib.virginia.edu/blog/documentation-photogrammetry/>.

Halliday, A. N., H. Wänke, J. -L Birck, and R. N. Clayton. 2001. "The Accretion, Composition and Early Differentiation of Mars." *Space Science Reviews* 96 (1): 197-230. doi:10.1023/A:1011997206080. <https://doi.org/10.1023/A:1011997206080> <https://link.springer.com/content/pdf/10.1023%2FA%3A1011997206080.pdf>.

Hanna, Romy D., Richard A. Ketcham, and Mike Zolensky. 2015. "Impact-Induced Brittle Deformation, Porosity Loss, and Aqueous Alteration in the Murchison CM Chondrite." *Geochimica Et Cosmochimica Acta* 171: 256-282. <https://www.sciencedirect.com.ezproxy.tcu.edu/science/article/pii/S0016703715005347?via%3Dihub>.

Herd, Christopher D. K., Erin L. Walton, Carl B. Agee, Nele Muttik, Karen Ziegler, Charles K. Shearer, Aaron S. Bell, et al. 2017. "The Northwest Africa 8159 Martian Meteorite: Expanding the Martian Sample Suite to the Early Amazonian." *Geochimica Et Cosmochimica Acta* 218: 1-26. doi:10.1016/j.gca.2017.08.037. <https://www.sciencedirect.com/science/article/pii/S0016703717305392/pdfft?md5=e683909a8b9fefafa2c05d4b1e13cfaacc&pid=1-s2.0-S0016703717305392-main.pdf&isDTMRedir=Y>

Herd, Christopher D. K., Lars E. Borg, John H. Jones, and James J. Papike. 2002. "Oxygen Fugacity and Geochemical Variations in the Martian Basalts: Implications for Martian Basalt Petrogenesis and the Oxidation State of the Upper Mantle of Mars." *Geochimica Et Cosmochimica Acta* 66 (11): 2025-2036. doi:10.1016/S0016-7037(02)00828-1. <https://search.proquest.com/docview/27798642>.

Hewins, Roger H., Brigitte Zanda, Munir Humayun, Alexander Nemchin, Jean-Pierre Lorand, Sylvain Pont, Damien Deldicque, et al. 2017. "Regolith Breccia Northwest Africa 7533: Mineralogy and Petrology with Implications for Early Mars." *Meteoritics & Planetary Science* 52 (1): 89-124. doi:10.1111/maps.12740. <https://onlinelibrary.wiley.com/doi/abs/10.1111/maps.12740> <https://onlinelibrary.wiley.com/doi/pdfdirect/10.1111/maps.12740>.

Howarth, Geoffrey H., John F. Pernet-Fisher, J. Brian Balta, Peter H. Barry, Robert J. Bodnar, and Lawrence A. Taylor. 2014. "Two-Stage Polybaric Formation of the New Enriched, Pyroxene-Oikocrystic, Lherzolitic Shergottite, NWA 7397." *Meteoritics & Planetary Science* 49 (10): 1812-1830. doi:10.1111/maps.12357. <https://api.istex.fr/ark:/67375/WNG-CTMM5B8Z-1/fulltext.pdf>.

Hudson Institute of Mineralogy, 1993-2022. "Merrillite." Mindat., last modified 16 September, accessed 09/20/, 2022, <https://www.mindat.org/min-6577.html>.

Humayun, M. and S. Yang. 2020. "Tin Abundances Require that Chassignites Originated from Multiple Magmatic." :
2. <https://www.hou.usra.edu/meetings/lpsc2020/pdf/1338.pdf>.

Jones, J. H. 2003. "Constraints on the Structure of the Martian Interior Determined from the Chemical and Isotopic Systematics of SNC Meteorites." *Meteoritics & Planetary Science* 38 (12): 1807-1814. doi:10.1111/j.1945-5100.2003.tb00016.x. <https://onlinelibrary.wiley.com/doi/abs/10.1111/j.1945-5100.2003.tb00016.x>

———. 1989. "Isotopic Relationships among the Shergottites, the Nakhrites and Chassigny." *Lunar and Planetary Science Conference Proceedings* 19: 465-474. <https://ui.adsabs.harvard.edu/abs/1989LPSC...19..465J> https://ui.adsabs.harvard.edu/link_gateway/1989LPSC...19..465J/ARTICLE.

Jones, John H. 1995. "Experimental Trace Element Partitioning." In *Rock Physics & Phase Relations*, 73-104: American Geophysical Union (AGU). <https://onlinelibrary.wiley.com/doi/abs/10.1029/RF003p0073> <https://agupubs.onlinelibrary.wiley.com/doi/10.1029/RF003p0073>.

Keifer and Li. 2016. "Water Undersaturated Mantle Plume Volcanism on Present-Day Mars." *Meteoritics & Planetary Science* 51 (11): 1993-2010. <https://onlinelibrary.wiley.com/doi/10.1111/maps.12720>.

Ketcham, Richard A. and William D. Carlson. 2001. "Acquisition, Optimization and Interpretation of X-Ray Computed Tomographic Imagery: Applications to the Geosciences." *Computers & Geosciences* 27 (4): 381-400. <https://www-sciencedirect-com.ezproxy.tcu.edu/science/article/pii/S0098300400001163?via%3Dihub>.

Koeppen, William C. and Victoria E. Hamilton. 2008. "Global Distribution, Composition, and Abundance of Olivine on the Surface of Mars from Thermal Infrared Data." *Journal of Geophysical Research* 113 (E5): E05001-n/a. doi:10.1029/2007JE002984. <https://api.istex.fr/ark:/67375/WNG-9RS3V0X1-P/fulltext.pdf>.

Lodders, K. and B. Fegley. 1997. "An Oxygen Isotope Model for the Composition of Mars." *Icarus* 126 (2): 373-394.

McCubbin, Francis M., Jeremy W. Boyce, Tímea Novák-Szabó, Alison R. Santos, Romain Tartèse, Nele Muttik, Gabor Domokos, et al. 2016. "Geologic History of Martian Regolith Breccia Northwest Africa 7034: Evidence for Hydrothermal Activity and Lithologic Diversity in the Martian Crust." *Journal of Geophysical Research: Planets* 121 (10): 2120-2149. doi:10.1002/2016JE005143. <https://onlinelibrary.wiley.com/doi/abs/10.1002/2016JE005143> <https://onlinelibrary.wiley.com/doi/pdfdirect/10.1002/2016JE005143> <https://agupubs.onlinelibrary.wiley.com/doi/full/10.1002/2016JE005143>.

McCubbin, Francis M., Stephen M. Elardo, Charles K. Shearer, Alexander Smirnov, Erik H. Hauri, and David S. Draper. 2013. "A Petrogenetic Model for the Comagmatic Origin of Chassignites and Nakhrites: Inferences from Chlorine-Rich Minerals, Petrology, and Geochemistry." *Meteoritics & Planetary Science* 48 (5): 819-853.
doi:10.1111/maps.12095. <https://onlinelibrary.wiley.com/doi/abs/10.1111/maps.12095>

McKay, D. S., E. K. Gibson, K. Thomas-Keprta, H. Vali, C. S. Romanek, S. J. Clemett, X. D. F. Chillier, C. R. Maechling, and R. N. Zare. 1996. "Search for Past Life on Mars: Possible Relic Biogenic Activity in Martian Meteorite ALH84001." *Science* 273 (5277): 924-930.
doi:10.1126/science.273.5277.924. <https://www.sciencemag.org/lookup/doi/10.1126/science.273.5277.924> <http://lunar.earth.northwestern.edu/courses/438/search.life.pdf>.

McSween, H. Y. 1994. "What we have Learned about Mars from SNC Meteorites." *Meteoritics* 29 (6): 757-779. <https://ui.adsabs.harvard.edu/abs/1994Metic..29..757M/abstract>.

McSween, H. Y., R. E. Arvidson, J. F. Bell, D. Blaney, N. A. Cabrol, P. R. Christensen, B. C. Clark, et al. 2004. "Basaltic Rocks Analyzed by the Spirit Rover in Gusev Crater." *Science (American Association for the Advancement of Science)* 305 (5685): 842-845.
doi:10.1126/science.3050842. <http://www.sciencemag.org/cgi/content/abstract/305/5685/842>

McSween, H. Y., Jr. Jan 1, 1985. "What we Know about Mars (but Otherwise Wouldn'T) if it is the Shergottite Parent Body .".

McSween, Harry Y. and Allan H. Treiman. 1998. "Planetary Materials." In *Planetary Materials*, edited by J. J. Papike. Vol. 36, 1. <http://www.minsocam.org/msa/rim/rim36.html#contents>.

MetBase, Mayne, Rhiannon and Gackstatter, Emily. "North West Africa 14904.", last modified May, <https://www.lpi.usra.edu/meteor/metbull.php?code=77472>.

Meyer, Charles. 2012. "ALH84001" Astromaterials Research & Exploration Science (ARES): NASA. <https://curator.jsc.nasa.gov/antmet/mmc/alh84001.pdf>

Mikouchi, T. 2009. "Petrological and Mineralogical Diversities within the Lherzolitic Shergottites Require a New Group Name?" : 2272. <https://ui.adsabs.harvard.edu/abs/2009LPI....40.2272M> https://ui.adsabs.harvard.edu/link_gateway/2009LPI....40.2272M/ARTICLE.

Mikouchi, Takashi. 2010. "Northwest Africa 1950: Mineralogy and Comparison with Antarctic Lherzolitic Shergottites." *Meteoritics & Planetary Science* 40 (11): 1621-1634. <https://onlinelibrary.wiley.com/doi/10.1111/j.1945-5100.2005.tb00135.x>.

Milton, Daniel J. and Paul S. de Carli. 1963. "Maskelynite: Formation by Explosive Shock." *Science* 140 (3567): 670-671.
doi:10.1126/science.140.3567.670. <http://www.sciencemag.org/cgi/content/abstract/140/3567/670>.

Mittlefehldt, David W. 1994. "ALH84001, a Cumulate Orthopyroxenite Member of the Martian Meteorite Clan." *Meteoritics* 29 (2): 214221. <https://onlinelibrary.wiley.com/doi/abs/10.1111/j.1945-5100.1994.tb00673.x>.

Mittlefehldt and D.W. 2005. "Achondrites ." In *Meteorites, Comets, and Planets: Treatise on Geochemistry*, edited by A. M. Davis and H. D. Holland: Elsevier Science and Technology.

Morgan, John W. and Edward Anders. 1979. "Chemical Composition of Mars." *Geochimica Et Cosmochimica Acta* 43 (10): 1601-1610. doi:10.1016/0016-7037(79)901807. <https://www.sciencedirect.com/science/article/pii/0016703779901807> <https://www.sciencedirect.com/science/article/pii/0016703779901807/pdf?md5=f935a2562f9f93e884597c524a763f48&pid=1-s2.0-0016703779901807-main.pdf&isDTMRedir=Y>.

Moser, D. E., G. A. Arcuri, D. A. Reinhard, L. F. White, J. R. Darling, I. R. Barker, D. J. Larson, et al. 2019. "Decline of Giant Impacts on Mars by 4.48 Billion Years Ago and an Early Opportunity for Habitability." *Nature Geoscience* 12 (7): 522-527.
doi:10.1038/s41561-019-0380-0. <https://www.nature.com/articles/s41561-019-0380-0> https://researchportal.port.ac.uk/portal/files/14002539/Moser_et_al_Mars_NatGeo_postprint.pdf <https://www.nature.com/articles/s41561-019-0380-0>.

Nekvasil, H., A. Dondolini, J. Horn, J. Filiberto, H. Long, and D. H. Lindsley. 2004. "The Origin and Evolution of Silica-Saturated Alkalic Suites: An Experimental Study." *Journal of Petrology* 45 (4): 693-721.
doi:10.1093/petrology/egg103. <https://api.istex.fr/ark:/67375/HXZ-40BK5HDZ-9/fulltext.pdf>.

Nyquist, L. E., D. D. Bogard, J. L. Wooden, H. Weismann, C. Y. Shih, B. M. Bansal, and G. McKay. 1979. "Early Differentiation, Late Magmatism, and Recent Bombardment on the Shergottite Parent Planet." *Meteoritics* 502: 502. <https://adsabs.harvard.edu/pdf/1979Metic..14..502N>.

Nyquist, L., Donald Bogard, C. -Y Shih, A. Greshake, Dieter Stöffler, and Otto Eugster. 2001. "Ages and Geologic Histories of Martian Meteorites." *Space Science Reviews* 96: 105-164.
doi:10.1023/A:1011993105172. https://www.researchgate.net/profile/Otto-Eugster/publication/225856700_Ages_and_Geologic_Histories_of_Martian_Meteorites/links/0deec524ec770d956b000000/Ages-and-Geologic-Histories-of-Martian-Meteorites.pdf.

Ogilvie, Paula, Roger L. Gibson, W. Uwe Reimold, Alexander Deutsch, and Ulrich HORNEMANN. 2011. "Experimental Investigation of Shock Metamorphic Effects in a

Metapelitic Granulite: The Importance of Shock Impedance Contrast between Components." *Meteoritics & Planetary Science* 46 (10): 1565-1586. doi:10.1111/j.1945-5100.2011.01250.x. <https://api.istex.fr/ark:/67375/WNG-28KNDCQ1-W/fulltext.pdf>.

Orr, Forman, Rankenburg, Evans, McDonald, Godel, and Benedix. 2022. Geochemical and Mineralogical Classification of Four New Shergottites: NWA 10441, NWA 10818, NWA 11043, and NWA 12335. Vol. 57 Wiley. doi:10.1111/maps.13816.

Papike, J. J., J. M. Karner, C. K. Shearer, and P. V. Burger. 2009. "Silicate Mineralogy of Martian Meteorites." *Geochimica Et Cosmochimica Acta* 73 (24): 7443-7485. <https://www.sciencedirect.com.ezproxy.tcu.edu/science/article/pii/S0016703709005651?via%3Dihub>.

Preibisch, Stephan, Stephan Saalfeld, and Pavel Tomancak. 2009. "Globally Optimal Stitching of Tiled 3D Microscopic Image Acquisitions." *Bioinformatics* 25 (11): 1463-1465. doi:10.1093/bioinformatics/btp184. <https://web-s-ebscohost-com.ezproxy.tcu.edu/ehost/pdfviewer/pdfviewer?vid=0&sid=42a090ce-ae1a-447a-8dc3-1b81f90f5e29%40redis>.

Rahib, Rachel R., Arya Udry, Geoffrey H. Howarth, Juliane Gross, Marine Paquet, Logan M. Combs, Dara L. Lacznak, and James M. D. Day. 2019. "Mantle Source to Near-Surface Emplacement of Enriched and Intermediate Poikilitic Shergottites in Mars." *Geochimica Et Cosmochimica Acta* 266: 463-496. doi:<https://doi.org/10.1016/j.gca.2019.07.034>. <https://www.sciencedirect.com/science/article/pii/S0016703719304582>.

Ruzicka, Alex, Jeffrey N. Grossman, and Laurence Garvie. 2014. "The Meteoritical Bulletin, no. 100." *Meteoritics & Planetary Science* (49): E1-E101. <https://www.lpi.usra.edu/meteor/metbull.php?code=54831>.

Sanloup, C., A. Jambon, and P. Gillet. 1999. "A Simple Chondritic Model of Mars." 112 (1-2): 43-54.

Santos, Alison R., Carl B. Agee, Francis M. McCubbin, Charles K. Shearer, Paul V. Burger, Romain Tartèse, and Mahesh Anand. 2015. "Petrology of Igneous Clasts in Northwest Africa 7034: Implications for the Petrologic Diversity of the Martian Crust." *Geochimica Et Cosmochimica Acta* 157: 56-85. doi:10.1016/j.gca.2015.02.023. <https://www.sciencedirect.com/science/article/pii/S0016703715001064/pdfft?md5=52f8a6f443502277430d1dc87371409b&pid=1-s2.0-S0016703715001064-main.pdf&isDTMRedir=Y>.

Sautter, V., J. A. Barrat, A. Jambon, J. P. Lorand, Ph Gillet, M. Javoy, J. L. Joron, and M. Lesourd. 2002. "A New Martian Meteorite from Morocco: The Nakhelite North West Africa 817." *Earth and Planetary Science Letters* 195 (3): 223-238. doi:10.1016/S0012-821X(01)00591-X. <https://www.sciencedirect.com/science/article/pii/S0012821X0100591X>

Schindelin, Johannes, Ignacio Arganda-Carreras, Erwin Frise, Verena Kaynig, Mark Longair, Tobias Pietzsch, Stephan Preibisch, et al. 2012. "Fiji: An Open-Source Platform for Biological-Image Analysis." *Nature Methods* 9 (7): 676-682.
doi:10.1038/nmeth.2019. <https://www.proquest.com/docview/1029876122?parentSessionId=ZjqqShZInLVMcniazLi7kKdKgc4EZlSYmsVnFuerd5I%3D&pq-origsite=summon&accountid=7090>.

Shih, C. -Y, L. E. Nyquist, D. D. Bogard, G. A. McKay, J. L. Wooden, B. M. Bansal, and H. Wiesmann. 1982. "Chronology and Petrogenesis of Young Achondrites, Shergotty, Zagami, and ALHA77005: Late Magmatism on a Geologically Active Planet." *Geochimica Et Cosmochimica Acta* 46 (11): 2323-2344. doi:10.1016/0016-7037(82)90205-8. [https://dx.doi.org/10.1016/0016-7037\(82\)90205-8](https://dx.doi.org/10.1016/0016-7037(82)90205-8).

Shining, 3. D. 2019. EinScan-SP Platinum Desktop 3D Scanner Quick Start Guide HangzhouShining 3D Tech Co., LTD.

Stöffler, Dieter. 2000. *Maskelynite Confirmed as Diaplectic Glass: Indication for Peak Shock Pressures Below 45 GPa in all Martian Meteorites*.

Stöffler, D., A. Bischoff, V. Buchwald, and A. E. Rubin. 1988. "Shock Effects in Meteorites." In *Meteorites and the Early Solar System*, edited by John F. Kerridge and Mildred Shapley Matthews, 165-202: The University of Arizona Press Tucson.

Stöffler, Dieter, Christopher Hamann, and Knut Metzler. 2018. "Shock Metamorphism of Planetary Silicate Rocks and Sediments: Proposal for an Updated Classification System." *Meteoritics & Planetary Science* 53 (1): 5-49.
doi:10.1111/maps.12912. <https://onlinelibrary.wiley.com/doi/abs/10.1111/maps.12912>.

Stolper, Edward M. and McSween, Harry Y. "Basaltic Meteorites.", <https://www.scientificamerican.com/article/basaltic-meteorites/>

Stolper, Edward and Harry Y. McSween. 1979. "Petrology and Origin of the Shergottite Meteorites." *Geochimica Et Cosmochimica Acta* 43 (9): 1475-1498.
doi:10.1016/0016-7037(79)90142-X. <https://www.sciencedirect.com/science/article/pii/001670377990142X>

Sun, Weidong and William McDonough. 1989. "Chemical and Isotopic Systematics of Oceanic Basalts: Implications for Mantle Composition and Processes." In *Geological Society, London, Special Publications*. Vol. 42. https://www.researchgate.net/profile/William-Mcdonough-3/publication/231575101_Chemical_and_isotopic_systematics_of_oceanic_basalts_Implications_for_mantle_composition_and_processes/links/56dd5bf708ae07e3f617e09e/Chemical-and-isotopic-systematics-of-oceanic-basalts-Implications-for-mantle-composition-and-processes.pdf.

Takenouchi, Atsushi, Takashi Mikouchi, and Akira Yamaguchi. 2018. "Shock Veins and Brown Olivine in Martian Meteorites: Implications for their Shockpressure–temperature Histories." 53 (11): 2259-2284. <https://onlinelibrary.wiley.com/doi/full/10.1111/maps.13120>.

Taylor, G. J. 2013. "The Bulk Composition of Mars." *Geochemistry* 73 (4): 401-420. doi:10.1016/j.chemer.2013.09.006. <https://www.sciencedirect.com/science/article/pii/S0009281913000767>.

Taylor, G. Jeffrey, W. Boynton, J. Brückner, H. Wänke, G. Dreibus, K. Kerry, J. Keller, et al. 2006. "Bulk Composition and Early Differentiation of Mars." *Journal of Geophysical Research* 111 (E3): E03S10-n/a. doi:10.1029/2005JE002645. <https://api.istex.fr/ark:/67375/WNG-QS8HG08W-J/fulltext.pdf>.

Treiman, Allan H. 2010. "The History of Allan Hills 84001 Revised: Multiple Shock Events." *Meteoritics & Planetary Science* 33 (4): 753-764. doi:10.1111/j.1945-5100.1998.tb01681.x. <https://onlinelibrary.wiley.com/doi/abs/10.1111/j.1945-5100.1998.tb01681.x>

Treiman, Allan H. 2005. "The Nakhelite Meteorites: Augite-Rich Igneous Rocks from Mars." *Geochemistry* 65 (3): 203-270. doi:10.1016/j.chemer.2005.01.004. <https://linkinghub.elsevier.com/retrieve/pii/S0009281905000152> https://www.lpi.usra.edu/science/treiman/nakhelite_rev.pdf.

Treiman, Gleason, and Bogard. 2000. "The SNC Meteorites are from Mars." *Planetary and Space Science* 48: 1213-1230. http://meteorite.unm.edu/site_media/pdf/MarsMeteorites.pdf.

The Meteoritical Society. "The Meteoritical Bulletin Database ." The Meteoritical Society., <https://www.lpi.usra.edu/meteor/>.

The Meteoritical Society and Meteorite Nomenclature Committee. 2015. "Guidelines for Meteorite Nomenclature." The Meteoritical Society., last modified July 2015, <https://www.lpi.usra.edu/meteor/docs/nc-guidelines.pdf>.

Udry, A., G. H. Howarth, C. D. K. Herd, J. M. D. Day, T. J. Lapen, and J. Filiberto. 2020. "What Martian Meteorites Reveal about the Interior and Surface of Mars." *Journal of Geophysical Research: Planets* 125 (12): e2020JE006523. doi:10.1029/2020JE006523. <https://onlinelibrary.wiley.com/doi/abs/10.1029/2020JE006523> https://digitalscholarship.unlv.edu/cgi/viewcontent.cgi?article=1459&context=geo_fac_articles <https://agupubs.onlinelibrary.wiley.com/doi/10.1029/2020JE006523>.

Udry, Arya and James M. D. Day. 2018. "1.34 Billion-Year-Old Magmatism on Mars Evaluated from the Co-Genetic Nakhelite and Chassignite Meteorites." *Geochimica Et Cosmochimica Acta* 238: 292-315. doi:10.1016/j.gca.2018.07.006. <https://www.sciencedirect.com/science/article/pii/S001670371830382X>

Van de Moortèle, B., B. Reynard, P. Rochette, M. Jackson, P. Beck, P. Gillet, P. F. McMillan, and C. A. McCammon. 2007. "Shock-Induced Metallic Iron Nanoparticles in Olivine-Rich Martian Meteorites." *Earth and Planetary Sciences Letters* 262 (1-2): 37-49. <https://www.sciencedirect.com/science/article/abs/pii/S0012821X07004360>.

Walton, E. L., A. J. Irving, T. E. Bunch, and C. D. K. Herd. 2012. "Northwest Africa 4797: A Strongly Shocked Ultramafic Poikilitic Shergottite Related to Compositionally Intermediate Martian Meteorites." *Meteoritics & Planetary Science* 47 (9): 1449-1474. doi:10.1111/j.1945-5100.2012.01407.x. <https://onlinelibrary.wiley.com/doi/abs/10.1111/j.1945-5100.2012.01407.x>

Walton, Erin L. and Cliff S. J. Shaw. 2009. "Understanding the Textures and Origin of Shock Melt Pockets in Martian Meteorites from Petrographic Studies, Comparisons with Terrestrial Mantle Xenoliths, and Experimental Studies." *Meteoritics & Planetary Science* 44 (1): 55-76. doi:10.1111/j.1945-5100.2009.tb00717.x. <https://api.istex.fr/ark:/67375/WNG-93JHH8DL-X/fulltext.pdf>.

Wasson, J. T. and G. W. Wetherill. 1979. "Dynamical Chemical and Isotopic Evidence regarding the Formation Locations of Asteroids and Meteorites." *Asteroids*: 926-974. <https://ui.adsabs.harvard.edu/abs/1979aste.book..926W/abstract>.

Weisberg, Michael K., Timothy J. McCoy, and Alexander N. Krot. 2006. "Systematics and Evaluation of Meteorite Classification." In *Meteorites and the Early Solar System II*, edited by Dante S. Lauretta and Harry Y. McSween, 19-52: University of Arizona Press.

Wooden, J. L., C. Y. Shih, L. E. Nyquist, B. M. Bansal, H. Weismann, and G. A. McKay. 1982. "Rb-Sr and Sm-Nd Isotopic Constraints on the Origin of EETA79001: A Second Antarctic Shergottite." Abstract. *Lunar Planet Sci.* no. 23 : 879-880

9. VITA

Personal

Emily Jane Gackstatter

Born June 3, 1996 in St. Louis, MO

Raised in Avon, CT

Daughter of Chris and Karen Gackstatter

Education

Avon High School | Avon, CT

Diploma, June 2014

Baylor University | Waco, TX

Bachelor of Science in Geology, May 2018

Texas Christian University | Fort Worth, TX

Master of Science in Geology, December 2022

Experience

Graduate Teaching Assistant

Texas Christian University, August 2020-May 2022

GIS Technician

Atmos Energy, May 2022-November 2022

Compliance Coordinator

Atmos Energy, November 2022-Present

10. ABSTRACT

CLASSIFICATION AND PETROGENESIS OF NEW MARTIAN METEORITE, NWA 14904

By Emily Jane Gackstatter, M.S., 2022

Department of Geologic Sciences
Texas Christian University

Thesis Advisor: Dr. Rhiannon Mayne, Professor of Environmental Sciences

NWA 14904 is a previously unstudied and therefore unclassified meteorite. NWA 14094 is a 800g single stone meteorite, purchased by a private collector who later approached the Monnig Meteorite Lab at Texas Christian University (TCU) for classification and a detailed study of the meteorite. As a result of this study, the sample received the official name and classification of NWA 14904, poikilitic shergottite. A detailed scientific study and petrogenetic model was created using 3D modeling, computed tomography (CT) scans, electron microprobe analyses (EMPA), scanning electron microprobe (SEM) analyses, and comparing NWA 14904 to the existing Martian meteorite suite.